Exclusive Photoproduction of Charged Pions in Hydrogen and Deuterium from 1 to 6 GeV

by

Lingyan Zhu

Submitted to the Department of Physics
in partial fulfillment of the requirements for the degree of

Doctor of Philosophy in Physics

at the

MASSACHUSETTS INSTITUTE OF TECHNOLOGY

February 2004

Author .....
Department of Physics
Dec 2, 2003

Certified by .....
Haiyan Gao
Associate Professor
Thesis Supervisor

Accepted by .....
Thomas J. Greytak
Professor & Associate Department Head for Education

Exclusive Photoproduction of Charged Pions in Hydrogen and Deuterium from 1 to 6 GeV

by

Lingyan Zhu

Submitted to the Department of Physics
on Dec 2, 2003, in partial fulfillment of the
requirements for the degree of
Doctor of Philosophy in Physics

Abstract

The study of the transition region in the description of exclusive processes and hadron structure, from the nucleon-meson degrees of freedom in meson-exchange models at low energy to the quark-gluon degrees of freedom in pQCD at high energy, is essential for us to understand the strong interaction. The differential cross section measurements for exclusive reactions at fixed center-of-mass angles enable us to investigate the constituent counting rule, which explicitly connects the quark-gluon degrees of freedom to the energy dependence of differential cross sections.

JLab Experiment E94-104 was carried out in Hall A with two high resolution spectrometers. It included the coincidence cross section measurement for the $\gamma n \to \pi^- p$ process with a deuterium target and the singles measurement for the $\gamma p \to \pi^+ n$ process with a hydrogen target. The untagged real photons were generated by the electron beam impinging on a copper radiator. The photon energies ranged from 1.1 to 5.5 GeV, corresponding to the center-of-mass energies from 1.7 to 3.4 GeV. The pion center-of-mass angles were fixed at 50°, 70°, 90°, and also 100°, 110° at a few energies.

The JLab E94-104 data presented in this thesis contain four interesting features. The data exhibit a global scaling behavior for both π^- and π^+ photoproduction at high energies and high transverse momenta, consistent with the constituent counting rule and the existing π^+ photoproduction data. This implies that the quark-gluon degrees of freedom start to play a role at this energy scale. The data suggest possible substructure of the scaling behavior, which might be oscillations around the scaling value. There are several possible mechanisms that can cause oscillations, for example the one associated with the generalized constituent counting rule involving quark orbital angular momentum. The data show an enhancement in the scaled cross section at center-of-mass energy near 2.2 GeV, where baryon resonances are not as well known as those at low energies. The differential cross section ratios for exclusive $\gamma n \to \pi^- p$

to $\gamma p \to \pi^+ n$ process at $\theta_{cm} = 90^\circ$ start to show consistency with the prediction based on one-hard-gluon-exchange diagrams at high energies.

Thesis Supervisor: Haiyan Gao
Title: Associate Professor

Acknowledgments

This thesis could never have been completed without the help of many people and I would like to express my earnest appreciation towards all of them.

First of all, I sincerely thank my research advisor Haiyan Gao, who provided me with constant encouragement and guidance both in research and in life. I admire her enthusiasm and devotion towards her work, as well as her wisdom and insight into physics. As a successful woman in physics, she is a role model for me. I feel lucky to be her student.

Next, I thank all the Jefferson Lab (JLab) staffs/technicians for providing high-quality beam and good working environment. I thank Hall A E94-104 collaboration members for their contributions to this experiment, especially Bogdan Wojtsekhowski, Jian-Ping Chen, Scot Spiegel, Robert Michaels, Nilanga Liyanage, Dave Meekins, Douglas Higinbotham, Arun Saha, John Lerose, Ed Folts and Hall A leader Kees de Jager at JLab, Roy Holt, John Arrington, Krishni Wijesooriya, Elaine Schulte and Paul Reimer at Argonne National Lab, Ron Gilman, Xiaodong Jiang and Kathy McCormick at Rutgers University, Xiaochao Zheng and Claude Williamson as well as Haiyan Gao's research group at Massachusetts Institute of Technology (MIT), Marius Coman and Pete Markowitz at Florida International University. Bogdan Wojtsekhowski played a leading role in preparing all the detectors for the experiment; Scot Spiegel did the technical work of assembling an aerogel detector; Jian-Ping Chen guided me into the research life at JLab; Roy Holt kept a close eye on the experiment and provided regular and stimulating suggestions. Haiyan Gao's research group was essential in accomplishing the experiment: postdoctoral associate Hong Xiang did an excellent job in coordinating the whole collaboration and technicians, in addition to assembling detectors and analyzing data; postdoctoral associate Dipangkar Dutta helped tremendously in both online and offline data analysis based on his former experiences and quick learning abilities; Wang Xu did the crucial work on software by tailoring the simulation program MCEEP and event decoding program ESPACE

for this experiment; Feng Xiong also provided important assistance to this experiment.

I would also thank many theorists for their helpful calculations and stimulating discussions: Robert Wiringa and Hartmuth Arenhövel on the momentum distribution of the neutron in the deuteron target, Pankaj Jain on the nuclear transparency of deuteron, Igor Strakovsky on the SAID/MAID model and baryon resonances, and Hanwen Huang on the $\frac{d\sigma/dt(\gamma n \to \pi^- p)}{d\sigma/dt(\gamma p \to \pi^+ n)}$ ratio.

In regard to the thesis itself, I thank thesis committee members, William Donnelly and June Matthews at MIT, for stimulating comments. Also, I thank Jian-Ping Chen, Douglas Higinbotham and especially Claude Williamson for careful reading of the thesis and helpful suggestions on thesis writing.

Last but not least, I thank my entire family especially my husband Min Qu, for love and support. I would also thank the fellow students and friends at MIT (Xiaochao Zheng, Zhengwei Chai, Bin Zhang, Yuan Xiao, Marat Rvachev, ...) and those at JLab (Lei Guo, Bitao Hu, Ting Chang, Mina Nozar, ...) for friendship and help.

Contents

List of Figures

List of Tables

Chapter 1

Introduction and Physics Motivations

1.1 Introduction

Quantum ChromoDynamics (QCD) is currently the fundamental theory for describing the strong interaction, but it is not amenable to analytical solutions. Therefore some dynamical models or theories have to be developed. Meson-exchange models in terms of the nucleon-meson degrees of freedom reproduce the nuclear physics data well at low energy, and perturbative QCD (pQCD) in terms of the quark-gluon degrees of freedom succeeds in explaining many experiments at high energy. But little is known about the transition between these two regions. Testing the constituent counting rule for the exclusive reactions is one way to study the transition of the subnuclear degrees of freedom.

The constituent counting rule establishes a direct connection between the quark-gluon degrees of freedom and the energy dependence of the differential cross section at fixed center-of-mass angles. This rule was first derived from simple dimensional counting [1, 2, 3] and was later confirmed in a short-distance pQCD approach [4]. It is consistent with many exclusive measurements [6, 7, 8, 9]. However, there are

still some puzzles. This rule begins to agree with experimental data at energies as low as 1 GeV [8], whereas pQCD is not expected to be valid at such low energies. Also, the hadron helicity conservation rule, another outcome of the same pQCD framework, does not agree with data in the same energy and momentum transfer region [10, 11]. The previously ignored parton orbital angular momentum seems to be essential to explain the hadron helicity nonconservation and other polarization measurements [12, 13]. In addition, there are some anomalies beyond the constituent counting rule in the extensively studied pp scattering process [14, 15, 16].

Single charged pion photoproduction is a good process that can be used to study the transition since the cross section decreases relatively slowly as the energy increases. And the π^-/π^+ cross section ratio is amenable to theoretical predictions since some non-perturbative factors may cancel out in leading order. There have been some previous measurements for π^+ photoproduction at a few GeV [9], but there are no data for π^- photoproduction above 2 GeV. It is important to measure both π^- and π^+ photoproduction at several GeV to test the constituent counting rule and to test the predictions for the charged pion ratio.

This thesis focuses on extracting the differential cross sections for the single charged pion photoproduction processes, $\gamma p \to \pi^+ n$ and $\gamma n \to \pi^- p$, one of the major goals of JLab experiment E94-104 [17]. The photon beam energy ranged from 1 to 6 GeV. The pion center-of-mass angles were fixed at 50°, 70°, 90° and also 100°, 110° at a few energies. The results at 90° have already been published [18].

This thesis is divided into four chapters. Chapter 1 introduces the theoretical and experimental background for JLab (Jefferson Lab) experiment E94-104, cross section measurements on single charged pion photoproduction processes at photon energies of several GeV. Chapter 2 describes the experimental apparatus used by this experiment that was carried out at Hall A of JLab. Chapter 3 shows the data analysis procedures for extracting the differential cross sections. The last chapter presents the results and discussion. Some basic definitions and formalism can be found in Appendix A.

1.2 Transition of the Subnuclear Degrees of Freedom

There are four known types of fundamental interactions in the universe: the strong interaction, the electromagnetic interaction, the weak interaction and the gravitational interaction. The comparative strengths of the forces between two protons just in contact are roughly $1{:}10^{-2}{:}10^{-7}{:}10^{-39}$ [19].

The strong interaction can be described by QCD, one of the components of the SU(3)×SU(2)×U(1) Standard Model. The strong interaction can be explained by the exchange of gluons between quarks with color charges (or simply colors). It is similar to the exchange of photons between particles with charges in the electromagnetic interaction, except that gluons carry colors whereas photons carry no electrical charge. A quark carries one of the three colors. There are three generations and six flavors (or types) of quarks in total. The mesons ($q\bar{q}$) and baryons (qqq) are colorless singlets made of quarks (q) and anti-quarks ($\bar{q}$).

The strength of the strong interaction is quantified by the strong coupling constant α_s. To leading order, α_s decreases as the momentum transfer μ increases according to [20]

$$\alpha_s(\mu) \sim \frac{4\pi}{(11 - 4n_f/3) \times \ln(\mu^2/\Lambda^2)} \ , \tag{1.1}$$

where n_f is the number of the quark flavors with mass less than μ and Λ is constrained experimentally to be $0.1 \sim 0.3$ GeV. There are several ways to determine the strong coupling constant at $\mu = M_Z$, the mass of the Z gauge boson. The average of the world data is $\alpha_s(M_Z) = 0.117 \pm 0.002$, corresponding to $\Lambda = 216^{+25}_{-24}$ MeV [20]. The strong coupling constant at any energy scale can be deduced from the world average [21]. For example, $\alpha_s(1\text{GeV}) = 0.500$ and $\alpha_s(5\text{GeV}) = 0.210$. Equation 1.1 illustrates the asymptotic freedom phenomenon: $\alpha_s \to 0$ as $\mu \to \infty$.

At sufficiently high energy scales where the strong coupling constant is small, pQCD can be used to calculate the strong interaction with the perturbative expansion

technique. The original and still one of the most powerful quantitative supports of pQCD is the description of the Q^2 (equal to the magnitude of Mandelstam variable t) evolution of the structure functions, which also provides the most precise method for determining the strong coupling constant. As an example, Figure 1-1 [20] compares the world data on the proton structure function F_2^p as a function of Bjorken x ($x = \frac{Q^2}{2m\nu}$ with ν the energy transfer) at two Q^2 values with a pQCD calculation (with MRST2001 parameterization [22]). The agreement is remarkably good. However pQCD cannot predict the structure function *a priori* at any particular energy scale.

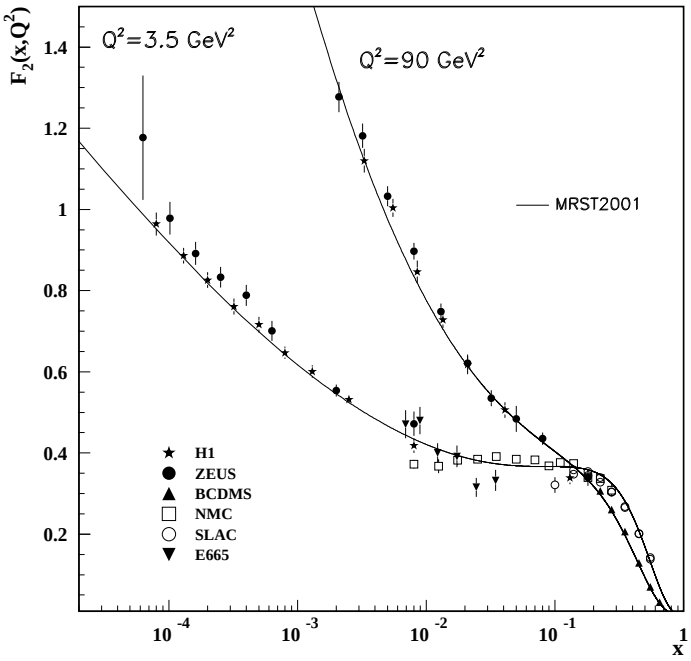

Figure 1-1: The proton structure function F_2^p as a function of Bjorken x at $Q^2 = 3.5, 90$ GeV^2.

At low energy scales, the strong coupling constant is large. The quarks and gluons are tightly bound in the mesons and nucleons, and the perturbative expansion technique is not valid. In 1935, Yukawa postulated that the strong interaction between neutrons and protons in the nucleus was due to the exchange of massive quanta and predicted a spinless quantum of mass around 100 MeV from the range of the strong force ($\sim$ 1 fm). The later discovered pion had the predicted properties. This initiated

the development of the meson-exchange models, which can describe the interaction between nucleons and other hadrons at low energy. Figure 1-2 [23] exhibits the success of this approach in pion photoproduction processes. However most meson-exchange models begin to lose their descriptive capabilities at energies of several hundred MeV.

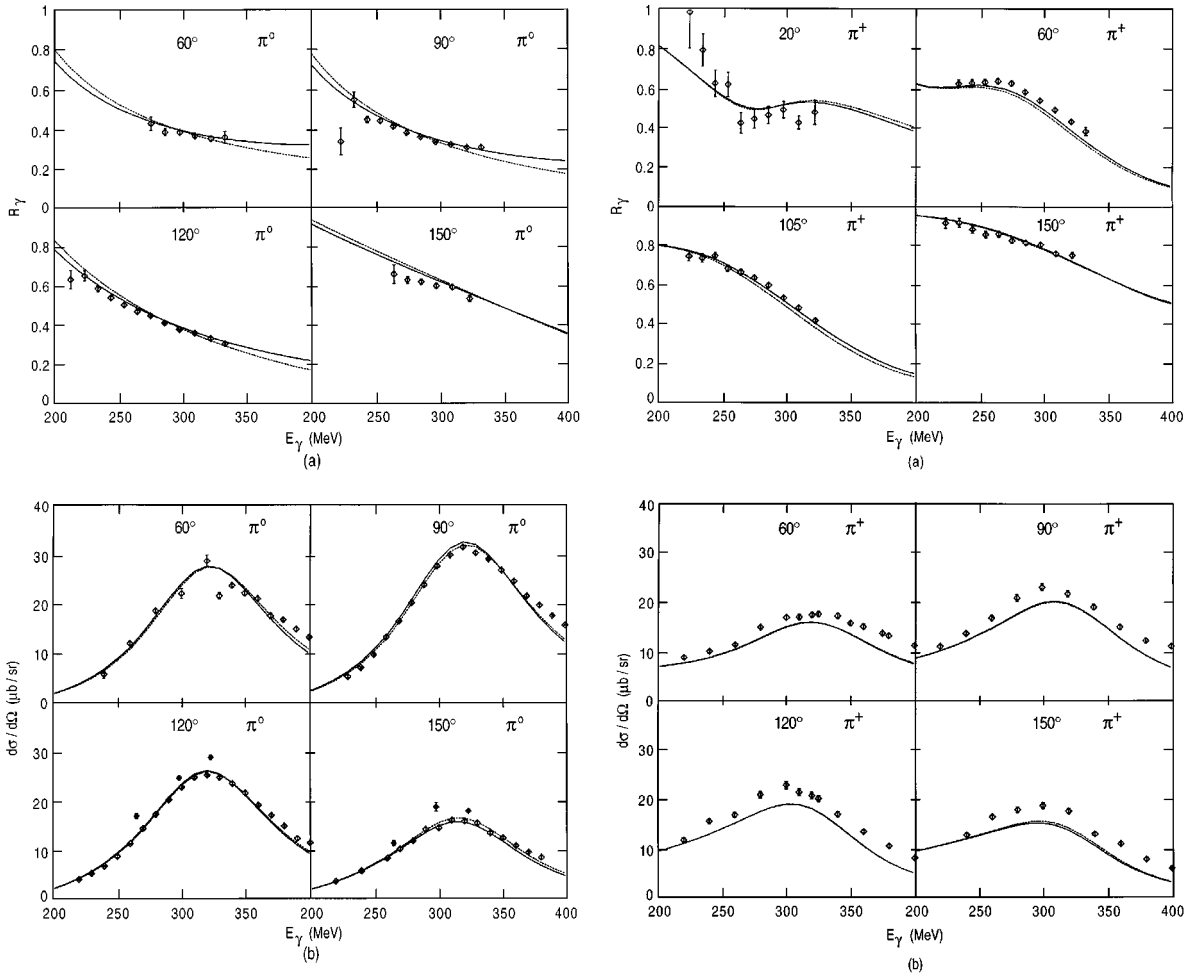

Figure 1-2: The photon-asymmetry ratios $R_\gamma = d\sigma_\parallel/d\sigma_\perp$ (a) and differential cross sections $d\sigma/d\Omega$ (b) at four angles in the center-of-mass frame for the $\gamma p \to \pi^0 p$ reaction (left) and $\gamma p \to \pi^+ n$ reaction (right). The solid and dotted curved are from the meson-exchange calculation with different parameterizations: $(g_{\omega NN}, G_M, G_E)$=(10.5,1.85,+0.025) and (7.0,1.95,-0.025). E_γ is the photon energy in the lab frame.

In summary, QCD describes the nature of the strong interaction, although it is not amenable to analytical solutions. The meson-exchange models with meson-nucleon

degrees of freedom succeed in modeling the strong interaction at low energies, while pQCD with quark-gluon degrees of freedom is valid at high energies. Studying the transition region of the subnuclear degrees of freedom will be essential for us to understand the strong interaction and develop models for medium energies.

1.3 Constituent Counting Rule

The constituent counting rule is also called the dimensional scaling rule. It states that

$$(d\sigma/dt)_{AB\to CD} \sim s^{-(n-2)} f(\theta_{cm}) \tag{1.2}$$

for exclusive reactions when $s \to \infty$. Here s and t are the Mandelstam variables (see Appendix A.2) and n is the total number of elementary fields (quarks, leptons or photons) which carry finite fractions of momentum. It predicts a scaling behavior of cross sections at fixed center-of-mass angle θ_{cm} and large s, for example $(d\sigma/dt)_{pp\to pp} \sim s^{-10}$, $(d\sigma/dt)_{\pi p\to \pi p} \sim s^{-8}$, $(d\sigma/dt)_{\gamma d\to pn} \sim s^{-11}$ and $(d\sigma/dt)_{\gamma N\to \pi N} \sim s^{-7}$. It can also predict the scaling of form factors. The constituent counting rule implies something of fundamental importance: the quark has not only a mathematical existence, giving current algebra, Bjorken scaling and the hadron spectrum, but a dynamical existence as well [2].

1.3.1 Theoretical Background

The constituent counting rule was originally derived from simple dimensional counting by Brodsky and Farrar [1], and simultaneously by Matveev *el al.* [3] in 1973. We will take the Brodsky and Farrar approach for pion photoproduction process $\gamma N \to \pi N$. Assuming that the process is dominated by the Feynman diagrams similar to Figure 1-3, the dimension of the invariant amplitude can be counted by using Feynman's rules and the renormalization of the spinors $u^\dagger u = 2E$. Each external fermion line contributes a dimension of energy $E^{0.5}$ to the invariant amplitude, while each external

boson line contributes a dimension of E^0. Each fermion propagator contributes a dimension of E^{-1}, while each external boson propagator contributes a dimension of E^{-2}. So the dimension of the invariant amplitude M is $(E^{0.5})^8 \cdot (E^{-1})^3 \cdot (E^{-2})^3 = E^{-5}$. If the only energy scale at large s and fixed θ_{cm} is the center-of-mass energy $\sqrt{s}$, then $M \sim s^{-5/2}$ and $(d\sigma/dt)_{\gamma N \to \pi N} \sim s^{-2} M^2 \sim s^{-7}$. Because the number of involved elementary fields n is 9, the power of s is thus $-(n-2)$, exactly as predicted by Equation 1.2.

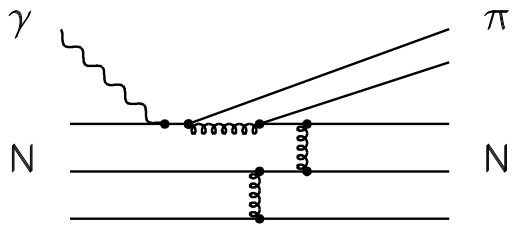

Figure 1-3: A typical Feynman diagram for the $\gamma N \to \pi N$ process.

Brodsky and Farrar also examined the required conditions for the simple dimensional derivation:
(a) the effective replacement of the composite hadron by constituents carrying finite fractions of the hadron momentum;
(b) the absence of any mass scale in the amplitude or binding corrections.
They showed that both condition (a) and (b) are natural features of renormalizable field theories, with certain dynamical assumptions concerning the nature of the wave function, the absence of infrared effects, and the accumulation of logarithms [2].

Later in 1980, Lepage and Brodsky proved [4] that the constituent counting rule can be a rigorous prediction of pQCD, up to calculable powers of the running coupling constant α_s or $(\ln Q^2/\Lambda^2)^{-1}$:

$$\frac{d\sigma}{dt}(AB \to CD) \sim \left(\frac{\alpha_s(p_\perp^2)}{s}\right)^{n-2} \left(\ln\frac{p_\perp^2}{\Lambda^2}\right)^{-2\sum_i \gamma_i} f(\theta_{cm}) \ , \tag{1.3}$$

where the transverse momentum $p_\perp = \sqrt{tu/s}$, and $\gamma_i = 0, -4/3\beta$ for a helicity

$|h| = 0, 1$ particle and $\gamma_i = -2/3\beta, -2/\beta$ for a helicity $|h| = 1/2, 3/2$ particle with $\beta = 11 - 4n_f/3$. Another outcome of this approach is the hadron helicity conservation:

$$h_A + h_B = h_C + h_D \ , \tag{1.4}$$

which leads to strong correlations between the final state helicities. The above results came from the calculation of an enormous number of connected tree diagrams for hard subprocesses (similar to that shown in Figure 1-3) without considering the parton orbital angular momentum, while the soft subprocesses, such as Landshoff diagrams [5] (similar to that shown in Figure 1-4) , were suppressed in leading order for example due to gluon radiation. The Landshoff diagrams, an independent scattering of pairs of constituents, would lead to $d\sigma/dt \sim s^{-8}$ for baryon-baryon scattering while the constituent counting rule predicts $d\sigma/dt \sim s^{-10}$ based on the calculation of hard subprocesses.

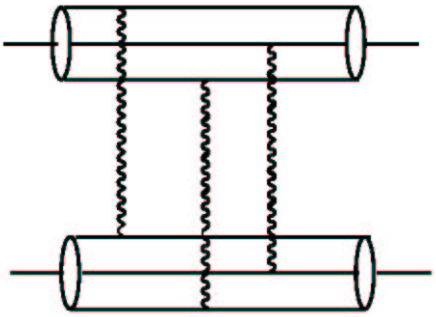

Figure 1-4: A typical Landshoff diagram for the baryon-baryon scattering.

The scaling behavior predicted by the constituent counting rule can also be reproduced with other phenomenological models. For the deuteron photodisintegration process for example, the Quark-Gluon String model (QGS) [24], the Reduced Nuclear Amplitudes (RNA) [25], the Asymptotic Meson Exchange Calculation (AMEC) [26] and the Hard Rescattering Mechanism (HRM) [27] can all describe the scaling behavior at $\theta_{cm} = 90°$ [8, 28]. Furthermore, QGS and HRM are in fair agreement with the asymmetric angular distribution of the deuteron photodisintegration data [28, 29].

1.3.2 Experimental Evidence

No matter how one rule can be derived, it should survive the experimental tests. The constituent counting rule is consistent with the experimental data for many processes, such as pp elastic scattering [6], hadron-hadron elastic scattering [7] and deuteron photodisintegration [8, 28].

The pp elastic scattering data for $s > 15$ GeV^2 and $|t| > 2.5$ GeV^2 exhibit the scaling behavior very clearly, as shown in Figure 1-5 [6]. The power of $\frac{1}{s}$ is equal to 9.7 ± 0.5, consistent with 10 as predicted by the constituent counting rule.

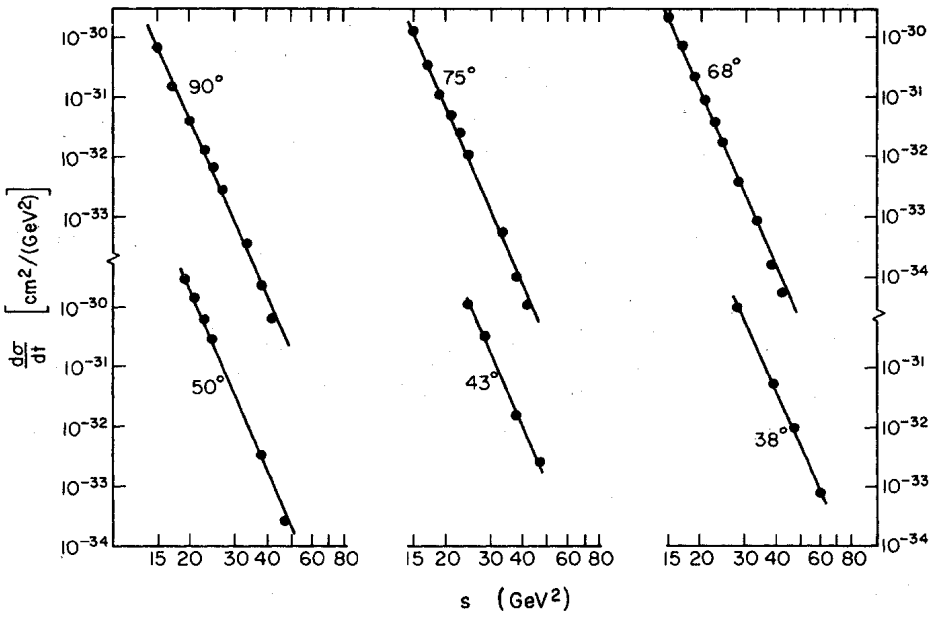

Figure 1-5: The pp elastic differential cross section $d\sigma/dt$ versus s at various center-of-mass angles. The parallel straight lines indicate the predicted scaling behavior.

Eight meson-baryon and two baryon-baryon exclusive reactions at $\theta_{cm} = 90°$ were measured at the AGS (the Alternate Gradient Synchrotron at BNL) with beam momenta of 5.9 GeV/c and 9.9 GeV/c. The fitted powers of $\frac{1}{s}$, as shown in Table 1.1 [7], are also consistent with what the constituent counting rule predicts, i.e. 8 for the meson-baryon reactions and 10 for the baryon-baryon reactions, except for reaction 15: $\pi^- p \to \pi^+ \Delta^-$. This indicates that nearly all of the listed exclusive reactions enter

Table 1.1: The cross section (in the unit of nb/GeV^2) scaling of E755 and E838 data at AGS for hadron-hadron interactions at $\theta_{cm} = 90°$. The nominal beam momentum was 5.9 GeV/c and 9.9 GeV/c for E838 and E755 respectively. There is also an overall systematic error of $\Delta n = \pm 0.3$ due to the systematic error of $\pm 13\%$ for E838 and that of $\pm 9\%$ for E755.

		Cross section		n-2
No.	Interaction	E838	E755	$(\frac{d\sigma}{dt} \sim 1/s^{n-2})$
1	$\pi^+ p \to p\pi^+$	132 ± 10	4.6 ± 0.3	6.7 ± 0.2
2	$\pi^- p \to p\pi^-$	73 ± 5	1.7 ± 0.2	7.5 ± 0.3
3	$K^+ p \to pK^+$	219 ± 30	3.4 ± 1.4	$8.3^{+0.6}_{-1.0}$
4	$K^- p \to pK^-$	18 ± 6	0.9 ± 0.9	≥ 3.9
5	$\pi^+ p \to p\rho^+$	214 ± 30	3.4 ± 0.7	8.3 ± 0.5
6	$\pi^- p \to p\rho^-$	99 ± 13	1.3 ± 0.6	8.7 ± 1.0
13	$\pi^+ p \to \pi^+ \Delta^+$	45 ± 10	2.0 ± 0.6	6.2 ± 0.8
15	$\pi^- p \to \pi^+ \Delta^-$	24 ± 5	≤ 0.12	≥ 10.1
17	$pp \to pp$	3300 ± 40	48 ± 5	9.1 ± 0.2
18	$\bar{p}p \to p\bar{p}$	75 ± 8	≤ 2.1	≥ 7.5

the scaling region at or below 5.9 GeV/c.

Deuteron photodisintegration is another channel that exhibits scaling behavior, as shown by Figure 1-6 [8, 28]. The onset of scaling in photon energy is different for different center-of-mass angles, i.e. $E_\gamma \sim 1, 1.5, 3, 4$ GeV for $\theta_{cm} = 90°, 70°, 53°, 37°$ respectively. The corresponding transverse momentum P_T is calculated to be around 1, 1.1, 1.3, 1.2 GeV/c by using the relation $P_T^2 = \frac{1}{2} M_d E_\gamma \sin^2\theta_{cm}$.

1.3.3 Puzzles and Anomalies

Despite the theoretical and experimental support for the constituent counting rule, there remain some puzzles and anomalies. First of all, it is surprising to see the onset of scaling as low as 1 GeV, such as in the photodisintegration data at $\theta_{cm} = 90°$ [8]. The applicability of pQCD to exclusive processes remains controversial in the GeV region. The pQCD calculation even fails to predict the magnitude of some fundamental quantities, such as the proton magnetic form factor $G_M^p(Q^2)$, as shown in Figure 1-7 [30]. This can be explained by the contributions from soft subprocesses. Hadron helicity conservation, another consequence of pQCD (this statement is cur-

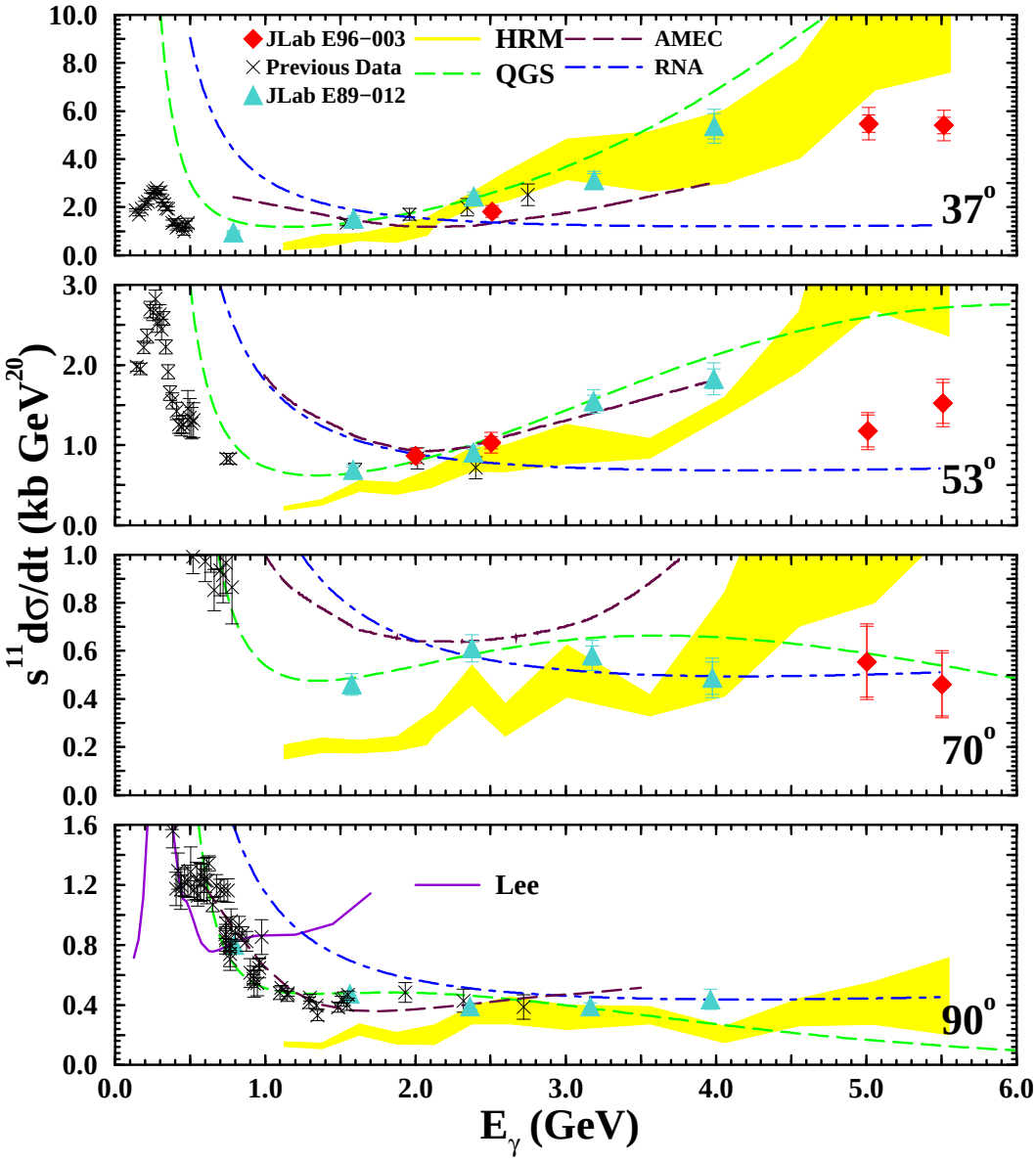

Figure 1-6: The scaled differential cross section of deuteron photodisintegration process versus photon energy at different proton center-of-mass angles. The JLab data are plotted with both statistical and total errors, while the previous data are plotted with statistical errors only.

rently under debate [31]), tends not to agree with polarization measurements, such as those from JLab for the photodisintegration process $d(\vec{\gamma},\vec{p})n$ up to 2.4 GeV [10] and neutral pion photoproduction $p(\vec{\gamma},\vec{p})\pi^0$ up to 4.1 GeV [11]. The nonzero parton orbital angular momentum, not taken into account by Lepage and Brodsky's approach [4], could cause violation of the hadron helicity conservation [12]. The orbital angular momentum could also cause asymptotic scaling of the proton form factor ratio: $F_2(Q^2)/F_1(Q^2) \sim (\log^2 Q^2/\Lambda^2)/Q^2$ with 0.2 GeV$\leq \Lambda \leq$0.4 GeV based on an explicit pQCD calculation [13] or $F_2(Q^2)/F_1(Q^2) \sim 1/\sqrt{Q^2}$ [31, 32] that agrees with the JLab Hall A data [33], while traditional pQCD predicts $F_2(Q^2)/F_1(Q^2) \sim 1/Q^2$.

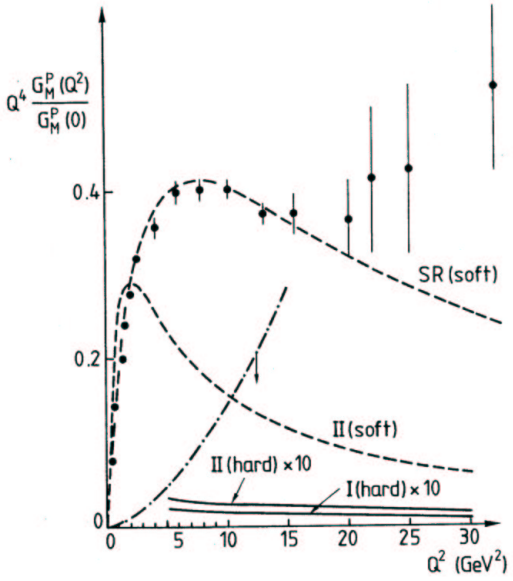

Figure 1-7: Proton magnetic form factor $G_M^p(Q^2)$.

Furthermore, several striking anomalies have been observed in pp scattering. One is the very large spin-spin correlation. The ratio of $(d\sigma/dt)_{\uparrow\uparrow}/(d\sigma/dt)_{\uparrow\downarrow}$ with spin normal to the scattering plane can reach 4 in pp elastic scattering at $\theta_{cm} = 90°$ [14]. Another anomaly is the oscillation of the differential cross section $d\sigma/dt$ around the scaling value in pp elastic scattering [15]. The last is the anomalous energy dependence of nuclear transparency (the attenuation of quasi-elastic pp scattering in the

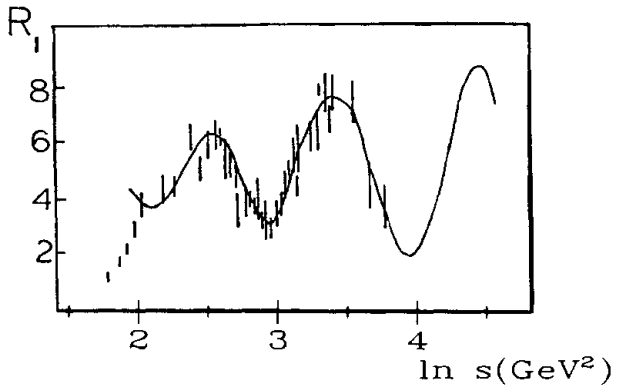

Figure 1-8: Oscillations of the scaled differential cross section $R_1(s) = \text{const} \cdot s^{10} d\sigma/dt$ around the scaling value in pp elastic scattering at $\theta_{cm} = 90°$.

nucleus) [16].

There exist different theoretical interpretations for the anomalies. An example is the interference mechanism in terms of nuclear interference between two types of subprocesses, the short-distance hard subprocesses and the long-distance soft (Landshoff) subprocesses [34]. This model can fit the oscillatory behavior in pp scattering very well (as shown in Figure 1-8), as well as the pp nuclear transparency data (as shown in Figure 1-9) and spin-spin correlation data. Alternatively, the above anomalies in pp scattering can be interpreted in terms of the interference of the pQCD background and two $J = L = S = 1, B = 2$ resonance structures associated with the strangeness and charm production thresholds [35]. The comparison with the data in terms of the spin correlation $A_{NN} = \frac{d\sigma_{\uparrow\uparrow} - d\sigma_{\uparrow\downarrow}}{d\sigma_{\uparrow\uparrow} + d\sigma_{\uparrow\downarrow}}$ is shown in Figure 1-10.

1.3.4 Recent Developments

Effective Strong Coupling Constant at Low Energy Scales [36]

The hadronic decay of the τ lepton was used to determine the effective strong coupling constant $\alpha_\tau(m'_\tau)$ for a hypothetical τ lepton mass in the range $0 < m'_\tau < m_\tau$. The definition of the effective strong coupling constant enables a fundamental study of

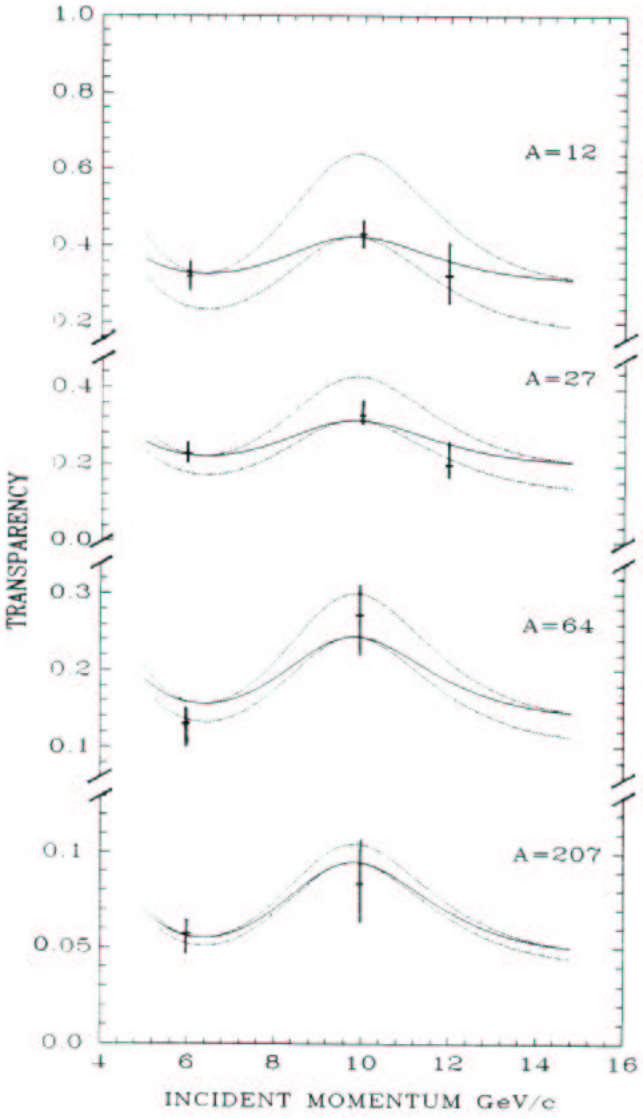

Figure 1-9: The energy dependence of nuclear transparency $T(s)$ for pp scattering. The band shows the complete range of sensitivity to the energy independent part of the nuclear phase δ_A between the two pQCD amplitudes, while the solid line represents the choice of $\delta_A = \delta_1$.

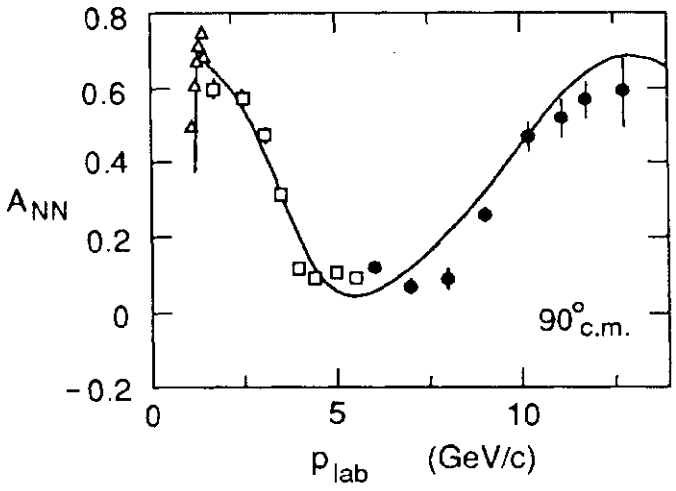

Figure 1-10: Spin-spin correlation in pp elastic scattering. The value of A_{NN} from pQCD alone is 1/3.

the strong coupling constant directly from first principles without any dependence on renormalization schemes. The results, as shown in Figure 1-11 [36], suggested that the physical strong coupling constant was effectively constant or frozen at low energy with s on the level of 1 GeV^2. The freezing of the strong coupling constant is required for deriving the constituent counting rule at low energy scales in the pQCD approach because the power of coupling constant α_s in the differential cross section is not small, close to $n-2$ with $n=9$ for pion photoproduction and $n=12$ for pp scattering, as shown in Equation 1.3.

Generalized Constituent Counting Rule [37]

As a simplest picture, the spin of a nucleon is the sum of the constituent quarks. This picture has been ruled out definitely by polarization measurements in the deep inelastic scattering region. The orbital angular momenta of the quarks and/or the gluons in the nucleon must contribute to the nucleon spin. There are many observables that may be potentially sensitive to the parton orbital angular momentum, although they do not directly measure it. For example, the proton form factor ratio F_2/F_1, as

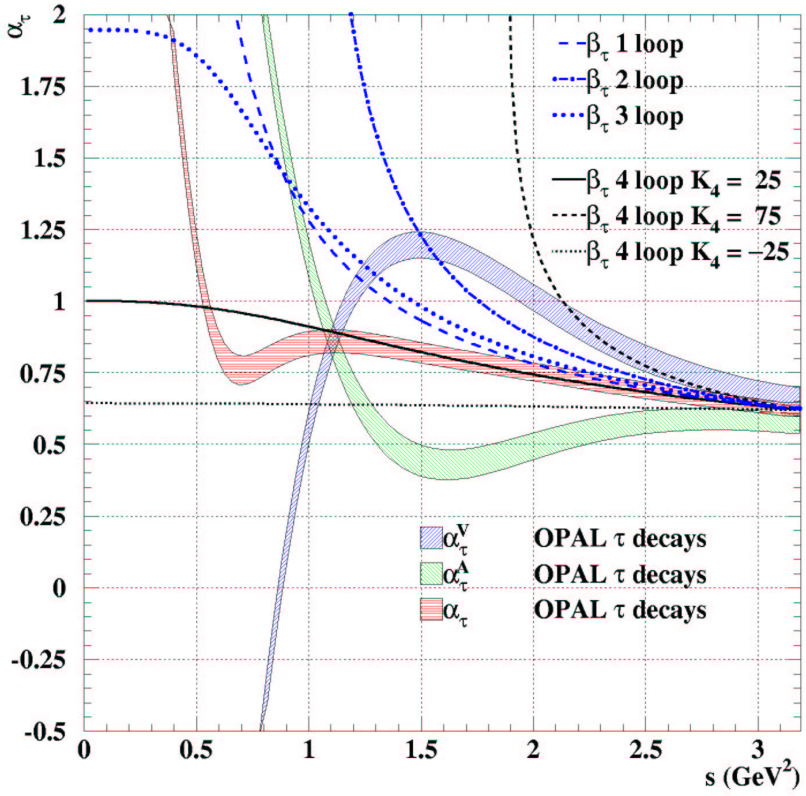

Figure 1-11: The effective strong coupling constant α_τ determined from non-strange hadronic decay of a hypothetical τ lepton are shown with error bands including statistical and systematic errors. The curves are from the traditional calculations to two-, three-, and four-loop order.

well as the twist-three spin-dependent structure function $g_T(x) = g_1(x) + g_2(x)$ and generalized or transverse momentum dependent parton distributions. [38]

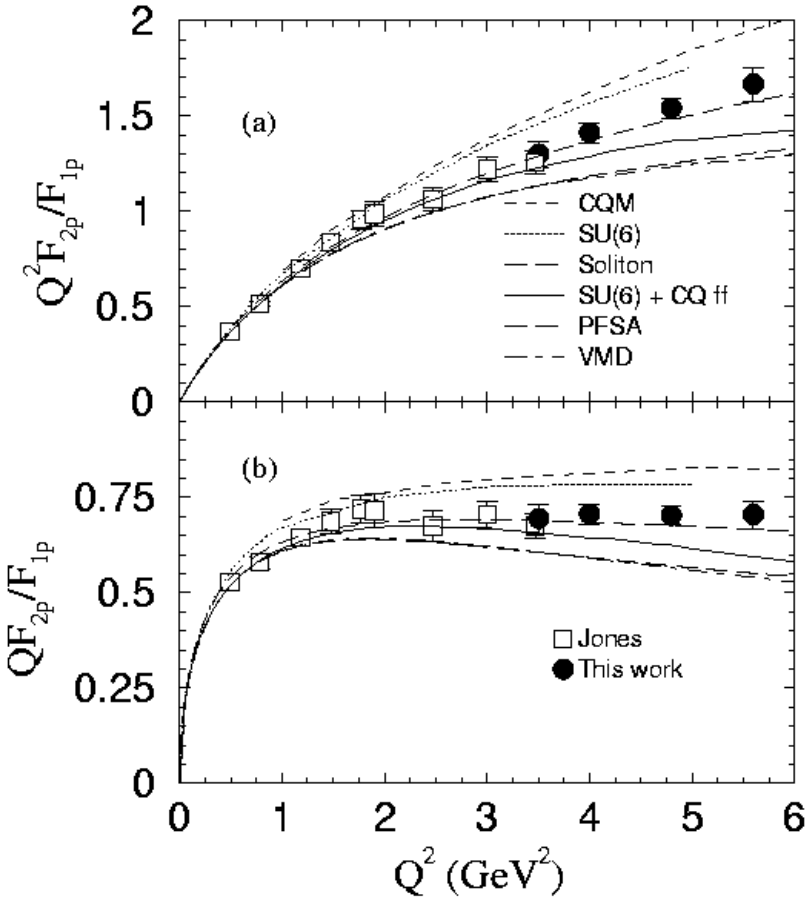

Figure 1-12: Proton form factor ratios F_{2p}/F_{1p} from JLab scaled by momentum transfer square Q^2 (a) or Q (b) versus Q^2, as well as some theoretical calculations. Those in open squares (Jones) were published in 2000, while those in solid circles (This work) were published in 2002.

The electromagnetic form factors of a nucleon are fundamental observables that contain important information about the internal structure of the nucleon. A dimensional counting and pQCD predicts that the hadron-helicity-conserving form factor $F_1(Q^2)$ scales as $1/Q^4$ and hadron-helicity-flip form factor $F_2(Q^2)$ scales as $1/Q^6$. So the form factor ratio $F_2(Q^2)/F_1(Q^2)$ scales as $1/Q^2$ [1, 2]. However this

is inconsistent with the high precision measurements at JLab with the recoil polarization technique, as shown in Figure 1-12 [33]. Though the validity of pQCD at GeV region remains controversial, the inconsistency may be solved by introducing the parton orbital angular momentum. The hereafter predicted scaling behavior of $(\log^2 Q^2/\Lambda^2)/Q^2$ with 0.2 GeV$\leq \Lambda \leq$0.4 GeV based on an explicit pQCD calculation [13] or $F_2(Q^2)/F_1(Q^2) \sim 1/\sqrt{Q^2}$ [31, 32] are both consistent with the JLab form factor data.

Including the nonzero parton orbital angular momentum may also change the expression of the constituent counting rule. Based on a hadronic light-cone wave function involving parton orbital angular momentum, which has been used to reproduce the JLab proton form factor data, a generalized constituent counting rule can be derived for hard exclusive processes by counting the soft mass dimensions of scattering amplitudes. For example, the wave function amplitude $\psi_n(x, k_\perp, l_z)$, with parton number n, space coordinate x, transverse momentum $k_\perp$ and orbital angular momentum component l_z, contains a mass scale $\Lambda^{n+|l_z|-1}$. Therefore a scattering amplitude involving $H = 1, ..., N$ hadrons contains a mass scale $\Lambda^{\sum_H (n_H+|l_{zH}|-1)}$. Hence for the hadronic reaction $A+B \to C+D+...$, the fixed-angle scattering cross section behaves like [37]

$$\Delta\sigma \sim s^{-1-\sum_H (n_H+|l_{zH}|-1)} , \tag{1.5}$$

where H sums over all hadrons involved. For parton orbital angular momentum $l_{zH} = 0$, this is just the traditional constituent counting rule mentioned before. As a result, the helicity flipped amplitudes for the $pp \to pp$ process were predicted to scale as $s^{-9/2}$ with $\sum_H |l_{zH}| = 1$ or s^{-5} with $\sum_H |l_{zH}| = 2$, while the helicity conserved amplitudes were known to scale as s^{-4}. The interference between different helicity amplitudes offers a new mechanism to explain the spin-spin correlation and oscillation around the scaling value in pp scattering. This can also cause the deviation from the traditional constituent counting rule for other exclusive processes, such as photoproduction of charged pions that will be discussed in this thesis. The detail investigation of the

scaling behavior may enable us to test the generalized counting rule, though the rigorous test should come from the polarization measurements allowing the separation of different helicity amplitudes.

Restricted Locality of Quark-hadron Duality [39]

The deviation from the constituent counting rule for exclusive processes may also be due to the breakdown of the locality of the quark-hadron duality. The quark-hadron duality is an empirical property of the data discovered by Bloom and Gilman before the advent of QCD [40]. It says that the production of resonances at lower energies and momentum transfers averages smoothly around the scaling curve measured at large momentum transfers, with an example shown in Figure 1-13 [41]. The sum over resonances can be related to the scaling behavior as a result of destructive interference. This is rather local at high energy due to the high density of the overlapping resonances, which is called the locality of quark-gluon duality. But the local degeneracy may not be reached at energies of a few GeV, which lead to the restricted locality of quark-gluon duality. The restricted locality may cause oscillations around the scaling value above the resonance region when different partial waves are not canceled locally.

The essential principles can be illustrated in a pedagogic model of a composite system with two spinless charged constituents, which is the simplest model for the realization of duality. The general form for the transition amplitude for Compton scattering $\gamma(\mathbf{k})\psi_0 \to \psi_N \to \psi_0\gamma(\mathbf{q})$ is

$$M = \sum_N < \psi_0(\mathbf{P_f}, \mathbf{r})|e_1 e^{-i\mathbf{q}\cdot\mathbf{r}/2} + e_2 e^{i\mathbf{q}\cdot\mathbf{r}/2}|\psi_N > \ < \psi_N|e_1 e^{i\mathbf{k}\cdot\mathbf{r}/2} + e_2 e^{-i\mathbf{k}\cdot\mathbf{r}/2}|\psi_0(\mathbf{P_i}, \mathbf{r}) > , \tag{1.6}$$

where ψ_N is the harmonic oscillator wave function with the main quantum number N and $\psi_0(\mathbf{P_i}, \mathbf{r})/\psi_0(\mathbf{P_f}, \mathbf{r})$ is the initial/final nucleon wave function. Taking the z axis along the incoming photon momentum direction, and explicitly including the angular

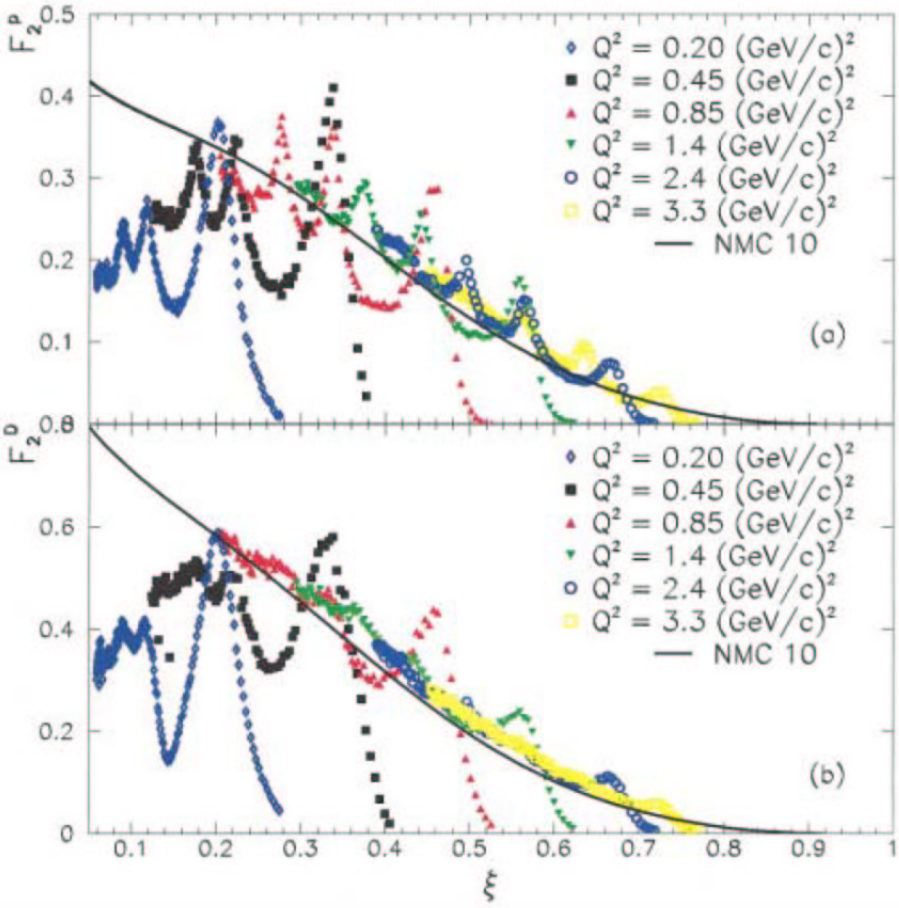

Figure 1-13: Structure function F_2 in the nucleon resonance region with hydrogen (a) and deuterium (b) targets, as functions of the Nachtmann scaling variable ξ ($\xi = 2x/(1+\sqrt{1+4M^2x^2/Q^2}$, identical to Bjorken scaling variable x but with corrections due to target mass M). The solid curves indicate a global fit to world's deep inelastic data by the New Muon Collaboration (NMC) for a fixed Q^2 of 10 (GeV/c)^2.

momentum L dependence in the energy spectrum, the transition amplitude can be expressed as

$$\begin{aligned} M &= \sum_{N=0}^{\infty} \left[(e_1^2 + e_2^2) \frac{1}{N!} \left(\frac{\mathbf{k} \cdot \mathbf{q}}{2\beta^2} \right)^N + 2e_1 e_2 \frac{1}{N!} \left(-\frac{\mathbf{k} \cdot \mathbf{q}}{2\beta^2} \right)^N \right] C_N e^{-(\mathbf{k}^2 + \mathbf{q}^2)/4\beta^2} \\ &= \sum_{N=0}^{\infty} \sum_{L=0(1)}^{N} \left[(e_1^2 + e_2^2) d_{00}^L(\theta) + 2e_1 e_2 d_{00}^L(\pi - \theta) \right] C_{NL} \mathcal{F}_{0N}^{(L)}(\mathbf{q}) \mathcal{F}_{N0}^{(L)}(\mathbf{k}) \ , \quad (1.7) \end{aligned}$$

where $\mathcal{F}_{N0}^{(L)}(\mathbf{k})$ denotes the transition (with momentum $\mathbf{k}$) to an excited state with quantum number (N, L), while $\mathcal{F}_{0N}^{(L)}(\mathbf{q})$ denotes the decay back to the ground state, $d_{00}^L(\theta)$ is the Wigner rotation function for relative angle change of θ between momentum $\mathbf{k}$ and $\mathbf{q}$ in the center-of-mass frame.

In this simple model, all $L =$ odd terms for a give N are proportional to $\cos\theta$ and hence vanish at $\theta = 90°$. Therefore

$$\begin{aligned} M_{\theta=90°} &= (e_1 + e_2)^2 e^{-(\mathbf{k}^2 + \mathbf{q}^2)/4\beta^2} \left[C_{00} (\frac{kq}{2\beta^2})^0 + \frac{1}{2!} \frac{1}{3} (-C_{22} + C_{20}) (\frac{kq}{2\beta^2})^2 \right. \\ &+ \left. \frac{1}{4!} \frac{1}{35} (3C_{44} - 10C_{42} + 7C_{40}) (\frac{kq}{2\beta^2})^4 + ... \right] \ , \quad (1.8) \end{aligned}$$

from which one can learn that:

- At high energies where the state degeneracy limit can be applied, all the terms with $N \neq 0$ and $L = 0$, ..., N would vanish due to the destructive interference and only the C_{00} term would survive, which gives the smooth scaling behavior.

- The L-degeneracy breaking effect for any given N leads to oscillations around the scaling value because different partial waves do not cancel locally. This is referred to as restricted locality.

The above procedures can be generalized to the physical exclusive processes by introducing an effective Lagrangian for quark-meson couplings. The general expression for the transition amplitudes for s and u channels (direct and virtual resonance

excitations) is

$$M_{fi}^{s+u} = e^{-(\mathbf{k}^2+\mathbf{q}^2)/6\alpha^2} \times \left\{ \sum_{n=0}^{\infty} (\mathcal{O}_d^{cc} + (-\frac{1}{2})^n \mathcal{O}_c^{cc}) \frac{1}{n!} \left(\frac{\mathbf{k}\cdot\mathbf{q}}{3\alpha^2} \right)^n + \sum_{n=1}^{\infty} (\mathcal{O}_d^{ci} + (-\frac{1}{2})^n \mathcal{O}_c^{ci}) \frac{1}{(n-1)!} \left(\frac{\mathbf{k}\cdot\mathbf{q}}{3\alpha^2} \right)^{n-1} + \sum_{n=2}^{\infty} (\mathcal{O}_d^{ii} + (-\frac{1}{2})^n \mathcal{O}_c^{ii}) \frac{1}{(n-2)!} \left(\frac{\mathbf{k}\cdot\mathbf{q}}{3\alpha^2} \right)^{n-2} \right\} , \quad (1.9)$$

where the multiplets are degenerate in n. The spin structures, charge and isospin operators have been included in the symbol $\mathcal{O}$. The superscript "c" ("i") stands for center-of-mass or c.m. (internal). Terms proportional to $(\mathbf{k}\cdot\mathbf{q}/3\alpha^2)^n$ denote correlations of c.m.-c.m. motions (superscript cc), while $(\mathbf{k}\cdot\mathbf{q}/3\alpha^2)^{n-1}$ and $(\mathbf{k}\cdot\mathbf{q}/3\alpha^2)^{n-2}$ denote the c.m.-internal (ci) and internal-internal correlations (ii) respectively. The subscript "d" ("c") denotes the direct (coherent) process in which the photon and meson couple to the same (different) quarks. The coherent process is suppressed by a factor of $(-1/2)^n$ in comparison with the direct one.

In the low energy regime, the degeneracy in n breaks. Multiplets of L and S dependent resonances can be separated in this model. This quantitatively described the resonances up to $E_\gamma \approx 500$ MeV. In the high energy limit where the degeneracy achieves, the dominant terms come from the correlation of the c.m.-c.m. motions and the scaling behavior can be realized at $\theta = 90^\circ$ as

$$\begin{aligned} M_{fi}^{s+u} &= (\mathcal{O}_d^{cc} + \mathcal{O}_c^{cc} e^{-\mathbf{k}\cdot\mathbf{q}/2\alpha^2}) e^{-(\mathbf{k}-\mathbf{q})^2/6\alpha^2} \\ &= (\mathcal{O}_d^{cc} + \mathcal{O}_c^{cc}) e^{-(\mathbf{k}-\mathbf{q})^2/6\alpha^2} \Big|_{\theta=90^\circ} \end{aligned} \quad (1.10)$$

where both direct and coherent process contribute and operators $\mathcal{O}_d^{cc}$ and $\mathcal{O}_c^{cc}$ are independent of n. For the kinematics just above the resonance region where the resonances are not degenerate, one may see effects of interference between resonances, which can cause deviations from the constituent counting rule.

1.4 Exclusive Charged Pion Ratio

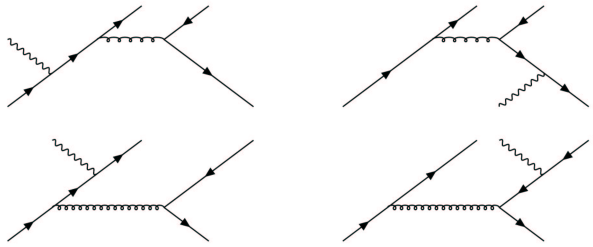

Figure 1-14: One-hard-gluon-exchange Feynman diagrams for the parton-level subprocess $\gamma q \to Mq$ in the single meson photoproduction $\gamma N \to MN$.

The exclusive charged pion ratio of $\frac{d\sigma/dt(\gamma n \to \pi^- p)}{d\sigma/dt(\gamma p \to \pi^+ n)}$ can be derived based on the one-hard-gluon-exchange Feynman diagrams [42, 43]. In Huang *et al.*'s approach [42], the helicity amplitude $M^M_{\mu'\nu',\mu\nu}$ for the photoproduction of a meson M as a function of Mandelstam variables s and t was assumed to factorize into the parton-level subprocess amplitude $H^M_{\mu'\nu',\mu\nu}$ and the nucleon form factors $R^M_i (i = V, A)$, where ν and ν' denote the helicity of the incoming and outgoing nucleon respectively, and μ and μ' denote the helicity of the incoming photon and outgoing meson. For example,

$$M^M_{\mu'+,\mu+}(s,t) = \frac{e}{2}\{H^M_{\mu'+,\mu+}(s,t)[R^M_V(t) + R^M_A(t)] + H^M_{\mu'-,\mu-}(s,t)[R^M_V(t) - R^M_A(t)]\} \ . \tag{1.11}$$

Evaluating the four Feynman diagrams in Figure 1-14 gives the parton-level subprocess amplitude for pseudoscalar meson ($\mu' = 0$) photoproduction

$$\begin{aligned}
H^{\pi^+}_{0+,++} &\propto f_M < 1/\tau >_M \frac{\sqrt{-2t}}{tu}(ue_u + se_d) \\
H^{\pi^+}_{0+,-+} &\propto f_M < 1/\tau >_M \frac{\sqrt{-2t}}{ts}(ue_u + se_d) \\
H^{\pi^-}_{0+,++} &\propto f_M < 1/\tau >_M \frac{\sqrt{-2t}}{tu}(ue_d + se_u) \\
H^{\pi^-}_{0+,-+} &\propto f_M < 1/\tau >_M \frac{\sqrt{-2t}}{ts}(ue_d + se_u) \ ,
\end{aligned} \tag{1.12}$$

where τ is the fraction of meson momentum carried by the active quark, f_M is the

decay constant of the meson, and $e_{u,d}$ is the charge of the u, d quark in units of positron charge. As $R_i^{\pi^+} \simeq R_i^{\pi^-} (i = V, A)$ due to isospin invariance, the exclusive charged pion ratio takes on a simple form:

$$\begin{aligned} \frac{d\sigma/dt(\gamma n \to \pi^- p)}{d\sigma/dt(\gamma p \to \pi^+ n)} &= (\frac{ue_d + se_u}{ue_u + se_d})^2 \frac{(s-u)^2 R_V^{\pi^-}(t)^2 + (s+u)^2 R_A^{\pi^-}(t)^2}{(s-u)^2 R_V^{\pi^+}(t)^2 + (s+u)^2 R_A^{\pi^+}(t)^2} \\ &\simeq (\frac{ue_d + se_u}{ue_u + se_d})^2 . \end{aligned} \tag{1.13}$$

1.5 Single Pion Photoproduction Experiments

Single pion photoproduction, $\gamma N \to \pi N$, is a relatively simple channel for studying the strong interaction. It has larger cross sections at high energy than other channels due to its slower decrease with energy, $d\sigma/dt \sim s^{-7}$. Furthermore, one can form the differential cross section ratio for charged pion photoproduction: $\frac{d\sigma(\gamma n \to \pi^- p)/dt}{d\sigma(\gamma p \to \pi^+ n)/dt}$, which might be amenable to some simple calculations since many factors may cancel out in the ratio.

To study the transition from nucleon-meson degrees of freedom to quark-gluon degrees of freedom, it is essential to investigate the GeV region where the transition seems to happen. While there were some measurements at SLAC (Stanford Linear Accelerator Center) for the $\gamma p \to \pi^+ n$ process at 4, 5 and 7.5 GeV [9], which exhibit a global scaling behavior expected by the constituent counting rule, there are no data between 2 and 4 GeV for $\gamma p \to \pi^+ n$, and no data beyond 2 GeV for $\gamma n \to \pi^- p$. The previous data sets for single pion photoproduction at $\theta_{cm} = 90°$ are shown in Figure 1-15 [44]. This thesis experiment, JLab E94-104 [17], was proposed to measure the cross section for charged pion photoproduction $d\sigma(\gamma n \to \pi^- p)/dt$ and $d\sigma(\gamma p \to \pi^+ n)/dt$ from 1 to 6 GeV and to study the details of scaling behavior. In addition, the differential cross section ratio for charged pion photoproduction will be formed and compared to theoretical predictions.

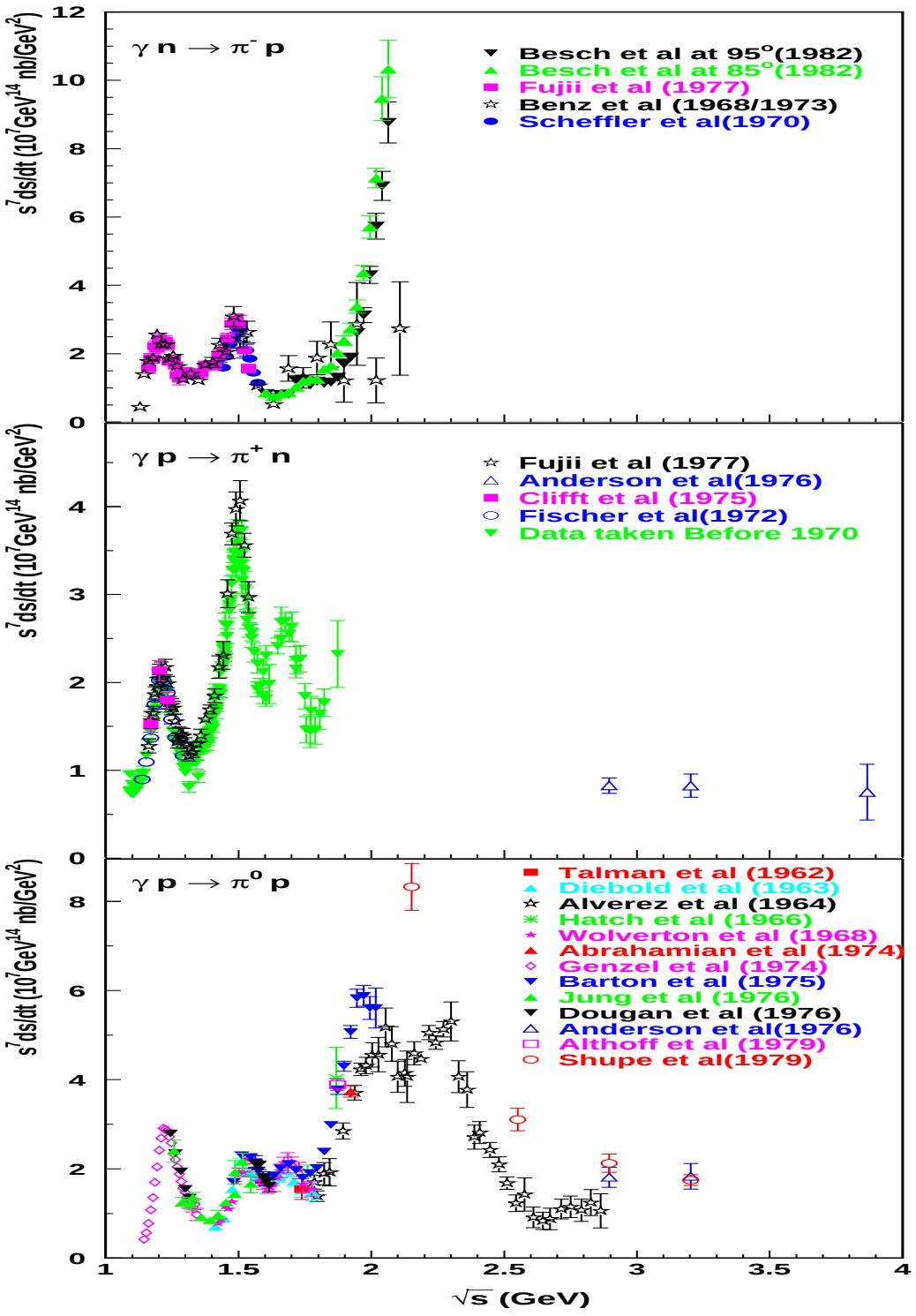

Figure 1-15: Scaled differential cross section $s^7 d\sigma/dt$ versus center-of-mass energy $\sqrt{s}$ for old single pion photoproduction data.

Chapter 2

JLab Hall A Experiment E94-104

2.1 Overview

The JLab experiment E94-104 [17], "The Fundamental $\gamma n \to \pi^- p$ Process in ^{2}H and ^{4}He in the 1.2-5.6 GeV Region", was proposed in 1994. It was carried out at Hall A in early 2001 and contained three sets of measurements:

- Exclusive cross sections were measured, for the $\gamma n \to \pi^- p$ process with a liquid deuterium (LD2) target and for the $\gamma p \to \pi^+ n$ process with a liquid hydrogen (LH2) target at pion center-of-mass angles of $50°, 70°$, $90°$ and $100°$, to investigate the scaling behavior predicted by the constituent counting rule. The exclusive charged pion ratio was formed and compared with theoretical predictions.

- Coincidence cross sections were measured, for the $\gamma n \to \pi^- p$ process with a cryogenic helium target at pion center-of-mass angles of $50°, 70°$ and $90°$, to study the nuclear transparency of ^{4}He and to search for possible signs of color transparency.

- Singles charged photo-pion yield ratios were measured with a liquid deuterium (LD2) target at pion center-of-mass angles of $50°, 70°, 90°$ and $100°$, to test

different theoretical predictions.

This thesis will focus on the first set of measurements and present the differential cross section results for the coincidence π^- and singles π^+ photoproduction processes. Real bremsstrahlung photons were generated by the electrons impinging on a copper radiator. A liquid hydrogen target was used as the proton target, while a liquid deuterium target was used as an effective neutron target. The outgoing pions and protons were detected by the two high resolution spectrometers (HRS) in Hall A. Based on two-body kinematics, the incident photon energies were reconstructed from the final states, i.e. the momentum and angle of the π^+ in the singles measurements, or momenta and angles of the π^- and p in the coincidence measurements. The photoproduction processes were simulated with a Monte Carlo simulation program for JLab Hall A to determine the acceptance. The differential cross section $\frac{d\sigma}{dt}$ was extracted by comparing data and simulation under the same conditions or cuts.

The coincidence kinematics for the $\gamma n \rightarrow \pi^- p$ process are listed in Table 2.1. Normally, the negative pions were detected by the spectrometer to the right of the beam line (viewed along the beam direction), and the protons detected by the left spectrometer. But a few kinematics, such as coin13r and coin16r, required the polarities of the spectrometers to be reversed, because a hardware problem in the right spectrometer limits its maximum momentum to be 3.16 GeV/c. The singles kinematics for $\gamma p \rightarrow \pi^+ n$ process are listed in Table 2.2. The positive pions were detected by the left spectrometer with positive polarity. The beam energies tabulated in Table 2.1 and Table 2.2 were the nominal values used to set the spectrometers, which may deviate from the measured ones by several MeV (see Section 2.2.2). The spectrometer momentum and angle settings were calculated by using photon energy of 75 MeV below the beam energy, i.e. $E_e - 75$ (MeV), where the multiple pion production processes were suppressed. It was informative to see the end point of the photon energy spectrum. The clear cutoff helped to check the reconstruction procedure and the background level. Therefore the photon energies were changed to be $E_e - 50$

Kin. (#)	E_e (GeV)	θ_{cm} (°)	P_L (GeV/c)	θ_L (°)	P_R (GeV/c)	θ_R (°)	$\sqrt{s}$ (GeV)	$-t$ (GeV/c)^2
coin1	1.173	50.0	+0.521	60.17	-0.953	28.33	1.71	0.253
coin2	1.173	70.0	+0.727	49.72	-0.838	41.45	1.71	0.467
coin3	1.173	90.0	+0.923	39.75	-0.706	56.66	1.71	0.709
coin4	1.721	50.0	+0.697	58.32	-1.433	24.46	1.99	0.433
coin5	1.721	70.0	+0.989	47.39	-1.238	36.02	1.99	0.798
coin6	1.721	90.0	+1.277	37.37	-1.015	49.73	1.99	1.212
coin18	1.875	50.0	+0.742	57.79	-1.566	23.64	2.06	0.484
coin20	1.875	90.0	+1.370	36.75	-1.099	48.21	2.06	1.355
coin7	2.558	50.0	+0.913	55.67	-2.108	20.96	2.35	0.696
coin8	2.558	70.0	+1.322	44.37	-1.794	31.02	2.35	1.282
coin9	2.558	90.0	+1.740	34.45	-1.438	43.18	2.35	1.948
coin7r	2.558	50.0	-2.108	20.96	+0.913	55.67	2.35	0.696
coin8r	2.558	70.0	-1.794	31.02	+1.322	44.37	2.35	1.282
coin9r	2.558	90.0	-1.438	43.18	+1.740	34.45	2.35	1.948
coin10	3.395	50.0	+1.113	53.21	-2.799	18.57	2.67	0.971
coin11	3.395	70.0	+1.642	41.74	-2.363	27.56	2.67	1.789
coin12	3.395	90.0	+2.195	32.01	-1.866	38.57	2.67	2.718
coin22	3.395	100.0	+2.466	27.69	-1.614	45.24	2.67	3.190
coin21	3.395	110.0	+2.725	23.65	-1.369	53.01	2.67	3.648
coin13r	4.232	50.0	-3.489	16.84	+1.300	51.04	2.95	1.248
coin14	4.232	70.0	+1.949	39.51	-2.929	25.05	2.95	2.299
coin15	4.232	90.0	+2.638	30.01	-2.291	35.18	2.95	3.494
coin16r	5.618	70.0	-3.863	22.08	+2.442	36.48	3.36	3.148
coin17	5.618	90.0	+3.359	27.38	-2.990	31.11	3.36	4.785

Table 2.1: Spectrometer settings for coincidence kinematics. E_e is the electron beam energy, θ_{cm} the pion center-of-mass angle, P_L (P_R) the central momentum for left (right) spectrometer with the sign indicating its polarity, and θ_L (θ_R) is the central scattering angle for left (right) spectrometer. s and t are the Mandelstam variables.

Kin. (#)	E_e (GeV)	θ_{cm} (°)	P_L (GeV/c)	θ_L (°)	$\sqrt{s}$ (GeV)	$-t$ (GeV/c)^2
sing2	1.173	70.0	+0.838	41.45	1.71	0.467
sing3	1.173	90.0	+0.706	56.66	1.71	0.709
sing4	1.721	50.0	+1.433	24.46	1.99	0.433
sing5	1.721	70.0	+1.238	36.02	1.99	0.798
sing6	1.721	90.0	+1.015	49.73	1.99	1.212
sing18	1.875	50.0	+1.566	23.64	2.06	0.484
sing19	1.875	90.0	+1.099	48.21	2.06	1.355
sing7	2.558	50.0	+2.108	20.96	2.35	0.696
sing8	2.558	70.0	+1.794	31.02	2.35	1.282
sing9	2.558	90.0	+1.438	43.18	2.35	1.948
sing10	3.395	50.0	+2.799	18.57	2.67	0.971
sing11	3.395	70.0	+2.363	27.56	2.67	1.789
sing12	3.395	90.0	+1.866	38.57	2.67	2.718
sing22	3.395	100.0	+1.614	45.24	2.67	3.190
sing21	3.395	110.0	+1.369	53.01	2.67	3.648
sing13	4.232	70.0	+2.929	25.05	2.95	2.299
sing14	4.232	90.0	+2.291	35.18	2.95	3.494
sing15	4.232	100.0	+1.967	41.36	2.95	4.101
sing16	5.618	90.0	+2.990	31.11	3.36	4.785
sing17	5.618	100.0	+2.547	36.69	3.36	5.615

Table 2.2: Spectrometer settings for singles kinematics. E_e is the electron beam energy, θ_{cm} the pion center-of-mass angle, P_L the central momentum for left spectrometer with the sign indicating its polarity, and θ_L is the central scattering angle for left spectrometer. s and t are the Mandelstam variables.

(MeV) and $E_e - 45$ (MeV) to calculate the spectrometer settings for kinematics at 1.721 GeV and 1.875 GeV respectively.

2.2 The Continuous Electron Beam

2.2.1 The Continuous Electron Beam Accelerator Facility

The JLab's Continuous Electron Beam Accelerator Facility (CEBAF) provides multi-GeV polarized electron beams. As a user facility for scientists worldwide, the primary mission of JLab is to conduct basic research that builds a comprehensive understanding of nuclei and nucleons. JLab also conducts applied research based on the technology developed for physics experiments, such as the Free Electron Laser (FEL) project.

CEBAF is the first large-scale application of superconducting radio-frequency (srf) electron accelerating technology. It can deliver a high-quality continuous polarized (>75%) electron beam with current up to 200 μA and energy up to 6 GeV. It consists of a pair of antiparallel superconducting linacs connected by two 180° bending arcs with a radius of 80 meters, in a racetrack shape shown in Figure 2-1 [45]. Three interlaced 499 MHz electron beams are injected from a state-of-the-art photocathode gun system that is capable of delivering beams of high polarization and high current to Hall A and Hall C (1$\sim$150 μA) while maintaining the high polarization and low current beam to Hall B (1$\sim$100 nA). Each linac consists a series of 20 cryomodules or 160 superconducting radio-frequency niobium cavities with 2 K helium coolant. Each niobium cavity contains the electric field that accelerates the electrons. The electrons can be circulated up to five times in the accelerator, gaining up to 1.2 GeV for each pass.

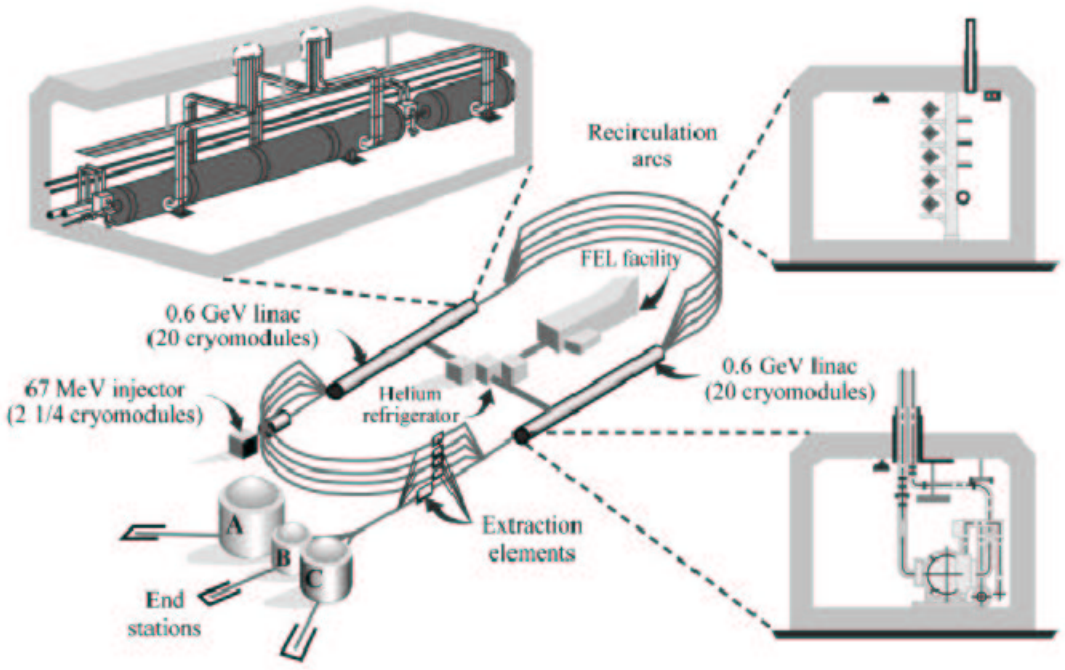

Figure 2-1: The schematic layout of CEBAF.

2.2.2 Beam Energy Measurement

The total energy of the electron beam can be determined absolutely to the precision of 0.02%, with either Arc or *ep* energy measurement.

The Arc energy measurement determines the beam momentum p from the bend angle θ of the electrons and the integral of the magnetic field $\int Bdl$ in the arc section of the beam line, according to [46]

$$p = k\frac{\int Bdl}{\theta} \ , \tag{2.1}$$

where $k = 0.2999792$ GeV rad T^{-1} m^{-1}/c. The bend angle is obtained by measuring the beam positions at the entrance and exit of the arc with four wire scanners (SuperHarps), as shown in Figure 2-2 [47]. The quadruples are turned off (dispersive mode) during the angle measurement. The magnetic field integral measurement is

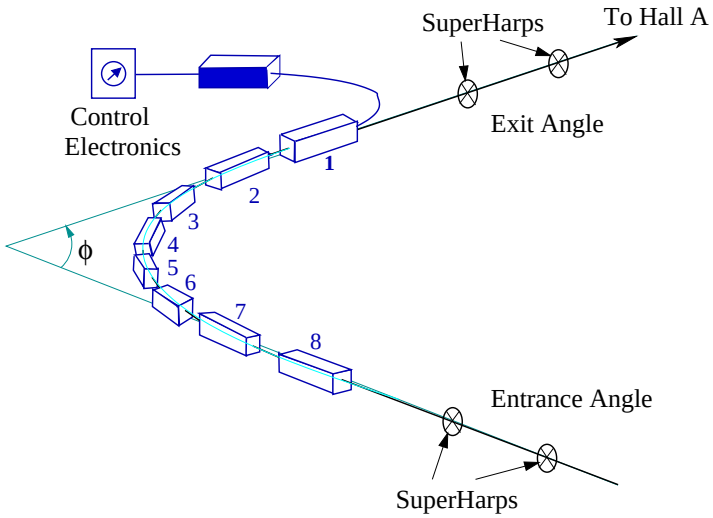

Figure 2-2: Schematic layout of the Arc energy measurement system.

determined by measuring the field of a reference magnet, powered in series with the eight dipoles in the arc vacuum that are inaccessible to a field measurement.

The beam energy can be determined from the Arc integral measurement alone by assuming the nominal bend angle of 34.2918°. The Arc integral measurement can be used as an approximation to the Arc energy measurement when the beam position measurement in the dispersive mode is not available.

The beam energy can also be determined from the current value of the field integral and the nominal bend angle, which is called the Tiefenback energy after correcting the quadruple effects based on previous comparisons between magnet settings and Arc beam energy measurement [48]. The Tiefenback energy is written into the data stream for each run. As shown in Figure 2-3 [49], Tiefenback energy agrees with Arc energy measurement within the uncertainty of 0.05% for beam energy above 1 GeV.

The *ep* energy measurement determines the beam energy by measuring *ep* elastic scattering with a stand-alone device 17 m upstream of the target, as shown in Figure 2-4 [46]. The relation between the beam energy E_e and the angle of the elastically

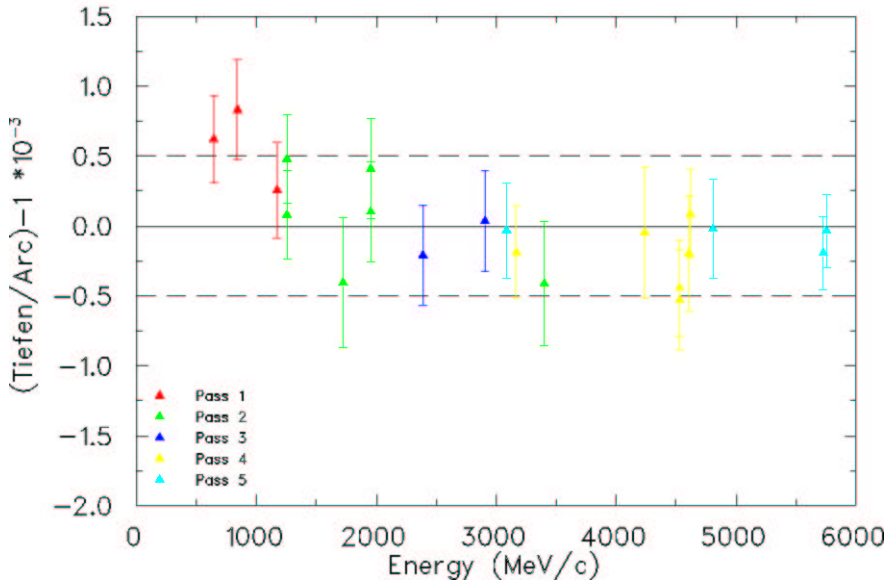

Figure 2-3: The comparison of Tiefenback energy with Arc energy measurement based on data taken from 1999 to 2002. The pass number is the number of times that the electrons are circulated in the accelerator.

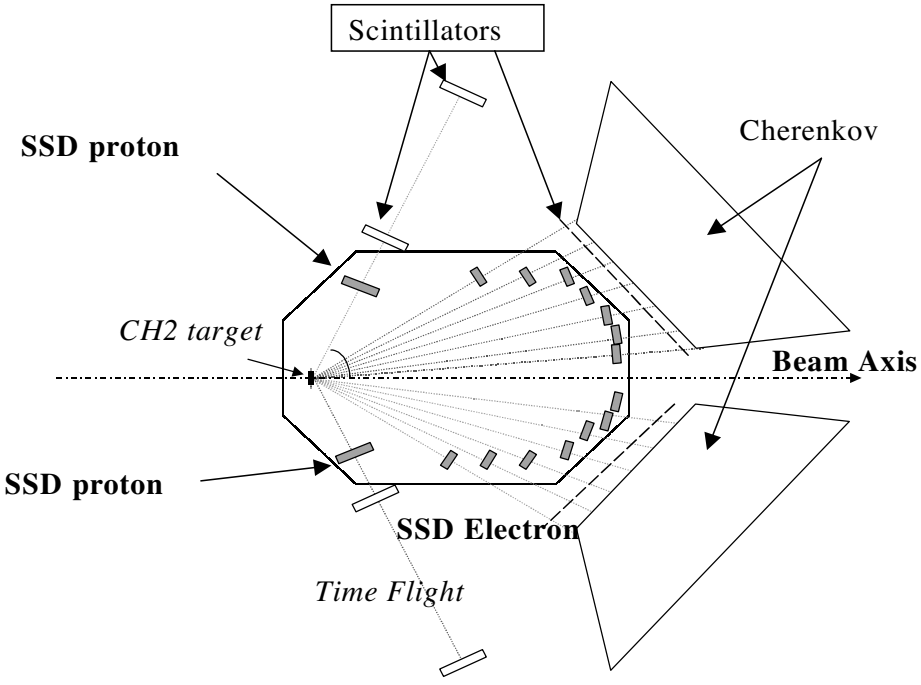

Figure 2-4: Schematic layout of the *ep* energy measurement system. SSD stands for Silicon Strip Detectors.

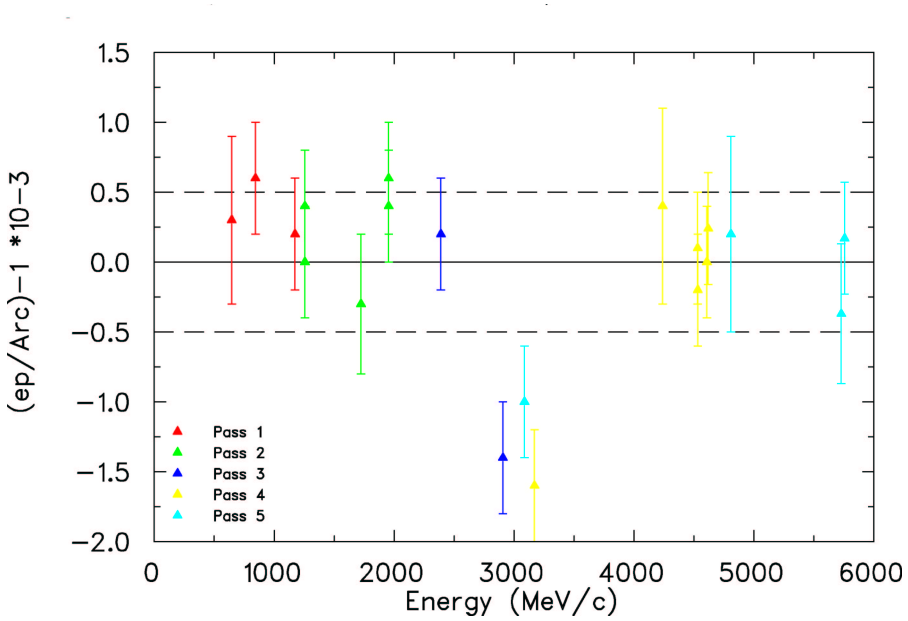

Figure 2-5: The comparison of *ep* energy measurement with Arc energy measurement based on data taken from 1999 to 2002. The pass number is the number of times that the electrons are circulated in the accelerator.

scattered electron θ_e and the recoil proton θ_p is

$$\begin{aligned} E_e &= M_p \frac{\cos\theta_e + \sin\theta_e/\tan\theta_p - 1}{1-\cos\theta_e} + O(m_e^2/E^2) \\ &= M_p(\cot\frac{\theta_e}{2}\cot\theta_p - 1) + O(m_e^2/E^2) \ , \end{aligned} \tag{2.2}$$

where m_e (M_p) is the rest mass of the electron (proton). There are two identical detection systems on both sides of the beam line to cancel some uncertainties in the beam position and direction.

As shown in Figure 2-5 [49], the Arc and *ep* energy measurements agree with each other within 0.05% except for beam energy around 3 GeV. Since the *ep* method uses different silicon strips to determine the electron angles for different energy ranges, the discrepancy around 3 GeV is conjectured to be caused by the misalignment of one particular silicon strip [46].

During the E94-104 experiment, both Arc and *ep* energy measurements were

planned for each beam energy, but not all were accomplished due to hardware problems. Table 2.3 lists all the energy measurements performed during the experiment and the beam energies used for the data analysis. The beam pass denotes the number of times that the electron beam is circulated in the accelerator. The overall relative uncertainty in beam energy determination was assigned to be 0.05%.

Beam Pass	Tiefenback (MeV)	Arc (MeV)	Arc integral (MeV)	*ep* (MeV)	Energy used (MeV)
1	1173.6	1173.3	1173.8	1173.6	1173.3
2	1722.7	-	1723.4	1722.8	1723.4
2	1876.9	-	-	-	1876.9
3	2560.6	-	2561.0	-	2561.5
4	3399.2	-	3400.0	3390.0	3400.0
5	4235.0	-	4236.4	-	4236.4
5	5615.0	5614.4	5617.0	-	5614.4

Table 2.3: Beam energy measurements for E94-104.

2.2.3 Beam Position Measurement

Two beam position monitors (BPMs), 7.516 m and 2.378 m upstream from the target, are used to determine the position and direction of the beam on the target. Each BPM is a cavity with a 4-wire antenna in one plane tuned to the RF frequency of the beam (1497 MHz). The standard difference-over-sum technique is used to compare the distances of the beam to the wires and hence determine the beam position in the plane. The combination of two BPMs gives the direction of the beam. BPM measures the beam position non-destructively and can be used to monitor the beam continuously. The BPM information is written event-by-event into the data stream, but with some delay. The average of the beam position from BPMs over 0.3 second is injected into the data stream every few seconds.

Two SuperHarps (wire scanners) provide absolute references to calibrate the BPMs. They are located at 7.345 m and 2.214 m upstream from the target respectively and

adjacent to the two BPMs. During the experiment E94-104, two sets of calibration data were taken by recording the readings of BPMs and SuperHarps for different beam positions. There were also some data taken to determine the pedestal positions of the BPM outputs.

2.2.4 Beam Current Measurement

The beam current is measured by two beam current monitors (BCMs), calibrated with the Unser monitor sandwiched between them, as shown in Figure 2-6 [50, 51].

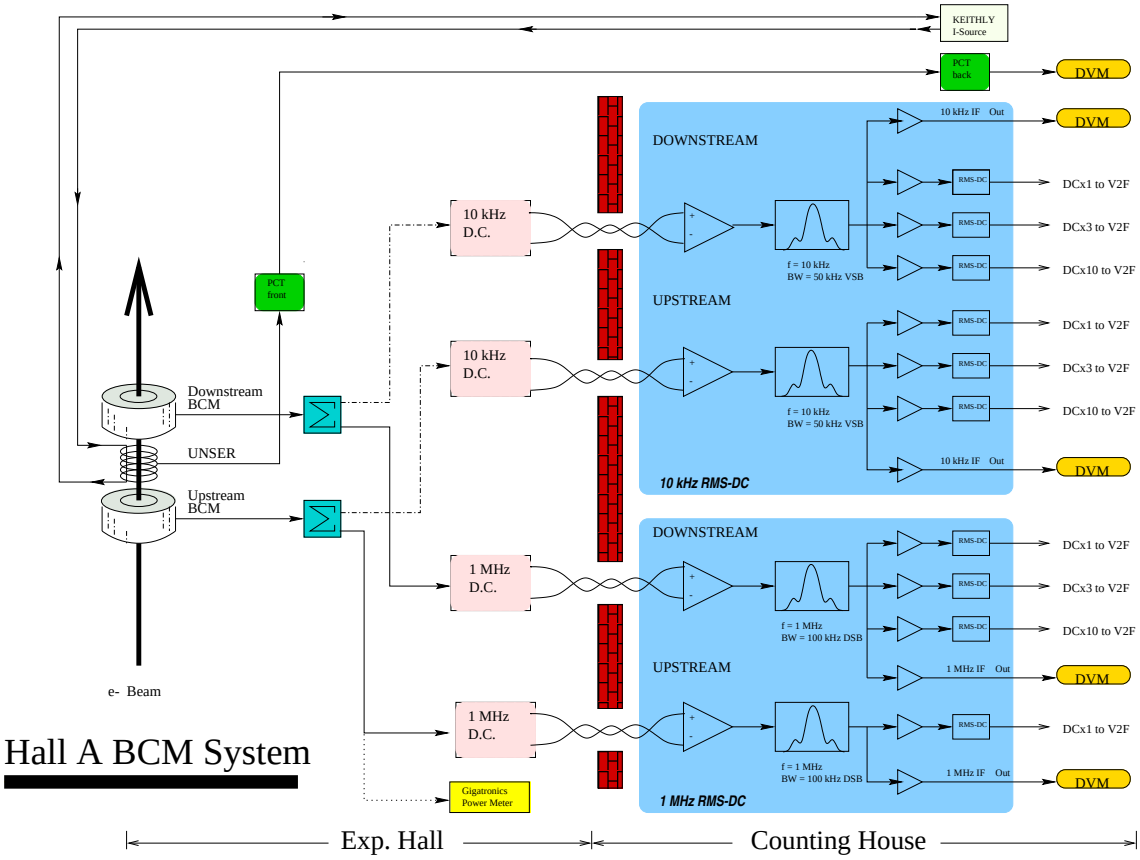

Figure 2-6: Schematic layout of the BCM system in Hall A.

The BCMs, cylindrical waveguides tuned to the frequency of the beam (1497 MHz), are used to monitor the beam linearly and continuously. When the electron beam passes, it excites the resonant transverse magnetic mode TM_{010}. The BCM

output, proportional to the beam current, is converted to a 10 kHz or 1 MHz (old system) signal by a down converter to reduce the frequency and is fed to an RMS-to-DC (RMS mean value to Direct Current) converter board with a 50 kHz bandpass filter to eliminate noise. The output is split into two sets, sampled data and integrated data. The sampled data are sent to a high precision Digital AC (Alternating Current) VoltMeter (DVM) whose digital output is proportional to the current averaged over one second. The integrated data are converted to voltage with a RMS-to-DC converter and then to frequency with a Voltage-to-Frequency converter (V2F) feeding into a scaler. The scaler reading is proportional to the integrated charge. Three amplifiers, with gain factors of 1, 3 and 10, are used to do the linear RMS-to-DC conversion for different current ranges. Due to the non-linear effect at low current and the saturation effect at high current, the DC×1 amplifier is normally used for beam current greater than 10 μA, the DC×10 amplifier for beam current below 30 μA, while the DC×3 amplifier for the range preferably between 1 μA to 200 μA. In total, there are six channels of charge outputs, u1/u3/u10 for the upstream BCM with different amplifiers, and d1/d3/d10 for the downstream BCM. As the E94-104 data were taken with currents ranging from 10 to 50 μA, the average of u3 and d3 was used to obtain the beam charge.

The Unser monitor, a Parametric Current Transformer, provides an absolute reference to calibrate BCMs. It cannot be used to monitor the beam continuously because the output signal drifts on a time scale of several minutes. During a typical calibration run, the beam current is ramped between zero and the maximum value for at least 5 cycles, dwelling at each step for 60 to 90 s. The time drift is measured by taking a zero current reading. The beam charge can be determined with an accuracy of 0.5% down to the current of 1 μA.

The calibration constants updated in January 2001 are listed in Table 2.4 [52]. Compared with those in May 1999, the upstream BCM calibration constants remained unchanged, while the downstream BCM constants dropped by around 3%. This

Scaler	u1	u3	u10	d1	d3	d10
Constant	1345	4114	12515	1303	4034	12728
Offset	92.1	167.1	102.6	72.2	91.1	199.5

Table 2.4: BCM calibration for experiment E94-104 in January of 2001. The charge (μC) is calculated as $\frac{\text{Scaler Readings}-\text{Offset}}{\text{Constant}}$.

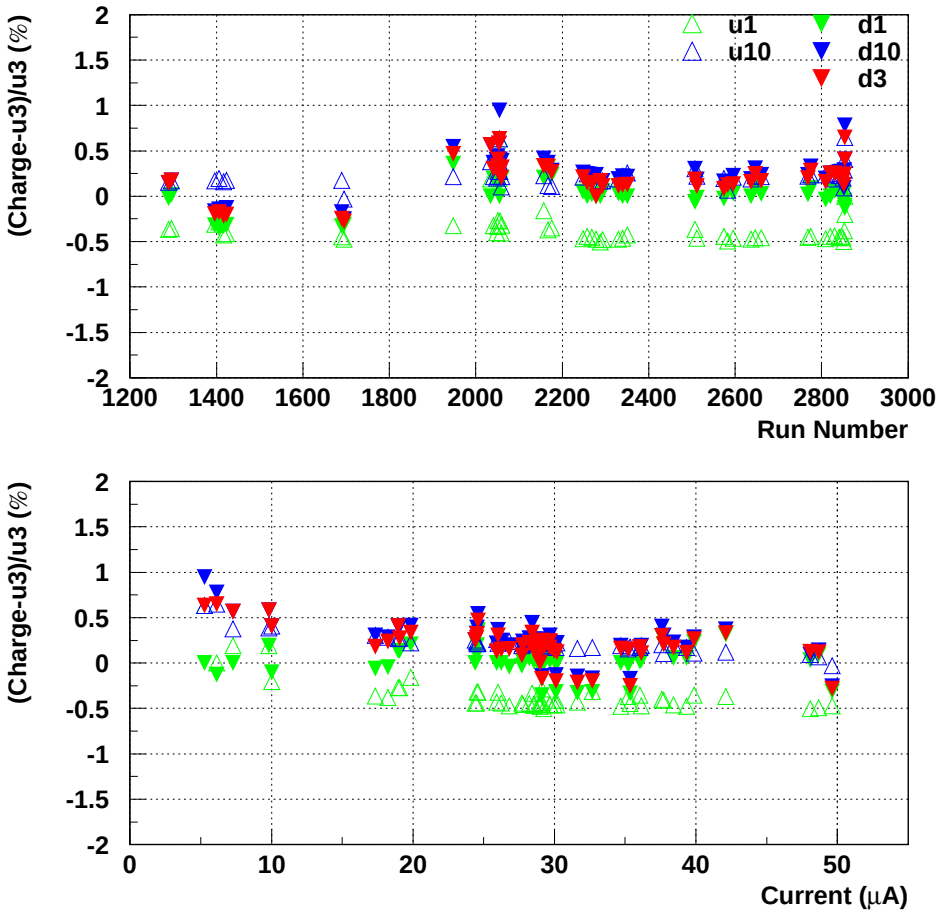

Figure 2-7: Comparison of different charge outputs. The production runs of experiment E94-104 ranged from 1211 to 2865.

was caused by the drift of the down converter's local oscillator frequency in the downstream BCM [50]. The consistency between different charge outputs and the stability of the calibration constants are illustrated in Figure 2-7.

2.2.5 Beam Rastering System

The size of the beam at the target is typically a few hundred micrometers in both horizontal and vertical direction. To prevent the target from being overheated locally, a beam raster is used for beam currents greater than several microamperes.

The raster in Hall A is driven by a pair of horizontal (x) and vertical (y) air-core dipoles located 23 meters upstream of the target. Both rectangular and circular patterns can be generated. The rectangular pattern, with a typical dimension of 2.5 mm $\times$ 2.5 mm, was used for experiment E94-104. Both magnets were driven with pure sine waves

$$\begin{aligned} x &= A_x \sin(\omega_x t) \\ y &= A_y \sin(\omega_y t) \ . \end{aligned} \tag{2.3}$$

The distribution of the rastered beam spots on the target is shown in Figure 2-8. The spikes around the edges are due to the sinusoidal rastering function. The rastering frequency is around 20 kHz, but with an irrational ratio for x and y component to avoid a closed Lissajous pattern.

2.3 The Photon Radiator

The untagged real photon beam is generated by electrons impinging on a copper bremsstrahlung radiator [51, 53, 54], located 72.6 cm upstream from the target. The photon energy is determined by kinematical reconstruction and the photon yield is obtained based on theoretical calculations. The electroproduction background is mea-

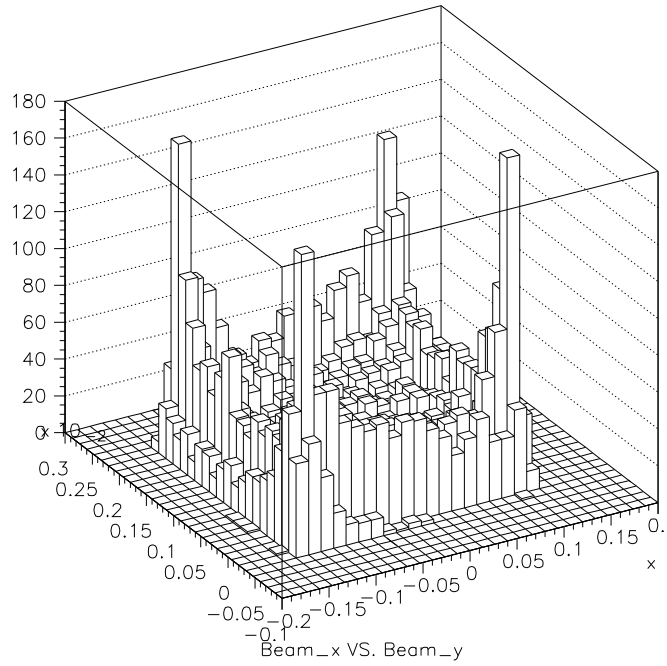

Figure 2-8: The distribution of beam spots on the target with the raster on (from run 2645).

sured with the radiator removed from the beam. The photon radiator in Hall A was used in the previous deuteron photodisintegration and neutral pion photoproduction experiments.

The photon radiator is a U-shaped, oxygen-free ladder with six available positions to mount foils. One position was empty, and the remaining five were occupied by copper foils of different thickness, i.e. 2.04%, 3.06%, 4.08%, 5.10% and 6.12% of a radiation length. The 6.12% foil was used for the production data of E94-104. Each foil is 6.35 cm wide and 3.175 cm high. The copper foil in the beam can be changed by moving the ladder up or down through manual or remote control of the stepping motor. To prevent the copper foil from being overheated, the maximum beam current with radiator is limited to 30 μA.

The photon yield produced by the radiator was calculated using Dave Meekins' thick-radiator codes [55], which were based on two papers [56, 57]. The calculation is expected to be accurate to 3% for high energy electron bremsstrahlung radiation with radiator thickness of less than 10% of a radiation length.

Figure 2-9 shows the data yield (or rate) for different radiator thickness. When the radiator thickness increases, the yield starts to increase linearly and then slows down, which is consistent with the thick-radiator calculation.

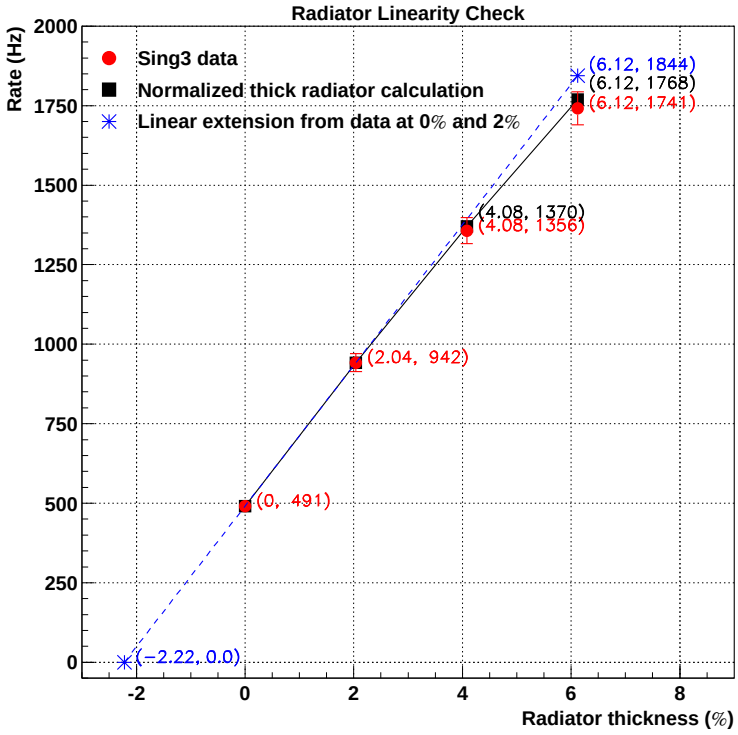

Figure 2-9: Radiator linearity check. The calculation was normalized to the two data points at the radiator thickness of 0% and 2% of a radiation length.

2.4 The Cryogenic Target

The cryogenic target system [46, 58] is mounted inside the scattering chamber at the center of the hall. The basic cryogenic target consists of three independent loops: a liquid hydrogen (LH2) loop, a liquid deuterium (LD2) loop and a gaseous helium loop. Each of the liquid loops, LH2 and LD2, contains two horizontal aluminum cylindrical target cells, 15 cm and 4 cm along the beam direction and 63.5 mm (2.5 in) in diameter. The upstream aluminum window is 71 μm (2.8 mil) thick, the downstream window is 102 μm (4 mil) thick while the side wall is 178 μm (7 mil)

Table 2.5: The density of the cryogenic targets used for E94-104.

Target	T (K)	P (psia)	Density Range (g/cm^3)	Density Used (g/cm^3)
LH2	19	18∼26	0.07224∼0.07231	0.0723
LD2	22	16∼22	0.1669 ∼0.1670	0.167
^{4}He	5.8	215∼225	0.1452 ∼0.1464	0.146

thick. The cells are cooled with 15 K helium coolant. The gaseous helium target, a vertical cylindrical aluminum cell, can be filled with either ^{3}He or ^{4}He gas. The cell diameter is 10.4 cm, which defines the target length, and the wall thickness is 0.33 mm (13 mil). The gaseous loop is cooled with 4.5 K coolant. All three loops were used during the experiment, although this thesis only discusses the data taken with the LH2 and LD2 targets.

All the cryogenic targets are mounted on a vertical lifter, which could be moved up and down to place the selected target into the beam. The switch between LH2 and LD2 target only takes a few minutes, while the switch between liquid and gaseous target usually takes about eight hours due to the change of coolant. Besides the cryogenic target cells, there are also some solid targets on the lifter: a BeO (Berryllium Oxide) target for beam spot display, single foil and 9-foil carbon targets for optics optimization, and 4 cm, 10 cm and 15 cm dummy targets for background measurements.

The density of the cryogenic target was determined from the temperature and the pressure, referring to the database in the NBS reports [59], as shown in Table 2.5. The uncertainty in the target density due to the temperature and pressure measurements is on the level of 0.1% for liquid target [60]. This is negligible compared to the uncertainty in the density due to local boiling, which is on the level of 1% (see Section 3.10.2).

Magnet Configuration	QQD_nQ with a vertical bend
Bend Angle	45°
Optical Length	23.4 m
Momentum Range for the Left Spectrometer	0.3 $\sim$ 4.0 GeV/c
Momentum Range for the Right Spectrometer	0.3 $\sim$ 3.16 GeV/c
Momentum Acceptance	$\pm$ 4.5%
Momentum Resolution (FWHM)	2.5×10^{-4}
Scattering Angular Range	12.5° $\sim$ 165°
Horizontal Angular Accuracy	$\pm$ 0.2 mr
Vertical Angular Accuracy	$\pm$ 0.6 mr
Horizontal Angular Acceptance	$\pm$ 28 mr
Vertical Angular Acceptance	$\pm$ 60 mr
Horizontal Angular Resolution (FWHM)	2 mr
Vertical Angular Resolution (FWHM)	6 mr
Solid Angle	$\sim$ 6 msr
Transverse Target Length Acceptance	$\pm$ 50 mm
Transverse Position Accuracy	$\pm$ 0.3 mm
Transverse Position Resolution (FWHM)	4.0 mm

Table 2.6: General characteristics of the HRS in Hall A based on the optics data taken at beam energy $E_e = 845$ MeV with the ^{12}C target. The horizontal angle is also called the in-plane angle, while the vertical angle is called the out-of-plane angle. The transverse target length is the projection of the target length onto the direction perpendicular to the spectrometer.

2.5 The High Resolution Spectrometers (HRS)

The core of the hall A equipment is a pair of nearly identical 4 GeV/c spectrometers capable of determining the momentum and angles of charged particles with high resolution. The general characteristics are summarized in Table 2.6 [46, 61, 62].

The configuration of the superconducting magnet system is QQD_nQ (Q: quadrupole; D: dipole) with a vertical bend, as shown in Figure 2-10 [46]. The vertical bend decouples, to first order, the reconstruction of vertex position along the target from that of the momentum. The quadrupole after the dipole makes it possible to have reasonably good horizontal position and angular resolution simultaneously. The bend angle of 45° is a compromise between cost and performance. The magnetic fields in

both dipoles are measured continuously with two arrays of three NMR field probes to the precision of 10^{-5}. The magnetic fields of the quadrupoles are monitored using Hall probes that are not very stable and reproducible over a long term, so the fields of the quadruples are set by their currents. Due to the hysteresis effect, the quadrupoles Q2 and Q3 require cycling when their momenta are raised, staying at the maximum current for a few minutes before being set to the desired value. The hysteresis effect in Q1 and dipole is so small that no cycling is necessary.

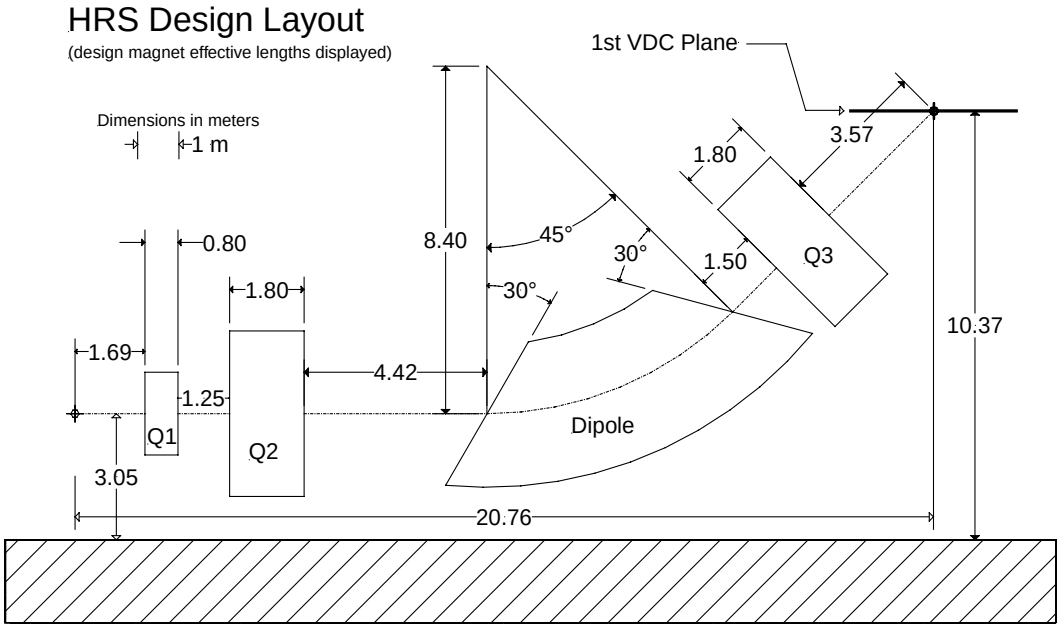

Figure 2-10: Design layout of the Hall A HRS magnet configuration.

The detector packages for both spectrometers are shown in Figure 2-11. When a particle goes through either spectrometer, the vertical drift chambers (VDCs) record its track, which can be used to reconstruct its momentum, scattering angle and reaction vertex at the target. The scintillator planes (S1/S2) provide timing information and generate triggers. For E94-104, the left spectrometer was optimized to detect positively charged particles while the right one was optimized to detect negatively charged particles. However, the polarities have to be switched for a few kinematics, such as coin13r and coin16r (see Table 2.1), due to a hardware problem in the right spectrom-

eter. Therefore, both spectrometers have to contain detectors to identify negatively and positively charged particles. Aerogel Čerenkov detectors (A1/A2/AM) provide particle identification for positively charged particles, mainly pions and protons. Gas Čerenkov, preshower/shower detector and pion rejector are used to discriminate negatively charged particles, mainly electrons and pions. The following is a description of all the detectors in more detail.

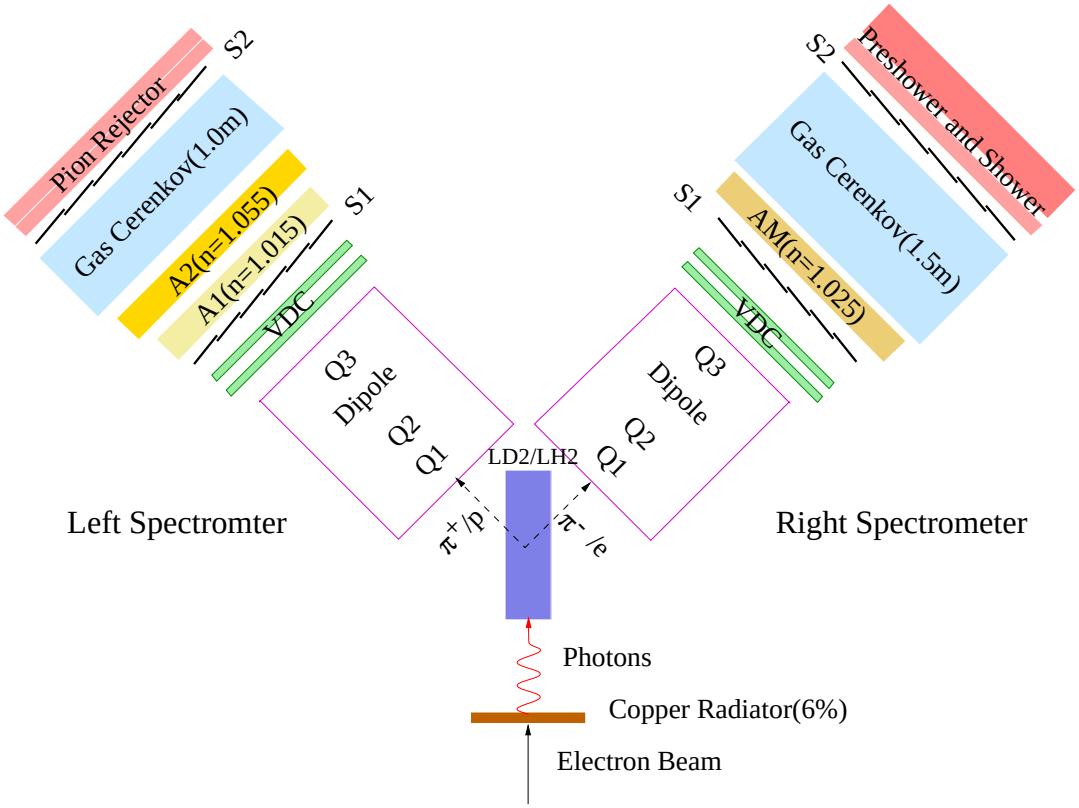

Figure 2-11: Schematic view of experimental setup for E94-104.

2.5.1 Vertical Drift Chambers (VDCs)

The trajectory of the charged particle is recorded by two VDCs. The concept of VDCs fits well into the scheme of a spectrometer with small acceptance, allowing a simple analysis algorithm and high efficiency. As shown in Figure 2-12 [46], two parallel VDCs are separated by 335 mm, and each VDC is composed of two wire

planes in a standard UV configuration, i.e. the 368 sense wires in one plane are orthogonal to those in the other plane. The VDCs are inclined at an angle of 45° with respect to the nominal particle trajectory. The lower horizontal VDC coincides with the spectrometer focal plane.

The VDCs, filled with a gas mixture of argon (62%) and ethane (38%), are operated at a high voltage of 4.0 kV. When a charged particle passes through the VDC, the gas along its trajectory will be ionized and electrons will drift along the electric field line towards the wires. Normally five to six adjacent wires will produce signals. From the shortest drift time to the wires in each plane, the spatial coordinates and then trajectory can be determined. The typical online spectra for VDCs are shown in Figure 2-13 [46].

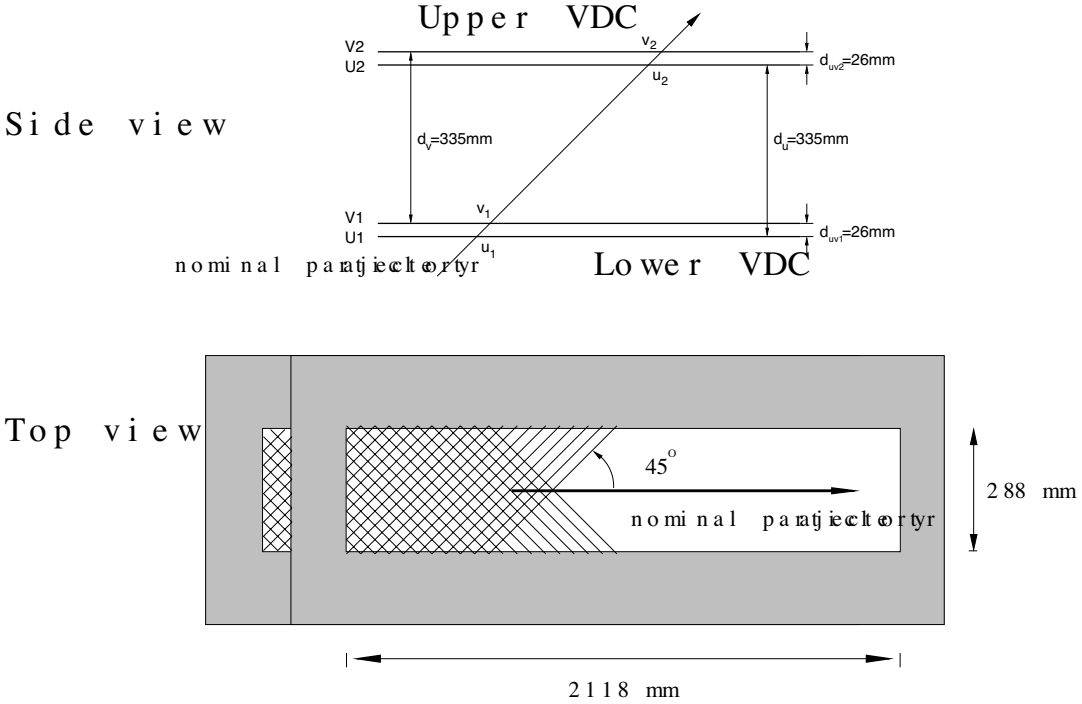

Figure 2-12: Schematic layout of the VDCs in Hall A.

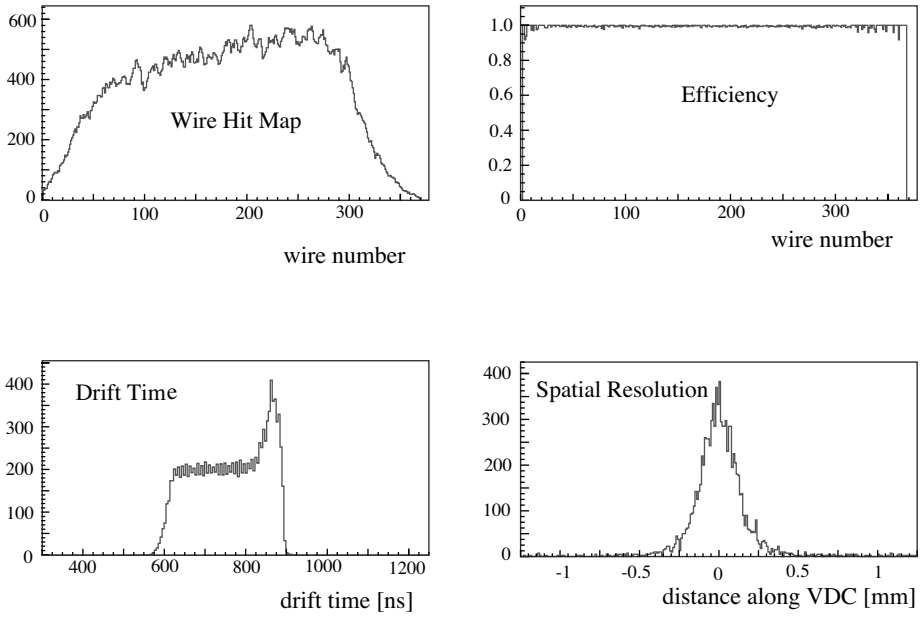

Figure 2-13: Typical online spectra from VDCs: top left, response as a function of the wire number; top right, single wire efficiency as a function of the wire number, which is the percentage of the events that a wire produce signal among the events that the two neighboring wires are fired; bottom left, drift time spectrum; bottom right, spatial resolution for events with hits in six adjacent wires.

2.5.2 Scintillators and Triggers

The trigger and timing information are provided by two primary scintillator planes (S1 and S2) in each spectrometer, separated by a distance of about 2 meters. Each plane is composed of six thin (5 mm) overlapping paddles made of plastic scintillator (BICON 408). The total active area of S1 is about 170 cm $\times$ 36 cm, with 30 cm $\times$ 36 cm for each paddle. The total active area of S2 is about 220 cm $\times$ 60 cm, with 37 cm $\times$ 60 cm for each paddle. The photons produced by the particle in the scintillator are collected by the two Photo-Multiplier tubes (PMTs) (2 inch Burle 8575) at the end of each paddle.

A typical ADC and TDC spectrum from the scintillators are shown in Figure 2-14, as well as the proton velocity distribution and coincidence time. The peak position of the ADC spectrum is proportional to the number of photons generated by the scintillator and the ionization energy loss of the particle. The peak position of the

TDC spectrum provides the timing information, to generate different types of triggers and to calculate the velocity of the particle with the time-of-flight technique. The coincidence time is the raw timing difference between the two spectrometers for a single event. The FWHM of the corrected coincidence timing peak can be improved to be about 1.4 ns after a very careful calibration [46].

There are basically five types of triggers generated from the timing information of the scintillators [64]:

T1: Main right arm trigger

T2: Loose right arm trigger

T3: Main left arm trigger

T4: Loose left arm trigger

T5: Coincidence of T1 and T3

Each type of triggers can be eliminated by setting a large prescale factor such as 65535, which means only one out of 65536 events with that type of triggers will enter the data stream. The prescale factors do not change the scaler readings.

The definition of triggers may vary for different experiments. During experiment E94-104, the main triggers for one spectrometer were formed when both scintillator planes (S1 and S2) were fired, normally implying that a charged particle passed through the spectrometer. The loose triggers were used to estimate efficiency. They were formed when only one scintillator plane, S1 or S2, was fired. Trigger T5 is a coincidence of T1 and T3, normally implying that two particles detected by the two spectrometers were produced at the target simultaneously.

2.5.3 Particle Identification Detectors

Several detectors in Figure 2-11 are used for particle identification, except the VDCs and scintillators. Aerogel Čerenkov detectors (A1/A2/AM) were used to separate different hadrons, while Gas Čerenkov, preshower/shower detector and pion rejector

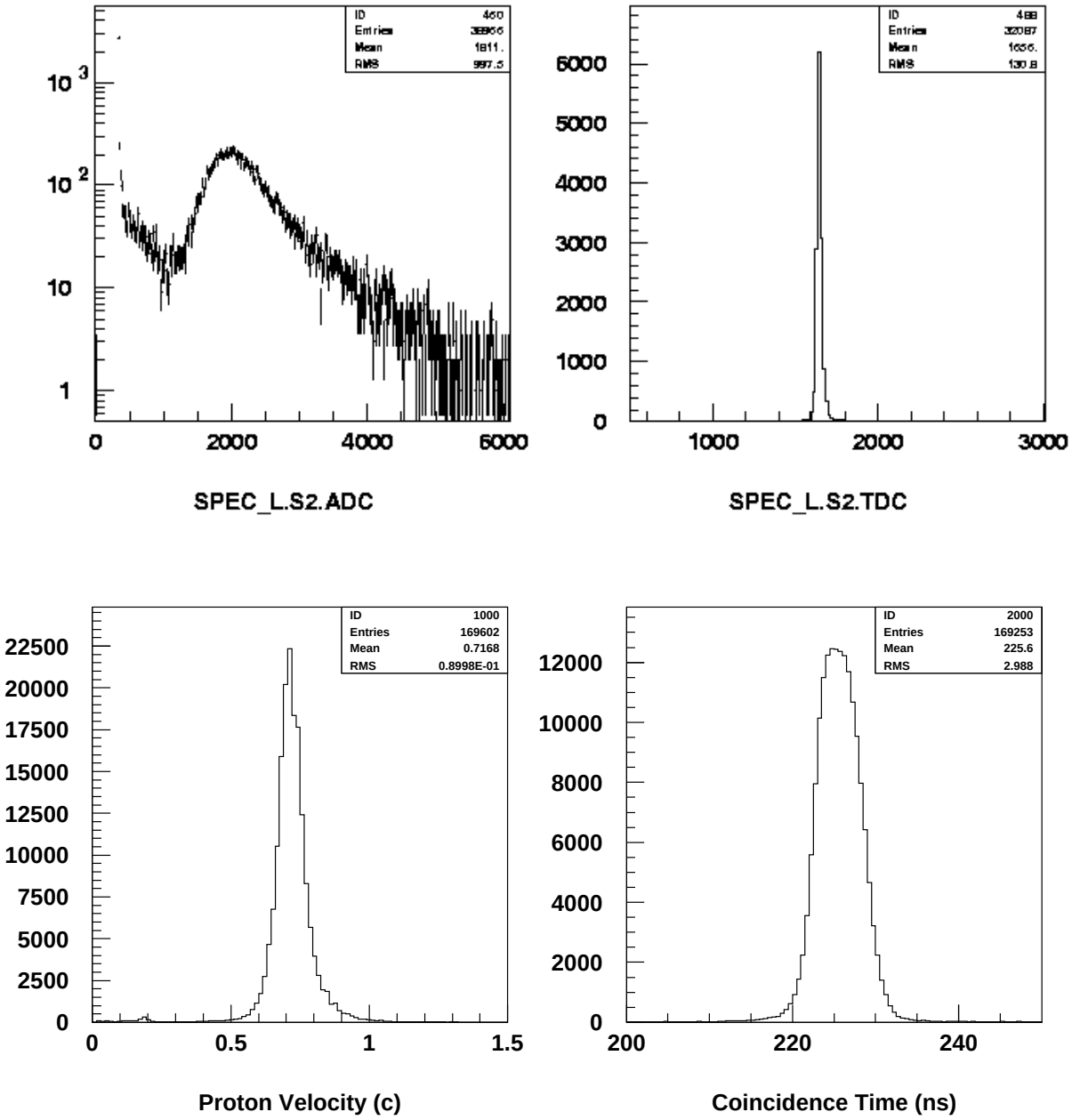

Figure 2-14: Some typical online spectra from scintillators (from run 2502). The upper two plots are the ADC and TDC spectrum from one PMT of the scintillators. The lower left plot is proton velocity distribution in the unit of light speed and the lower right one is coincidence time spectrum in the unit of nanosecond.

were used to separate electrons from pions. The right spectrometer was optimized to separate pions and electrons, while the left one was optimized to separate pions and protons. Different types of particles, represented by different colors in Figure 2-15, can be easily identified. The combination of the gas Čerenkov detector with preshower/shower detector can provide a pion suppression factor of 10^5 [46, 47].

Since some kinematics require reversed polarities of the spectrometers, each spectrometer contained a complete set of particle identification detectors. Figure 2-16 shows some spectra from the particle identification detectors with reversed polarities of the spectrometers. Different types of particles can be separated, though not as well as the case with normal polarities of the spectrometers.

Gas Čerenkov Detectors

There was a gas Čerenkov detector between scintillator S1 and S2 in each spectrometer. It was built by Saclay and INFN and was used for particle identification based on Čerenkov radiation. Čerenkov radiation occurs when a particle travels faster than the speed of light in the medium. The detector housing is made of steel with thin tedlar entry and exit windows, similar to the one shown in Figure 2-17 [65]. The detector is filled with carbon dioxide (CO_2) at the pressure of one atmosphere, resulting in an index of refraction $n = 1.00041$. The photons from the Čerenkov radiation are reflected to the ten PMTs (5 inch Burle 8854) around the detector by ten light spherical mirrors.

With index of refraction $n = 1.00041$, the threshold for generating Čerenkov radiation is 17 MeV for electrons and 4.8 GeV for pions. Therefore electrons can be separated from pions and other hadrons over the whole momentum range of the spectrometers.

The gas Čerenkov detector in the right spectrometer, 1.5 m thick, produced many photoelectrons for an incident $\beta = 1$ (light speed) particle, with the mean number around 10. It allows an electron identification with 98-99% efficiency and with about

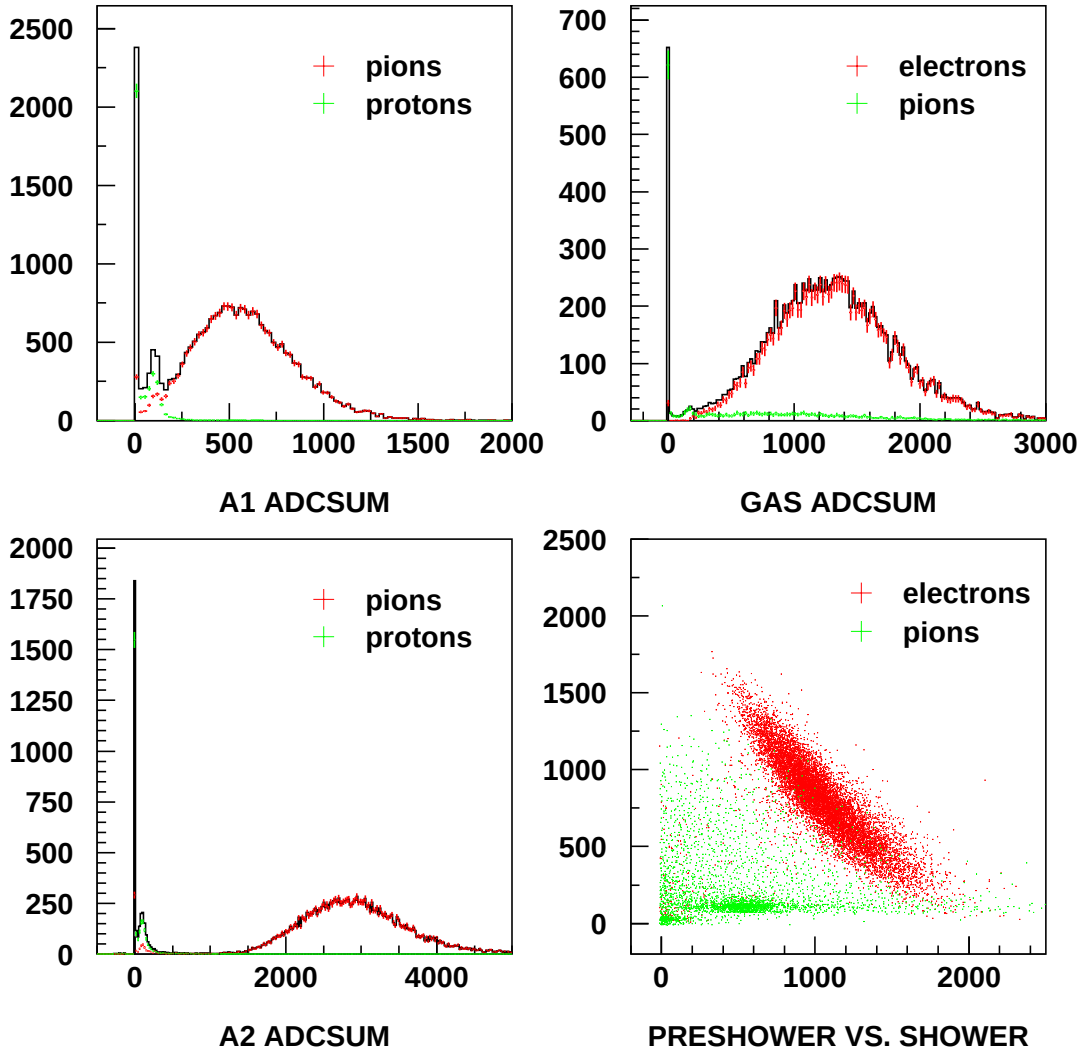

Figure 2-15: Performance of particle identification detectors with normal polarities of the spectrometers (at central momenta of 1.866 GeV). The 'ADCSUM' is the sum of the calibrated ADC spectra from the PMTs to detect Čerenkov photons. With the pedestal at 0, the single photoelectron peak of A1/A2 and gas Čerenkov detector was calibrated to be channel 100 and channel 150 respectively. The sum of preshower and shower ADC was calibrated to be the electron energy in MeV. The black line is the spectrum without any cuts on particle type, i.e. the sum of the red and green spectrum.

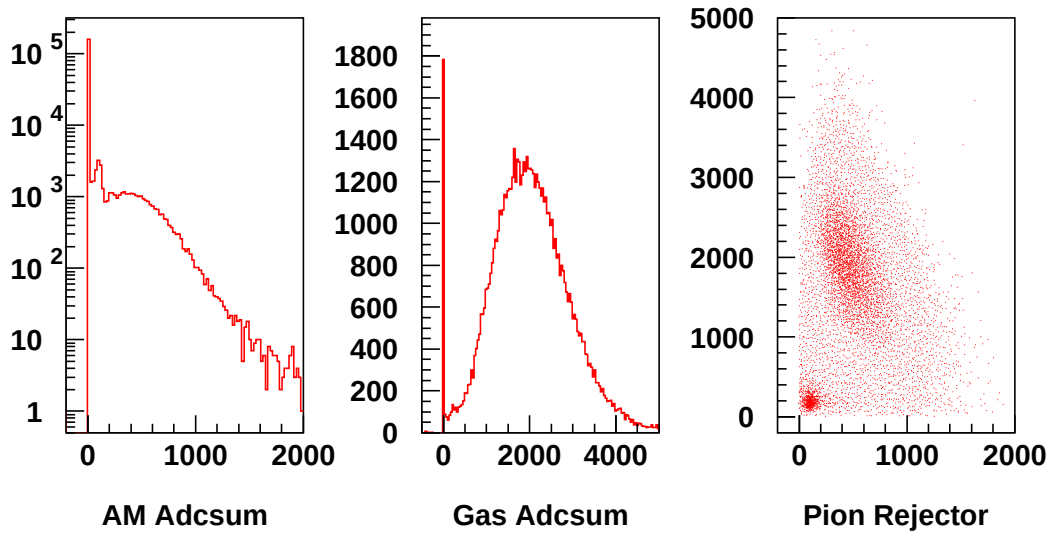

Figure 2-16: Spectra from particle identification detectors with reversed polarities of the spectrometers (at central momenta of 1.794 GeV). The 'Adcsum' is the sum of the calibrated ADC spectra from the PMTs to detect Čerenkov photons. With the pedestal at 0, the single photoelectron peak of AM and gas Čerenkov detector was calibrated to be channel 100 and channel 250 respectively.

1% hadron leak-through [46]. The gas Čerenkov detector in the left spectrometer, 1.0 m thick, also produced many photoelectrons for a $\beta = 1$ particle, with the mean number around 8.

Aerogel Čerenkov Detectors

Three silicon aerogel Čerenkov detectors were used for E94-104, AM (Aerogel detector with Mirrors) in the right spectrometer and A1/A2 in the left spectrometer, mainly to separate pions and protons based on Čerenkov radiation. The index of refraction for the aerogel in AM was determined to be 1.0250 [66]. The nominal indices of refraction for the aerogel in A1 and A2 are 1.015 and 1.055 respectively, which were checked by optical index measurements to a precision of 0.004.

The aerogel detector AM was built by the University of Regina group in collaboration with INFN/Sanita and INFN/Lecce. The photons are reflected by mirrors to the 26 Burle 8854 PMTs on the sides of the detector. The design parameters and con-

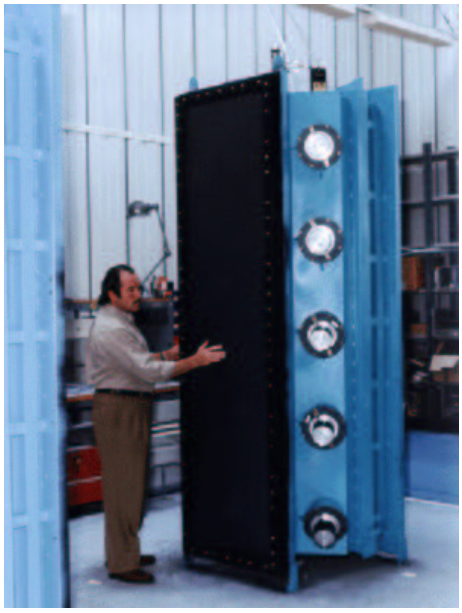

Figure 2-17: Gas Čerenkov Detector.

struction techniques can be found in reference [68]. The radiator is 9 cm hydrophilic aerogel, supplied by Airglass AB. It is protected against moisture absorption by continuously flushing of dry CO_2 gas at a slight overpressure in the gastight enclosure. With the refraction index of 1.025, the momentum threshold for generating Čerenkov radiation is 0.62 GeV for pions and 4.2 GeV for protons. The average number of photoelectrons is 7.3 for $\beta = 1$ particles [66].

The two aerogel detectors A1 and A2 are of similar designs and were assembled by the collaboration of JLab, Florida International University (FIU), MIT and Photonis company for experiments E94-104 and E98-108, which were carried out during the same period. E94-104 requires pion and proton separation over almost the entire momentum range of the spectrometer, while E98-108 requires stringent particle identification to separate kaons from large pion and proton backgrounds around 2 GeV. These requirements can be satisfied by the combination of A1 and A2, as shown by the different threshold momenta in Figure 2-18. The layouts of the detectors are shown schematically in Figure 2-19 [69]. The radiator of A1 is 9 cm aerogel, and that of A2 is 5 cm aerogel. There are 24 PMTs installed in A1 and 26 PMTs in

A2. The average number of photoelectrons generated by a $\beta = 1$ particle is about 8 for A1 and about 30 for A2. The average number of photoelectrons can also be estimated by using the Monte Carlo simulation program developed for the diffusely reflective aerogel Čerenkov detector [67]. The ability to identify particles is shown in Figure 2-15.

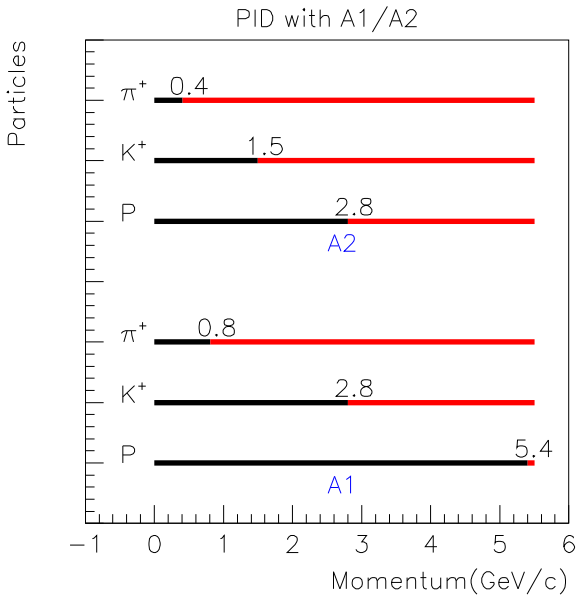

Figure 2-18: Particle Identification with A1 and A2. The numbers at the joints of black and red line are the threshold momenta for producing Čerenkov radiation

The major differences between the aerogel detector AM and the newly built aerogel detectors A1 and A2 are discussed below:

Aerogel: The humid weather at JLab may cause hydrophilic aerogel to increase weight and lose light transmission [70], so flushing the dry CO_2 gas is necessary to ensure the performance of AM. To avoid the baking and flushing, a hydrophobic type of aerogel with a waterproof coating, produced by Matsushita Electric Works, was used for A1 and A2. The aerogel is very fragile, especially the type used for A1 with small index of refraction. A vacuum lift was used to handle the aerogel blocks, as

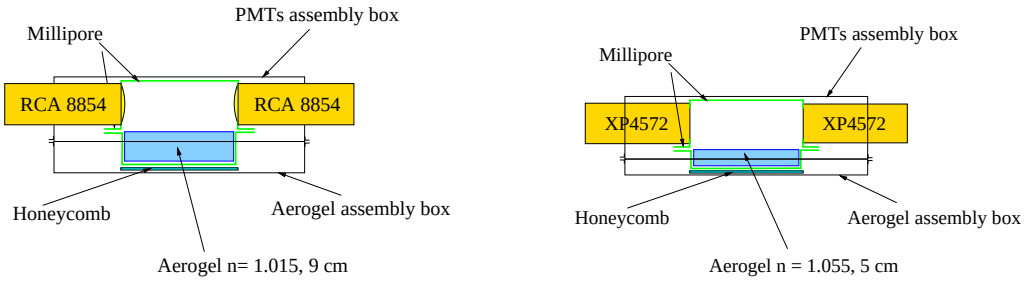

Figure 2-19: Schematic layout of aerogel Čerenkov detector A1 (left) and A2 (right). The volume of aerogel radiator is $32\times170\times9$ cm^3 for A1 and $30\times192\times5$ cm^3 for A2. Particles enter from the bottom of the figure.

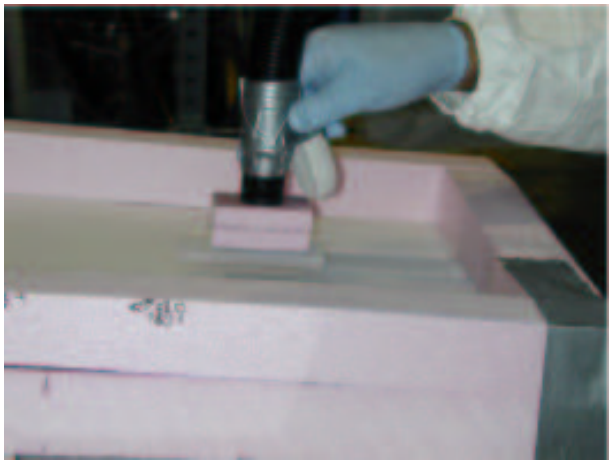

Figure 2-20: A cut piece of A1 aerogel is being moved with a vacuum lift.

shown in Figure 2-20.

Magnetic field shielding: Individual magnetic shielding for a PMT is useful to ensure the good performance of the PMT, but it will affect the photon collection when it distances the PMT from the aerogel and narrows the opening solid angle. The magnetic field in the detector hut at the location of the aerogel detector was found to be below 0.5 Gauss. For the type of PMTs used for A1, a small but stable 5% reduction was observed in the efficiency to detect photons [71]. For the type of PMTs used for A2, a larger effect around 15% was found. No individual magnetic shielding was designed for A1 and A2. But if necessary, overall magnetic shielding could be added to A1 and A2.

Millipore paper: Due to the short diffusion length in aerogel, the directionality of photons in the aerogel detectors is not very good. About 4 PMTs in AM may be fired for a single track event [66]. Therefore the diffusely reflective box design was used for A1 and A2. One or two layers of 0.22 μm Millipore filter paper, with an average reflectivity of 95%, covers the inner walls of the detector. The performance of Millipore paper was compared with that of PTFE Teflon, which was used in previous detectors. The Millipore paper proved to be a better choice with smaller fraction of background light and higher reflectivity [72]. Millipore paper is too fragile to be cut and installed directly, so white paper was used to back the Millipore paper during the assembly. The effect of covering the outer edge the PMTs, used for both A1 and A2, was investigated [73]. It was found that the collection efficiency can be improved by 15% with an appropriate cover ring.

PMTs: For Čerenkov detectors, the historical choice is the Burle 8854 ("Quantacon"), which has a high quantum efficiency across the ultraviolet and visible spectrum. However, as aerogel has a modest ultraviolet transmission spectrum, the Photonis XP4572B/D1 was chosen for A2 because of its lower price and higher collection efficiency, though it is not sensitive to ultraviolet photons. With a radiator that approximated the aerogel spectrum, a factor of two improvement was found in collection

efficiency [74]. It was also found that adding an amplifier in the base could improve the performance of the PMTs, so all the bases for A2 were modified.

Figure 2-21 shows two pictures taken during the assembly of A2. The inner side of the light box is covered by small pieces of Millipore paper. Thin double sticky tapes were used to glue the Millipore paper together with the white paper and then with the detector. Thin carbon fiber sheet and aluminum strips were used to hold the paper in the light box. The dimensions of each aerogel block are around $10\times10\times1$ cm^3. To pack the aerogel blocks as tightly as possible, two pieces of thin foam were placed by the sides of the aerogel and some squeezable material, like weather stripping, was inserted between the foam and the aerogel box. Before each PMT was installed, it was painted black and then glued to a guide tube with silicone. The gluing is necessary to hold the PMT in place, but causes some troubles in PMT replacement. The guide tube has to be replaced together with the PMT because it is very difficult to separate them.

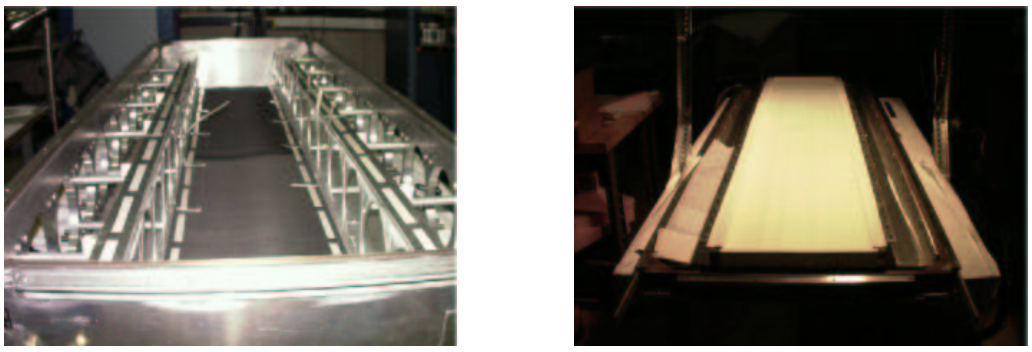

Figure 2-21: Pictures of A2 taken during the assembling (left:light box, right:aerogel box).

Preshower/shower Detector and Pion Rejector

To enhance the ability to separate electrons and hadrons, a lead glass counter was installed in each spectrometer in addition to the gas Čerenkov detector. It is called pion rejector in the left spectrometer and preshower/shower detector (or total shower

detector) in the right spectrometer. Figure 2-22 [46] shows the schematic layouts and Figure 2-23 [75] shows the pictures of the preshower and shower detector. During experiment E94-104, there are 24×2 and 16×5 lead glass blocks with PMT in the preshower and shower detector respectively, while there are 17×2×2 blocks in the two layers of the pion rejector.

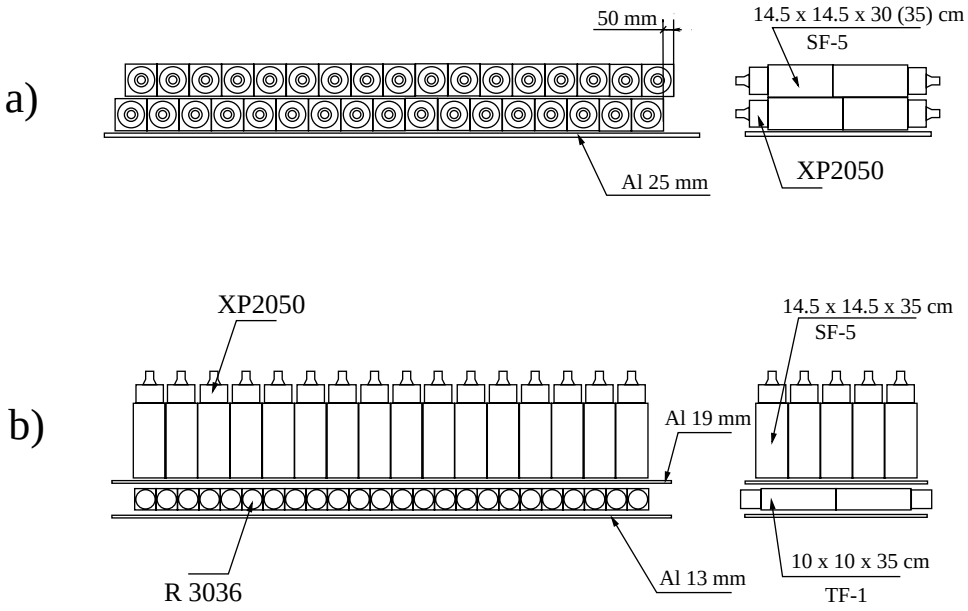

Figure 2-22: Schematic layouts of the lead glass counters: (a) the pion rejector in the left spectrometer; (b) preshower/shower detector in the right spectrometer. Particles enter from the bottom of the figure.

2.6 Data Control System

A distributed system based on the application framework of the Experimental Physics and Industrial Control System (EPICS) [76] is used to monitor and control the various Hall A instruments, as well as the JLab accelerator. The basic components of the system are [46, 51]:

- Operator Interfaces (OPI): UNIX based workstations able to run various EPICS tools like the Motif-based Display Editor/Manager (MEDM) for display and


Figure 2-23: Preshower and Shower Detector under construction. The preshower detector is composed of 24×2 lead glass blocks. The shower detector is re-assembled before E94-104 to 5 columns×16 rows from 6 columns×16 rows.

control.

- Input/Output Controllers (IOC): VME based crates containing a single board computer and various I/O (Input/Output) modules as well as interfaces to other I/O buses like the serial RS-232 or GPIB (General Purpose Instrumentation Bus).

- Local Area Network (LAN): the communication path connecting the IOCs and OPIs.

At present, there are eighteen IOCs permanently located in Hall A. Some of the IOCs are dedicated to a specific purpose while others handle all signals to/from a region of the hall. Examples of the specific purpose IOCs are those controlling the distribution of cryogenic fluids (helium and nitrogen) for the superconducting magnets and cryogenic targets. Examples of the region allocated IOCs are those located in the detector hut of each spectrometer and those dealing with the basic infrastructure of each spectrometer (i.e. magnet power supplies, magnet cooling, collimators and vacuum). The number of records being handled by the IOCs is on the level of several

thousand.

Figure 2-24 is an example of the OPI. With this MEDM, the users can control many functions, such as setting the central momentum and angles for both spectrometer, selecting the collimators, adjusting the high voltages of the detectors, and monitoring beam position, beam current and VDC gas flow.

2.7 Data Acquisition System

The data acquisition (DAQ) system in Hall A uses CODA (CEBAF On-line Acquisition) developed by the JLab data acquisition group for nuclear physics experiments at JLab [46, 77]. CODA is a toolkit composed of software and hardware from which a data acquisition system can be built to manage the acquisition, monitoring and storage of data. The typical CODA system is constructed from modular components (usually programs) that are spread over a network of processors. These processors may take the form of embedded CAMAC, VME or FASTBUS modules, or PC/Workstation systems. The custom hardware elements include the trigger supervisor (TS) that synchronizes the readout of the front-end crates and handles the dead time logic of the system. The most important custom software components are the readout controller (ROC) running on the front-end crates, the event builder (EB), event recorder (ER), event transfer (ET) and finally RunControl. The RunControl is the graphical user interface from which users can select experimental configurations, start and stop runs, and reset, transfer and monitor CODA components.

For each event with a trigger accepted by the trigger supervisor, data are gathered from the front-end boards by the ROC component, which buffers the data in memory and sends these buffers via the network to the EB running on a workstation. The EB builds events from fragments sent by the various ROC's and passes them to the ER which writes data to a local disk. The data are subsequently written to tapes in the MSS (Mass Storage tape Silo). Through the ET system, various additional pieces

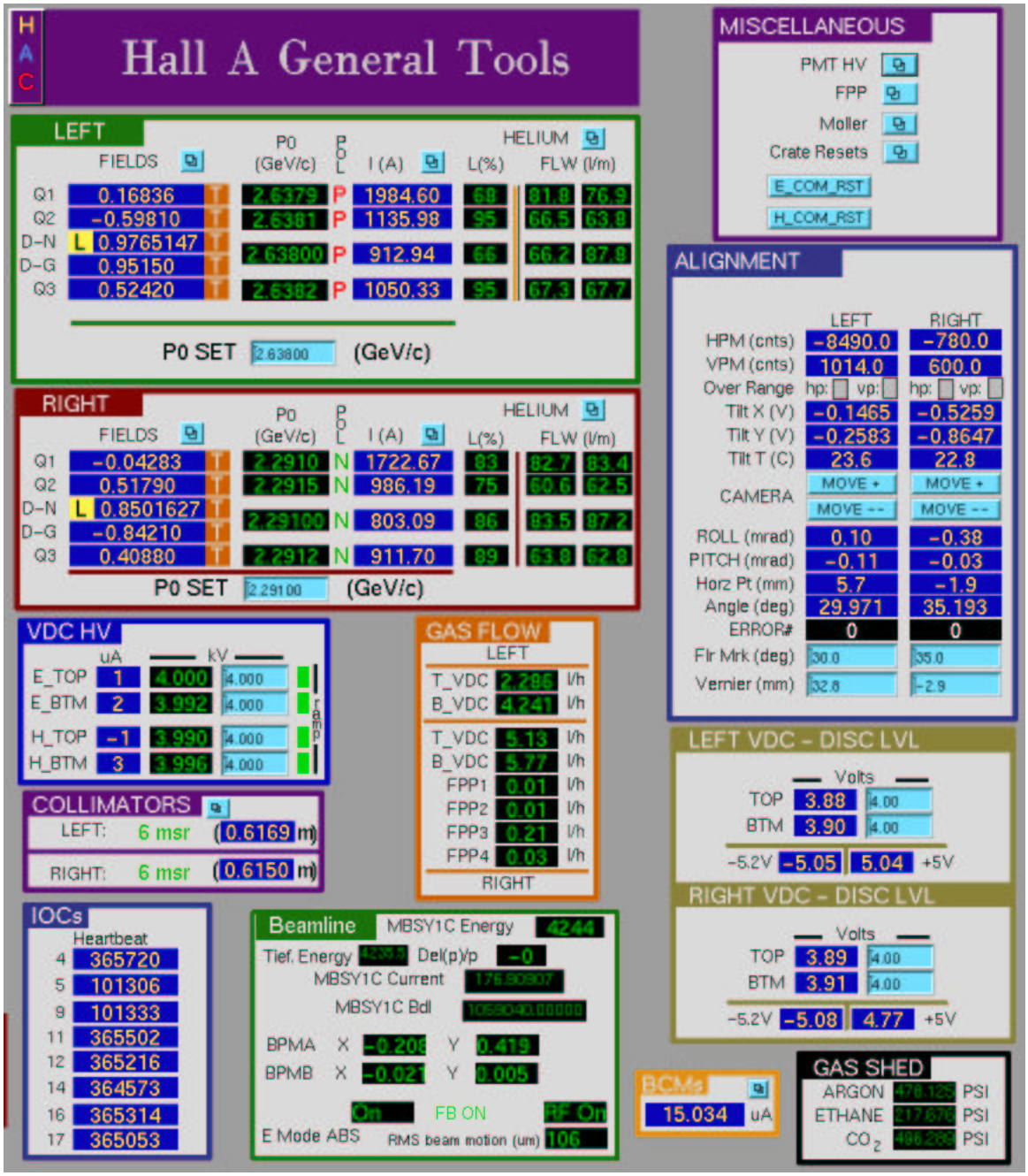

Figure 2-24: Hall A Main Control Screen. The settings were for kinematics coin15.

of data, from the control system and scalers for example, are inserted into the data stream every few seconds. In addition, the ET system is used by analysis clients to obtain a random sample of data in real time.

As shown in Figure 2-25 [78], three types of data will be collected by the data acquisition system, the detector readouts, the scaler readings and the EPICS variables.

The performance of the DAQ system has been modeled by a Poisson distribution that relates the dead time to the trigger rate. The 2 kHz trigger rate typically results in ~20% dead time.

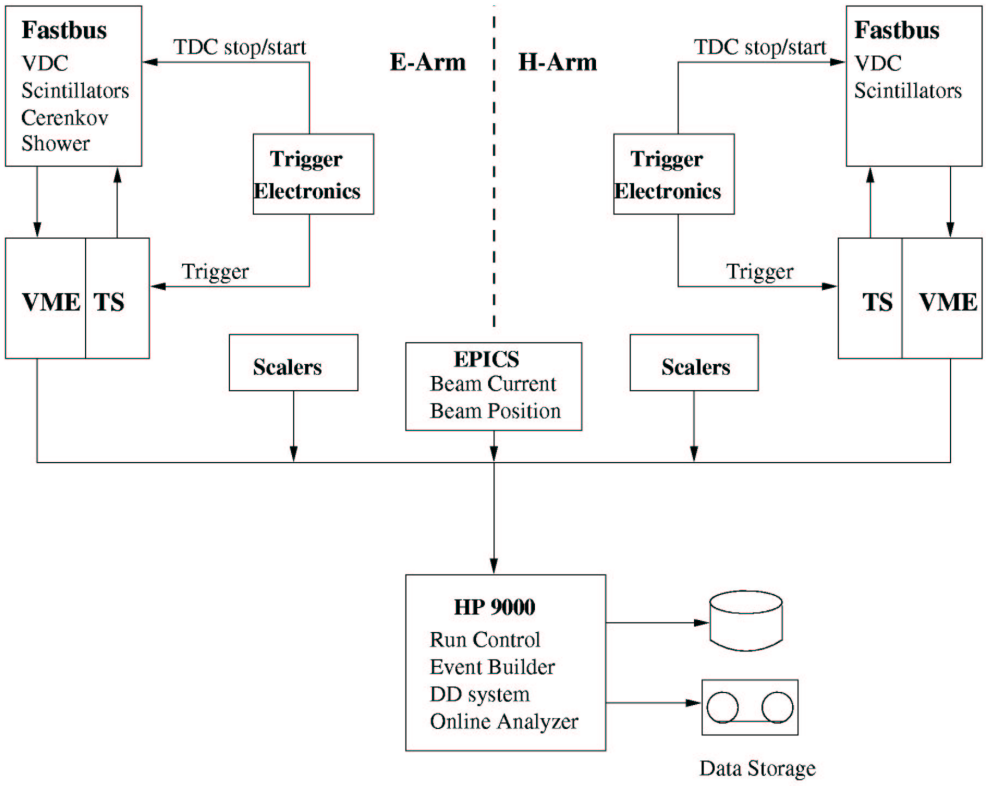

Figure 2-25: Schematic layout of the DAQ system in Hall A. The E-Arm (H-Arm) is named Left (Right) Spectrometer during E94-104. The abbreviation DD system stands for Data Distribution system that was used in data transfer.

Chapter 3

Data Analysis

3.1 Overview

Major procedures in the data analysis are shown as a flow chart in Figure 3-1. The raw data from the data acquisition (DAQ) system were replayed or decoded by an event processing program, ESPACE (Event Scanning Program for Hall A Collaboration Experiments) [79] using CERNLIB [80] packages. The outputs were histograms and ntuples (similar to multi-dimension matrices) of physical variables in the HBOOK [81] format, which can be read by the analysis tool PAW [82]. The yield from the data was obtained by applying cuts or conditions on certain variables in the ntuples, such as trigger type, particle type, spectrometer acceptance and reconstructed photon energy. Next, the yield was normalized by beam charge and computer deadtime. To extract the differential cross sections, simulations were carried out by using the modified MCEEP (Monte Carlo for $(\underline{e}, \underline{e'p})$) program [83] written for JLab Hall A. The inputs to the simulations include the spectrometer settings, the beam energy and the trial differential cross section $(\frac{d\sigma}{dt})_{\rm mc}$ for the $\gamma N \to \pi N$ process. The acceptance, bremsstrahlung photon yield and momentum distribution of the neutron in the deuteron target were considered in the simulation. The raw differential cross section $(\frac{d\sigma}{dt})_{\rm data}$ was extracted by comparing the background subtracted yield from the data

($Y_{\rm data}$) with the yield from the Monte Carlo simulation ($Y_{\rm mc}$) with the same set of cuts:

$$(\frac{d\sigma}{dt})_{\rm data} = (\frac{d\sigma}{dt})_{\rm mc} * \frac{Y_{\rm data}}{Y_{\rm mc}} \ . \tag{3.1}$$

Finally to extract the physical differential cross section, some corrections such as the nuclear transparency of deuterium, the detection efficiency and nuclear absorption in the detection material were applied to the raw differential cross section.

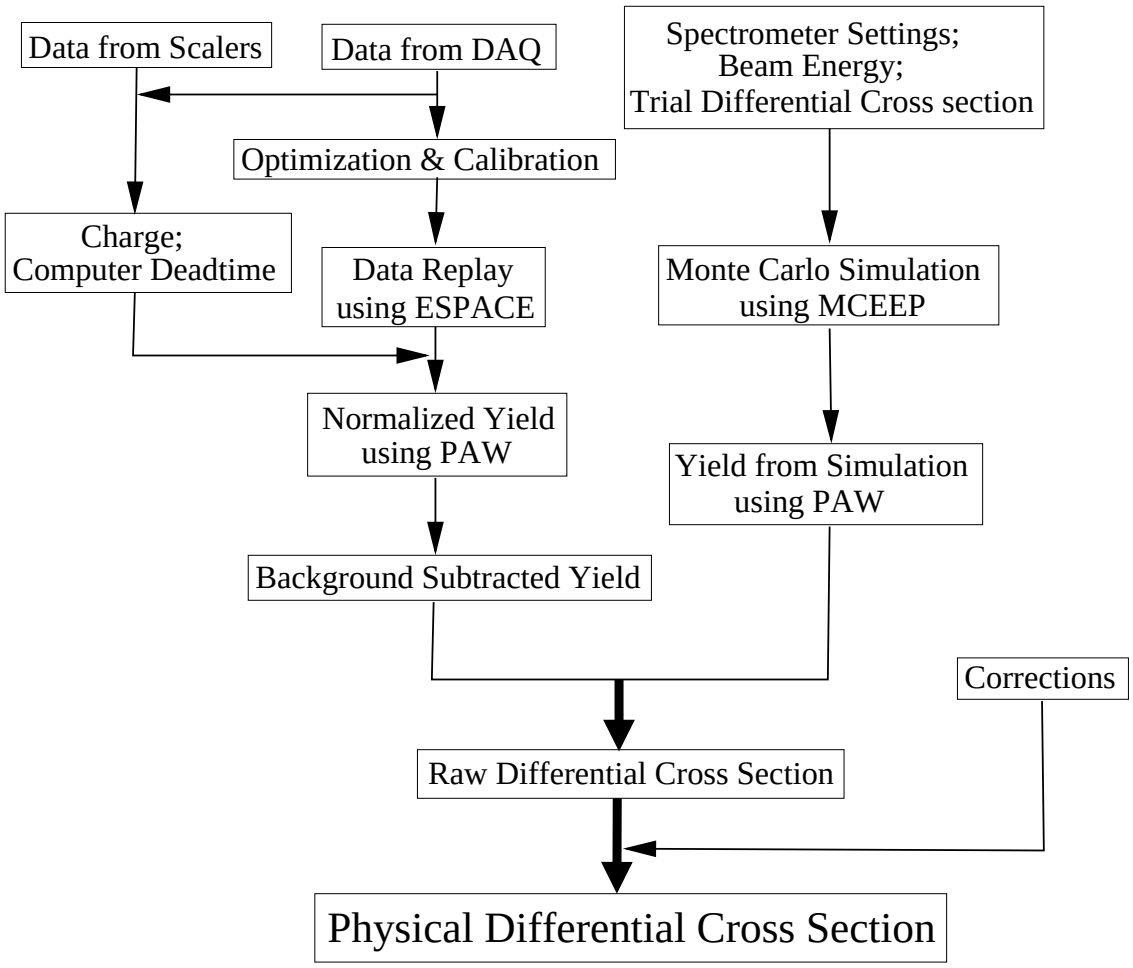

Figure 3-1: The data analysis flow chart.

3.2 Kinematics

The goal of this thesis is to extract the differential cross section for single pion photoproduction from the data of JLab experiment E94-104, which included the singles data with a hydrogen target for the $\gamma p \to \pi^+ n$ process and coincidence data with a deuterium target for the $\gamma n \to \pi^- p$ process, as shown in Table 3.1. The electron beam energy E_e ranged from 1.1 to 5.6 GeV, corresponding to the center-of-mass energy $\sqrt{s}$ from 1.71 to 3.36 GeV. The pion center-of-mass angles were 50°, 70°, 90°, and even 100°, 110° for a few beam energies.

3.3 Data Replay with ESPACE

3.3.1 Overview

The FORTRAN-based program ESPACE (Event Scanning Program for hall A Collaboration Experiments) [46, 79] is the standard physics event processing software in JLab Hall A. It was originally developed at Mainz and improved at MIT before being introduced to Hall A in 1995. It was written in FORTRAN 77 with the addition of many VMS-type (DEC Fortran) extensions such as structures and pointers. The program interface is supplied by the KUIP CERNLIB [80] and therefore has a PAW [82]-like look.

ESPACE can decode, filter, calibrate, and/or compute variables from the raw data with cuts. The variables range from raw detector signals like the value of a scintillator TDC channel, to much more elaborate ones like the reconstructed coordinates of the reaction vertex in the target.

3.3.2 Major Modifications to ESPACE

As shown in Figure 2-11, many particle identification detectors were used for experiment E94-104. The ESPACE version prior to E94-104 could handle the shower-type

Table 3.1: The kinematics of JLab experiment E94-104 to measure the differential cross section for single pion photoproduction $\gamma N \rightarrow \pi^{+/-} N$. The spectrometer settings for each kinematics were listed in Table 2.1 and Table 2.2.

Singles $\gamma p \longrightarrow \pi^+ n$

	Beam Energy E_e (GeV)						
	1.173	1.721	1.875	2.558	3.395	4.232	5.618
$\theta_{cm} = 50°$	-	sing4	sing18	sing7	sing10	-	-
$\theta_{cm} = 70°$	sing2	sing5	-	sing8	sing11	sing13	-
$\theta_{cm} = 90°$	sing3	sing6	sing19	sing9	sing12	sing14	sing16
$\theta_{cm} = 100°$	-	-	-	-	sing22	sing15	sing17
$\theta_{cm} = 110°$	-	-	-	-	sing21	-	-

Coincidence $\gamma n \longrightarrow \pi^- p$

	Beam Energy E_e (GeV)						
	1.173	1.721	1.875	2.558	3.395	4.232	5.618
$\theta_{cm} = 50°$	coin1	coin4	coin18	coin7	coin10		-
				coin7r		coin13r	
$\theta_{cm} = 70°$	coin2	coin5	-	coin8	coin11	coin14	
				coin8r			coin16r
$\theta_{cm} = 90°$	coin3	coin6	coin20	coin9	coin12	coin15	coin17
				coin9r			
$\theta_{cm} = 100°$	-	-	-	-	coin22	-	-
$\theta_{cm} = 110°$	-	-	-	-	coin21	-	-

detector (preshower/shower detector or the pion rejector) only for the right spectrometer, and could handle only one aerogel Čerenkov detector for each spectrometer. For this experiment, it was modified to include a second aerogel Čerenkov detector and the pion rejector in the left spectrometer [84]. In addition, the electron/hadron (e/h) notation was changed to right/left (r/l) notation in the interface of ESPACE to avoid the naming confusion due to the exchange of detector packages of the two Hall A spectrometers in the summer of 2000.

3.4 Optics

3.4.1 Coordinate Systems

There are several coordinate systems used in JLab Hall A [62, 79]: the hall coordinate system, the target coordinate system (or spectrometer reconstructed coordinate system), the detector coordinate system, the transport coordinate system and the focal plane coordinate system. Ideally, the VDC U1 plane is the spectrometer focal plane, and the last three coordinate systems share the origin (the intersection of central wire 184 of the VDC U1 plane and the central wire projection of the VDC V1 plane), and the Y-axes (all perpendicular to the dispersive direction). However their Z-axes (and therefore X-axes) have different orientations. The Z-axis in the detector coordinate system points vertically up in the lab. The Z-axis in the transport coordinate system is rotated by 45° and coincides with the central ray of the spectrometer. The Z-axis in the focal plane coordinate system coincides with the local ray direction, which changes along the dispersive direction. While the last three coordinate systems are very useful for the optics calibration and Monte Carlo simulation, the first two coordinate systems are used more often to define physical variables in the data analysis. Following are the definitions for these two coordinate systems.

Hall Coordinate System

Its origin is the center of the hall, defined by the intersection of the electron beam and the vertical symmetry axis of the target system. Ideally, it is always pointed to by the two spectrometers. The Z-axis is along the beamline and points to the beam dump, the Y-axis is vertically up and the X-axis points to the left of the beamline, as shown in Figure 3-2 [79]. The reaction vertex z_{react} is defined in this coordinate system.

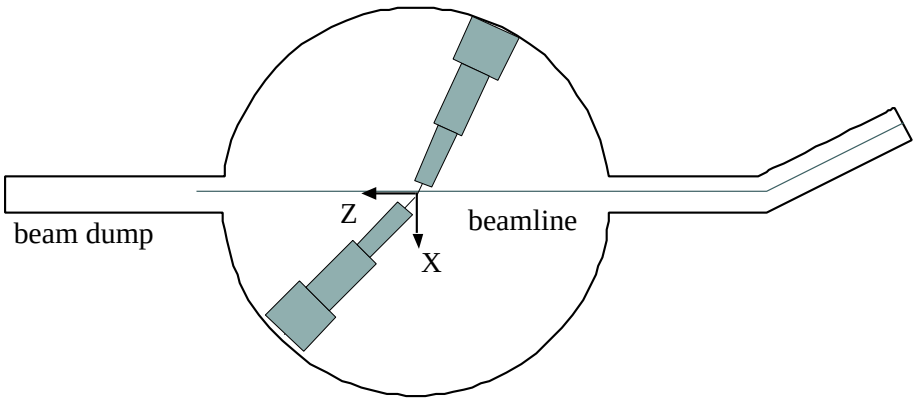

Figure 3-2: The hall coordinate system (top view). Y-axis points vertically up in the lab.

Target Coordinate System

The two spectrometers have different target coordinate systems. The Z-axis is along the central axis of the spectrometer, defined to be perpendicular to the sieve slit (a collimator with many holes) and passing through the center of the central hole. Its origin is the Hall A center ideally, defined to be the point at a certain distance Z_0 away from the sieve slit, 1.181 (1.178) m for left (right) spectrometer. The X-axis points vertically down, and the Y-axis points to the left of the spectrometer, as shown in Figure 3-3 [79]. The out-of-plane angle (θ_{tg}) and the in-plane angle (ϕ_{tg}) are defined to be $\frac{dx_{tg}}{Z_0}$ and $\frac{dy_{tg}}{Z_0}$ respectively. The reaction vertex y_{tg} is also defined in this coordinate system.

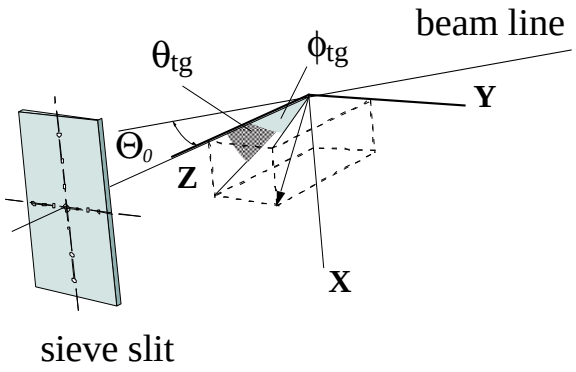

Figure 3-3: The target coordinate system.

3.4.2 Spectrometer Mispointing

As the front end of the spectrometer is not firmly fixed to the pivot, the spectrometer may not point to the nominal center exactly. There is a system for measuring mispointing with LVDT (Linear Variable Differential Transformer), which is attached to the collimator box in front of Q1 and touches the target scattering chamber [60]. The spectrometer angles were determined from the floor marks about 10 m away from the center of the hall, and corrected for the horizontal mispointing. The angles were further corrected by about 0.3 mr based on the comparison between LDVT and survey results.

3.4.3 Optics Optimization and Checks

The optics matrix, in the database read by ESPACE, allows the reconstruction of target variables (see Figure 3-3) and momentum from the coordinates of the detected particles at the focal plane, following

$$
\begin{aligned}
y_{tg} &= \sum_{j,k,l} Y_{jkl} \theta_{fp}^{j} y_{fp}^{k} \phi_{fp}^{l} \\
\theta_{tg} &= \sum_{j,k,l} T_{jkl} \theta_{fp}^{j} y_{fp}^{k} \phi_{fp}^{l} \\
\phi_{tg} &= \sum_{j,k,l} P_{jkl} \theta_{fp}^{j} y_{fp}^{k} \phi_{fp}^{l}
\end{aligned}
$$

$$\delta = \sum_{j,k,l} D_{jkl}\theta_{fp}^{j} y_{fp}^{k} \phi_{fp}^{l} \ , \tag{3.2}$$

where $\delta = \frac{P-P_0}{P_0}$ is the deviation from the central momentum, and the matrix elements Y_{jkl}, T_{jkl}, P_{jkl} and D_{jkl} are polynomials in x_{fp} that was calculated using the beam position and spectrometer displacement in the vertical direction. Since the target variables and momentum cannot be measured independently, three variables were introduced as

$$\begin{aligned} z_{react} &= -(y_{tg} + D)\frac{\cos\phi_{tg}}{\sin(\Theta_0 + \phi_{tg})} + x_{beam}\cot(\Theta_0 + \phi_{tg}) \\ y_{sieve} &= y_{tg} + Z_0 \tan\phi_{tg} \\ x_{sieve} &= x_{tg} + Z_0 \tan\theta_{tg} \ , \end{aligned} \tag{3.3}$$

where D is the mispointing of the spectrometer, Z_0 is the distance of the sieve slit from the hall center, z_{react} is the position of the reaction vertex along the beam direction, and x_{sieve}/y_{sieve} are the coordinates of the particles at the position of the sieve slit. A 9-foil carbon target with different z_{react} and sieve slits with different x_{sieve}/y_{sieve}, as well as different momentum settings, are generally used to take optics data, from which the optics matrix elements could be fitted by using ESPACE and an optimization program [62]. The optics was checked for E94-104, and minor errors due to the exchange of the detector packages were corrected [85]. In addition, the z_{react} was re-optimized, which improved the optics at large $|y_{tg}|$. The reconstructed z_{react} and x_{sieve}/y_{sieve} with the new database are plotted in Figure 3-4 and Figure 3-5.

The central momentum of the spectrometer P_0 is determined by measuring the magnetic field B_0 in the dipole. A series of $^{12}C(e,e'p)$ measurements made in 1999 and 2000 were used to fit the spectrometer constants. The results are shown in Table 3.2 [86].

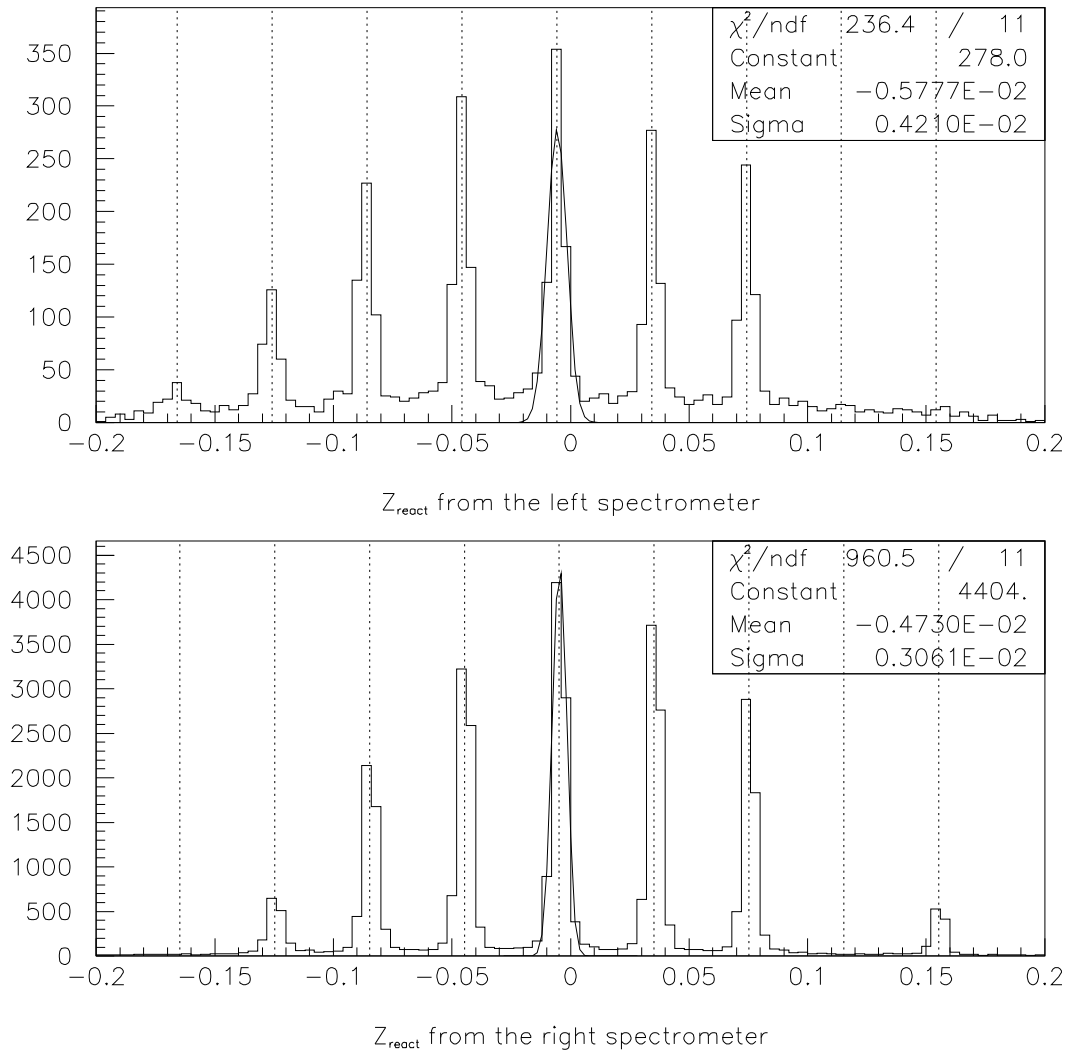

Figure 3-4: The reconstructed z_{react} in meters (kin:sing10; run#:2807). For each spectrometer, the central momentum was set to be $P_0 = 2.799$ GeV/c, and the scattering angle to be $\Theta_0 = 18.5°$. The seven foils of the 9-foil carbon target can be seen clearly, with one foil missing and one foil out of spectrometer acceptance. The lines indicate the expected foil positions with an interval of 0.04 m. The target is displaced several millimeters towards the upstream or negative direction.

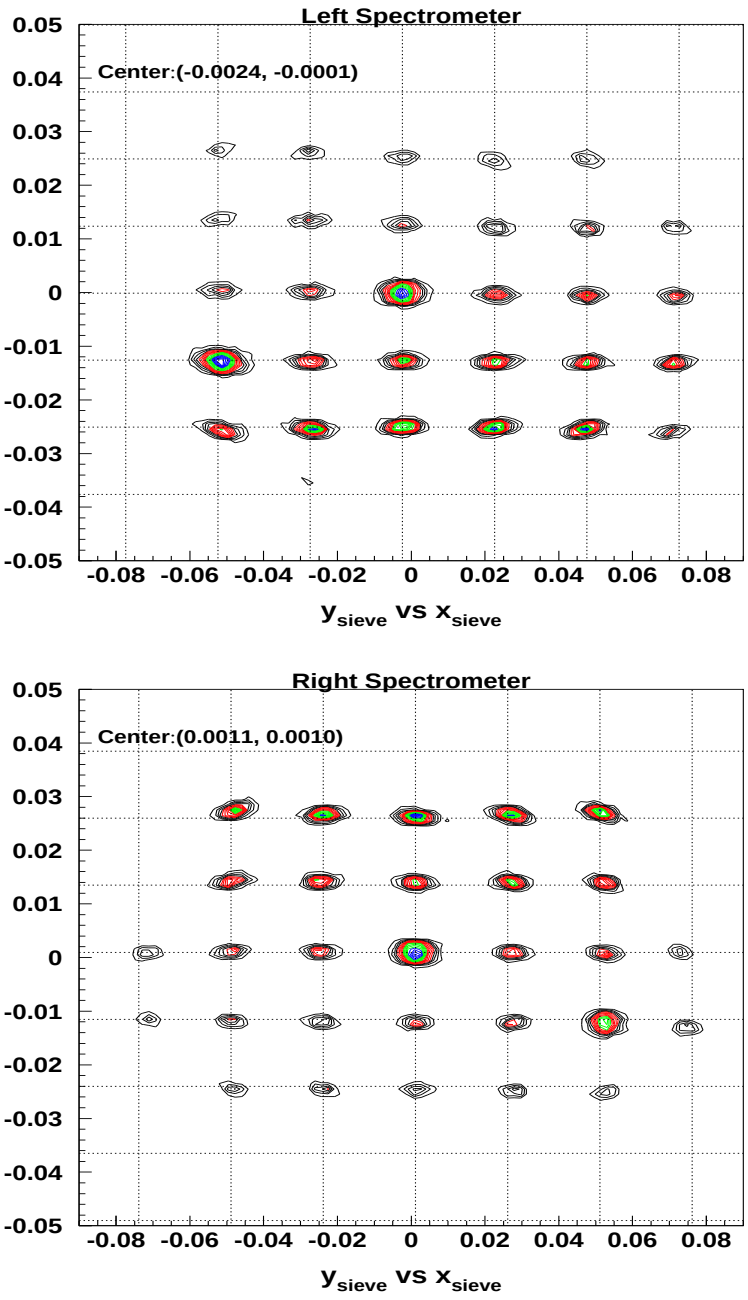

Figure 3-5: The reconstructed (x_{sieve}, y_{sieve}) in meters from both spectrometers (run#:1176) with the carbon target and sieve slits. For each spectrometer, the central momentum was set to be $P_0 = 1.170$ GeV/c, and the scattering angle to be $\Theta_0 = 12.5°$. The lines indicate the expected hole positions with an interval of 0.025 m in x direction and 0.0125 m in y direction.

Table 3.2: Spectrometer constants Γ_i ($i = 0 \sim 3$) for the two spectrometers, which relate the central momentum P_0 (MeV) and magnetic field B_0 (kG) of the dipole with the polynomial relation $P_0 = \sum_{i=0}^{3} \Gamma_i B_0^i$.

Spectrometer	Γ_0	Γ_1	Γ_2	Γ_3
Left	0.0	270.2 $\pm$ 0.15	0.0	(-1.6$\pm$0.7) e-3
Right	0.0	269.8 $\pm$ 0.15	0.0	(-1.6$\pm$0.7) e-3

3.5 Acceptance Analysis

The so-called R-function was generated for each event in both data analysis and simulation to optimize the cuts on different acceptance variables, i.e. θ_{tg}, ϕ_{tg}, y_{tg} and δ (see Section 3.4 for definitions). The R-function is defined to be the minimal distance to the acceptance boundary in terms of several two-dimensional polygons. It helps to select events in the central region of the spectrometer acceptance in a systematic and efficient way, where the optics matrix elements were well tuned. This method was originally used by Marat Rvachev in the E89-044 data analysis [87], and was later refined by John Lerose [88], an optics expert in Hall A, and by Zhengwei Chai in the E91-011 data analysis [89]. Chai's version, discussed below, was used to analyze the E94-104 data.

Six two-dimensional boundaries were defined for each spectrometer, out of any two combinations of the four acceptance variables, θ_{tg}, ϕ_{tg}, y_{tg} and δ. Each boundary is a polygon defined in a two-dimension plot of the data, with an example shown in Figure 3-6. For each event, the magnitude of the distance to the boundary was normalized based on the maximal length. The sign of the distance was positive for the events inside the polygon. The R-function for a single spectrometer, useful for singles π^+ data analysis, was defined to be the minimal distance to the six boundaries, while that for two spectrometers, useful for coincidence π^- data analysis, was defined by twelve two-dimension boundaries.

The coordinates of the vertices of the polygonal boundaries defined by the data

were written into a file, which would be read to calculate the R-function in both data and simulation. For data, a Fortran file was written to read the old ntuple in the HBOOK file generated by ESPACE and create a new one with the R-function. For simulation, the source codes of MCEEP were modified to compute and output the newly defined R-function.

The cut $R > 0.1$ was used for all the E94-104 data analysis. The events surviving this cut are plotted in Figure 3-8 and Figure 3-9, which are in the central region of the acceptance as expected. With cuts on the R-function or R, the acceptance dependence of the data to simulation ratio can be clearly seen in Figure 3-7. For a very large range of acceptance cuts, the change in the data to simulation ratio was only a few percent, therefore the uncertainty in differential cross section due to acceptance cuts was taken to be 3%.

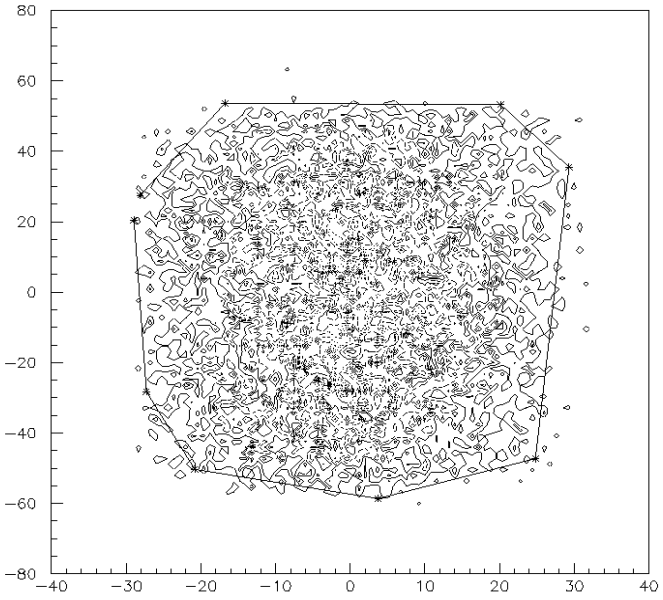

Figure 3-6: Definition of a two-dimensional polygonal boundary for the left spectrometer (kin:coin15).

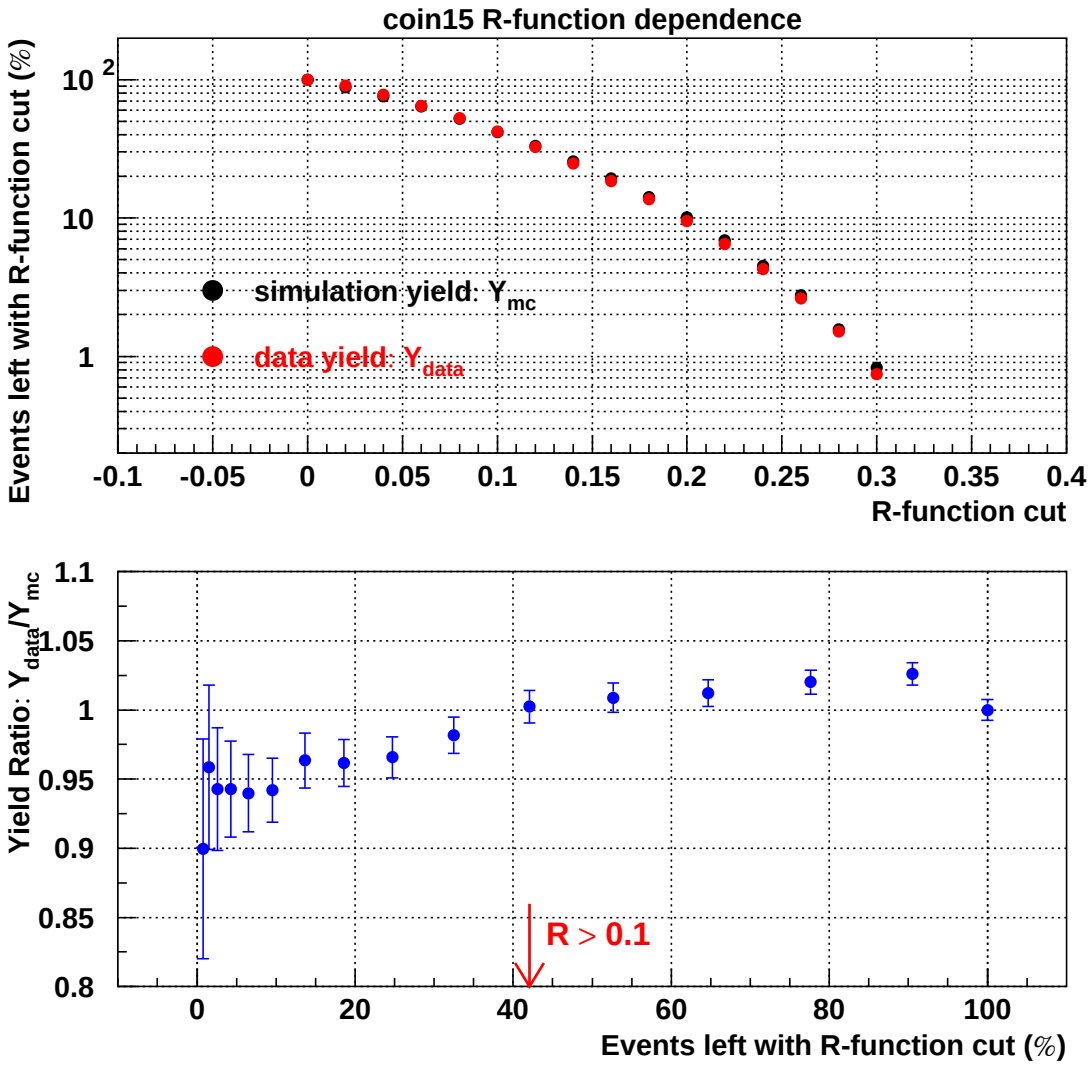

Figure 3-7: The R-function cut dependence of the data to simulation ratio. The yields with cut $R > 0$ from both data and simulation were normalized to unit. For each points, there were also some loose one-dimensional cuts on acceptance in addition to the R-function cut.

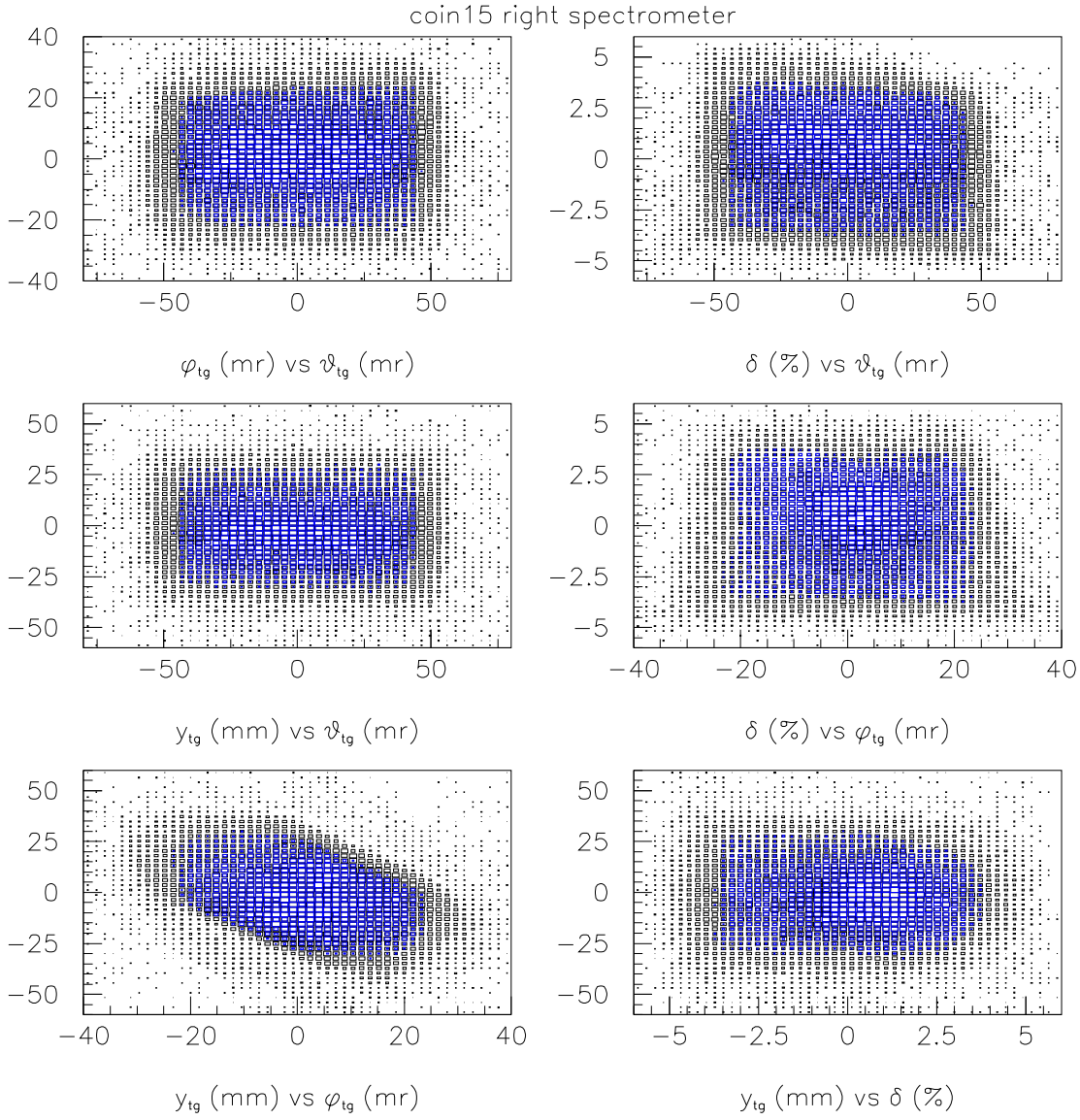

Figure 3-8: Left spectrometer acceptance (kin:coin15). The blue points represent the data surviving the R-function cut $R > 0.1$.

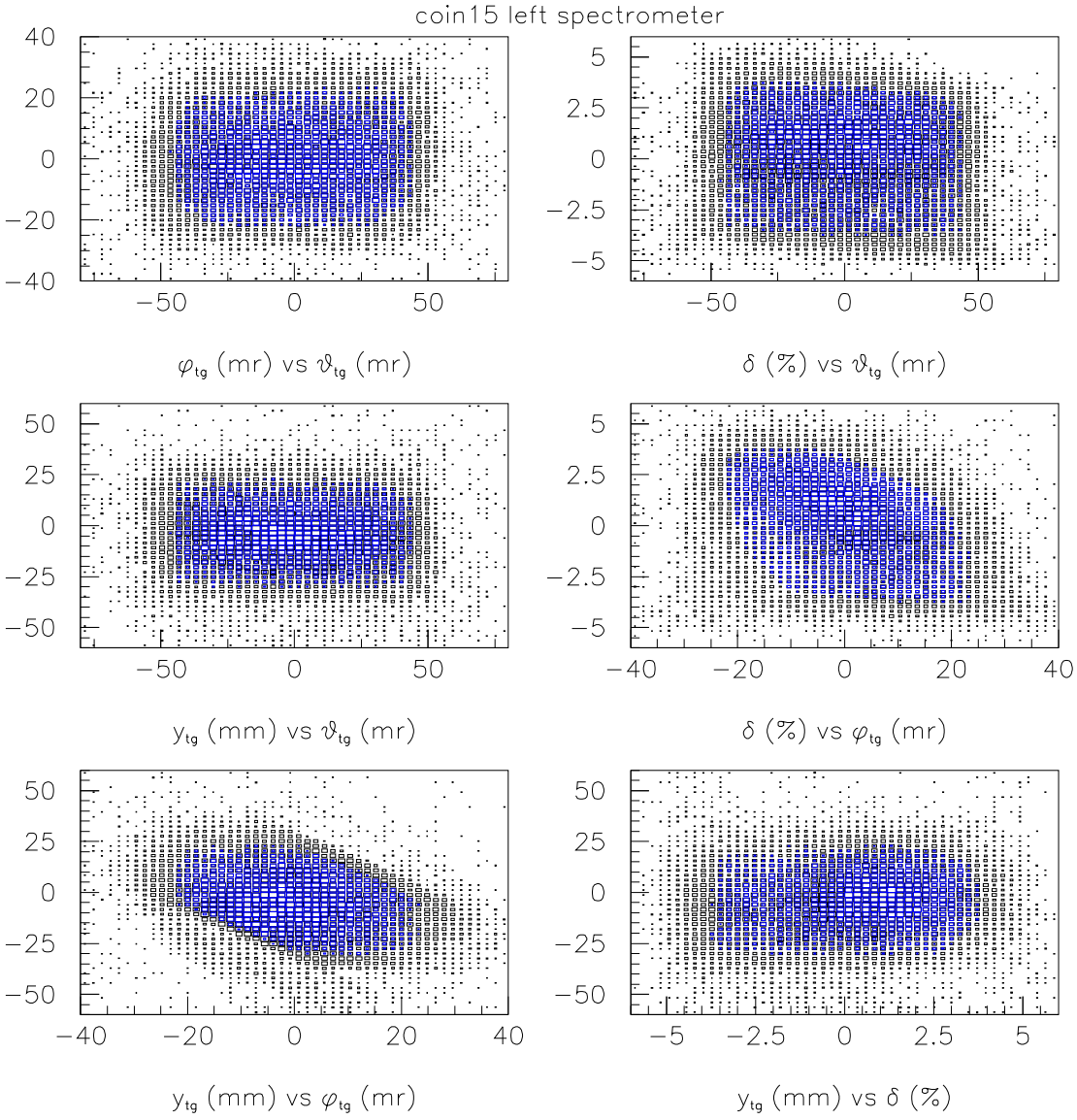

Figure 3-9: Right spectrometer acceptance (kin:coin15). The blue points represent the data surviving the R-function cut $R > 0.1$.

3.6 Particle Identification Analysis

3.6.1 Detector Calibrations

There were many PMTs to detect photons in particle identification detectors, i.e. two gas Čerenkov detectors, three aerogel Čerenkov detectors, and two shower-type detectors including the pion rejector and the total shower (preshower/shower) detector for experiment E94-104. The sum of the ADC spectra from individual PMTs (ADCSUM) was often used to identify the type of particles, which relates to the velocity of the particle in the Čerenkov detectors, and energy deposit in the shower-type detectors. To get a better ADCSUM spectrum, the ADC spectra were calibrated [90], by aligning their pedestal positions and signal peaks. The offsets and gains were put into the database, which were read by ESPACE to generate the ADCSUM spectrum based on the corrected ADC spectra. As an example, Figure 3-10 shows the corrected ADC spectra from the aerogel detector A1.

Most calibration constants were stable during the whole experiment, while some changed with time due to PMT/base replacement and High Voltage adjustment, such as PMT#9 in the left arm gas Čerenkov detector and some PMTs in the pion rejector.

3.6.2 Proton and Pion Separation

The aerogel Čerenkov detectors A1/A2/AM (see Section 2.5.3) were utilized to separate positive particles, dominantly proton and pions. The A1 and A2 detectors were used for normal polarity data, while AM was used for reversed polarity data. The particle identification with aerogel detectors was consistent with other methods available at low momentum, for example by measuring the Time-Of-Flight (or β) of the particle and the energy deposit in the scintillators. Generally speaking, pions fire aerogel detectors and produce large ADCSUM values, while protons give very small signals and form the pedestals. But the unphysically large ADCSUM of 10^{15} comes from protons due to pedestal suppression when the ADC values below some cutoff

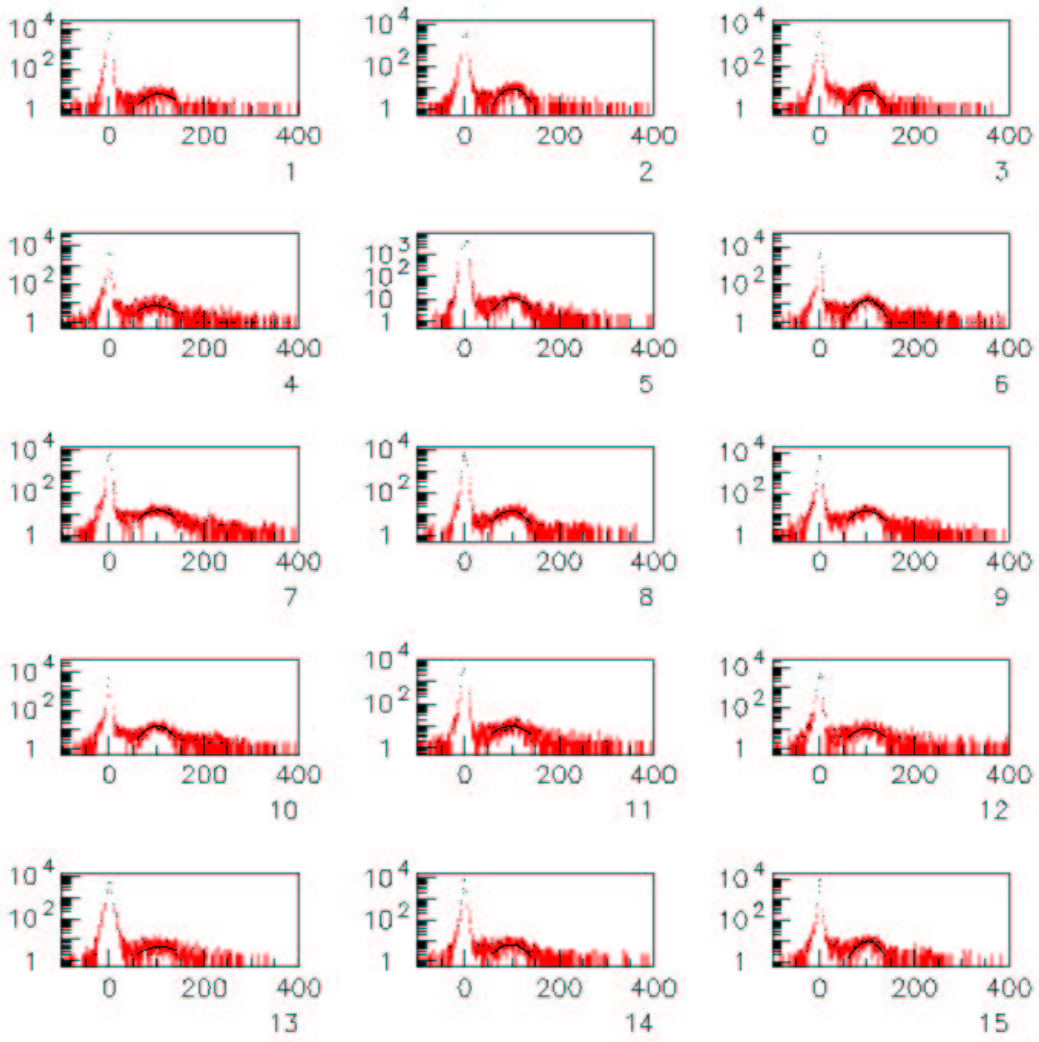

Figure 3-10: The corrected ADC spectra from the aerogel detector A1 (n=1.015). Only the first 15 out of 24 spectra were shown. The pedestals were centered at channel 0 while the single photoelectron peaks were centered at channel 100.

were not recorded into the data stream. For the coincidence $\gamma n \to \pi^- p$ measurement, the protons need to be identified. For the singles $\gamma p \to \pi^+ n$ measurement, the pions need to be selected instead.

Proton Selection for Coincidence Measurement

The criterion of *(A1 not fired).or.(A2 not fired)* was used to select protons, except for some low-momentum kinematics when pions barely fire A1, for which the criterion of *(A2 not fired)* was used instead. Here the criterion of *not fired* referred to the condition when the aerogel ADCSUM is much smaller than that produced by $\beta = 1$ particles, or unphysically large. The proton selection cut excluded few events in the coincidence measurement due to the high proton to pion ratio, as shown in Figure 3-11 and Table 3.3.

Table 3.3: Corrections and uncertainties for coincidence kinematics at $\theta_{cm} = 90°$ due to proton selection. The proton/pion and pion/total ratios in the left spectrometer were obtained using the criterion of *(A1 not fired).or.(A2 not fired)* to identify protons except for coin3 where *(A2 not fired)* was used.

Kinematics	coin3	coin6	coin20	coin9	coin12	coin15	coin17
P_L (GeV/c)	0.923	1.277	1.370	1.740	2.195	2.638	3.359
proton/pion	125	1574	1324	1946	592	297	146
pion/total (%)	0.79	0.06	0.08	0.05	0.17	0.34	0.68
Correction (%)	0	0	0	0	0	0	0
Uncertainty (%)	1	1	1	1	1	1	1

Actually the above criterion may underestimate the proton to pion ratio. The identified 'pions' in Table 3.3 may originally be protons, which knock out some δ-electrons (or knock-on electrons) on their flight path. The measured pion/total ratio gives the upper limit of the probability for a proton to produce δ-electrons. The probability can be estimated using the collision theory for charged particles and free electrons [91], as what was done for gas Čerenkov detector [92]. A crude estimation

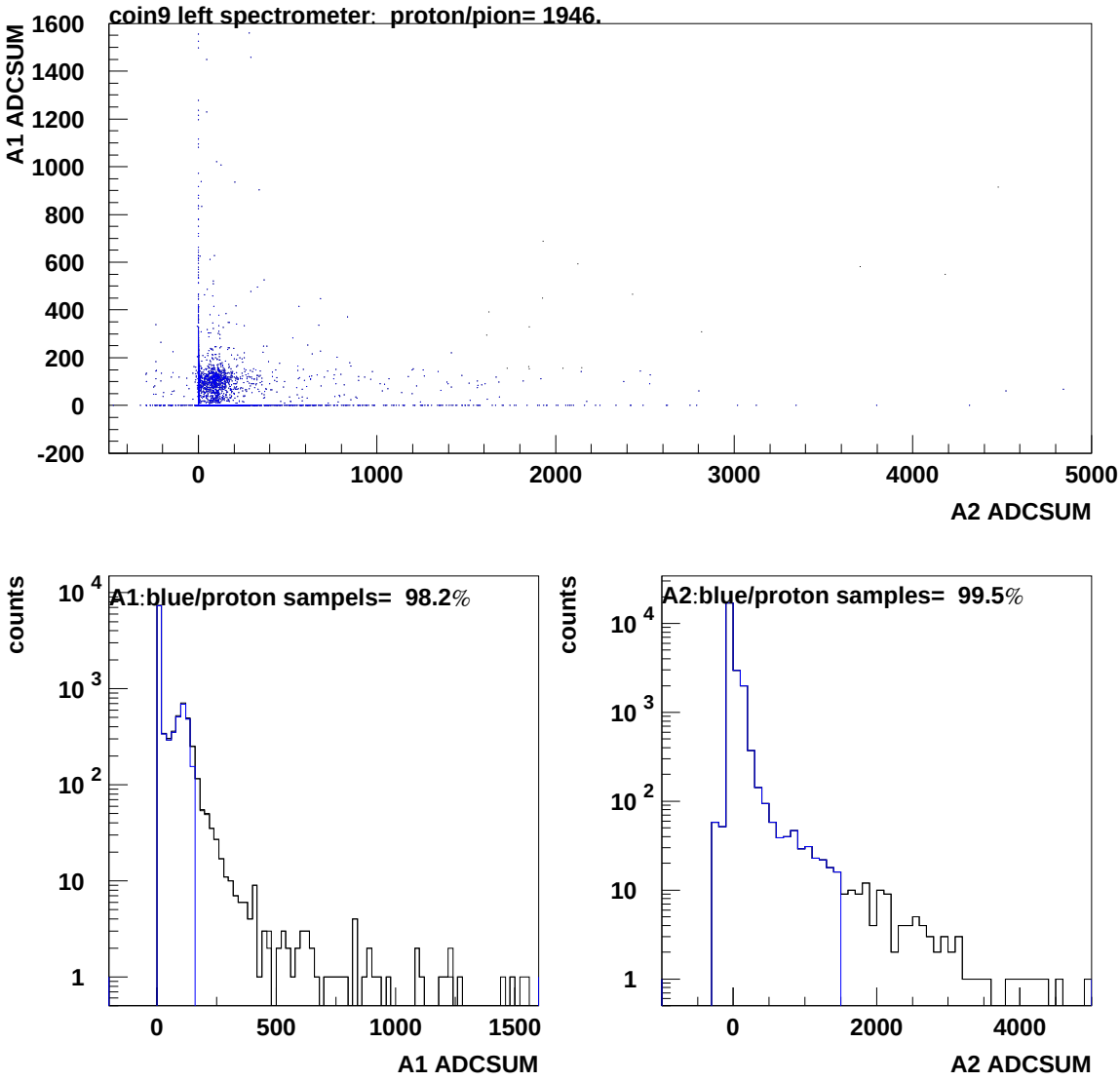

Figure 3-11: Proton selection (blue points) for coincidence kinematics coin9 (P_L = 1.74 GeV/c) based on the criterion of *(A1 not fired).or.(A2 not fired)*, i.e. $(not.150 < A1\ ADCSUM < 50000).or.(not.1500 < A2\ ADCSUM < 50000)$. The blue curves were used to estimate the pion detection efficiency of the individual aerogel Čerenkov detector based on the proton samples defined by the other detector.

could reproduce the momentum dependence of the probability, close to zero at low momentum and then increasing as momentum increases.

As shown in Table 3.3, no correction factor was applied to the final differential cross section for proton selection in the coincidence measurement, and the systematic uncertainty was taken to be 1% to cover the uncertainty in the inefficiency of proton detection (due to δ-electrons for example) while the pion contamination (the misidentification of pions as protons) can be ignored due to the high proton to pion ratio.

Pion Selection for Singles Measurement

The criterion of *(A1 fired).and.(A2 fired)* was used to select positive pions for singles kinematics, except for some low-momentum kinematics where the criterion of *(A2 fired)* was used. By defining good samples using the other aerogel detector, the proton contamination and pion detection efficiency of the cut on one aerogel detector can be estimated, as shown in Figure 3-12. The correction applied to the cross section was the sum of the pion detection inefficiencies of two aerogel detectors. The combined proton contamination, as the product of the contamination in the two individual detectors, was very small.

But due to the impurity of the samples and the correlation of the two detectors, the pion/proton ratio and δ-electron production were also considered in estimating the corrections and systematic uncertainties in Table 3.4. For example, the upper limit of the probability to knock out δ-electrons can be 0.7% for a proton with momentum of 3.4 GeV/c, according to the pion/total ratio in Table 3.3, so the upper limit of proton contamination can be 7% because of the small pion/proton ratio (0.09) for sing16 in Table 3.4. The uncertainty for sing16 was assigned to be 4% to combine the uncertainty in pion detection inefficiency and half of the upper limit of the proton contamination.

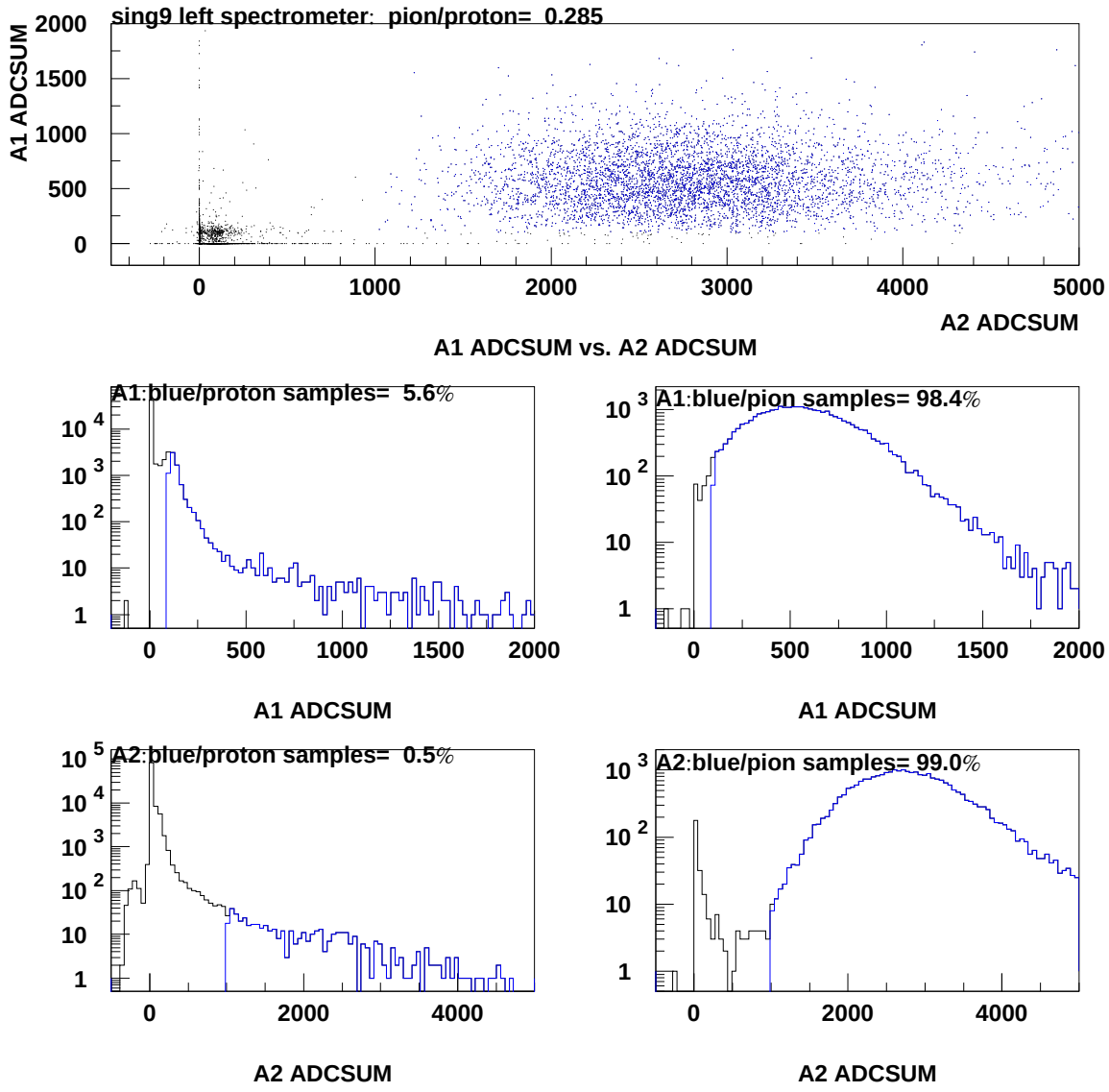

Figure 3-12: Pion selection (blue points) for singles kinematics sing9 (P_L = 1.74 GeV/c) based on the criterion of *(A1 fired).and.(A2 fired)*, i.e. $(100 < A1\ ADCSUM < 50000).and.(1000 < A2\ ADCSUM < 50000)$. The blue curves were used to determine the proton contamination and pion detection efficiency of the cut on one detector, aerogel detector A1 or A2, based on the proton or pion samples defined by the other detector.

Table 3.4: Corrections and uncertainties for singles kinematics at $\theta_{cm} = 90°$ due to pion selection. The pion/proton ratios in the left spectrometer were obtained using the criterion of *(A1 fired).and.(A2 fired)* to identify pions except for sing3 where the criterion of *(A2 fired)* was used.

Kinematics	sing3	sing6	sing19	sing9	sing12	sing14	sing16
P_L (GeV/c)	0.923	1.277	1.370	1.740	2.195	2.638	3.359
pion/proton	0.74	0.86	0.76	0.29	0.08	0.10	0.09
Correction (%)	1	3	2	2	2	2	2
Uncertainty (%)	2	2	2	2	3	3	4

3.6.3 Pion Selection for Coincidence Measurement

The pion selection from the electron background in the coincidence measurement was realized by using the combination of the gas Čerenkov and shower-type detector, i.e. the long gas Čerenkov and total shower (preshower/shower) detector for normal polarity kinematics, the short gas Čerenkov and pion rejector detector for reversed polarity kinematics. The pions give much smaller signals than electrons in these detectors. For gas Čerenkov detector, the cut $(GAS\ ADCSUM < 300).or.(GAS\ ADCSUM > 50000)$. was used to identify pions, while the single photoelectron peaks were aligned to be at channel 150. For the shower-type detector, a two-dimensional graphic cut was defined for each kinematics.

Similarly to what is done for the singles pion selection, the electron contamination and pion detection efficiency of the cut on one detector can be obtained by defining good samples based on the other detector, as shown in Figure 3-13. The corrections and systematic uncertainties in Table 3.5 were thus estimated. The corrections were dominated by inefficiencies, with negligible contribution from electron contaminations.

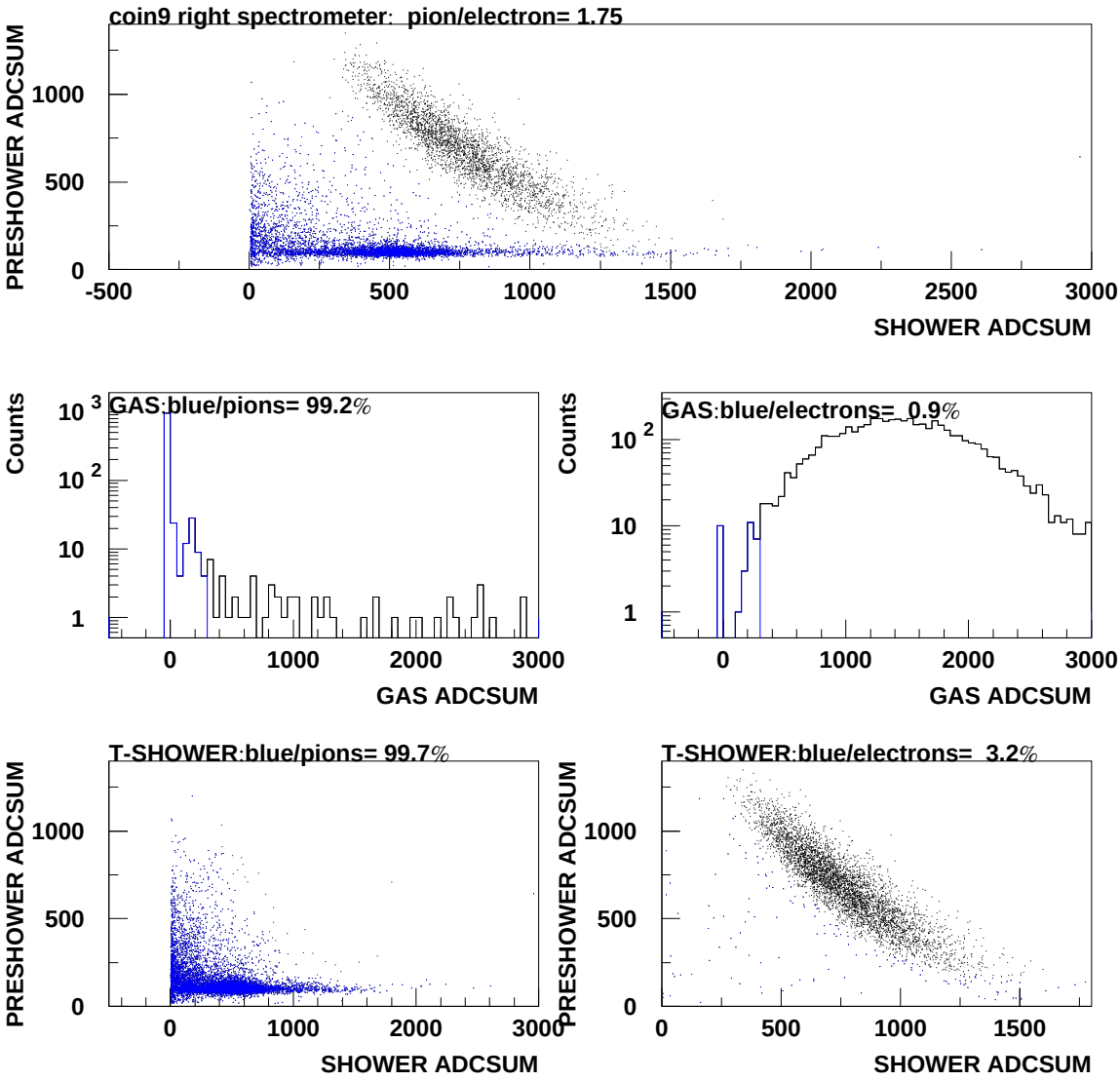

Figure 3-13: Pion selection (blue points) for coincidence kinematics coin9 ($P_R = 1.438$ GeV/c) based on the criterion of *(GAS not fired).and.(TOTAL SHOWER not fired)*. The blue curves were used to estimate the electron contamination and pion detection efficiency of the cut on one detector, gas Čerenkov or total shower detector, based on the electron and pion samples defined by the other detector.

Table 3.5: Corrections and uncertainties for coincidence kinematics at $\theta_{cm} = 90°$ due to pion selection. The pion/electron ratios in the right spectrometer were obtained using the criterion of *(GAS not fired).and.(TOTAL SHOWER not fired)* to identify pions.

Kinematics	coin3	coin6	coin20	coin9	coin12	coin15	coin17
P_R (GeV/c)	0.706	1.015	1.099	1.438	1.866	2.291	2.990
pion/electron	2.3	1.6	1.5	1.8	0.3	0.3	0.2
Correction (%)	2	2	2	1	1	1	1
Uncertainty (%)	2	2	2	2	2	2	2

3.7 Background Subtraction

The data taken with the radiator and production target contained various backgrounds, such as those from the electroproduction process and those from the end caps of the target. Therefore each complete kinematics consisted of four different configurations, i.e.

(1) Radiator In, Production Target In;

(2) Radiator In, Production Target Out;

(3) Radiator Out, Production Target In;

(4) Radiator Out, Production Target Out.

'Production Target In' means using the LD2 target in the coincidence measurements and using the LH2 target in the singles measurements. 'Production Target Out' means using the LH2 target in the coincidence measurements and using the dummy target in the singles measurements.

The backgrounds were subtracted from the coincidence π^- or singles π^+ production yield according to

$$\begin{aligned} Y_{\rm data}(\pi^-) &= (Y_{\rm in,LD2} - Y_{\rm in,LH2}) - f(E_\gamma) * (Y_{\rm out,LD2} - Y_{\rm out,LH2}) \\ Y_{\rm data}(\pi^+) &= (Y_{\rm in,LH2} - Y_{\rm in,Dummy}) - f(E_\gamma) * (Y_{\rm out,LH2} - Y_{\rm out,Dummy}) \end{aligned} \quad (3.4)$$

where the 'in' or 'out' represents using or removing the radiator during the data taking. The factor $f(E_\gamma)$ is less than unity due to the interaction between the radiator and the electron beam. The values for different beam energies were shown in Section 3.8.4. For most kinematics, the yield without the radiator was about one third of that with radiator. And the yield without the production target, especially for coincidence cases, was much smaller than the production yield.

3.8 Monte Carlo Simulation with MCEEP

3.8.1 Overview

The Monte Carlo simulation was done by using MCEEP (Monte Carlo for $(\underline{e}, \underline{e'p})$) [83], a computer program designed for coincidence $(e, e'X)$ experiments in Hall A. It was modified [84] in the kinematics, cross section and bremsstrahlung photon yield calculation to simulate the photoproduction processes: coincidence $n(\gamma, \pi^- p)$ and singles $p(\gamma, \pi^+)n$. The program was also modified to generate the R-function to define the acceptance cuts (see Section 3.5).

The MCEEP program employs a uniform random sampling method to populate the experimental acceptance. An event is defined as one combination of variables that completely specifies the reaction in the lab. The cross section is considered as the weight of the event. A block diagram of the MCEEP simulation is shown in Figure 3-14 [83]. The blocks to the right of the thick arrow are the subroutines called by the main program MCEEP. Indented subroutines are within the main Monte Carlo event loop. At the start of the Monte Carlo event loop, the lab coordinates for both scattered particle and ejectile at the target are generated randomly and then converted to transport vectors, directly related to the spectrometer optics. After various operations affecting the cross section in the subroutine SPECTROMETER(1) such as the spectrometer misalignments, the transport vectors are then converted back to lab coordinates. The process is repeated in subroutine SPECTROMETER(2) to

consider the operations that only affect the kinematics, such as multiple scattering. The outputs of MCEEP are histograms and ntuples, which can be read by the analysis tool of PAW after they are included into a HBOOK file by an external program (mceep_util).

For the photoproduction processes $\gamma N \to \pi^{+/-} N$, the subroutine PHYS_CHOICE was modified to include a new option, which was called TWOBODY. The subroutine KINEM_TWOBODY and GAMPI_TWOBODY were written to calculate the corresponding kinematics and cross section. The momentum distribution of the neutron inside the deuteron target was considered in these two subroutines. The subroutine CHANGEANGLE and LORENTZTRAN were used to calculate the differential cross section in the lab when the neutron target is not at rest. The bremsstrahlung photon energy was randomly generated in the beginning of the subroutine KINEM_TWOBODY and the bremsstrahlung photon yield spectrum could be obtained in the subroutine BREMSP, called by GAMPI_TWOBODY. The pion survival factor was also included in the cross section calculation in the subroutine GAMPI_TWOBODY. Besides, the codes on energy loss were also modified since pions behave more like protons than electrons, and photons lose no energy in the target.

3.8.2 Kinematics

A new subroutine KINEM_TWOBODY tailored for $\gamma N \to \pi N$ processes was written to replace the old kinematics calculation. The major steps are listed below:

- Random generation of the photon energy within a 1000 MeV window below the beam energy.
- Random generation of different components of the Fermi momentum or the momentum distribution of neutrons inside the deuteron target $\vec{P}_f$, with the magnitude distribution specified by an input data file.
- Random generation of the momentum components of the outgoing pion $\vec{P}_\pi$ in

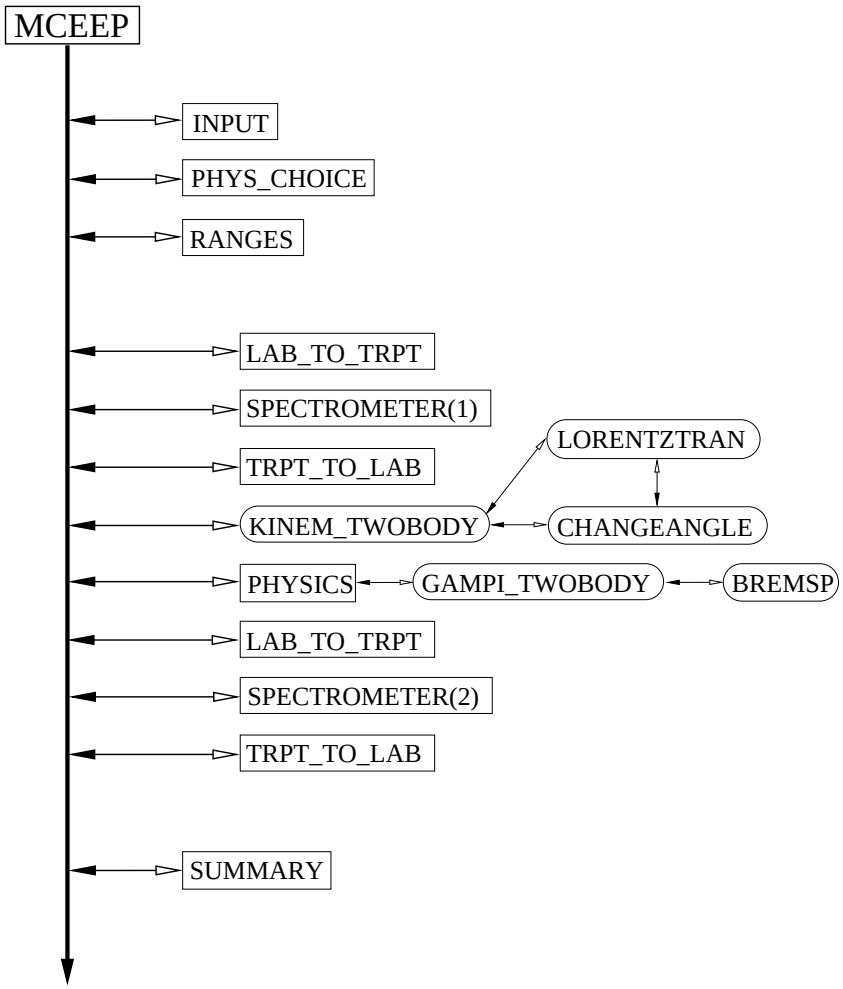

Figure 3-14: Block diagram of the modified Monte Carlo simulation program MCEEP. The blocks with rounded corners are the new subroutines written for the $\gamma N \rightarrow \pi^{+/-} N$ process.

the lab frame, with the magnitude being the solution of equation $ax^2+bx+c=0$ with coefficients

$$\begin{aligned} a &= (E_f+E_\gamma)^2-(\vec{P}_\gamma\cdot\hat{P}_\pi+\vec{P}_f\cdot\hat{P}_\pi)^2 \\ b &= -(\vec{P}_\gamma\cdot\hat{P}_\pi+\vec{P}_f\cdot\hat{P}_\pi)(m_\pi^2+m_t^2-m_p^2+2E_\gamma E_f-2\vec{P}_\gamma\cdot\vec{P}_f) \\ c &= (E_f+E_\gamma)^2m_\pi^2-\left(E_\gamma E_f-\vec{P}_\gamma\cdot\vec{P}_f+\frac{m_\pi^2+m_t^2-m_p^2}{2}\right)^2 , \end{aligned} \tag{3.5}$$

where $\vec{P}_f$ and E_f are the Fermi momentum and energy.

- Calculation of the momentum of the outgoing proton in the lab frame by using momentum conservation

$$\vec{P}_p=\vec{P}_\gamma+\vec{P}_f-\vec{P}_\pi , \tag{3.6}$$

and then the direction of the proton, which will be used to determine whether the event will fall into the spectrometer acceptance or not.

3.8.3 Cross Section

A new subroutine GAMPI_TWOBODY called by PHYSICS was written to calculate the cross section, based on a Fortran code on single pion photoproduction [93]. The main steps are described below:

- Determination of the scattering angle in the center-of-mass frame. First to calculate the lab momentum magnitude $|\vec{P}_\pi|$ of outgoing pion assuming the target is at rest, which satisfies the equation $ax^2+bx+c=0$ with coefficients

$$\begin{aligned} a &= (m_p+P_\gamma)^2-P_\gamma^2\cos^2\theta_{lab} \\ b &= -P_\gamma\cos\theta_{lab}(2P_\gamma m_p+m_\pi^2) \\ c &= (m_p+P_\gamma)^2m_\pi^2-(P_\gamma m_p-\frac{m_\pi^2}{2})^2 . \end{aligned} \tag{3.7}$$

Then to derive the center-of-mass scattering angle using Lorentz transformation

$$\begin{aligned} \beta_c &= \frac{E_\gamma}{E_\gamma + m_p} \, , \gamma_c = \frac{1}{\sqrt{1-\beta_c^2}} \\ P_\pi^{tran}|_{cm} &= P_\pi^{tran}|_{lab} = P_\pi \cos\theta_{lab} \\ P_\pi^{long}|_{cm} &= \gamma_c (P_\pi^{long}|_{lab} - \beta_c \cdot \sqrt{P_\pi^2 + m_\pi^2}) \\ \tan\theta_{cm} &= \frac{P_\pi^{tran}|_{cm}}{P_\pi^{long}|_{cm}} \, . \end{aligned} \tag{3.8}$$

- The differential cross section $\frac{d\sigma}{dt}$ for π^+ photoproduction at fixed center-of-mass angle was assumed to be

$$\frac{d\sigma}{dt} = \frac{0.69 F_{survive}}{(1+\cos\theta_{cm})^4 (1-\cos\theta_{cm})^5} \cdot (\frac{s_0}{s})^7 \, , \tag{3.9}$$

where the angular distribution was fitted to SLAC data in the several GeV region [9]. The factor of 0.69 and $s_0 = 10.263$ came from these SLAC data at 5 GeV. The s^{-7} dependence was also consistent with the constituent counting rule. For π^- photoproduction, there was another factor of 0.25 from the assumption of $\pi^-/\pi^+ = 0.25$, though the overall normalization factor did not affect the final cross section extraction. The pion survival factor $F_{\rm survive}$ was calculated by

$$F_{\rm survive} = \exp(-\frac{\rm L}{\gamma_\pi \tau_\pi \beta_\pi c}) \, , \tag{3.10}$$

with the flight length L of 25 m and lifetime of $\tau_\pi = 2.6 \times 10^{-8}$ s.

- The Jacobian of the transformation from $d\sigma/dt$ to $d\sigma/d\Omega_{cm}$ is

$$\begin{aligned} \frac{dt}{d\Omega_{cm}} &= \frac{|P_i| \cdot |P_f|}{\pi} \\ &= \frac{E_\gamma m_p}{\sqrt{s}} \cdot \sqrt{(\frac{s - m_\pi^2 + m_p^2}{2\sqrt{s}})^2 - m_p^2} \cdot \frac{1}{\pi} \, , \end{aligned} \tag{3.11}$$

where the Mandelstam variable $s = 2E_\gamma m_p + m_p^2$.

- The Jacobian of the transformation from $d\sigma/d\Omega_{cm}$ to $d\sigma/d\Omega_{lab}$ is

$$\frac{d\Omega_{cm}}{d\Omega_{lab}} = \frac{[\sin^2\theta_{cm} + (\cos\theta_{cm} + \frac{v_c}{v_b'})^2/(1-\beta_c^2)]^{3/2}}{(1 + \frac{v_c}{v_b'}\cos\theta_{cm})/\sqrt{1-\beta_c^2}} \ , \tag{3.12}$$

where v_c is the velocity of the center-of-mass frame in the lab frame, $\beta_c{=}v_c/c = \frac{E_\gamma}{E_\gamma + m_p}$, and v_b' is the velocity of the particle in the center-of-mass frame.

- For π^- photoproduction with a nontrivial initial momentum distribution, we first transformed the lab frame to the target rest frame, and calculated the photon energy, pion momentum, scattering angle and cross section there. Then we determined the Jacobian from the target rest frame to the lab frame to get the cross section in the lab frame:

  - The Lorentz transformation matrix (subroutine LORENTZTRAN called by KINEM_TWOBODY) is

$$\begin{pmatrix} 1+\frac{v_x^2}{v^2}(\gamma-1) & \frac{v_x v_y}{v^2}(\gamma-1) & \frac{v_x v_z}{v^2}(\gamma-1) & i\frac{V_1}{c} \\ \frac{v_y v_x}{v^2}(\gamma-1) & 1+\frac{v_y^2}{v^2}(\gamma-1) & \frac{v_y v_z}{v^2}(\gamma-1) & i\frac{V_2}{c} \\ \frac{v_z v_x}{v^2}(\gamma-1) & \frac{v_z v_y}{v^2}(\gamma-1) & 1+\frac{v_z^2}{v^2}(\gamma-1) & i\frac{V_3}{c} \\ -i\frac{V_1}{c} & -i\frac{V_2}{c} & -i\frac{V_3}{c} & -i\frac{V_4}{c} \end{pmatrix} ,$$

    where $V_i = (\gamma v_i, \gamma i c)$.

  - The Jacobian of the transformation from the target-rest frame $d\sigma/d\Omega_t$ to $d\sigma/d\Omega_{lab}$ is,

$$\begin{aligned} \frac{d\Omega_t}{d\Omega_{lab}} &= \sin\theta_t \left| \frac{\partial\theta_t}{\partial\theta_{lab}} \cdot \frac{\partial\phi_t}{\partial\phi_{lab}} - \frac{\partial\phi_t}{\partial\theta_{lab}} \cdot \frac{\partial\theta_t}{\partial\phi_{lab}} \right| \\ &\sim \sin\theta_t \left| \frac{\triangle\theta_t}{\triangle\theta_{lab}} \cdot \frac{\triangle\phi_t}{\triangle\phi_{lab}} - \frac{\triangle\phi_t}{\triangle\theta_{lab}} \cdot \frac{\triangle\theta_t}{\triangle\phi_{lab}} \right| \ , \end{aligned} \tag{3.13}$$

where the subscript t denotes the target-rest frame and the angles in the lab frame were defined in such a way that $\theta_{lab} = 90°$. The differentials were obtained in a numerical way (in subroutine CHANGEANGLE) by shifting the angles in the lab frame.

3.8.4 Bremsstrahlung Photon Yield

The subroutine BREMSP was embedded in the simulation to calculate the photon yield from an infinitely thin radiator, based on reference [56]. In this approach, the photon yield is proportional to the thickness of the radiator. Later, the photon yield calculation was corrected by using the thick-radiator codes, written by Dave Meekins [55] based on reference [56, 57], which considered energy losses of the electron beam in the radiator and was expected to achieve a precision of 3%. Here the photon yield is no longer proportional to the thickness of the radiator, which is consistent with the radiator linearity study shown in Figure 2-9. Figure 3-15 shows the comparison of photon yields from the thin-radiator and thick-radiator codes. For 6.12% copper radiator, the thin-radiator approach overestimated the yield by about 15%. The exact corrections for all the beam energies are listed in Table 3.6.

Table 3.6: Correction to the differential cross section due to the change in photon yield ($Y_{\rm thin}/Y_{\rm thick} - 1$) by switching from thin-radiator codes to thick-radiator ones.

E_e (MeV)	1173.3	1723.4	1876.9	2561.5	3400.0	4236.4	5614.4
Correction (%)	11.3	12.8	13.4	15.3	15.4	16.9	19.9

As the radiator absorbs and scatters electrons, the data with radiator out would overestimate the electron-induced background of the data with radiator in when the photon energy is close to the end point. To subtract the electroproduction background, the expression $Y_{in} - f(E_\gamma) \cdot Y_{out}$ with $f(E_\gamma) < 1$ is used to obtain the correct photoproduction yield. The $f(E_\gamma)$ calculated by a code written by Meekins [55] are shown in Table 3.7.

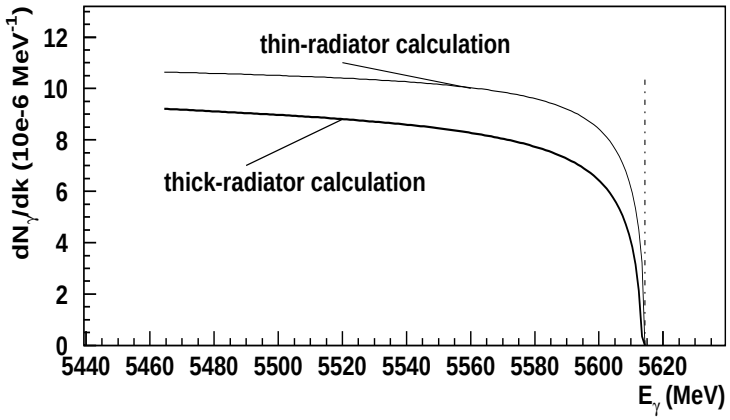

Figure 3-15: Comparison of bremsstrahlung photon spectrum generated with thick-radiator and thin-radiator codes, for the electron beam at 5614 MeV and 6.12% copper radiator.

Table 3.7: Calculation of $f(E_\gamma)$ factor for different beam energies.

E_e(MeV)	1173.3	1723.4	1876.9	2561.5	3400.0	4236.4	5614.4
$f(E_\gamma)$ Factor	0.791	0.764	0.758	0.738	0.720	0.706	0.688

3.9 Shape Comparison between Data and Simulation

In this section, the distributions of different variables from the data were compared with those from the Monte Carlo simulation, including

- Acceptance variables for coincidence $d(\gamma,\pi^-p)p$ process, i.e. θ_{tg}, ϕ_{tg}, y_{tg} and δ (see Section 3.4) from both spectrometers.

- Acceptance variables for singles $p(\gamma,\pi^+)n$ process, i.e. θ_{tg}, ϕ_{tg}, y_{tg} and δ (see Section 3.4) from the spectrometer detecting the positive pions.

- Reconstructed photon energy for coincidence $d(\gamma,\pi^-p)$ process using

$$E_\gamma = \frac{E_\pi E_p - P_\pi P_p \cos(\theta_\pi+\theta_p) - m_d(E_\pi+E_p) + \frac{1}{2}(m_\pi^2+m_p^2+m_d^2-m_p^2)}{E_\pi+E_p-m_d-P_\pi\cos\theta_\pi - P_p\cos\theta_p} \,. \tag{3.14}$$

  If one ignores the binding energy of the deuteron, the above formula can be approximated by

$$E_\gamma = \frac{E_\pi E_p - P_\pi P_p \cos(\theta_\pi+\theta_p) + \frac{1}{2}(m_\pi^2+m_p^2-m_n^2)}{E_\pi+E_p-P_\pi\cos\theta_\pi - P_p\cos\theta_p} \,. \tag{3.15}$$

- Reconstructed photon energy for singles $p(\gamma,\pi^+)n$ process using

$$E_\gamma = \frac{E_\pi m_t - \frac{1}{2}(m_t^2+m_\pi^2-m_n^2)}{m_t - E_\pi + P_\pi\cos\theta_\pi^{lab}} \,, \tag{3.16}$$

  where m_t refers to the mass of proton.

- Reconstructed momentum distribution for coincidence $d(\gamma,\pi^-p)p$ process using

$$\begin{aligned} P_x &= P_\pi \sin(\Theta_R-\phi_\pi)\sin\theta_\pi + P_p\sin(\Theta_L+\phi_p)\sin\theta_p \\ P_y &= -P_\pi\sin(\Theta_R-\phi_\pi)\cos\theta_\pi + P_p\sin(\Theta_L+\phi_p)\cos\theta_p \end{aligned}$$

$$\begin{aligned} P_z &= P_\pi \cos(\Theta_R - \phi_\pi) + P_p \cos(\Theta_L + \phi_p) - E_\gamma \\ |P_f| &= \sqrt{P_x^2 + P_y^2 + P_z^2} \end{aligned} \tag{3.17}$$

where $\Theta_{L/R}$ is the scattering angle setting of the left/right spectrometer. $\phi_{\pi/p}$ and $\theta_{\pi/p}$ are defined in the target coordinate system (see Figure 3-3).

- Reconstructed center-of-mass angle for the coincidence $d(\gamma, \pi^- p)p$ process using the Lorentz transformation

$$\begin{aligned} P_{cm}^{\text{trans}} &= P_{lab} \sin \Theta_{lab} \\ P_{cm}^{\text{long}} &= \gamma P_{lab} \cos \Theta_{lab} - \gamma \beta E_{lab} \\ \Theta_{cm} &= \arctan(P_{cm}^{\text{trans}} / P_{cm}^{\text{long}}) \ , \end{aligned} \tag{3.18}$$

where the momentum P and energy E belong to the outgoing pion, β is the velocity of the center-of-mass frame observed in the lab frame and $\gamma = 1/\sqrt{1-\beta^2}$.

- Reconstructed center-of-mass angle for the singles $p(\gamma, \pi^+)n$ process similarly to the coincidence case.

The results from the data are symbolized by solid circles (for coincidence kinematics) or solid squares (for singles kinematics), while those from simulation are plotted as lines, as shown in Figure 3-16 to Figure 3-22. Each simulated spectrum was multiplied by an arbitrary normalization factor in order to compare its shape with that of the data spectrum. Except for the photon energy comparisons, only one typical kinematics is shown for each comparison, i.e. coin15 with $E_e = 4236.4$ MeV and $\theta_{cm} = 90°$ for the coincidence cases, and sing14 with $E_e = 4236.4$ MeV and $\theta_{cm} = 90°$ for the singles cases.

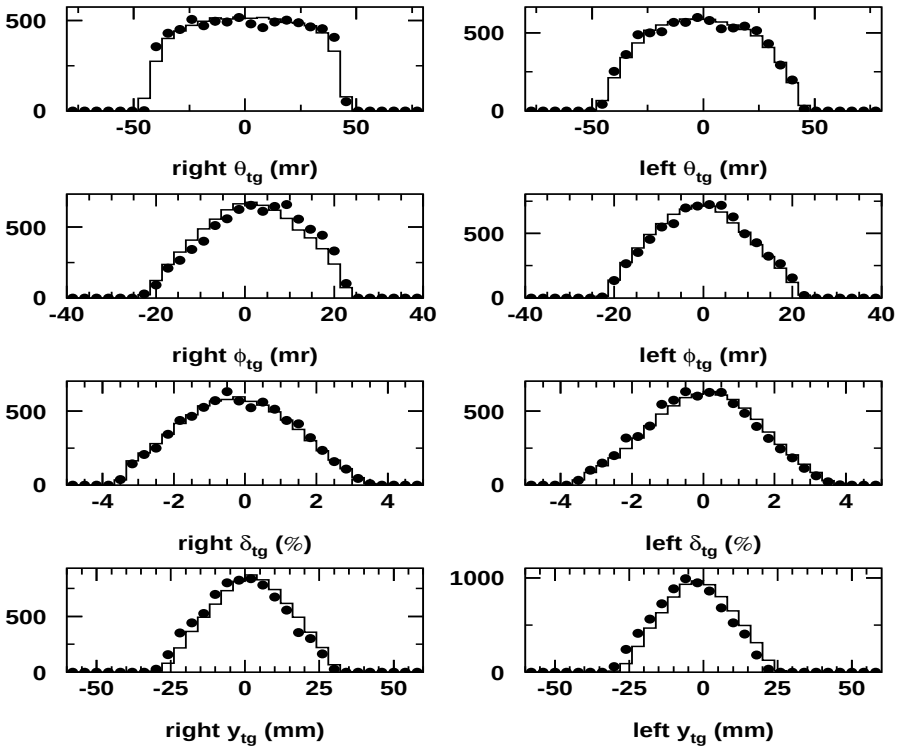

Figure 3-16: Shape comparison of acceptance variables (see Section 3.4 for definitions) from left and right spectrometers between data and simulation for coincidence π^- photoproduction (kin:coin15). The results from data are plotted in symbols, while those from simulation are plotted in lines.

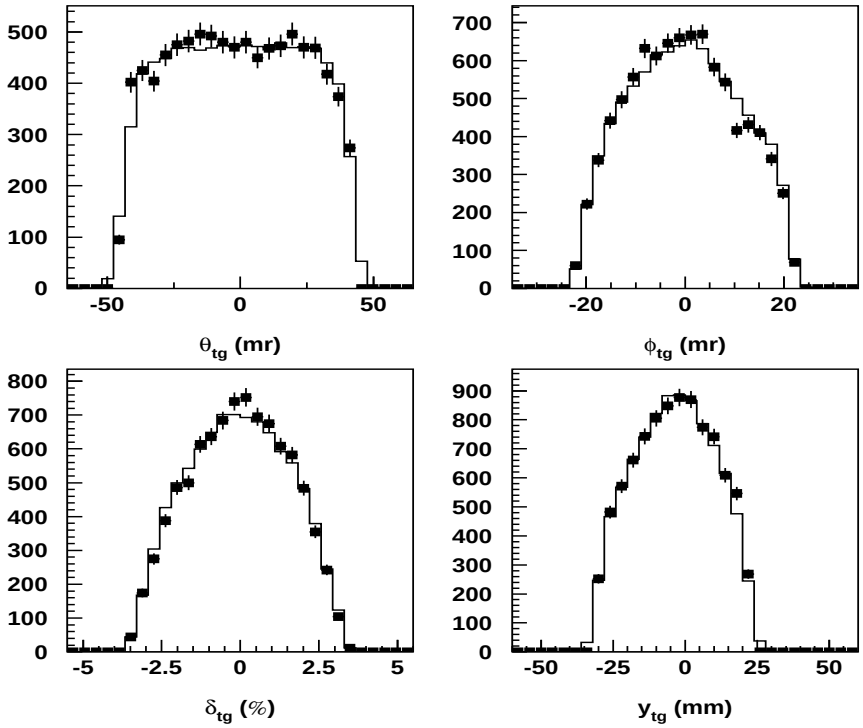

Figure 3-17: Shape comparison of acceptance variables (see Section 3.4 for definitions) from left spectrometers between data and simulation for singles π^+ photoproduction (kin:sing14). The results from data are plotted in symbols, while those from simulation are plotted in lines.

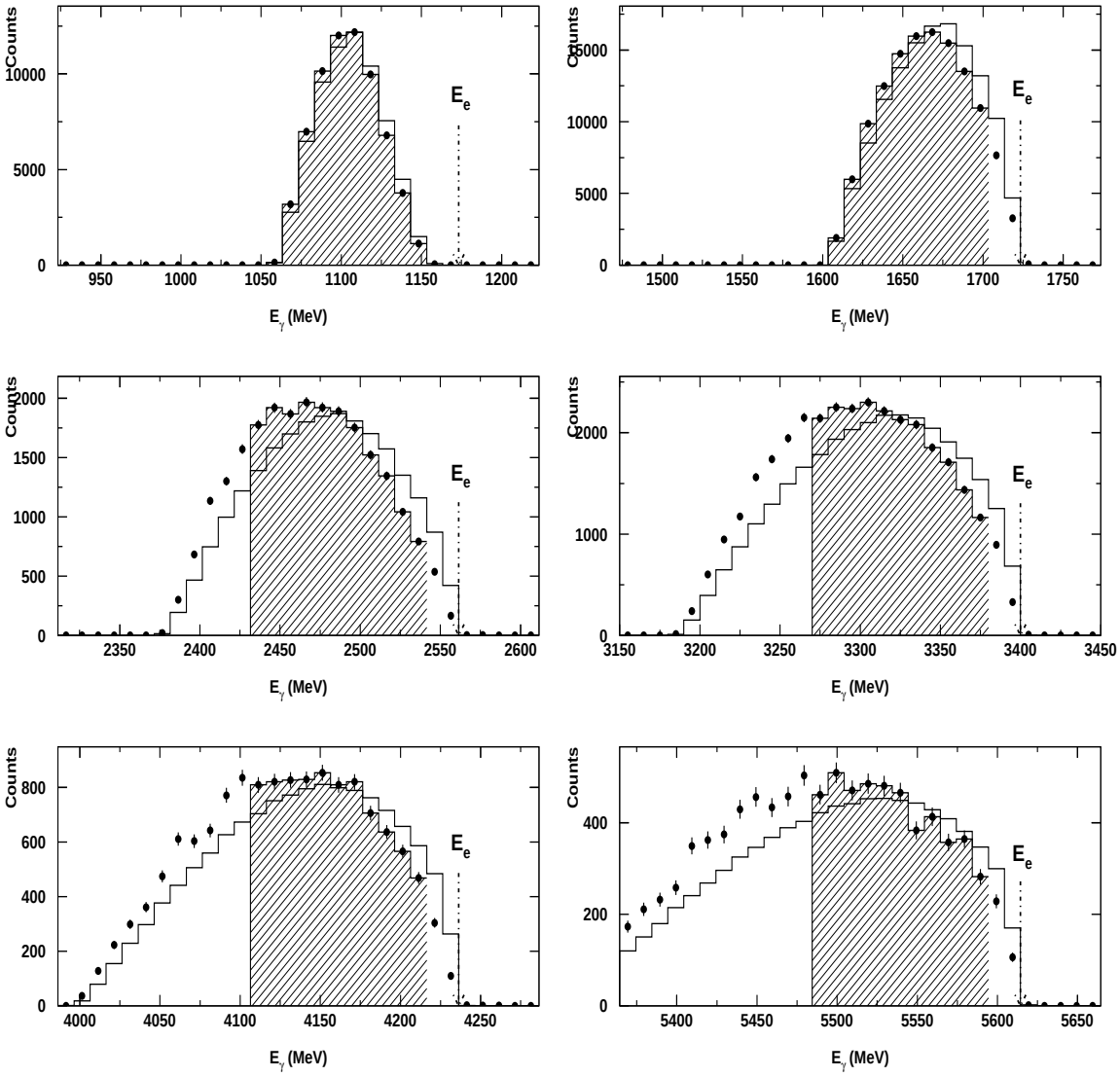

Figure 3-18: Shape comparison of reconstructed photon energy between data and simulation for coincidence π^- photoproduction at $\theta_{cm} = 90°$. The results from data are plotted in symbols, while those from simulation are plotted in lines. The electron beam energies are 1173.3, 1723.4, 2561.5, 3400.0, 4236.4 and 5614.4 MeV. The comparison at beam energy 1876.9 MeV (not shown here) is very similar to that at 1723.4 MeV. The shaded events were chosen to extract differential cross section.

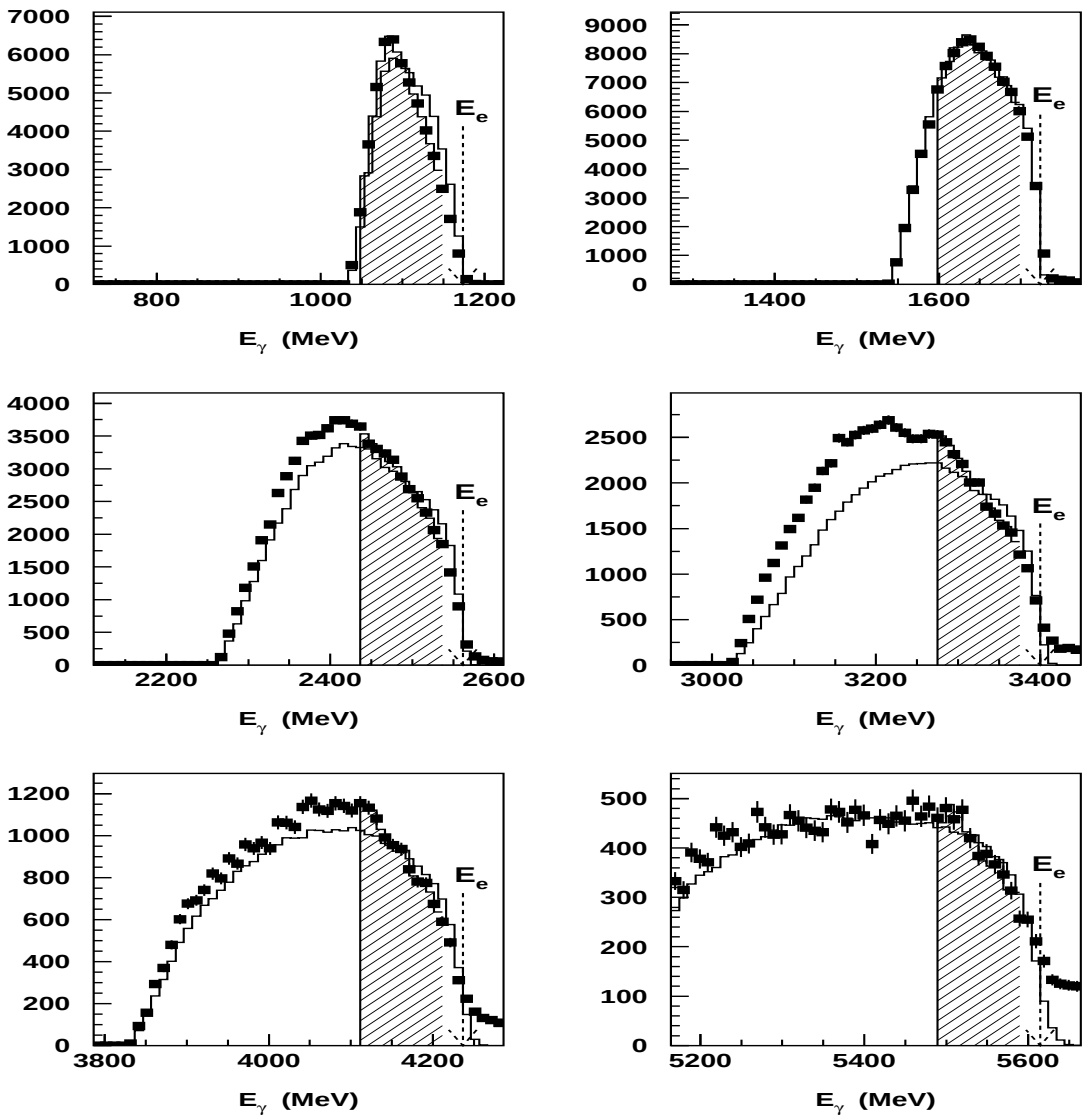

Figure 3-19: Shape comparison of reconstructed photon energy between data and simulation for singles π^+ photoproduction at $\theta_{cm} = 90°$. The results from data are plotted in symbols, while those from simulation are plotted in lines. The electron beam energies are 1173.3, 1723.4, 2561.5, 3400.0, 4236.4 and 5614.4 MeV. The comparison at beam energy 1876.9 MeV (not shown here) is very similar to that at 1723.4 MeV. The shaded events were chosen to extract differential cross section.

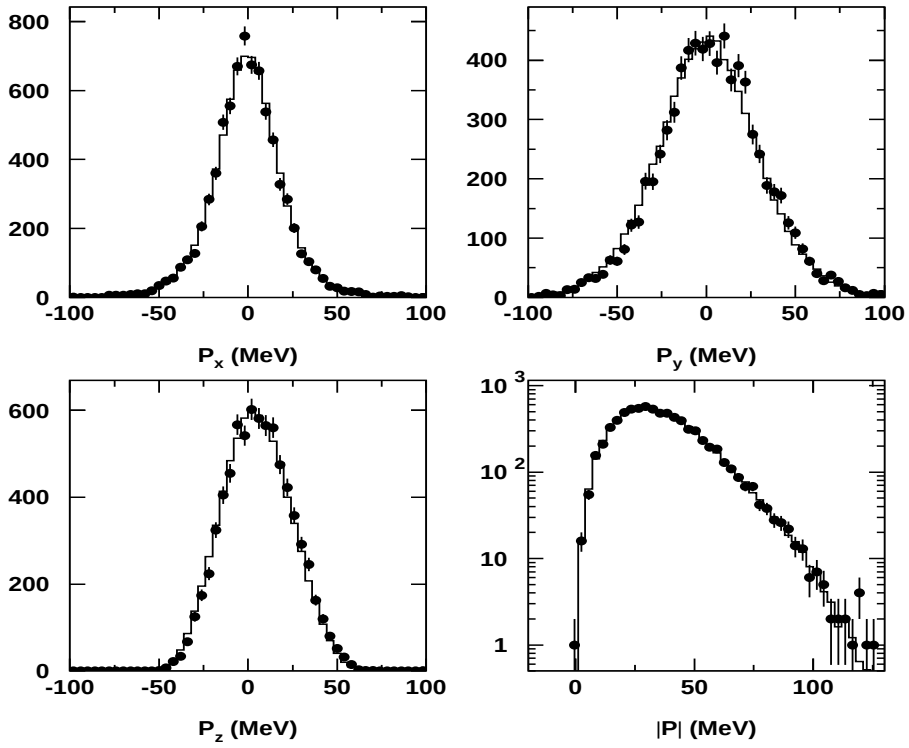

Figure 3-20: Shape comparison of reconstructed momentum distribution of the neutron in the deuterium target between data and simulation for coincidence π^- photoproduction (kin:coin15). The results from data are plotted in symbols, while those from simulation are plotted in lines.

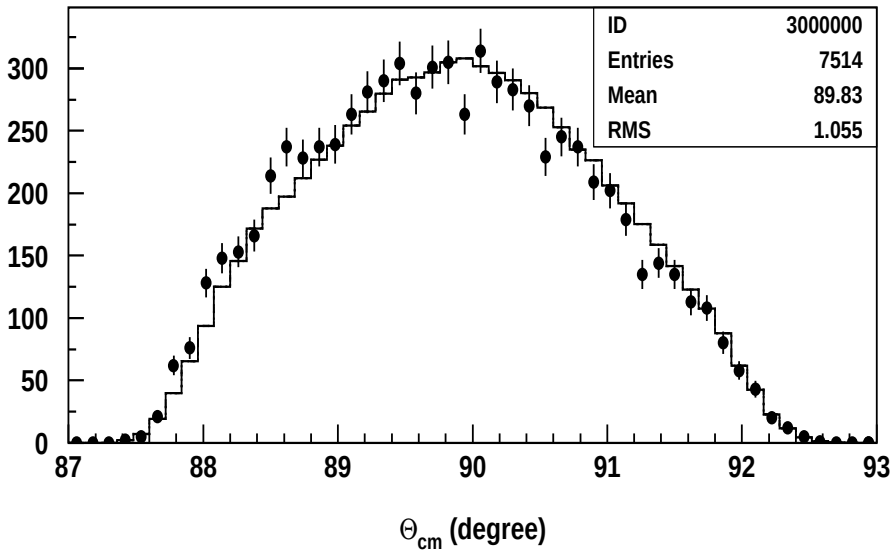

Figure 3-21: Shape comparison of reconstructed center-of-mass angle between data and simulation for coincidence π^- photoproduction (kin:coin15). The results from data are plotted in symbols, while those from simulation are plotted in lines. The nominal center-of-mass angle is 90 degrees.

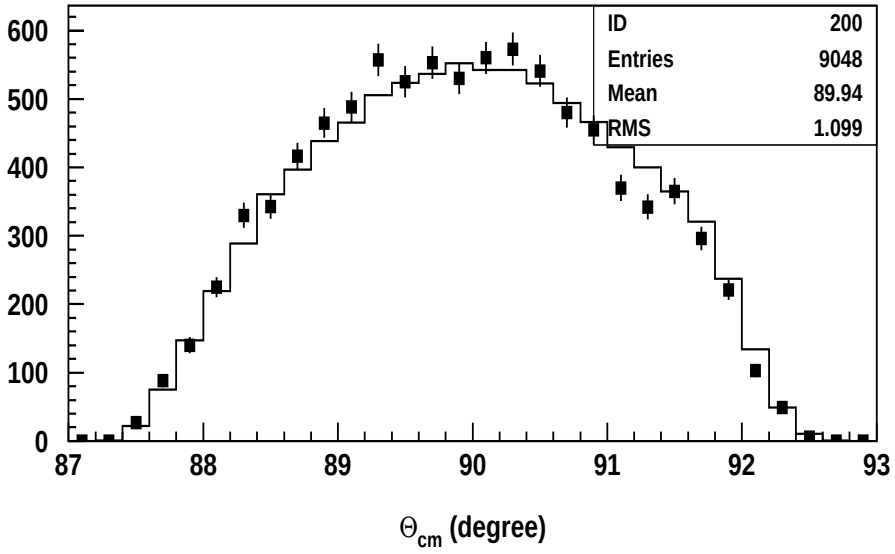

Figure 3-22: Shape comparison of reconstructed center-of-mass angle between data and simulation for singles π^+ photoproduction (kin:sing14). The results from data are plotted in symbols, while those from simulation are plotted in lines. The nominal center-of-mass angle is 90 degrees.

3.10 Corrections and Systematic Errors

Table 3.8 and 3.9 list the corrections applied to the raw cross section for kinematics at $\theta_{cm} = 90°$, as well as estimations of the systematic errors. The kinematics at other center-of-mass angles have similar breakdowns.

Table 3.8: Corrections and systematic errors for coincidence π^- photoproduction at $\theta_{cm} = 90°$.

	Coin3	Coin6	Coin20	Coin9	Coin12	Coin15	Coin17	Error_sys
Photon Yield	11.3%	12.8%	13.4%	15.3%	15.4%	16.9%	19.9%	3.0%
Target Density	2.0%	2.0%	2.0%	1.0%	2.0%	2.0%	2.0%	1.0%
Tracking	3.0%	1.5%	1.5%	1.0%	1.0%	1.0%	1.0%	3.0%
Scintillator/Trigger	2.0%	2.0%	2.0%	2.0%	2.0%	2.0%	2.0%	1.0%
PID	2.0%	2.0%	2.0%	1.0%	1.0%	1.0%	1.0%	2.2%
Muon Contamination	-6.6%	-6.2%	-6.1%	-5.7%	-5.1%	-4.6%	-3.7%	3.0%
Transparency	22.5%	37.0%	27.7%	23.2%	22.1%	21.0%	19.3%	5.0%
Nuclear Absorption	7.5%	12.0%	11.4%	11.5%	11.8%	12.2%	11.8%	4.2%
Acceptance	0.0%	0.0%	0.0%	0.0%	0.0%	0.0%	0.0%	3.0%
Dead Time	0.0%	0.0%	0.0%	0.0%	0.0%	0.0%	0.0%	2.0%
Trial Cross Section	0.0%	0.0%	0.0%	0.0%	0.0%	0.0%	0.0%	2.2%
Energy Loss	0.0%	0.0%	0.0%	0.0%	0.0%	0.0%	0.0%	2.0%
Random Coincidence	0.0%	0.0%	0.0%	0.0%	0.0%	0.0%	0.0%	1.0%
f(E_gamma)	0.0%	0.0%	0.0%	0.0%	0.0%	0.0%	0.0%	1.0%
Momentum Distribution	0.0%	0.0%	0.0%	0.0%	0.0%	0.0%	0.0%	1.0%
Beam Charge	0.0%	0.0%	0.0%	0.0%	0.0%	0.0%	0.0%	1.0%
Total	49.6%	74.9%	63.2%	57.0%	58.7%	60.7%	63.4%	10.1%

3.10.1 Photon Yield and $f(E_\gamma)$ Calculation

The corrections related to the radiator were presented in Section 3.8.4. The corrections in the photo yield due to the replacement of the thin-radiator calculation with thick-radiator calculation were about 15% at several GeV beam energy, with 3% uncertainties. The $f(E_\gamma)$ factor, being used in subtracting the radiator out background (also see section 3.7), was calculated to be around 0.7 at several GeV. Assuming that

Table 3.9: Corrections and systematic errors for singles π^+ photoproduction at $\theta_{cm} = 90°$.

	Sing3	Sing6	Sing19	Sing9	Sing12	Sing14	Sing16	Error_sys
Photon Yield	11.3%	12.8%	13.4%	15.3%	15.4%	16.9%	19.9%	3.0%
Target Density	1.5%	1.5%	0.5%	1.5%	1.5%	2.0%	1.5%	1.0%
Tracking	0.0%	0.0%	0.0%	0.0%	0.0%	0.5%	1.5%	2.0%
Scintillator/Trigger	1.0%	1.0%	1.0%	1.0%	1.0%	1.0%	1.0%	1.0%
PID	1.0%	3.0%	2.0%	2.0%	2.0%	2.0%	2.0%	3.0%
Muon Contamination	-6.6%	-6.2%	-6.1%	-5.7%	-5.1%	-4.6%	-3.7%	3.0%
Nuclear Absorption	1.7%	2.7%	2.8%	5.1%	3.9%	4.2%	4.2%	3.0%
Acceptance	0.0%	0.0%	0.0%	0.0%	0.0%	0.0%	0.0%	3.0%
Dead Time	0.0%	0.0%	0.0%	0.0%	0.0%	0.0%	0.0%	2.0%
Trial Cross Section	0.0%	0.0%	0.0%	0.0%	0.0%	0.0%	0.0%	2.2%
Energy Loss	0.0%	0.0%	0.0%	0.0%	0.0%	0.0%	0.0%	2.0%
f(E_gamma)	0.0%	0.0%	0.0%	0.0%	0.0%	0.0%	0.0%	1.0%
Beam Charge	0.0%	0.0%	0.0%	0.0%	0.0%	0.0%	0.0%	1.0%
Total	9.5%	14.7%	13.3%	19.5%	19.0%	22.7%	27.7%	8.1%

the uncertainty of the $f(E_\gamma)$ is still 3%, the resulted uncertainty in final cross section is around 1% since the yield with radiator out is about one third of the yield with radiator in.

3.10.2 Target Density Correction

The decrease in target density due to local boiling caused by nonzero electron beam current should be corrected in the cross section extraction. Figure 3-23 shows the relative target density ρ as a function of beam current I by looking at the normalized yield, which can be parameterized as:

$$\begin{aligned} \text{LD2}: \quad \rho(\text{I}) &= \rho(0)(1 - 0.00072 \times I); \\ \text{LH2}: \quad \rho(\text{I}) &= \rho(0)(1 - 0.00048 \times I). \end{aligned} \tag{3.19}$$

The target density corrections can thus be estimated by using the average current for each kinematics. The corresponding uncertainties were estimated to be 1% mainly

due to the systematic errors, in BCM measurement for low currents for example [94].

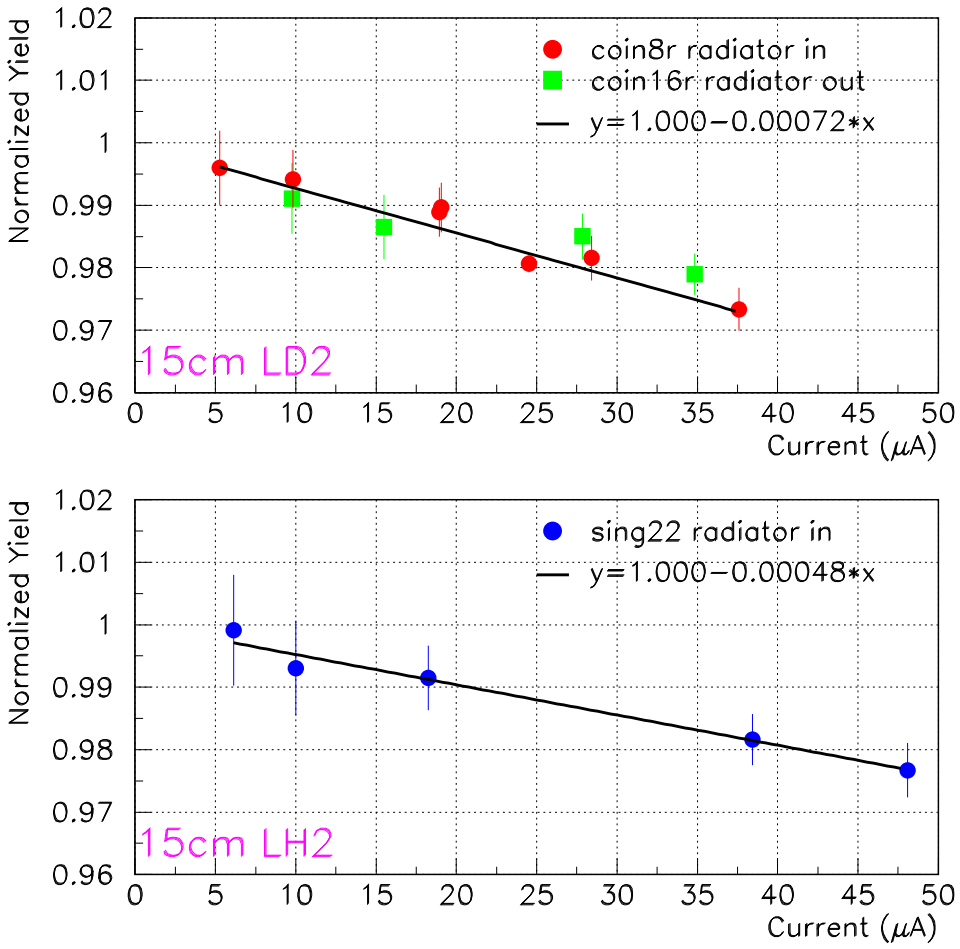

Figure 3-23: Normalized yield versus current for LD2 and LH2 targets.

3.10.3 Detector Efficiency

Tracking Efficiency

The single wire efficiency of the VDCs, with samples defined by two neighboring wires, is very close to 100%, as indicated by the online spectra in Figure 2-13.

In the data analysis, there is no cut to require a single track. But multi-track events, dominated by two-track events, may still cause inefficiency in tracking when

a wrong track was recorded instead of the production one. The ratios of multi-track to single-track events for kinematics at $\theta_{cm} = 90^0$, as well as the corrections were shown in Table 3.10. As there was still a very good chance for the production track of the multi-track events to be recorded, the applied corrections were assigned to be less than half of the ratios.

The track reconstruction itself may cause detection inefficiency too. It was found that about 98% of events with good coincidence timing had at least one track, which would increase to 99% if positive signals in some particle identification detectors were further required. The inefficiency here might be due to the fact that the acceptance of scintillators and PID detectors is larger than that of VDCs. During the data analysis when only the events in the central region of the acceptance were selected, this kind of inefficiency should be negligible. Furthermore, a few percent of the one-track events have unrealistic acceptance variables, such as the reaction vertex z_{react}. This might be related to the multiple scattering or track reconstruction algorithm in ESPACE. As the multiple scattering will be considered in the simulation and material absorption correction, uncertainties instead of corrections were assigned for these types of inefficiencies.

In summary, the corrections due to tracking were estimated by the multi-track to single-track ratios. The uncertainties assigned for tracking were 3% for coincidence kinematics and 2% for singles kinematics to account for the uncertainties due to multi-track events and track reconstruction.

Scintillator/Trigger Efficiency

Special runs were taken with all the prescale factors set to be 1 in order to measure scintillator/trigger efficiency. The particle identification and acceptance cuts were applied to select good samples, which ensured that the detected particles passed through the scintillators. The scintillator/trigger efficiency was obtained by checking the percentage of these samples that have good triggers. The measured efficiency was

Table 3.10: The ratios of multi-track to one-track events for coincidence and singles runs at $\theta_{cm} = 90^0$ and the corrections for tracking.

E_e (MeV)	1173.3	1723.4	1876.9	2561.5	3400.0	4236.4	5614.4
Coin. $\frac{\text{n-track}}{\text{1-track}}$ (%)	8.5	3.8	3.5	1.4	2.1	2.1	3.0
Coin. Correction (%)	3.0	1.5	1.5	1.0	1.0	1.0	1.0
Coin. Uncertainty (%)	±3.0	±3.0	±3.0	±3.0	±3.0	±3.0	±3.0
Sing. $\frac{\text{n-track}}{\text{1-track}}$ (%)	0.3	0.7	0.3	0.4	0.5	1.1	3.5
Sing. Correction (%)	0.0	0.0	0.0	0.0	0.0	0.5	1.5
Sing. Uncertainty (%)	±2.0	±2.0	±2.0	±2.0	±2.0	±2.0	±2.0

98.8±1.1% and 98.8±0.7% for the right and left spectrometer respectively, as shown in Figure 3-24. Since the peaks of the scintillator ADC spectra were much higher than the threshold to generate a TDC signal, the inefficiency of the scintillator itself should be negligible. The measured inefficiency here might arise from trigger generation.

The corrections applied to the cross sections due to scintillator/trigger inefficiency were 2% for coincidence kinematics and 1% for singles kinematics, with 1% uncertainty for both cases.

Particle Identification Efficiency

The discussion of particle identification efficiency can be found in Section 3.6. Corrections for different kinematics were 1∼3%, with uncertainties of 2∼3%.

3.10.4 Pion Survival Factor and Muon Contamination

The pion decay loss was considered as the survival factor in the simulation by using the pion flight length of 25 m and pion lifetime of 26 ns. The survival factor ranges from 53% to 89% for different pion momenta. The nominal flight length from the target to the first plane of the VDC is 23.4 m. The scintillator planes S1 and S2 are located about 1.3 m and 3.3 m farther. The change in survival factor is $1 \sim 3\%$ if one

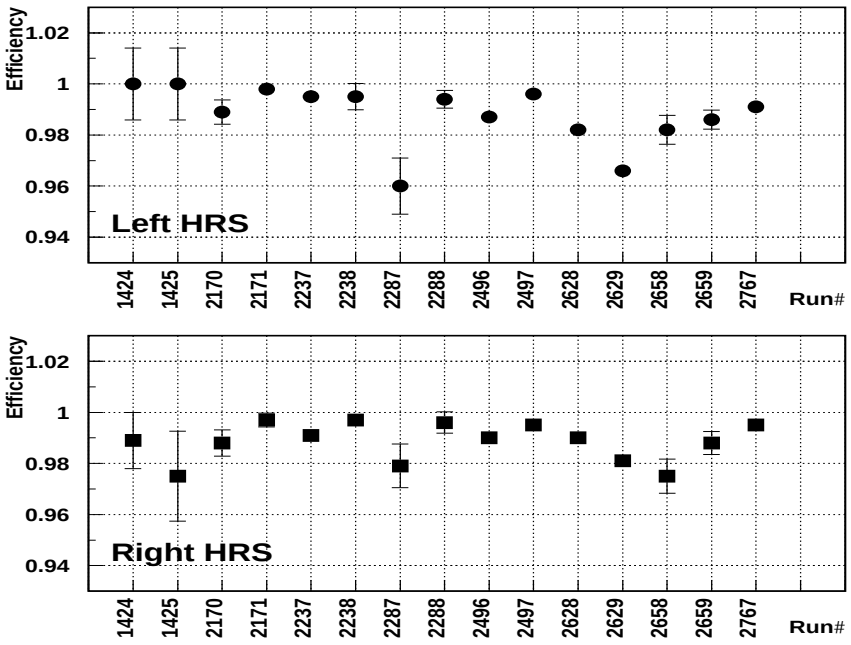

Figure 3-24: Scintillator/trigger efficiency.

changes the flight length by 1 meter for the kinematics of this experiment. However, since some of the muons from pion decay may still fall into the acceptance and be misidentified as pions, which is called muon contamination here, the calculation above may underestimate the effective pion survival factor and should be corrected back.

The corrections due to muon contamination were estimated by using the simulation program SIMC [95], modified for Hall A and embedded with the COZY magnet model. It could be roughly parameterized as [96]:

$$\text{Correction}(\mu \hookrightarrow \pi)(\%) = -0.75 \times (10 - 1.7 * P_0) \ , \tag{3.20}$$

where P_0 is the central momentum setting of the spectrometer in GeV. The applied corrections were therefore $-7 \sim -3\%$ for different kinematics with uncertainty of 3%, which was estimated by adjusting the acceptance cuts.

3.10.5 Nuclear Transparency of Deuterium

The nuclear effect must be considered to obtain the cross section for $\gamma n \to \pi^- p$ from the measurement of $d(\gamma, \pi^- p)p$ with deuterium as the effective neutron target. The deuterium target is not 100% transparent because the produced pions and protons may fall out of the spectrometer acceptance due to the final state interaction with the proton spectator inside the nucleus of deuterium. The measured transparencies for $d(e, e'p)$ quasi-elastic scattering, in Figure 3-25 [97], show little Q^2 dependence above $Q^2 \simeq 2$ (GeV/c)^2) and agree well with the Glauber calculation. The fitted value of 0.904±0.013 [97] was used to deduce the transparency for the coincidence photoproduction $d(\gamma, \pi^- p)$, based on the Glauber formulation where the transparency t_G is related to the effective cross section σ as [98]

$$t_G(\vec{r}, \vec{p}) = exp\{-\int_0^\infty ds\rho(\vec{r} + \hat{p}s)\sigma\} \ , \tag{3.21}$$

where $\rho(\vec{r}+\hat{p}s)$ is the density of the nuclear medium. The transparency for $d(\gamma, \pi^- p)$ was scaled from that of $d(e, e'p)$ by replacing the total pn scattering cross section with the total pp and $\pi^- p$ scattering cross sections. The corrections for transparency applied to coincidence cross section results of E94-104 are shown in Table 3.11 for the kinematics with $\theta_{cm} = 90°$. Also listed in the table is the transparency for $d(\gamma, \pi^- p)$ that Pankaj Jain [99] obtained with the Glauber calculation including correlations and assuming the effective cross section equal to σ_{total} or $\sigma_{\text{total}} - \sigma_{\text{elastic}}/2$. The systematic uncertainties in the transparency were assigned to be 5% to account for the uncertainties in the transparency measurement for $d(e, e'p)$ and those in the effective cross sections.

3.10.6 Nuclear Absorption

The produced particles, pions and protons in the coincidence measurement and pions in the singles measurement, have to go through a lot of material in the target and

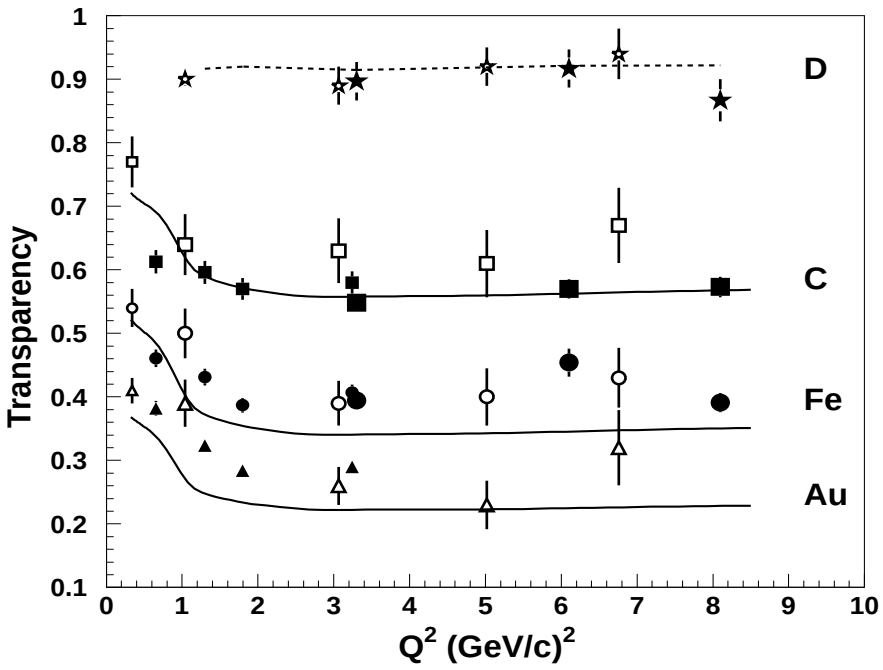

Figure 3-25: Transparency for $(e, e'p)$ quasi-elastic scattering from deuterium (D) as well as that from carbon (C), iron (Fe) and gold (Au). The errors for solid stars include statistical and the point-to-point systematic uncertainties ($\pm 2.3\%$). The errors for open stars include statistical and the net systematic uncertainties ($\pm 3.8\%$). The dash curve is a Glauber calculation.

Table 3.11: Correction due to deduced transparency for $d(\gamma, \pi^- p)$ from $d(e, e'p)$ at $\theta_{cm} = 90°$, as well as the calculated transparecy Jain A ($\sigma_{eff} = \sigma_{\text{total}}$) and Jain B ($\sigma_{eff} = \sigma_{\text{total}} - \sigma_{\text{elastic}}/2$) [99].

Kinematics	Transparency	Correction(%)	Uncertainty(%)	Jain A	Jain B
coin 3	0.816	22.5	± 5.0	-	-
coin 6	0.726	37.1	± 5.0	0.729	0.799
coin20	0.794	26.0	± 5.0	0.764	0.823
coin 9	0.812	23.2	± 5.0	0.787	0.837
coin12	0.819	22.1	± 5.0	0.789	0.833
coin15	0.827	21.0	± 5.0	0.795	0.832
coin17	0.838	19.3	± 5.0	0.812	0.844

spectrometers before being detected. The loss in the material is called nuclear absorption. The major sources of nuclear absorption for high energy protons are listed in Table 3.12. The absorption was calculated based on the thickness [28, 46, 100] and effective absorption length of the material in the flight path of the produced particles. The effective absorption length $\bar{\lambda}$ was estimated from the nuclear collision length λ_T and nuclear interaction length λ_I [20] as $2\lambda_T\lambda_I/(\lambda_T + \lambda_I)$ by assuming that half of the elastic and quasi-elastic scattering contribute to the absorption. The density of aerogel was deduced from the refractive index n as $4(n-1)$ [20].

In addition, the nuclear absorption was adjusted due to different flight lengths in the target, and different effective absorption lengths for pions and protons at various momenta. The flight length could be calculated from the scattering angle and the geometry of the target. The energy dependence of the effective absorption length was deduced from Figure 3-26 [20].

The correction due to nuclear absorption was 7$\sim$12% for coincidence measurement with the LD2 target, and 2$\sim$5% for singles measurement with the LH2 target, as partly listed in Table 3.8 and Table 3.9. The uncertainty for each produced hadron was assigned to be 3%, which was estimated by adjusting the effective absorption length.

3.10.7 Computer and Electronics Deadtime

The computer deadtime was calculated as the ratio of missed triggers in the data stream from DAQ to the input triggers from scalers [101]. It was corrected run-by-run during the data analysis. For most runs of experiment E94-104, the computer deadtime was less than 20%. The uncertainty was estimated to be on the level of 10% of the correction itself.

The electronics deadtime (EDT) were measured directly by checking the detection of the well-defined and recognizable test pulses [53, 102, 103]. The measured EDT during E94-104 was very small, less than 0.5% for most runs, due to the low trigger

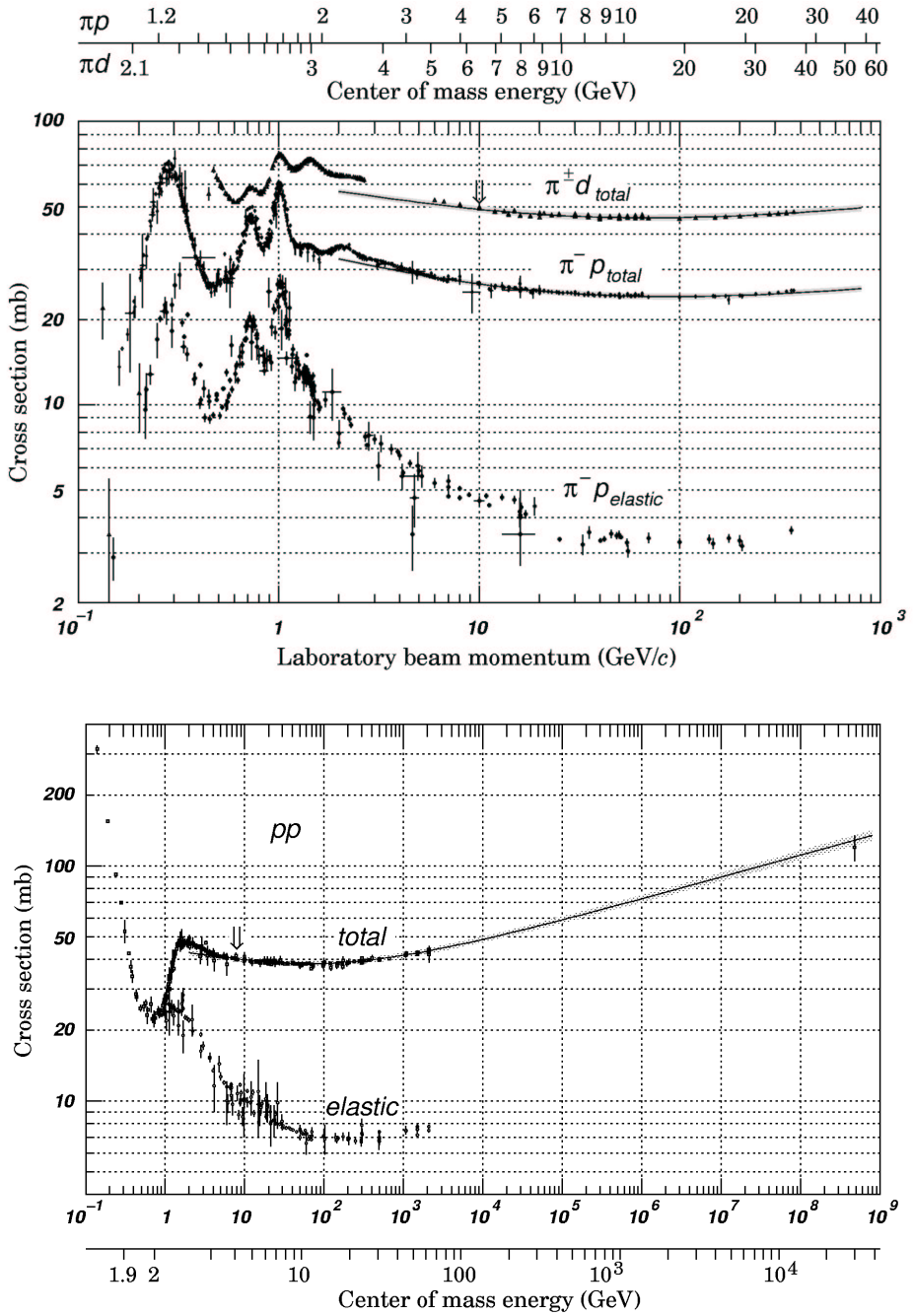

Figure 3-26: The total and elastic cross section for pp and πp collisions as a function of laboratory beam momentum and total center-of-mass energy.

Table 3.12: Major nuclear absorption in the target and spectrometer for high energy protons.

Material	Thickness (cm)	Density (g/cm^3)	λ (g/cm^2)	Absorption (%)
15cm LD2 (19K)	5.5	0.1670	49.8	1.84
15cm LH2 (22K)	5.5	0.0723	46.8	0.85
air	300.	1.21e-3	73.4	0.49
S1 (Polystyrene)	0.5	1.032	68.3	0.76
S2 (Polystyrene)	0.5	1.032	68.3	0.76
A1 (Aerogel)	9.0	0.060	75.5	0.72
A2 (Aerogel)	5.0	0.220	75.5	1.46
Short Gas Čerenkov (CO_2)	100.	1.98e-3	73.6	0.27
AM (aerogel)	9.0	0.100	75.5	1.19
Long Gas Čerenkov (CO_2)	150.	1.98e-3	73.6	0.40

rate and omission of Memory Lookup Unit (MLU). The MLU was used in previous experiments to check the hit pattern of the scintillators and generate main triggers.

In summary, the computer deadtime correction was considered during the data analysis run-by-run and electronics deadtime was ignored. The uncertainty in the total deadtime correction was assigned to be 2%, which was dominated by that for the computer deadtime.

3.10.8 Random Coincidence Background

For all the coincidence kinematics of E94-104, the random coincidence rates were very low compared to the production rates, with a typical spectrum of coincidence time shown in Figure 2-14. The cut $|tc - \bar{tc}| < 10$ was used to extract the cross sections, while the yield differences between cut $|tc - \bar{tc}| < 10$ and $|tc - \bar{tc}| < 20$ helped us to estimate random coincidence backgrounds, as shown in Table 3.13. Also listed in the table are the assigned corrections and uncertainties.

Table 3.13: Corrections and uncertainties due to random coincidence background. The spectrometer settings for each kinematics can be found in Table 2.1.

Kinematics	$\bar{tc}$ (ns)	$Y_{\lvert tc-\bar{tc}\rvert<20}/Y_{\lvert tc-\bar{tc}\rvert<10}-1$ (%)	Correction (%)	Uncertainty (%)
coin 3	223	1.0	0.0	±1.0
coin 6	239	0.6	0.0	±1.0
coin20	241	0.5	0.0	±1.0
coin 9	248	0.3	0.0	±1.0
coin12	252	0.5	0.0	±1.0
coin15	254	0.4	0.0	±1.0
coin17	255	0.4	0.0	±1.0
coin 2	205	1.4	0.0	±1.0
coin 5	226	0.6	0.0	±1.0
coin 8	240	0.4	0.0	±1.0
coin11	246	0.5	0.0	±1.0
coin14	249	0.3	0.0	±1.0
coin 1	167	4.5	-2.0	±2.0
coin 4	200	1.1	0.0	±1.0
coin18	206	0.9	0.0	±1.0
coin 7	221	0.9	0.0	±1.0
coin10	232	0.8	0.0	±1.0
coin22	254	0.5	0.0	±1.0
coin21	255	0.4	0.0	±1.0

3.10.9 Other Systematic Uncertainties

Uncertainty due to the Trial Cross Section

The final cross section, extracted by comparing data and simulation, depended on the angular distribution and energy dependence of the trial cross section, the cross section input to the simulation. Instead of searching for the exact form of the angular distribution and energy dependence of the actual cross section, the cross section fitted to SLAC data at high energy [9] was used (see Section 3.8.3) and its deviation from the actual cross section was considered as the systematic uncertainty.

The angular distribution of the trial cross section fitted to SLAC data at high energy is shown in Figure 3-27 [9], while the actual angular distributions for both coincidence and singles kinematics are shown in the last section of thesis. The two angular distributions were not exactly the same, especially at backward angles. The resulting systematic uncertainty was estimated by checking the change of the final cross section after replacing the trial angular distribution with a constant. The changes were very small, as listed in Table 3.14, which may be due to the small acceptance of the Hall A spectrometers. In the comparison, the mean center-of-mass angles were determined from the data, which deviated from those determined from the simulation by 0.2° at most. Based on Table 3.14, the systematic uncertainties due to the angular distribution were assigned to be 1%, 2% and 3% for kinematics at $\theta_{cm} = 90°, 100°$, at $\theta_{cm} = 70°, 110°$, and at $\theta_{cm} = 50°$ respectively.

The trial cross section used in the simulation had a s^{-7} energy dependence, which was suggested by the SLAC data at high energy [9] and was consistent with the constituent counting rule. The actual energy dependences for both coincidence and singles kinematics are shown in Figure 4-4 and Figure 4-5. The data, especially at low energy, do not have the s^{-7} energy dependence. The resulting systematic uncertainty was assigned to be 2%, by checking the change of the final cross section after replacing the trial s^{-7} energy dependence with a constant, as listed in Table 3.15.

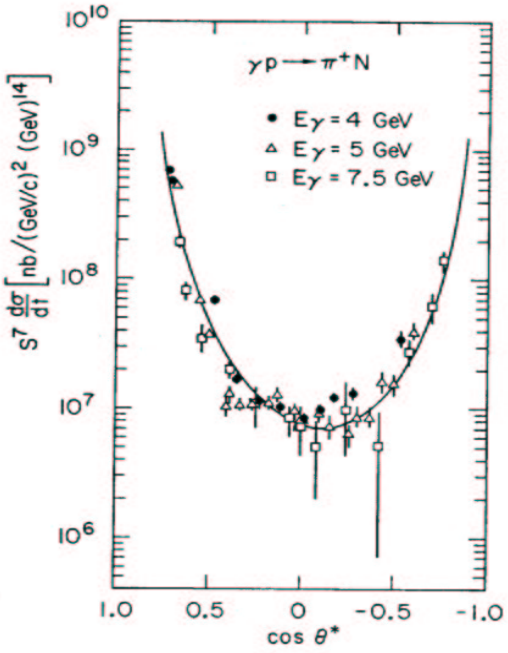

Figure 3-27: Angular distribution of the scaled cross section $s^7 d\sigma/dt$ for the reaction $\gamma p \to \pi^+ n$. θ^* is the pion center-of-mass angle. The solid line shows the empirical fit, $(1-\cos\theta^*)^{-5}(1+\cos\theta^*)^{-4}$.

Table 3.14: Relative cross section change caused by replacing the trial angular distribution of $d\sigma/dt \sim (1-\cos\theta_{cm})^{-5}(1+\cos\theta_{cm})^{-4}$ in the simulation with a constant.

E_e (MeV)	1173.3	1723.4	1876.9	2561.5	3400.0	4236.4	5614.4
sing. $\theta_{cm} = 110^o$	-	-	-	-	+0.1%	-	-
sing. $\theta_{cm} = 100^o$	-	-	-	-	+0.0%	+0.1%	+0.2%
sing. $\theta_{cm} = 90^o$	-0.1%	+0.2%	+0.2%	+0.2%	+0.2%	-0.0%	-0.0%
sing. $\theta_{cm} = 70^o$	-0.8%	+0.1%	-	+0.1%	-0.8%	-1.2%	-
sing. $\theta_{cm} = 50^o$	-	+2.0%	+2.4%	+1.1%	+1.3%	-	-
coin. $\theta_{cm} = 110^o$	-	-	-	-	+0.2%	-	-
coin. $\theta_{cm} = 100^o$	-	-	-	-	+0.2%	-	-
coin. $\theta_{cm} = 90^o$	+0.5%	+0.2%	+0.2%	+0.1%	+0.4%	-0.1%	-0.1%
coin. $\theta_{cm} = 70^o$	+1.7%	+0.9%	-	-0.2%	-0.6%	+0.3%	+2.7%
coin. $\theta_{cm} = 50^o$	+2.2%	+1.5%	+1.6%	-1.0%	+1.7%	+2.4%	-

Table 3.15: Relative cross section change caused by replacing the trial energy dependence of $d\sigma/dt \sim s^{-7}$ in the simulation with a constant.

E_e (MeV)	1173.3	1723.4	1876.9	2561.5	3400.0	4236.4	5614.4
sing. $\theta_{cm} = 110^o$	-	-	-	-	-0.6%	-	-
sing. $\theta_{cm} = 100^o$	-	-	-	-	-0.5%	-0.5%	+0.0%
sing. $\theta_{cm} = 90^o$	-2.4%	-0.5%	-0.4%	-0.7%	-0.7%	-0.4%	-0.2%
sing. $\theta_{cm} = 70^o$	-2.3%	-0.3%	-	-0.6%	-0.6%	-0.6%	-
sing. $\theta_{cm} = 50^o$	-	+0.0%	+0.3%	-0.2%	-0.3%	-	-
coin. $\theta_{cm} = 110^o$	-	-	-	-	-0.9%	-	-
coin. $\theta_{cm} = 100^o$	-	-	-	-	-1.3%	-	-
coin. $\theta_{cm} = 90^o$	-2.2%	-0.2%	+0.1%	-0.8%	-0.9%	-0.3%	+1.0%
coin. $\theta_{cm} = 70^o$	-2.7%	+0.4%	-	-0.6%	-0.7%	-1.0%	-3.6%
coin. $\theta_{cm} = 50^o$	-3.4%	-1.2%	-1.3%	-0.4%	-0.6%	-2.9%	-

Uncertainty Due to Energy Loss and Multiple Scattering

The hadron energy loss was considered in MCEEP by smearing the mean energy loss with a Laudau, Vavilov or Gaussian distribution depending on the thickness of the material. The mean energy loss per unit path length is calculated from the Bethe-Bloch formula [83]

$$-\frac{dE}{dx} = 2\pi N_a r_e^2 m_e c^2 \rho \frac{Z}{A}\frac{z^2}{\beta^2}[\ln(\frac{2m_e\gamma^2 v^2 W_{max}}{I^2}) - 2\beta^2 - \delta - 2\frac{C}{Z}] \ , \qquad (3.22)$$

where I is the mean excitation potential of the material, δ is the density correction, C is the shell correction. And W_{max} is the maximum energy transfer in a single collision, which can be approximated by $2m_e c^2\beta^2\gamma^2$ when the incident particle is much heavier than the electron. The mean energy loss for the E94-104 kinematics ranged from 2 to 4 MeV, which was then used to correct the momentum in the photon energy reconstruction so that the end point coincided with the electron beam energy.

The multiple scattering was considered in MCEEP by smearing the angles based

Table 3.16: The changes of coincidence/singles yields by turning off the energy loss and the multiple scattering calculations in simulation for kinematics at $\theta_{cm} = 90°$.

E_e (MeV)	1173.3	1723.4	1876.9	2561.5	3400.0	4236.4	5614.4
Coin.ΔY_{mc}(%)	4.4	2.3	2.2	2.0	1.4	1.3	1.1
Sing.ΔY_{mc}(%)	1.9	2.3	2.3	1.8	2.4	2.3	2.8

on a Gaussian distribution with width [83]

$$\sigma = \frac{\chi_c^2}{1+F^2}[\frac{1+\upsilon}{\upsilon}\ln(1+\upsilon) - 1] \tag{3.23}$$

with $\upsilon = 0.5\frac{\chi_c}{\chi_\alpha}\frac{1}{1-F}$, characteristic angle $\chi_c^2 = 0.157[Z(Z+1)X/A][z/(p\beta)]$, screening angle $\chi_\alpha^2 = 2.007 \times 10^{-5} Z^{2/3}[1 + 3.34(Zz\alpha/\beta)^2]/p^2$, where p is the momentum in MeV/c, X is the path length in g/cm^2, $\alpha \approx 1/137$. The Gaussian distribution can reproduce the Moliere distribution for Coulomb scattering very well when F is chosen to be 0.99.

The energy loss and the multiple scattering calculations can be turned off in the MCEEP simulation. The uncertainties due to the energy loss and multiple scattering were assigned to be 2% by looking at the corresponding yield changes, based on Table 3.16.

Momentum Distribution

The nucleons in the deuteron are not at rest. The momentum distribution calculated with the Argonne V18 model [104] was originally used in the simulation. Later more models were tried, such as different versions of the one boson exchange models as well as the Full Bonn and Paris models [105]. It can be seen from Figure 3-28 that different calculations differ little at momenta less than 400 MeV.

The difference in the tail of the momentum distribution barely affects the cross section results, less than 1%, which may due to the acceptance constraint in Hall A.

But it was found that changing the binning of the momentum distribution can affect the simulation significantly [100]. If the binning size was narrowed from 10 MeV to 0.25 MeV, the yield from the simulation would decrease by 10∼20% before it flattened out, and the shape comparison of the reconstructed the momentum distribution between the data and simulation would be apparently improved on the low momentum end. This may be related to the sampling method. Finally, the OBEPQ-A model with 0.25 MeV binning was used in the simulation. The reconstructed momentum distribution from simulation reproduced that from data very well, as shown in Figure 3-20. The corresponding uncertainty in the final cross section was assigned to be 1% to cover the model and binning dependence of the momentum distribution.

Two Pion Background

For the singles measurement, only the pion was detected. It is possible that the pion may come from two pion production processes such as $\gamma p \longrightarrow \rho N \longrightarrow \pi\pi N$, $\gamma p \longrightarrow \pi\Delta \longrightarrow \pi\pi N$ instead of $\gamma p \longrightarrow \pi^+ n$. Due to the creation of a second pion, the reconstructed photon energy of the pion from the two pion process would be lower than the actual photon energy. The difference between the maximal reconstructed photon energy and the end point (electron energy) will hereafter be called the two pion threshold. If the two pion threshold is more than 125 MeV, the two pion background can be ignored due to the photon energy cut of $E_e - 125 < E_\gamma < E_e - 25$ in the data analysis.

It is easy to calculate the two pion threshold assuming a fixed center-of-mass angle for the detected pion ($\pi 1$). The momentum of the detected pion is fixed in both the lab and center-of-mass frame with relative velocity $\beta = E_e/(E_e + m_t)$ for the end point. Mathematically the second pion and the recoil nucleon should move at the same velocity to minimize the $E_N + E_{\pi 2}$ and maximize $E_{\pi 1}$ and reconstructed E_γ. Thus

$$E_{\pi 1,cm} \leq \frac{E_{cm}^2 + m_{\pi 1}^2 - (m_N + m_{\pi 2})^2}{2E_{cm}} \ . \tag{3.24}$$

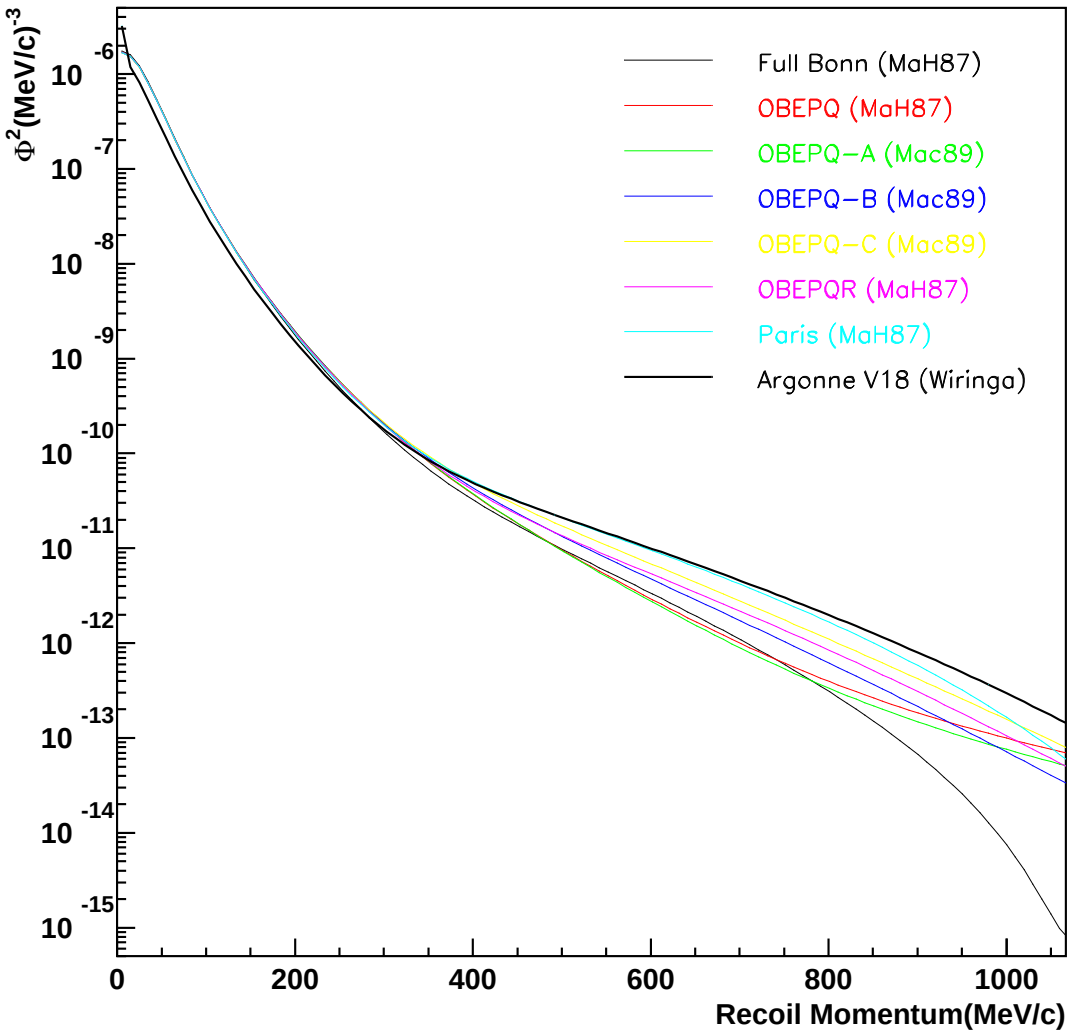

Figure 3-28: Momentum distribution of the nucleon in the deuterium with different models. The curve with Argonne V18 was from Robert Wiringa, and the rest, with models described in Reference MaH87 [106] and Mac89 [107], were generated by the Fortran code provided by Hartmuth Arenhövel.

The two pion thresholds calculated in this way [55] are listed in Table 3.17. It shows that the two pion production would not survive the photon energy cut for all singles kinematics.

Table 3.17: Two pion threshold (MeV) for the singles kinematics with hydrogen target.

E_e (MeV)	1173.3	1723.4	1876.9	2561.5	3400.0	4236.4	5614.4
$\theta_{cm} = 110^o$	-	-	-	-	333	-	-
$\theta_{cm} = 100^o$	-	-	-	-	286	296	307
$\theta_{cm} = 90^o$	212	227	230	242	251	257	264
$\theta_{cm} = 70^o$	184	191	-	197	201	203	-
$\theta_{cm} = 50^o$	-	167	168	170	171	-	-

Actually, the physical two pion threshold may be even higher than what was calculated. As a check, a code was written [108] to simulate the two pion process $\gamma p \longrightarrow \rho N$ and $\gamma p \longrightarrow \pi\Delta$ as a two step process: the production of ρ or Δ with any center-of-mass angle and its decay into the detected pion. The minimum of the difference between the beam energy and the reconstructed photon energy for the kinematics at $E_e = 5614.4$ MeV and $\theta_{cm} = 90°$ was 372 MeV. As expected, it is larger than the calculated two pion threshold.

For coincidence kinematics, the additional constraint on the acceptance of the recoil nucleon tends to raise the two pion threshold, while the initial momentum of the neutron may lower it. The extreme case should be that the second pion is at rest in the center-of-mass frame. Then from four-momentum conservation $p_\gamma + p_t = p_{\pi 1} + p_{\pi 1} + p_{\pi 1}$ and $p_t^2 = m_t^2$, it can be derived that at the end point, the reconstructed photon energy is

$$E_\gamma = E_e - \frac{m_{\pi 2}^2/2 + \gamma m_{\pi 2}(E_{\pi 1} + E_N) - \beta\gamma m_{\pi 2}(|\vec{p}|_{\pi 1}\cos\theta_{\pi 1} + |\vec{p}|_N\cos\theta_N) - (1-\beta)\gamma m_{\pi 2} E_e}{E_{\pi 1} + E_N - |\vec{p}|_{\pi 1}\cos\theta_{\pi 1} - |\vec{p}|_N\cos\theta_N} \tag{3.25}$$

As the momentum and angular acceptance is small in Hall A, the central values of

momentum and angles were used to calculate the two pion threshold according to the above formula. The results are listed in Table 3.18. For all coincidence kinematics, producing a second pion will at least cost 189 MeV in the reconstructed photon energy. The two pion background can therefore be neglected for coincidence kinematics.

Table 3.18: Two pion threshold (MeV) for the coincidence kinematics with deuterium target.

E_e (MeV)	1173.3	1723.4	1876.9	2561.5	3400.0	4236.4	5614.4
$\theta_{cm} = 110^o$	-	-	-	-	241	-	-
$\theta_{cm} = 100^o$	-	-	-	-	247	-	-
$\theta_{cm} = 90^o$	189	211	216	232	253	271	298
$\theta_{cm} = 70^o$	196	220	-	244	266	286	315
$\theta_{cm} = 50^o$	197	222	228	248	272	294	-

3.11 Data taken with Reversed Polarities

As mentioned before, a hardware problem with the right spectrometer required the polarities of the spectrometers to be reversed for two kinematics (see Section 2.1). Though the polarities should not affect physics results, the performance of the particle identification detectors affected the data analysis. The particle identification was optimized for data acquisition with normal polarities. The aerogel detector AM in the right spectrometer was not as good as the combination of two aerogel detectors (A1 and A2) in the left spectrometer in identifying protons. But since the proton signals are very clean with very low pion background, this barely affected the results. The gas Čerenkov detector and pion rejector in the left spectrometer did not work as well as the gas Čerenkov detector and preshower/shower detector in the right spectrometer to identify pions, especially the PMT#7 and #9 in the left gas Čerenkov detector. A tighter cut on momentum ($-4\% < \delta < 0\%$) was applied in the data analysis to avoid using the bad PMTs in the left gas Čerenkov detector. The pion rejector was only

used to estimate the corrections since the high voltages were adjusted many times. The shape of the reconstructed photon energy spectrum from the data agreed with that from the simulation, as shown in Figure 3-29.

For a consistency check, there were also some data taken with both normal polarities and reversed polarities. The yield differences were within 5% between kinematics coin7 and coin7r, coin8 and coin8r, coin9 and coin9r, which were comparable to the systematic uncertainties (on the level of 10%).

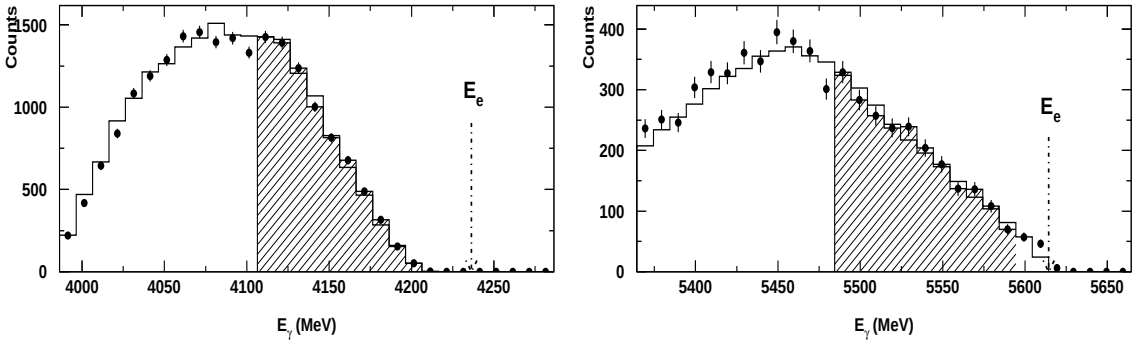

Figure 3-29: Shape comparison of reconstructed photon energy between data and simulation for coincidence π^- photoproduction with reversed polarities. The plot on the left is for kinematics coin13r, with $E_e = 4236.4$ MeV and $\theta_{cm} = 50°$. The plot on the right is for kinematics coin16r, with $E_e = 5614.4$ MeV and $\theta_{cm} = 70°$.

Chapter 4

Results and Discussion

The E94-104 data were analyzed to obtain the differential cross section for the coincidence $\gamma n \to \pi^- p$ and singles $\gamma p \to \pi^+ n$ processes. The plots of scaled differential cross section $s^7 d\sigma/dt$ versus the center-of-mass energy at fixed center-of-mass angles exhibit a global scaling behavior for both π^- and π^+ photoproduction, consistent with the constituent counting rule. Possible substructure of the scaling behavior is suggested by the data. The data also show an enhancement in the scaled cross section at the center-of-mass energy near 2.2 GeV. Finally, the charged pion ratio $\frac{d\sigma/dt(\gamma n \to \pi^- p)}{d\sigma/dt(\gamma p \to \pi^+ p)}$ was formed and compared with theoretical predictions.

4.1 Differential Cross Section

The differential cross sections $d\sigma/d\Omega$ and $s^7 d\sigma/dt$ extracted from the JLab experiment E94-014 are shown in Table 4.1 and Table 4.2 at different beam energies and center-of-mass angles.

The angular distributions for all the energies are plotted in Figure 4-1 and Figure 4-2. Also plotted in the two figures are the SLAC π^+ data at $E_\gamma = 4, 5, 7.5$ GeV and the fit curve [9]. Both our π^+ and π^- data at two highest energies, i.e. $E_\gamma = 4.2, 5.5$ GeV, as well as the forward angle data at $E_\gamma = 3.3$ GeV, seem to be

Table 4.1: Differential cross sections for the $\gamma n \to \pi^- p$ process followed by the statistical and systematic errors.

E_e (GeV)	E_γ (GeV)	$\sqrt{s}$ (GeV)	θ_{cm} (°)	$(\frac{d\sigma}{d\Omega})_{cm}$ (μb/sr)	$s^7 \frac{d\sigma}{dt}$ (10^7 nb $\cdot$ GeV^{12})
5.614	5.536	3.36	89.6	(4.22 ± 0.09 ± 0.42)E-04	1.28 ± 0.03 ± 0.13
	5.529	3.36	70.5	(1.05 ± 0.03 ± 0.12)E-03	3.17 ± 0.08 ± 0.35
4.236	4.158	2.95	89.8	(2.56 ± 0.04 ± 0.26)E-03	1.71 ± 0.03 ± 0.17
	4.157	2.95	69.8	(3.64 ± 0.07 ± 0.40)E-03	2.43 ± 0.05 ± 0.27
	4.141	2.94	50.1	(2.95 ± 0.07 ± 0.32)E-02	19.3 ± 0.45 ± 2.13
3.400	3.321	2.67	90.1	(5.66 ± 0.06 ± 0.57)E-03	1.20 ± 0.01 ± 0.12
	3.321	2.67	69.8	(1.50 ± 0.02 ± 0.16)E-02	3.19 ± 0.03 ± 0.35
	3.322	2.67	49.8	(6.63 ± 0.09 ± 0.73)E-02	14.1 ± 0.20 ± 1.55
	3.320	2.67	100.0	(1.34 ± 0.03 ± 0.13)E-02	2.85 ± 0.06 ± 0.28
	3.322	2.67	110.0	(2.60 ± 0.04 ± 0.26)E-02	5.53 ± 0.09 ± 0.55
2.561	2.481	2.36	89.9	(8.24 ± 0.10 ± 0.82)E-02	4.24 ± 0.05 ± 0.42
	2.482	2.36	69.8	(6.18 ± 0.08 ± 0.68)E-02	3.19 ± 0.04 ± 0.35
	2.484	2.36	49.7	(9.06 ± 0.02 ± 1.00)E-02	4.69 ± 0.09 ± 0.52
1.877	1.815	2.07	89.9	(3.68 ± 0.02 ± 0.37)E-01	4.58 ± 0.03 ± 0.46
	1.813	2.07	49.9	(4.74 ± 0.07 ± 0.52)E-01	5.88 ± 0.09 ± 0.65
1.723	1.659	2.00	89.9	(4.96 ± 0.02 ± 0.50)E-01	4.20 ± 0.02 ± 0.42
	1.660	2.00	69.9	(6.35 ± 0.04 ± 0.70)E-01	5.40 ± 0.03 ± 0.59
	1.659	2.00	49.9	(7.47 ± 0.06 ± 0.82)E-01	6.33 ± 0.05 ± 0.70
1.173	1.104	1.72	90.2	(6.83 ± 0.04 ± 0.68)E-01	1.17 ± 0.01 ± 0.12
	1.105	1.72	70.2	1.48 ± 0.01 ± 0.16	2.55 ± 0.01 ± 0.28
	1.105	1.72	50.2	3.79 ± 0.02 ± 0.42	6.53 ± 0.04 ± 0.72

Table 4.2: Differential cross sections for the $\gamma p \to \pi^+ n$ process followed by the statistical and systematic errors.

E_e (GeV)	E_γ (GeV)	$\sqrt{s}$ (GeV)	θ_{cm} (°)	$(\frac{d\sigma}{d\Omega})_{cm}$ (μb/sr)	$s^7 \frac{d\sigma}{dt}$ (10^7 nb $\cdot$ GeV^{12})
5.614	5.535	3.36	89.8	(2.55 ± 0.15 ± 0.20)E-04	0.77 ± 0.05 ± 0.06
	5.537	3.36	100.0	(2.44 ± 0.11 ± 0.19)E-04	0.74 ± 0.03 ± 0.06
4.236	4.156	2.95	89.9	(1.40 ± 0.03 ± 0.11)E-03	0.94 ± 0.02 ± 0.08
	4.156	2.95	69.7	(1.79 ± 0.03 ± 0.16)E-03	1.19 ± 0.02 ± 0.11
	4.156	2.95	100.0	(1.14 ± 0.03 ± 0.09)E-03	0.76 ± 0.02 ± 0.06
3.400	3.319	2.67	89.9	(3.67 ± 0.05 ± 0.29)E-03	0.78 ± 0.01 ± 0.06
	3.319	2.67	69.7	(1.78 ± 0.01 ± 0.16)E-02	3.79 ± 0.03 ± 0.34
	3.321	2.67	49.7	(1.58 ± 0.01 ± 0.14)E-01	33.6 ± 0.18 ± 3.02
	3.320	2.67	100.0	(8.02 ± 0.11 ± 0.64)E-03	1.71 ± 0.02 ± 0.14
	3.320	2.67	109.9	(9.51 ± 0.23 ± 0.76)E-03	2.02 ± 0.05 ± 0.16
2.561	2.481	2.35	90.0	(5.88 ± 0.05 ± 0.47)E-02	3.03 ± 0.03 ± 0.24
	2.481	2.35	69.9	(1.01 ± 0.01 ± 0.09)E-01	5.21 ± 0.05 ± 0.47
	2.483	2.35	49.8	(3.29 ± 0.03 ± 0.30)E-01	17.0 ± 0.13 ± 1.53
1.877	1.801	2.06	89.6	(2.42 ± 0.01 ± 0.19)E-01	2.91 ± 0.01 ± 0.23
	1.805	2.07	49.6	(9.01 ± 0.04 ± 0.81)E-01	11.0 ± 0.05 ± 0.99
1.723	1.647	1.99	89.6	(2.89 ± 0.02 ± 0.23)E-01	2.38 ± 0.01 ± 0.19
	1.648	1.99	69.5	(5.95 ± 0.03 ± 0.54)E-01	4.91 ± 0.03 ± 0.44
	1.650	1.99	49.6	1.15 ± 0.01 ± 0.10	9.49 ± 0.05 ± 0.85
1.173	1.097	1.71	90.0	1.35 ± 0.01 ± 0.11	2.26 ± 0.01 ± 0.18
	1.098	1.72	70.0	3.13 ± 0.01 ± 0.28	5.27 ± 0.02 ± 0.47

consistent with the fit curve. But it is not necessarily true for other cases.

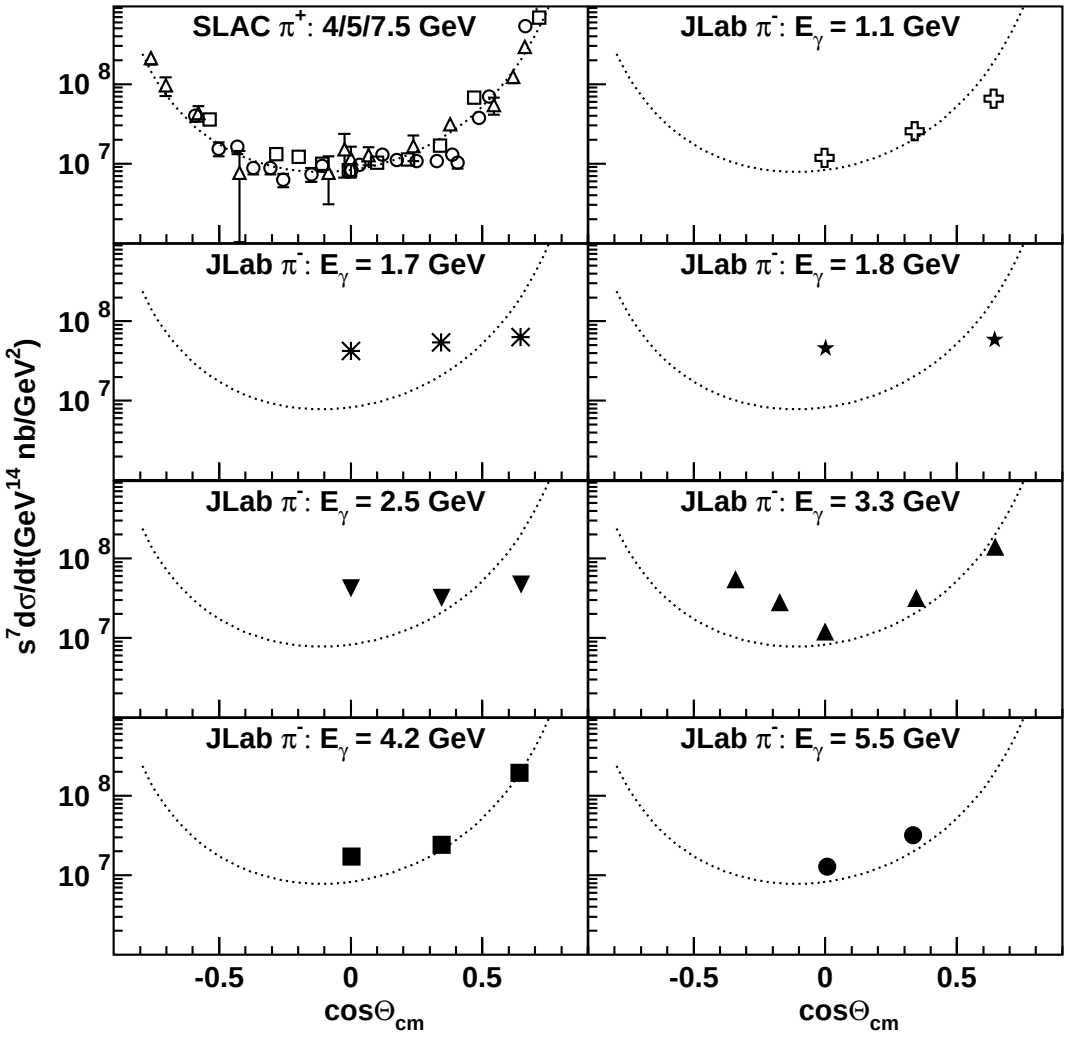

Figure 4-1: Angular distributions from the JLab E94-104 for the $\gamma n \to \pi^- p$ process, as well as those from the SLAC data for the $\gamma p \to \pi^+ n$ process at photon energy of 4 GeV (in open squares), 5 GeV (in open circles), and 7.5 GeV (in open triangles). The curve in each panel is the empirical fit of SLAC data: $0.828e7 \cdot (1-\cos\Theta_{\rm cm})^{-5} \cdot (1+\cos\Theta_{\rm cm})^{-4}$.

It is worth mentioning that the pQCD calculations involving gluon self-coupling [109] could not reproduce the angular distribution of the SLAC data well, especially at the backward angles, as shown in Figure 4-3. The discrepancy may be due to the relatively low values of s, t and u. The main contamination of their leading-twist predictions came from the t-channel (photoproduction via pion exchange) meson resonances

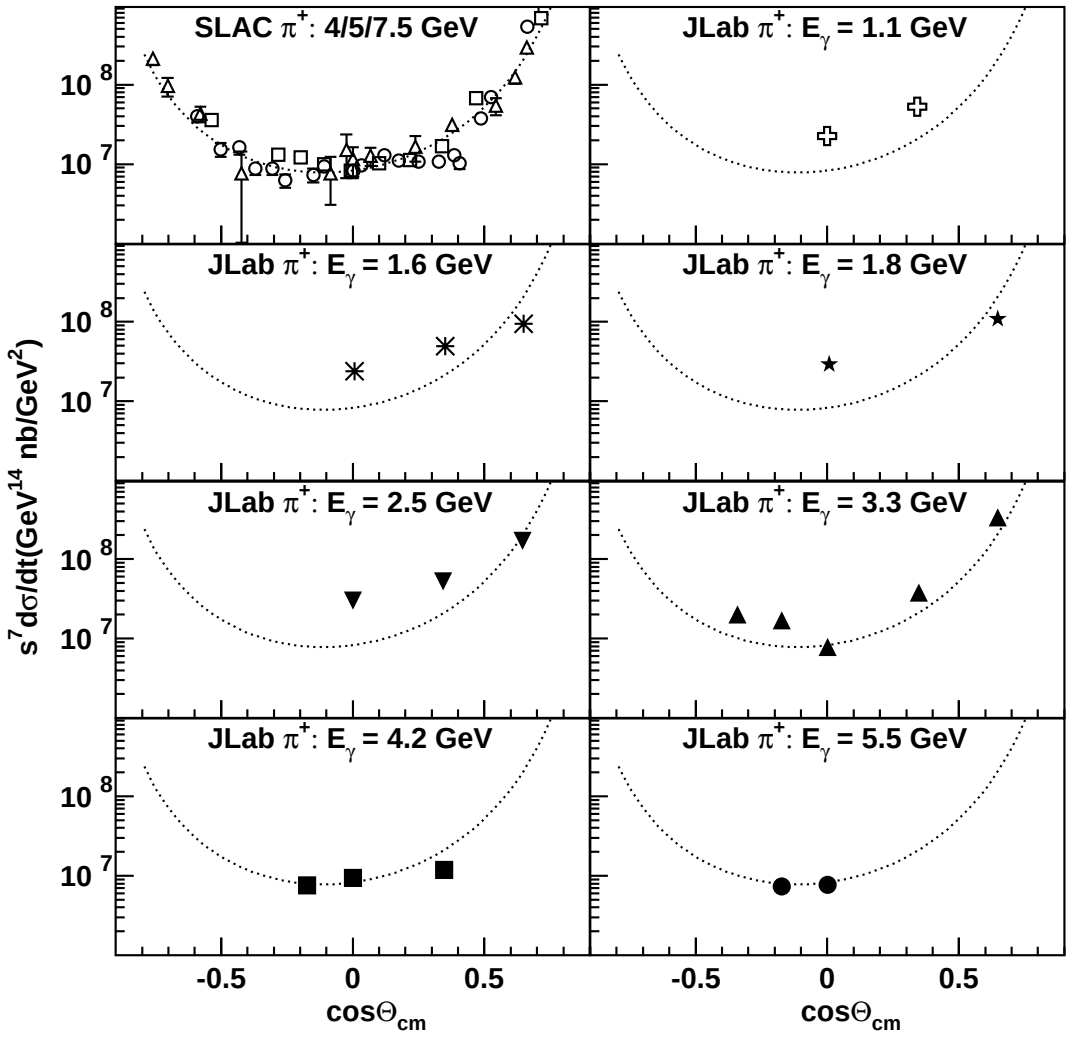

Figure 4-2: Angular distributions from JLab E94-104 for the $\gamma p \to \pi^+ n$ process, as well as those from the SLAC data for the $\gamma p \to \pi^+ n$ process at photon energy of 4 GeV (in open squares), 5 GeV (in open circles), and 7.5 GeV (in open triangles). The curve in each panel is the empirical fit of SLAC data: $0.828e7 \cdot (1-\cos\Theta_{\rm cm})^{-5} \cdot (1+\cos\Theta_{\rm cm})^{-4}$.

at forward angles, and from the u-channel (photoproduction via nucleon exchange) baryon resonances at backward angles. It required larger values of u than t to be outside the resonance region and to agree with the calculations.

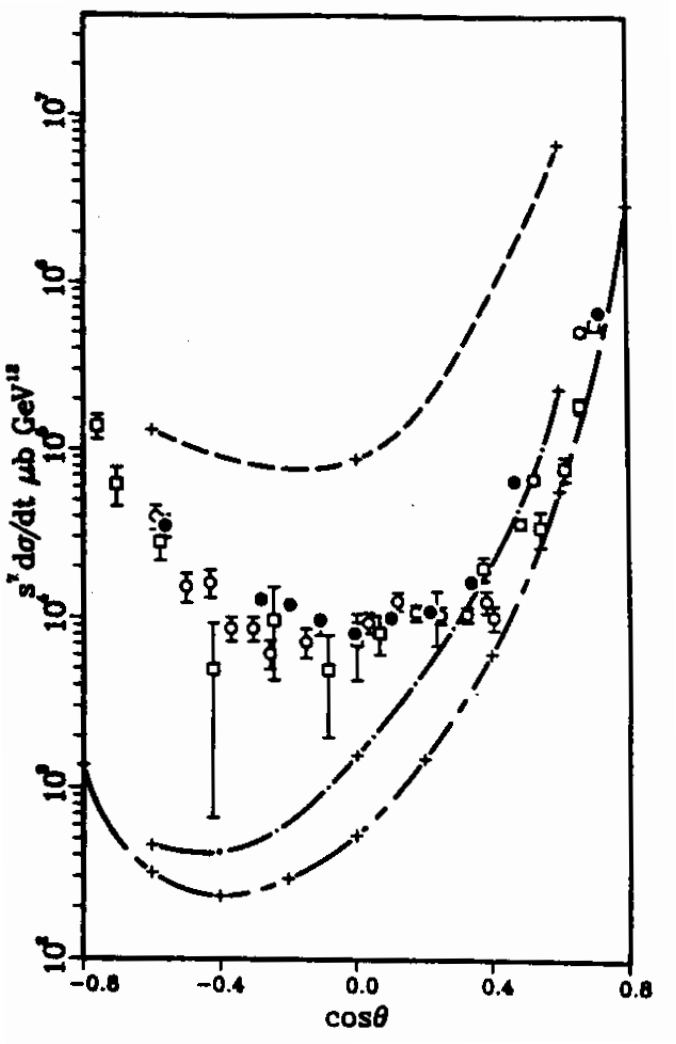

Figure 4-3: The comparison of the angular distributions from pQCD calculation with different wave functions (in different curves) with those from SLAC data at photon energy of 4 GeV (in solid circles), 5 GeV (in open circles), and 7.5 GeV (in open squares).

4.1.1 Comparison with the World Data

As shown in Figure 4-4 and Figure 4-5, our data from JLab experiment E94-104 (in solid circles) greatly extend the single pion photoproduction measurements at several GeV, by running from the resonance region to the scaling region. The differential cross sections of the $\gamma n \to \pi^- p$ process with $\sqrt{s}$ greater than 2.2 GeV were measured for the first time. The differential cross section data for the $\gamma p \to \pi^+ n$ process also fill a blank region not covered by the world data.

Our data agree within uncertainties with the world data in the overlapping energy region, except with the Besch *et al.* data [110] (in open triangles). The Besch *et al.* data were taken with the Bonn synchrotron and seemed to suggest a very sharp peak in the scaled cross section for the $\gamma n \to \pi^- p$ process with $\sqrt{s}$ around 2.0 GeV. Our data confirm the scaled cross section enhancement around that region, but with a much lower peak. We do not know exactly where the discrepancy comes from, though our momentum resolution (0.02%) is much better than that of Besch *et al.* (4%). The broad structure suggested by our data is seen in all three channels of pion photoproduction and the preliminary results from JLab Hall B are consistent with our results [111].

4.1.2 Scaling at High Energy

According to the constituent counting rule, the differential cross section $d\sigma/dt$ at a fixed center-of-mass angle for the $\gamma n \to \pi^- p$ and $\gamma p \to \pi^+ n$ processes should scale as s^{-7}, which will be a straight line on a logarithmic scale. And the scaled differential cross section $s^7 d\sigma/dt$ should be a constant independent of the center-of-mass energy. The non-scaled differential cross sections $d\sigma/dt$ are plotted against center-of-mass energies in Figure 4-6 with the constituent counting rule prediction represented by the solid lines. The high energy scaled cross section $s^7 d\sigma/dt$ for both π^+ photoproduction and π^- photoproduction at the same center-of-mass angle are

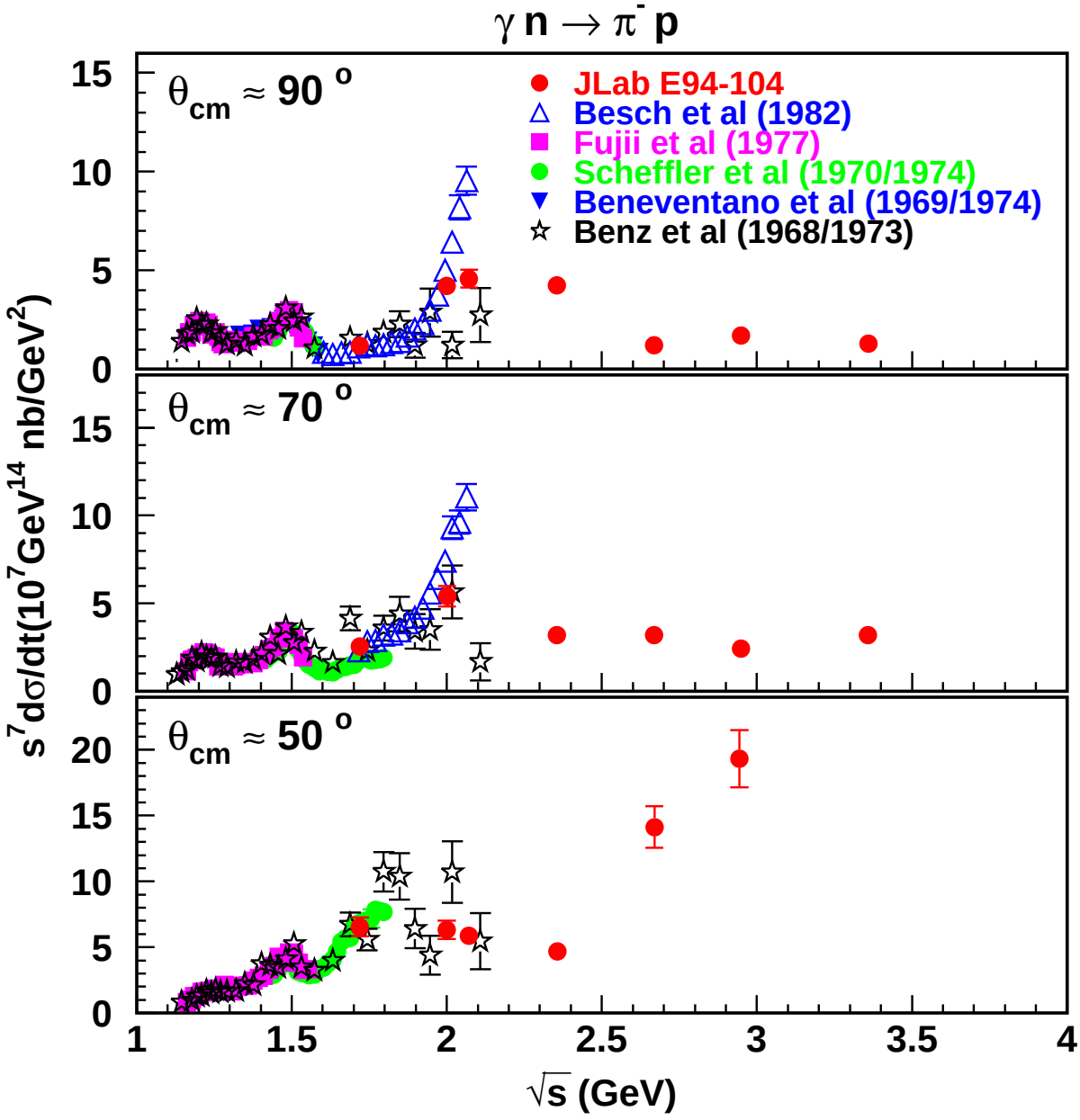

Figure 4-4: Scaled cross section $s^7 \frac{d\sigma}{dt}$ versus center-of-mass energy $\sqrt{s}$ for the $\gamma n \to \pi^- p$ process. The open triangles were averaged from the Besch *el al.* data at $\theta_{cm} = 85°$ and 95° [110].

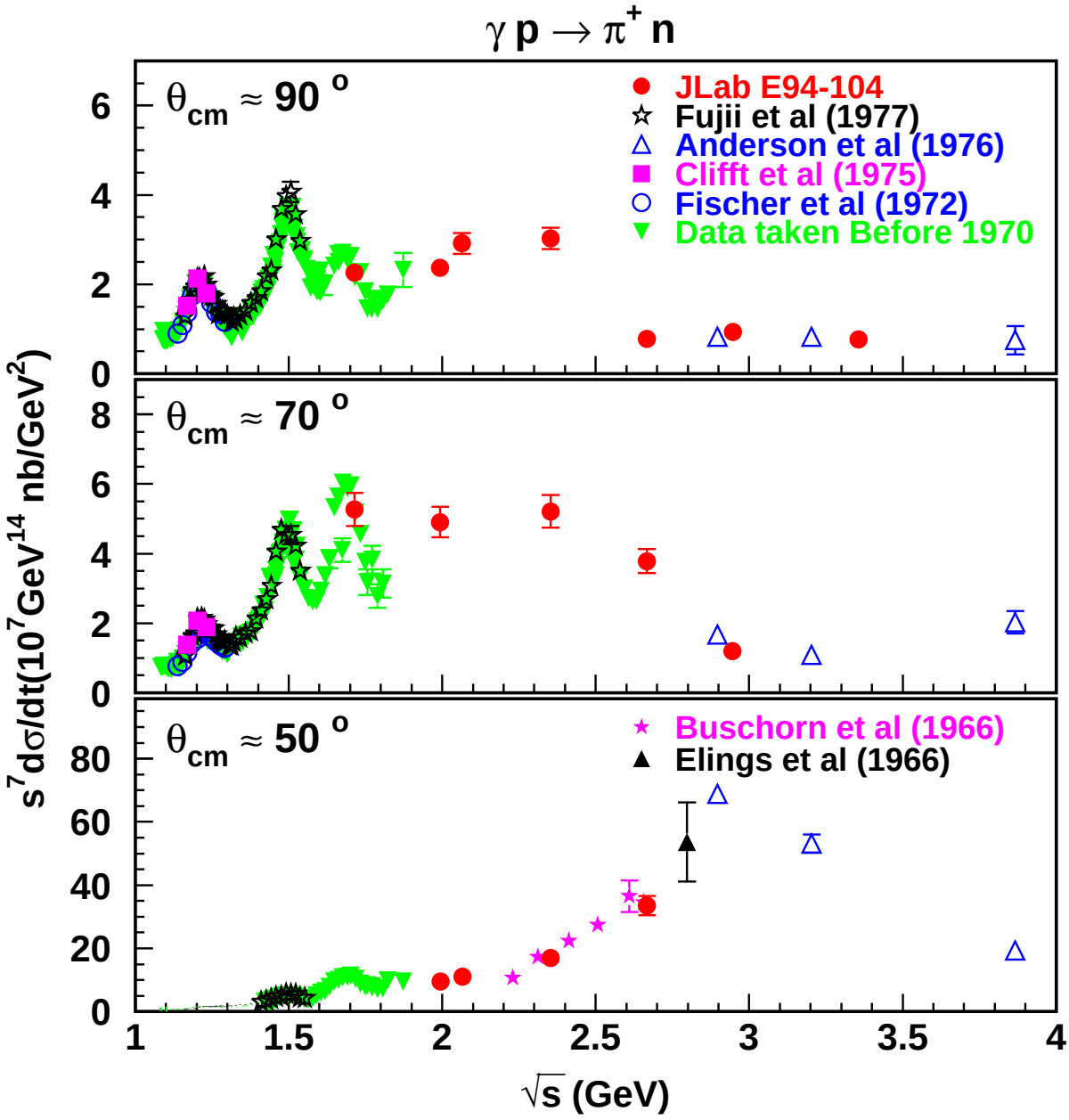

Figure 4-5: Scaled cross section $s^7 \frac{d\sigma}{dt}$ versus center-of-mass energy $\sqrt{s}$ for the $\gamma p \to \pi^+ n$ process.

plotted together in Figure 4-7, Figure 4-8 and Figure 4-9.

For both π^- and π^+ photoproduction processes, the data with $\sqrt{s} > 2.7$ GeV at $\theta_{cm} = 90°$ and $\sqrt{s} > 3.0$ GeV at $\theta_{cm} = 70°$ indicate the scaling behavior predicted by the constituent counting rule. The fitted power of $\frac{1}{s}$ based on the three highest points at $\theta_{cm} = 90°$ from our data was 6.9±0.2 for the $\gamma n \to \pi^- p$ process and 7.1±0.2 for the $\gamma p \to \pi^+ p$ process, consistent with the prediction of 7. This may have some theoretical implications, for example the validity of quark-gluon degrees of freedom and the freezing of the running strong coupling constant at several GeV (see Section 1.3.4). The pQCD derivation of the constituent counting rule requires the coupling constant to have little dependence on energy scales. However, one has to admit that it is dangerous to claim scaling from just a few points though we see similar scaling behavior for both π^- and π^+ photoproduction processes and the photon energy is extended to 7.5 GeV by including the SLAC data [9] for the π^+ case. Other reasons could produce the same scaling behavior. For example, the low energy points for the π^+ at $\theta_{cm} = 70°, 90°$ seem to scale around 2 GeV (see Figure 4-5), which might be due to the two resonance structures. Nevertheless it is worthwhile to further check the scaling at higher energy and with finer binning.

There is no sign of scaling for the data at $\theta_{cm} = 50°$ up to center-of-mass energy of 3.0 GeV for the π^- case and 3.9 GeV for the π^+ case. This is not surprising since the deuteron photodisintegration data [8, 28] (see Section 1.3) at forward angles do not scale as early as those at 90°. The photodisintegration data at $\theta_{cm} = 53°$ seem to scale when the photon energy is greater than 3 GeV while the data at $\theta_{cm} = 90°$ scale when the photon energy is greater than 1 GeV. The corresponding center-of-mass energies are 3.8 GeV and 2.7 GeV respectively. But since the Landshoff diagrams (see Section 1.3.1) and generalized constituent counting rule with nonzero parton orbital angular momentum (see Section 1.3.4) predict different scaling behaviors from that predicted by the traditional constituent counting rule, it is worthwhile to check the data at $\theta_{cm} = 50°$ for the possible scaling with different powers of s, for example s^{-6} or

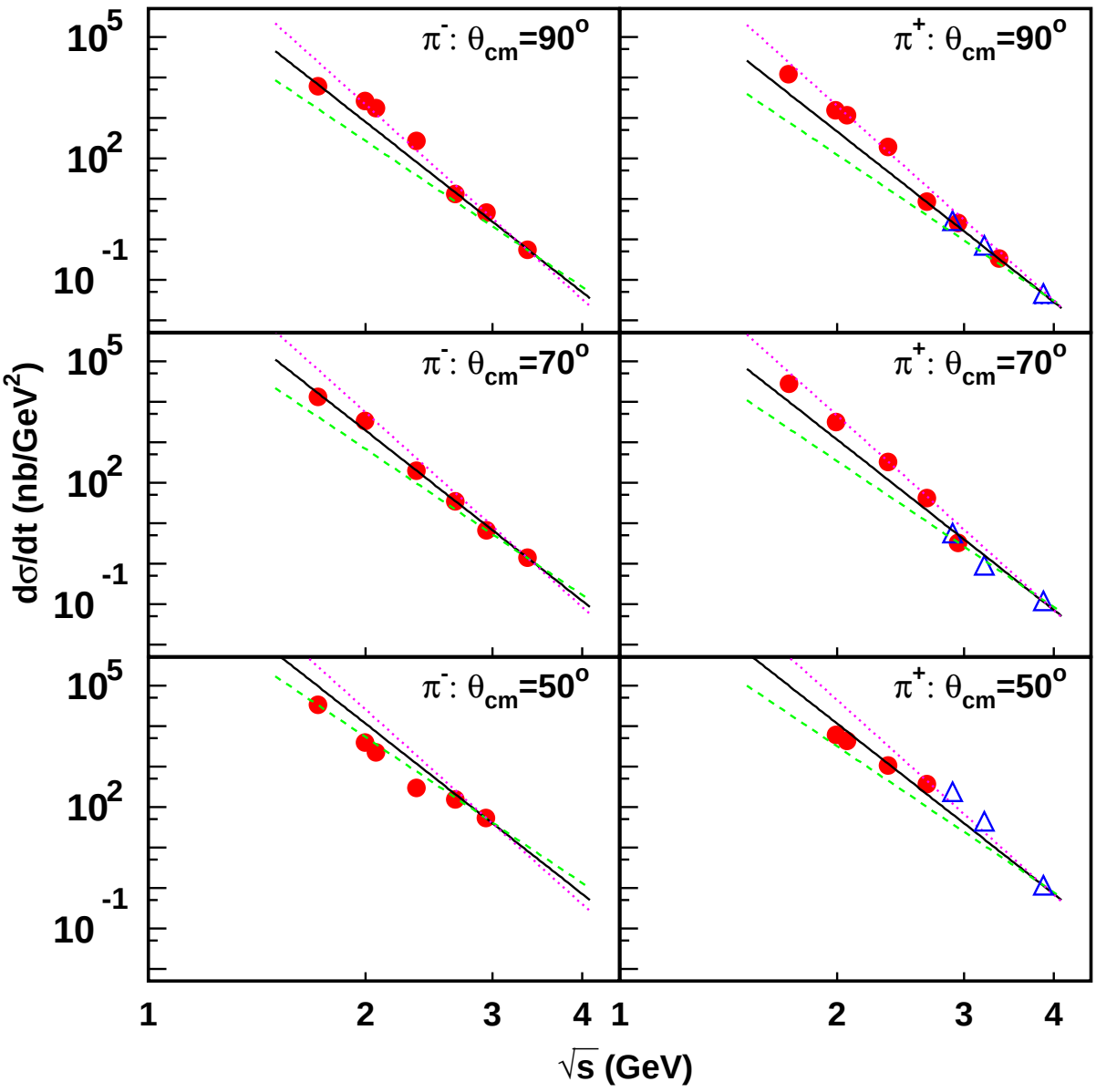

Figure 4-6: The differential cross section $\frac{d\sigma}{dt}$ versus center-of-mass energy $\sqrt{s}$ for the $\gamma n \to \pi^- p$ and $\gamma p \to \pi^+ n$ processes at different center-of-mass angles. The data in solid circles are from the JLab experiment E94-104, while open triangles are SLAC data [9]. The solid, dashed and dotted curves represent the s^{-7}, s^{-6}, s^{-8} scaling behavior respectively with normalization factors so that they all go through the last point in each plot. The constituent counting rule predicts the s^{-7} scaling behavior.

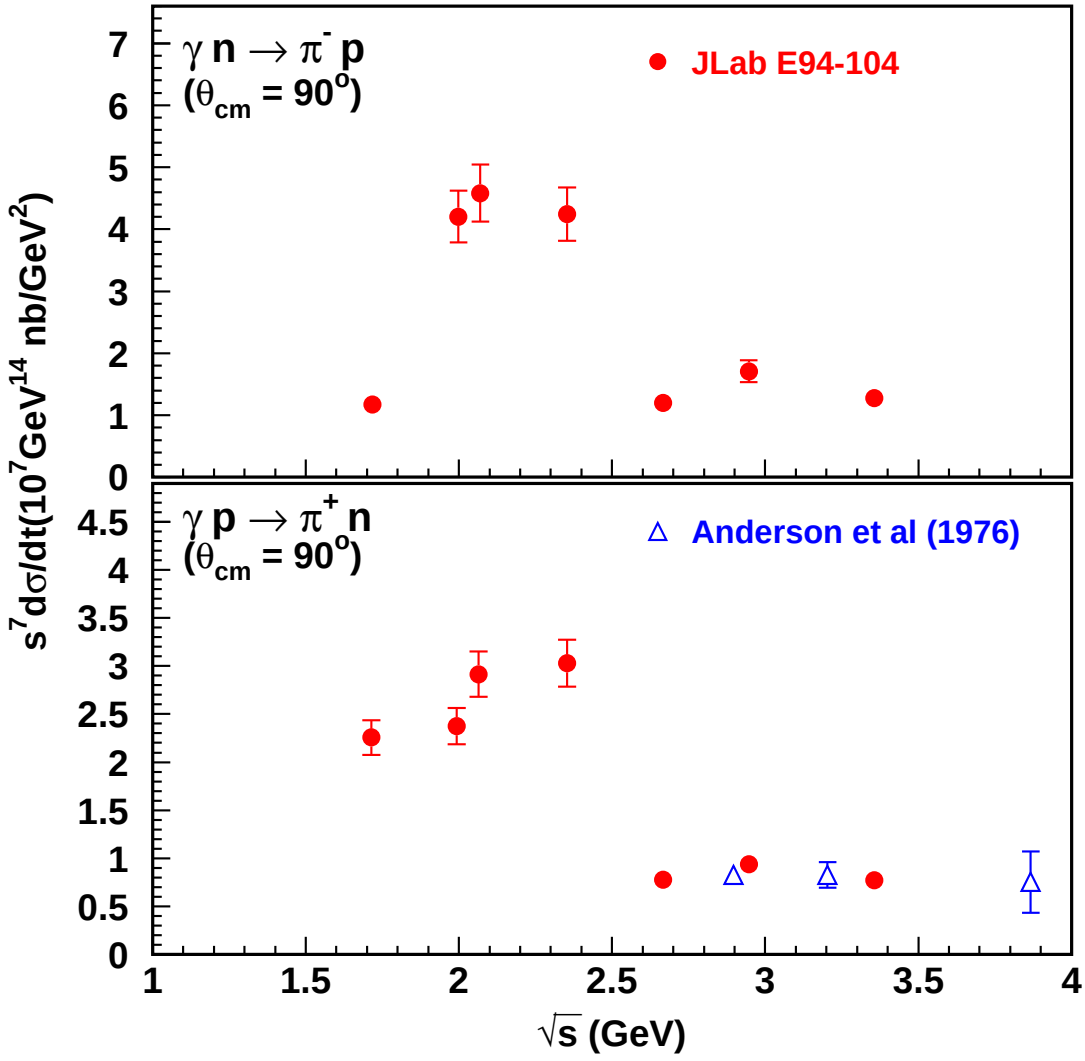

Figure 4-7: The scaled differential cross section $s^7 \frac{d\sigma}{dt}$ versus center-of-mass energy $\sqrt{s}$ at $\theta_{cm} = 90^\circ$ for the $\gamma n \to \pi^- p$ and $\gamma p \to \pi^+ n$ processes.

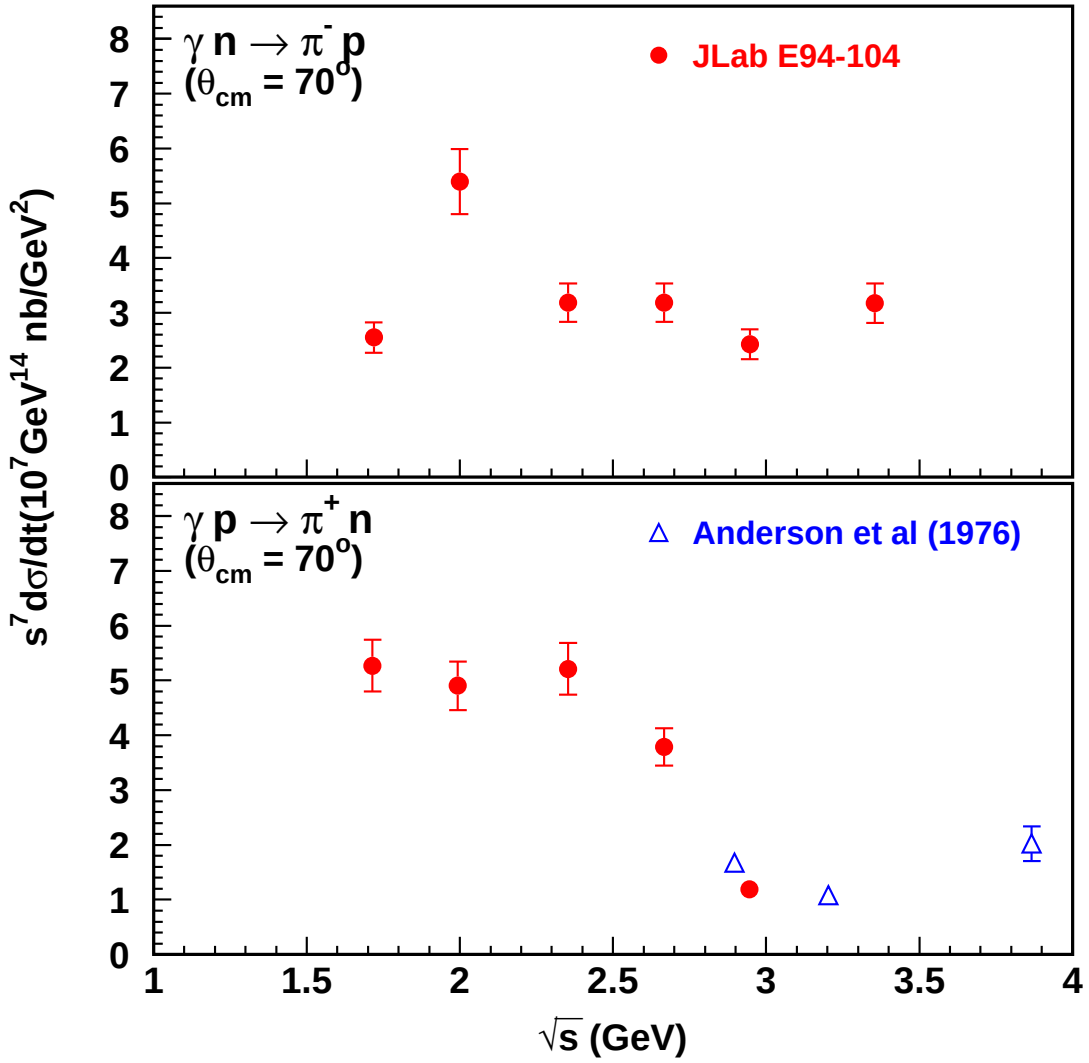

Figure 4-8: The scaled differential cross section $s^7 \frac{d\sigma}{dt}$ versus center-of-mass energy $\sqrt{s}$ at $\theta_{cm} = 70^\circ$ for the $\gamma n \to \pi^- p$ and $\gamma p \to \pi^+ n$ processes.

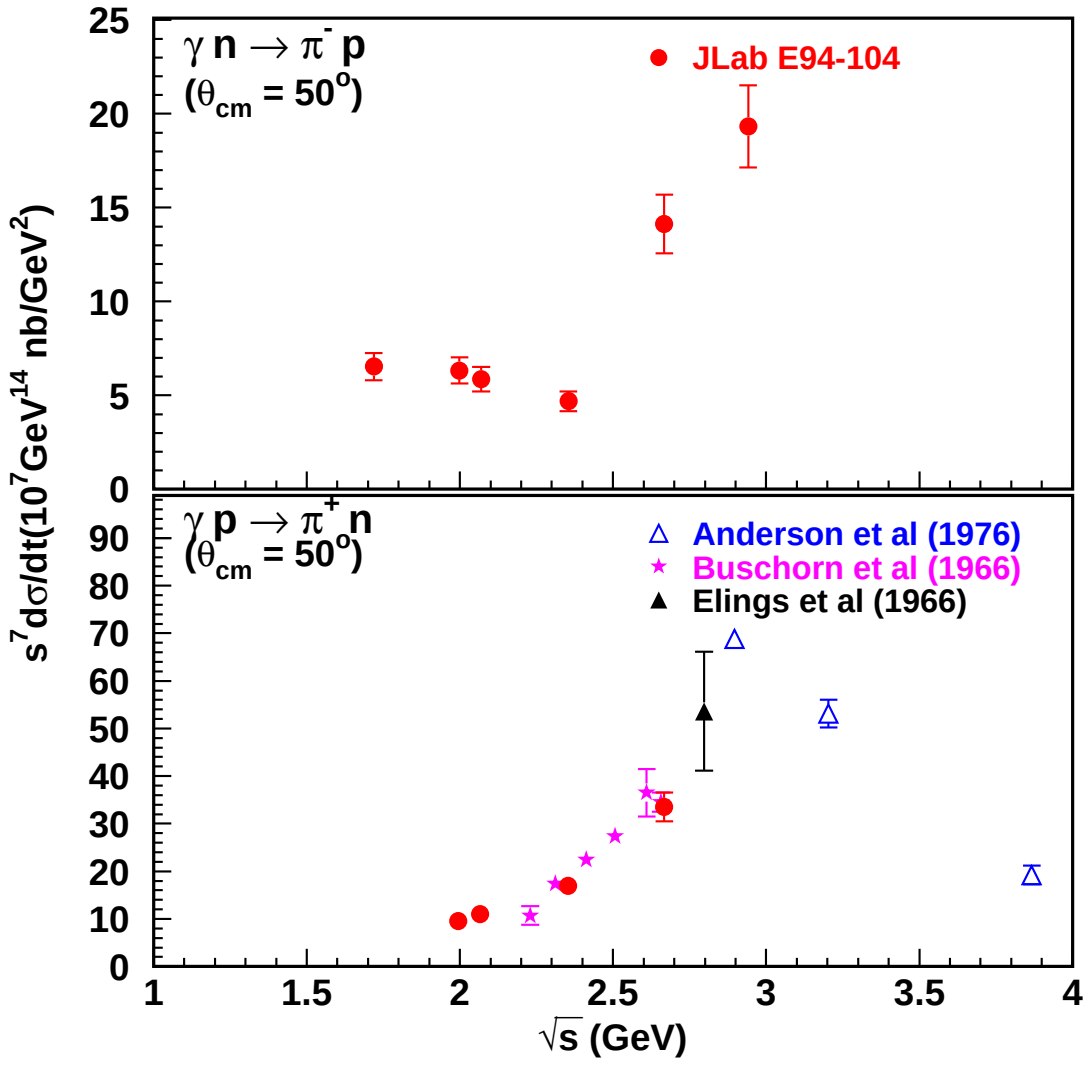

Figure 4-9: The scaled differential cross section $s^7 \frac{d\sigma}{dt}$ versus center-of-mass energy $\sqrt{s}$ at $\theta_{cm} = 50^\circ$ for the $\gamma n \to \pi^- p$ and $\gamma p \to \pi^+ n$ processes.

s^{-8} instead of s^{-7}. Figure 4-10 and Figure 4-11 show the adjusted scaled differential cross sections and there is no clear evidence that the data scale as s^{-6} or s^{-8}.

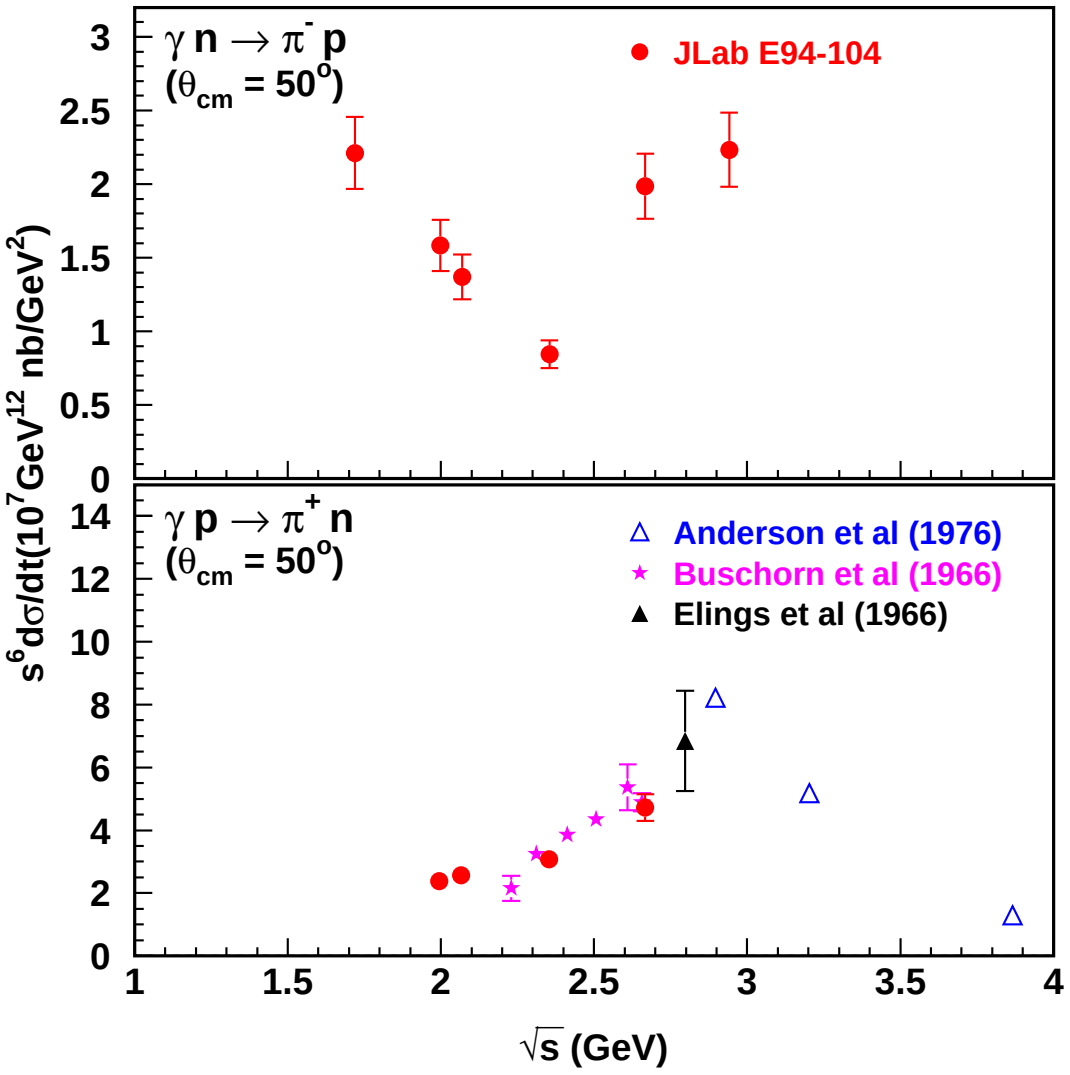

Figure 4-10: The s^6 scaled differential cross section $s^6 \frac{d\sigma}{dt}$ versus center-of-mass energy $\sqrt{s}$ at $\theta_{cm} = 50°$ for the $\gamma n \to \pi^- p$ and $\gamma p \to \pi^+ n$ processes.

The scaled invariant amplitudes are plotted in Figure 4-12 and Figure 4-13 against center-of-mass energy $\sqrt{s}$ and against transverse momentum P_T, similar to what was done for neutral pion photoproduction on the deuteron [112]. The invariant

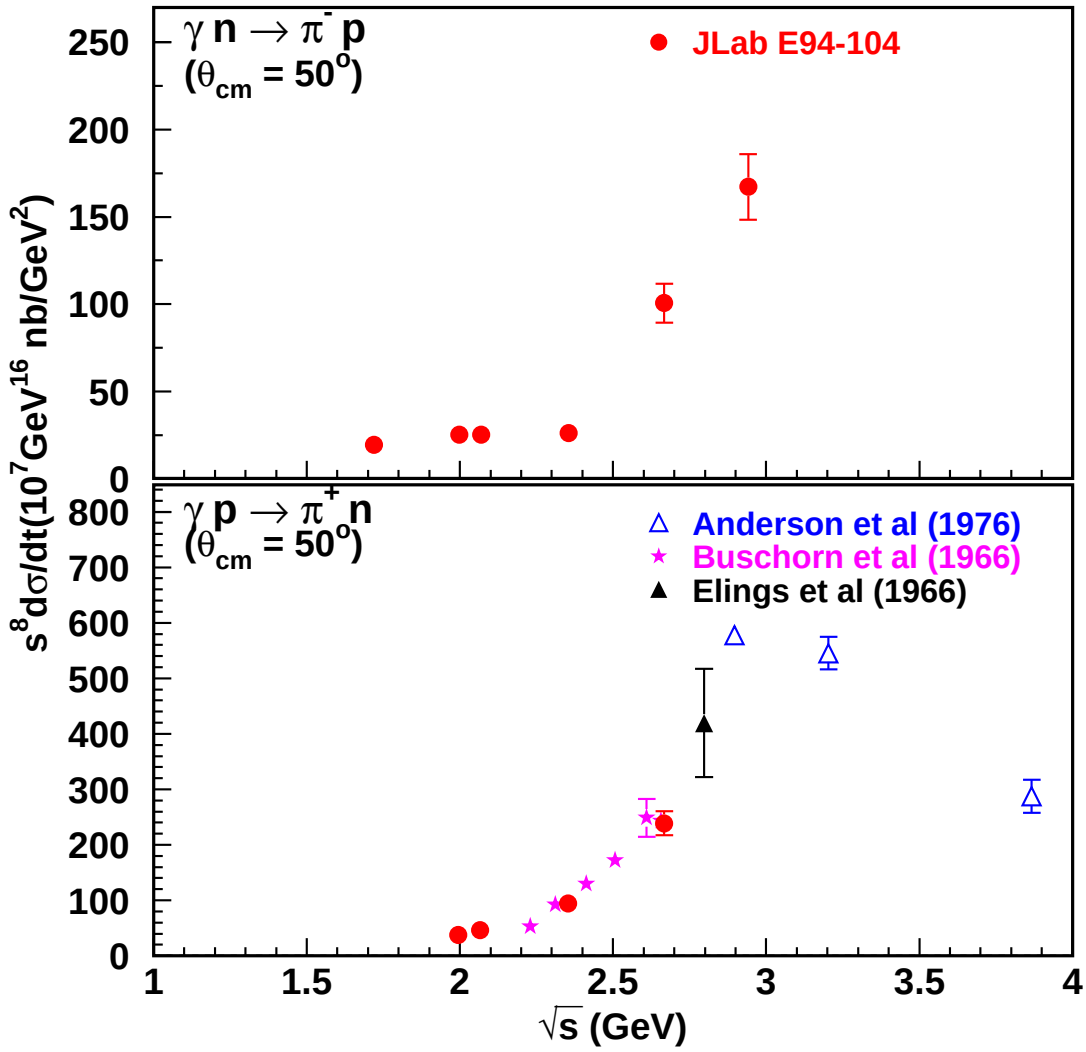

Figure 4-11: The s^8 scaled differential cross section $s^8 \frac{d\sigma}{dt}$ versus center-of-mass energy $\sqrt{s}$ at $\theta_{cm} = 50°$ for the $\gamma n \to \pi^- p$ and $\gamma p \to \pi^+ n$ processes.

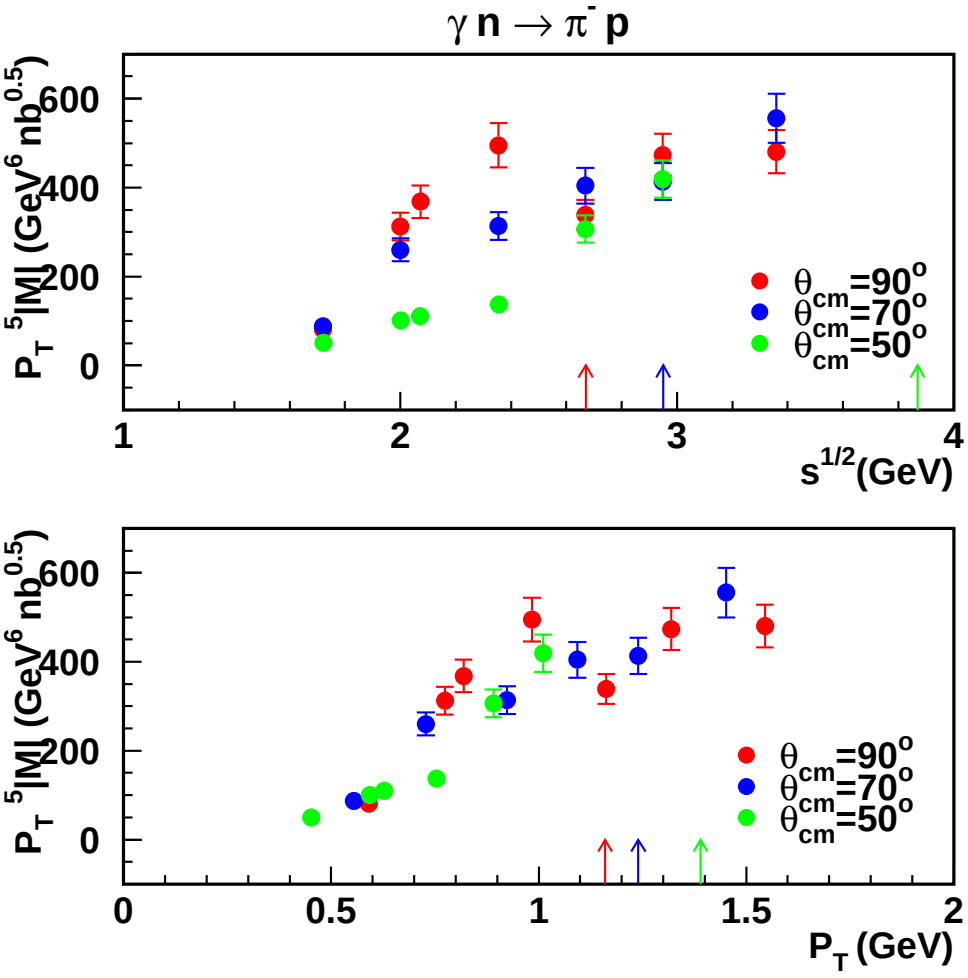

Figure 4-12: Scaled amplitude $P_T^5|M|$ versus center-of-mass energy $\sqrt{s}$ and transverse momentum P_T for the $\gamma n \to \pi^- p$ process. All the data points came from JLab E94-104. The arrows indicate the position below which the data do not scale for either π^+ or π^- photoproduction.

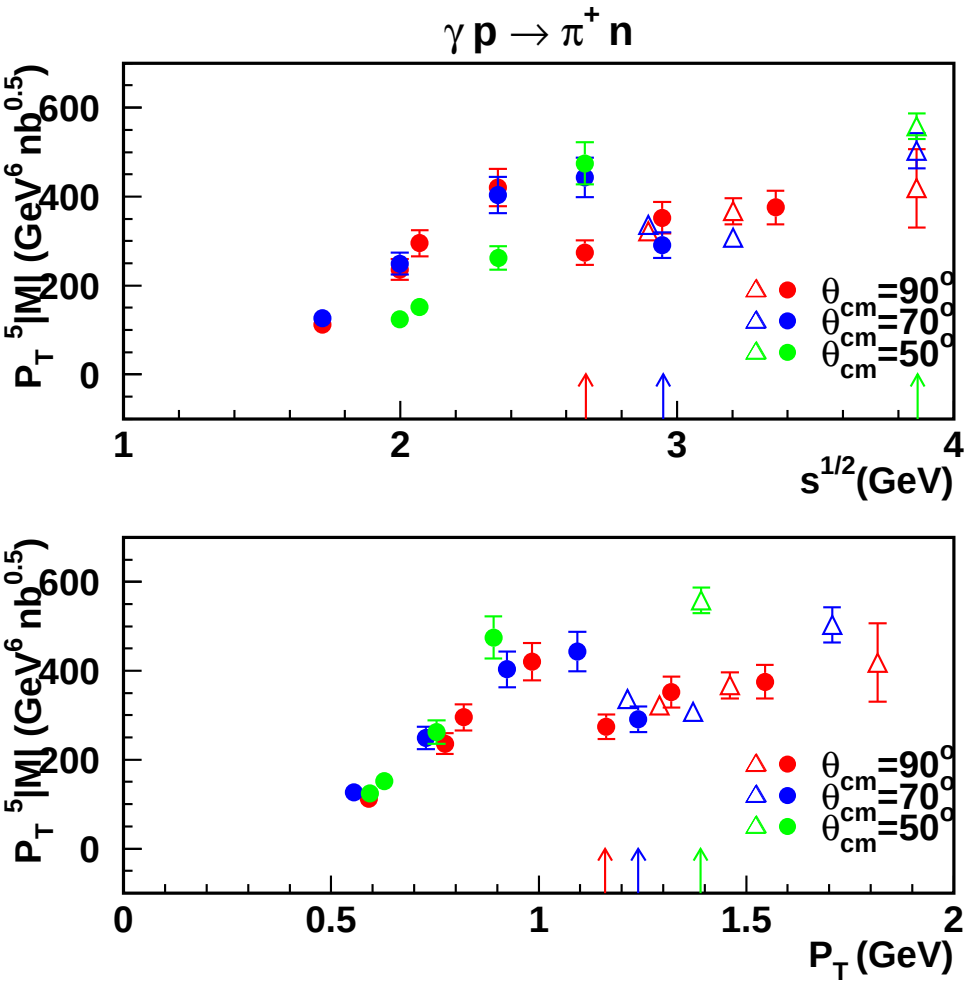

Figure 4-13: Scaled amplitude $P_T^5|M|$ versus center-of-mass energy $\sqrt{s}$ and transverse momentum P_T for the $\gamma p \to \pi^+ n$ process. The data points in solid circles came from JLab E94-104, while those in open triangles are SLAC data [9]. The arrows indicate the position below which the data do not scale for either π^+ or π^- photoproduction.

amplitudes were calculated from the differential cross section by using

$$|M| = 4(s - m_N^2)\sqrt{\pi \frac{d\sigma}{dt}(\gamma N \to \pi N)} \ , \tag{4.1}$$

and the transverse momentum was calculated by using $P_T = |\vec{p}_\pi| \sin\theta_\pi$ from the pion momentum $\vec{p}_\pi$ and scattering angle θ_π. Since the arrows in different colors (indicating the possible onset of scaling for different angles) are closer in terms of transverse momentum than in terms of the center-of-mass energy, the transverse momentum may be a better choice to describe the scaling onset than the center-of-mass energy. The photoproduction data seem to reach the scaling region when the transverse momentum is around 1.2 GeV/c. As a comparison, the deuteron photodisintegration data start to exhibit scaling when transverse momentum ranges from 1.0 to 1.3 GeV/c at $\theta_{cm} = 36^\circ \sim 90^\circ$, while the corresponding center-of-mass energy ranges from 2.7 to 4.3 GeV. Another interesting point is that the scaled amplitudes have much less dependence on center-of-mass angle than do the scaled cross sections, which might just be due to kinematical reasons.

4.1.3 Possible Substructure of Scaling

If one looks at the scaling points at high energies ($\sqrt{s} \geq 2.7$ GeV) more carefully, one can see some substructure in both processes, as shown in Figure 4-14 [18]: the point around 3.0 GeV is higher than those at 2.7 GeV and 3.4 GeV. This might be a hint of possible oscillations around the scaling value, similar to what was observed in the *pp* elastic scattering data [15] (see Figure 1-8). The future measurements planned at JLab Hall A [113], with finer binning in beam energy, are essential for the confirmation of such oscillatory scaling behavior.

The substructure in the pion photoproduction data can not be explained by the SAID [115] or MAID [116] calculation, which are only available for the low energies: up to $E_\gamma = 2$ GeV (or $\sqrt{s} = 2.2$ GeV) for the SAID calculation and up to $E_\gamma = 1.25$

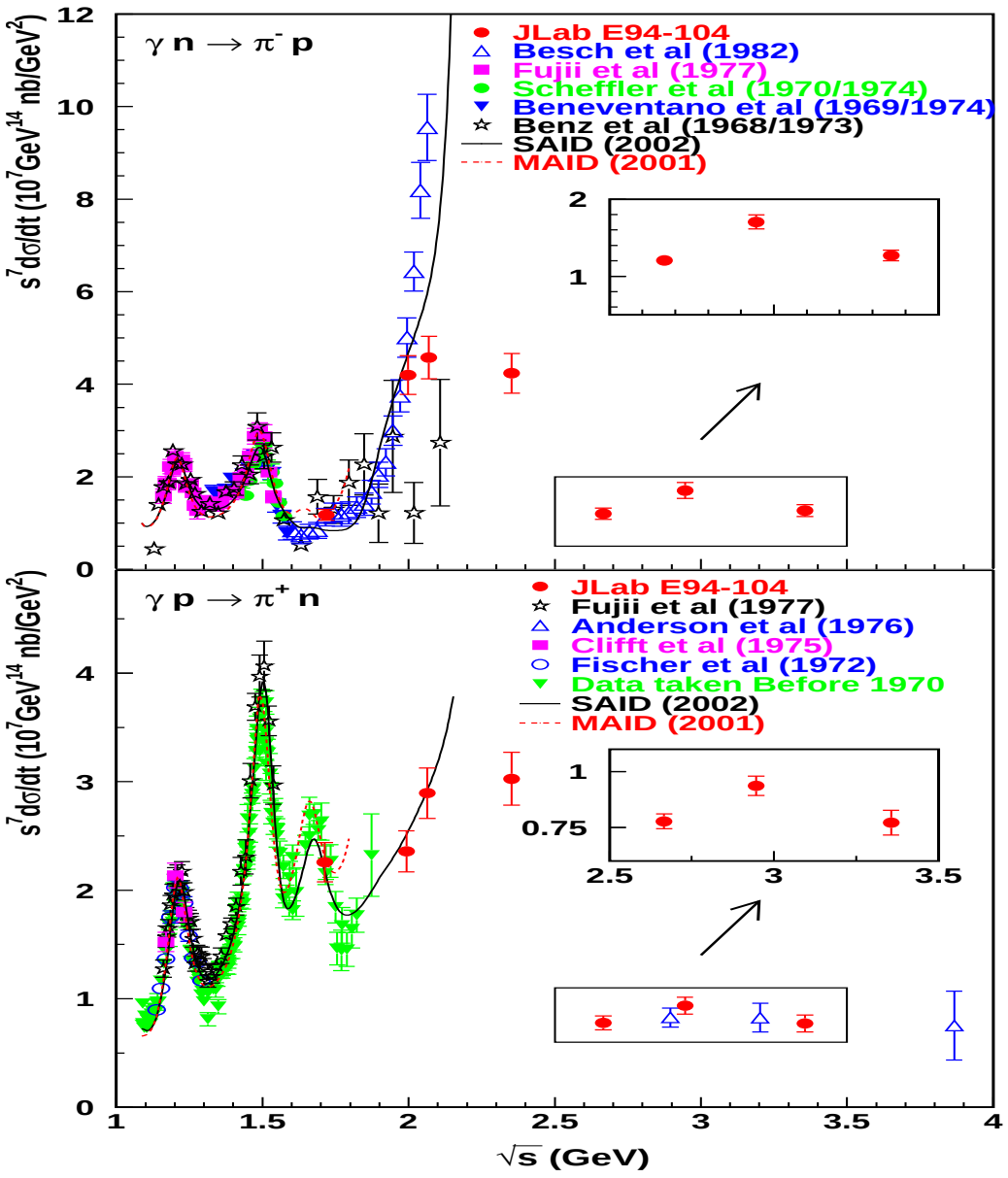

Figure 4-14: The scaled differential cross section $s^7 \frac{d\sigma}{dt}$ versus center-of-mass energy $\sqrt{s}$ for the $\gamma n \to \pi^- p$ process (upper panel) and $\gamma p \to \pi^+ n$ process (lower panel) at $\theta_{cm} = 90°$. The error bars in the insets include only point-to-point uncertainties to highlight the possible substructure of scaling. The solid line was obtained from the recent partial-wave analysis of the single pion photoproduction data up to $E_\gamma = 2$ GeV [115], while the dashed line was obtained from the MAID analysis up to $E_\gamma = 1.25$ GeV [116]

GeV (or $\sqrt{s} = 1.8$ GeV) for the MAID calculation. SAID is a partial-wave analysis of a large database of world data including polarized and unpolarized measurements for pion photoproduction and pion-nucleon scattering. The analysis will be very difficult to extend into the high energy region where a single resonance can be barely separated from other resonances or background. Many reasons such as the non-resonant behavior of partial-wave amplitudes can cause cross section enhancement. The highest resonance in the current SAID calculation is the $F_{37}(1950)$. MAID is a simple model (unitary isobar model or dynamical model) for photoproduction and electroproduction of pions, etas and kaons on nucleons. The non-resonant background and the nucleon resonances are considered in a unitary way. The highest resonance for the current calculation is the $D_{33}(1700)$. The dynamical model differs from the unitary isobar model by dynamically adding pion loop effects to the background. MAID is also difficult to extend into the high energy region.

The substructure or the possible oscillatory scaling behavior in pion photoproduction may come from the same mechanism as in the case of pp scattering, i.e. the interference between the long-distance (due to Landshoff diagrams similar to Figure 1-4) amplitude and short-distance amplitude [34] (see Section 1.3.3), or the interference between resonances with a pQCD background [35] (see Section 1.3.3). But it may also be due to other mechanisms, such as high energy resonances around 3 GeV [20], the interference between the amplitudes associated with different helicity changes based on the generalized counting rule [37] (see Section 1.3.4), or the breaking of the local quark-hadron duality above the resonance region [39] (see Section 1.3.4). Next I will say more about the last two possible mechanisms.

Introducing the parton angular orbital momentum can solve many puzzles, such as the hadron helicity nonconservation and the asymptotic scaling proton form factor ratio of $F_2(Q^2)/F_1(Q^2) \sim 1/\sqrt{Q^2}$ which are different from the pQCD prediction. The generalized constituent counting rule was derived for hard exclusive processes involving parton orbital momentum and hadron helicity flip. It predicts that

$M(\gamma N_\uparrow \to \pi N_\downarrow) \sim s^{-3}$ and $d\sigma/dt(\gamma N_\uparrow \to \pi N_\downarrow) \sim s^{-8}$ for the helicity flipped case, while $M(\gamma N_\uparrow \to \pi N_\uparrow) \sim s^{-5/2}$ and $d\sigma/dt(\gamma N_\uparrow \to \pi N_\uparrow) \sim s^{-7}$ for the helicity conserved case. The interference between the amplitudes with different helicity changes offers a new mechanism to explain the possible oscillations around the scaling value. But the resulting oscillation pattern should be different from that caused by interference between the short-distance and long-distance amplitude. At sufficiently large energy, the helicity flipped amplitude will become negligible while the long-distance amplitude will overwhelm the traditional scaling one (the helicity conserved amplitude or short-distance amplitude) due to the different energy dependence.

The locality of quark-gluon duality means that the local averages of physical variables measured in the resonance region are equal to those measured in the deep-inelastic or scaling region. The locality of quark-gluon duality can be realized in a simple model of a composite system with two spinless charged constituents described by harmonic oscillator wave functions with principal quantum number N and orbital angular momentum L ($\leq N$). The destructive interference between the high density of overlapping resonances leads to the smooth scaling behavior at high energies. But for medium energies, the locality of quark-gluon duality may break down and a sizable oscillation around the scaling value may appear above the resonance region due to the orbital angular momentum dependence of the resonances, as shown by the dotted curve with $n \leq 4$ (n is similar to N but in a more generalized approach) in Figure 4-15. There is no orbital angular momentum involved for the solid curve with $n \leq 2$ since $L \leq N$ and $L =$ odd terms vanish at $\theta_{cm} = 90°$. In this mechanism, the energy increase reduces the oscillation amplitude, and the Q^2 dependence may be nontrivial. If a subset of resonances are relatively suppressed at large Q^2, there will be significant shifts in the position and magnitude of oscillations. The deviation pattern produced by the resonance degeneracy breaking requires no simple periodicity. The experimental data can thus distinguish this mechanism from others.

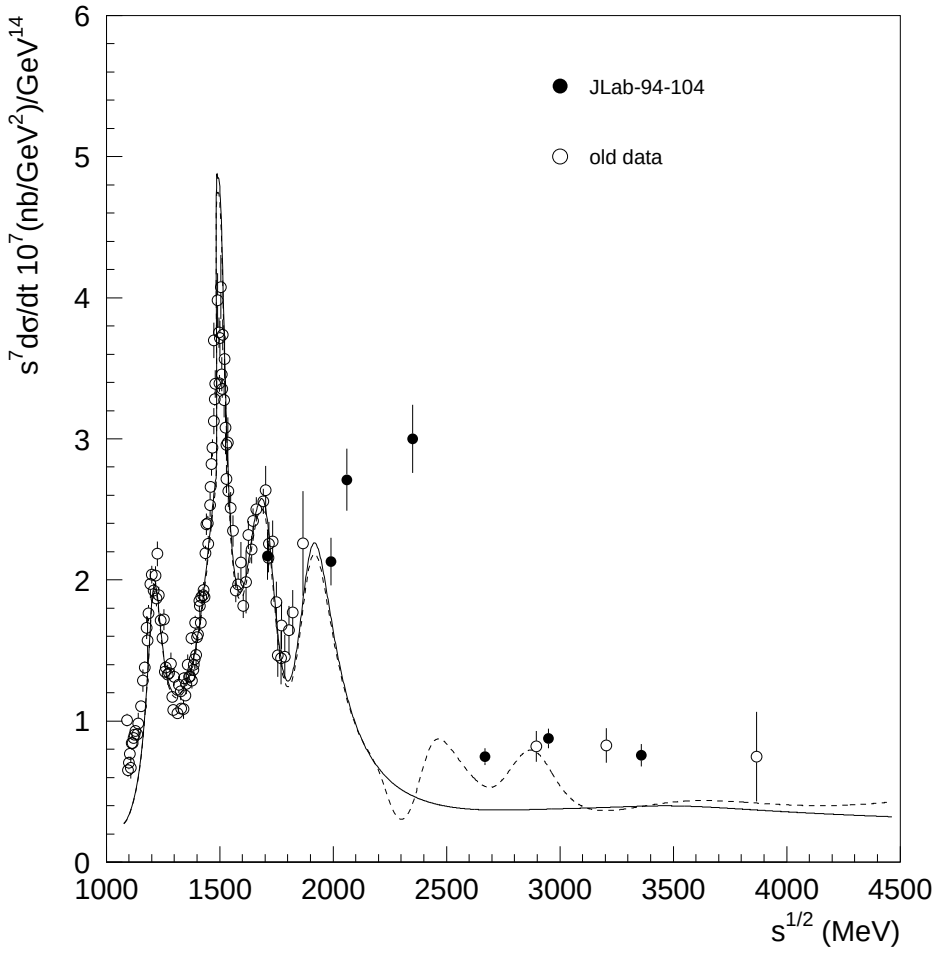

Figure 4-15: Energy Dependence of the scaled differential cross section for π^+ photoproduction at $\theta_{cm} = 90°$. The empty circles are the old data from Reference [44] and the solid dots are the new data from JLab [18]. The solid curve denotes degeneracy breaking for $n \leq 2$, while the dotted for $n \leq 4$. n is similar to the principal quantum number for the harmonic oscillator wave function.

4.1.4 Cross Section Enhancement around 2.2 GeV

Another interesting feature of the differential cross section results is an apparent enhancement for both channels of the charged pion photoproduction at $\theta_{cm} = 90°$, at a center-of-mass energy ranging approximately from 1.8 to 2.5 GeV, as shown in Figure 4-14. Note that it is the scaled cross sections $s^7 d\sigma/dt$ that are plotted. As for the non-scaled cross section $d\sigma/d\Omega$, the data at 2.4 GeV are about fourteen times higher than those at 2.7 GeV, as shown in Table 4.1 and Table 4.2. The similar cross section enhancement was also observed in neutral pion photoproduction (see Figure 1-15). The angular distributions may not be the same for all the data around the enhancement, and the details of the enhancement are different at $\theta_{cm} = 70°$ and especially $\theta_{cm} = 50°$ (see Figure 4-4 and Figure 4-5 for example).

Some speculation can be made about the enhancement. It might be due to the known baryon resonances around this energy, for example $G_{17}(2190)$, $H_{17}(2220)$ and $G_{19}(2250)$, as shown in Table 4.3 [20], just as the case at lower energies. It might relate to some missing resonances [114], which were predicted by the constituent quark model but have not been seen experimentally. The value of center-of-mass energy hints that the enhancement might be associated with the strangeness production threshold, which is around 2 GeV to produce a ϕ meson of mass 1 GeV. The resonances at strangeness and charm production thresholds were assumed in an approach to explain the strong spin-spin correlation and oscillatory scaling in elastic pp scattering [35]. It is worthwhile to mention that a broad bump near 2.2 GeV appears in the cross section for the $\pi^- p \to$ total process, while it is not clear for $\pi^- p$ elastic scattering due to the poor quality of the data, as shown in Figure 3-26 [20].

4.2 Exclusive Charged Pion Ratio π^-/π^+

One can form the exclusive charged pion ratio $\frac{d\sigma/dt(\gamma n \to \pi^- p)}{d\sigma/dt(\gamma p \to \pi^+ p)}$, which is different from the inclusive one $\frac{d\sigma/dt(\gamma d \to \pi^- X)}{d\sigma/dt(\gamma d \to \pi^+ X)}$. Though the two types of ratios agree with each other at

Table 4.3: The summary of main N and Δ resonances with certain existences in $N\pi$ channel. Also listed are the photon decay amplitudes $A^N_{\rm helicity}$ to $N\gamma$.

Mass (MeV)	L_{2I2J}	Width (MeV)	$A^p_{1/2}$ ($\mathrm{GeV}^{-0.5}$)	$A^p_{3/2}$ ($\mathrm{GeV}^{-0.5}$)	$A^n_{1/2}$ ($\mathrm{GeV}^{-0.5}$)	$A^n_{1/2}$ ($\mathrm{GeV}^{-0.5}$)
$\Delta(1232)$	P_{33}	120	$A^N_{1/2}$:	-0.135±0.006	$A^N_{3/2}$:	-0.255±0.008
$N(1440)$	P_{11}	350	-0.065±0.004	-	0.040±0.010	-
$N(1520)$	D_{13}	120	-0.024±0.009	0.166±0.005	-0.059±0.009	-0.139±0.011
$N(1535)$	S_{11}	150	0.090±0.030	-	0.046±0.027	-
$\Delta(1620)$	S_{31}	150	$A^N_{1/2}$:	0.027±0.011	$A^N_{3/2}$:	-
$N(1650)$	S_{11}	150	0.053±0.016	-	-0.015±0.021	-
$N(1675)$	D_{15}	150	0.019±0.008	0.015±0.009	-0.043± 0.012	-0.058±0.013
$N(1680)$	F_{15}	130	-0.015±0.006	0.133±0.012	0.029±0.010	-0.033±0.009
$\Delta(1700)$	D_{33}	300	$A^N_{1/2}$:	0.104±0.015	$A^N_{3/2}$:	0.085±0.022
$N(1720)$	P_{13}	150	0.018±0.030	-0.019±0.020	0.001±0.015	-0.029±0.061
$\Delta(1905)$	F_{35}	350	$A^N_{1/2}$:	0.026±0.011	$A^N_{3/2}$:	-0.045±0.020
$\Delta(1910)$	P_{31}	250	$A^N_{1/2}$:	0.003±0.014	$A^N_{3/2}$:	-
$\Delta(1950)$	F_{37}	300	$A^N_{1/2}$:	-0.076±0.012	$A^N_{3/2}$:	-0.097±0.010
$N(2190)$	G_{17}	450	-0.055/-0.030	0.081/0.180	-0.042/-0.085	-0.126/0.007
$N(2220)$	H_{19}	400	-	-	-	-
$N(2250)$	G_{19}	400	-	-	-	-
$\Delta(2420)$	H_{311}	400	$A^N_{1/2}$:	-	$A^N_{3/2}$:	-

low energies and low $|t|$, they differ a lot at high energies. For example, the exclusive ratio at $|t| = 2.7$ (GeV/c)^2 and $\theta_{cm} = 90°$ is around 1.5, while the corresponding inclusive ratio is only around 0.8, as shown in Figure 4-16 and Figure 4-17 [117]. It is speculated that the inclusive ratio at high energies might be dominated by multi-pion production processes since the cross section ratio for π^+ photoproduction $\frac{d\sigma/dt(\gamma p \to \pi^+ n)}{d\sigma/dt(\gamma d \to \pi^+ X)}$ deviates from unity [118].

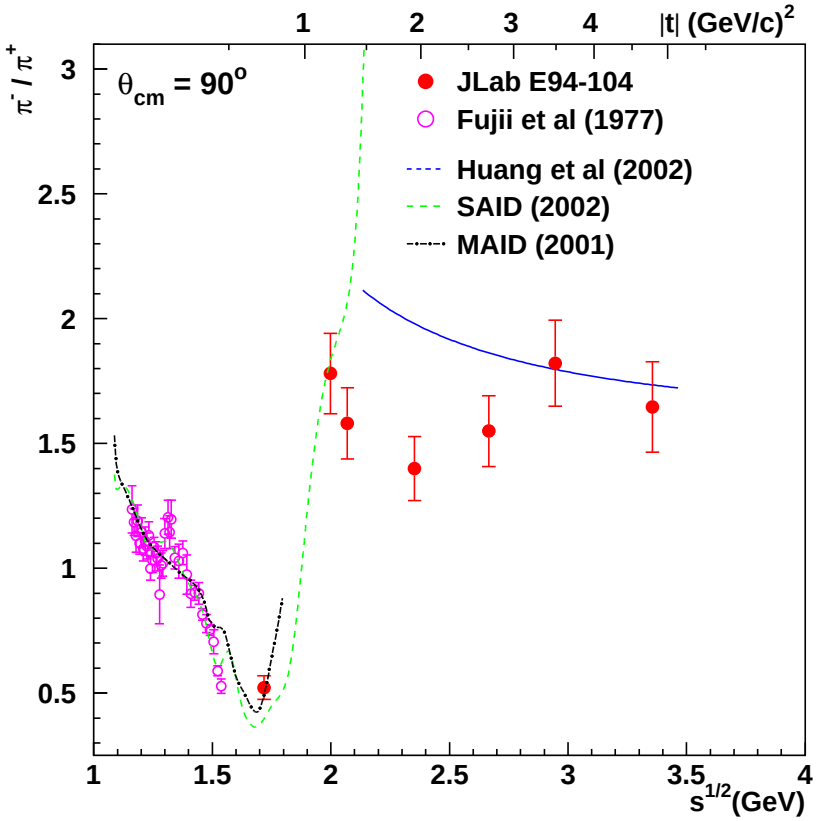

Figure 4-16: Exclusive charged pion ratio $\frac{d\sigma/dt(\gamma n \to \pi^- p)}{d\sigma/dt(\gamma p \to \pi^+ p)}$.

The exclusive charged pion ratios have some oscillations at low energies due to the isospin dependence of the resonances, which can be described by the SAID [115] and MAID [116] calculations (see Section 4.1.3) available at low energies. The big jump around 2 GeV might be associated with the isospin-dependent resonances nearby, or with the strangeness production threshold (around 2 GeV for ϕ production). The lowest order (leading-twist) calculation based on one-hard-gluon-exchange di-

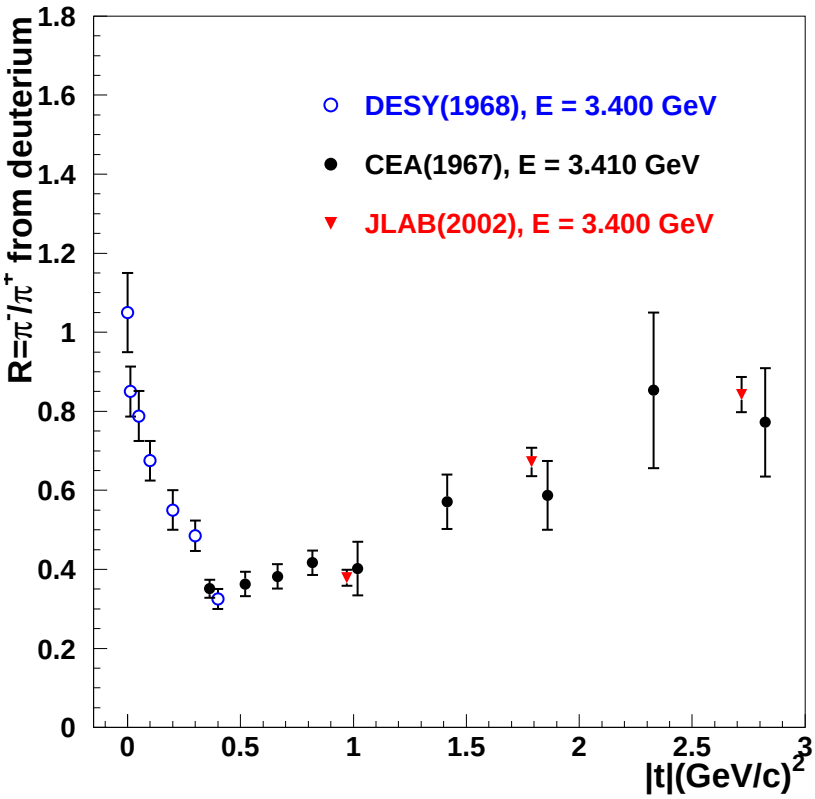

Figure 4-17: Inclusive charged pion ratio $\frac{d\sigma/dt(\gamma d \to \pi^- X)}{d\sigma/dt(\gamma d \to \pi^+ X)}$ at 3.4 GeV. The results from the JLab data [117] at $\theta_{cm} = 50°, 70°, 90°$ were shown together with the previous data taken with CEA (Cambridge Electron Accelerator) [119] and DESY (Deutsches Elektronen-Synchrotron) [120].

agrams [42, 43], which is only valid at high energies, predicts a smooth and simple behavior (see Section 1.4)

$$\frac{d\sigma/dt(\gamma n \to \pi^- p)}{d\sigma/dt(\gamma p \to \pi^+ n)} \simeq (\frac{ue_d + se_u}{ue_u + se_d})^2 \tag{4.2}$$

after the nonperturbative components represented by the form factors are divided out in the ratio. The form factors parameterize the soft physics that controls the emission and absorption of a quark by a baryon. The theoretical prediction seems to agree with the $\theta_{cm} = 90^\circ$ data at the two highest energies ($E_e = 4.2, 5.6$ GeV).

The charged pion ratio was also calculated to higher orders (twist-2 and twist-3) within the handbag mechanism considering both quark helicity flip and non-flip [121]. The handbag mechanism is characterized by the fact that only one quark from the incoming and one quark from the outgoing nucleon participate in the hard subprocess, while all other partons are spectators. The more precise approach led to the same result as the leading-twist prediction when $|C_2^P| >> |C_3^P|$, The invariant functions $|C_i^P|$ $(i = 1, 4)$ are the coefficients for the four gauge invariant covariants into which the meson photoproduction amplitudes can be decomposed. Both $|C_2^P|$ and $|C_3^P|$ contribute only to the quark helicity conserving amplitudes while $|C_1^P|$ and $|C_4^P|$ generate quark helicity flips. The charged pion ratio will become infinity at large s if $|C_3^P|$ is dominant, which is clearly not supported by our data.

But since the calculation was for massless particles, there is some sizable uncertainty in the ratio prediction due to the nucleon mass at energy scale of several GeV, as estimated by the difference between the solid and dashed curves in Figure 4-18. The calculation shown by the dashed curve considers the nucleon mass by using the identification [122] of the Mandelstam variables with the experimental ones ($s_{\rm exp}$, $t_{\rm exp}$, $u_{\rm exp}$)

$$s = s_{\rm exp} - m_p^2 \ , t = t_{\rm exp} \ , u = u_{\rm exp} - m_p^2 \ , \tag{4.3}$$

so that $s + t + u \sim 0$. Figure 4-18 also shows that the agreement at forward angles

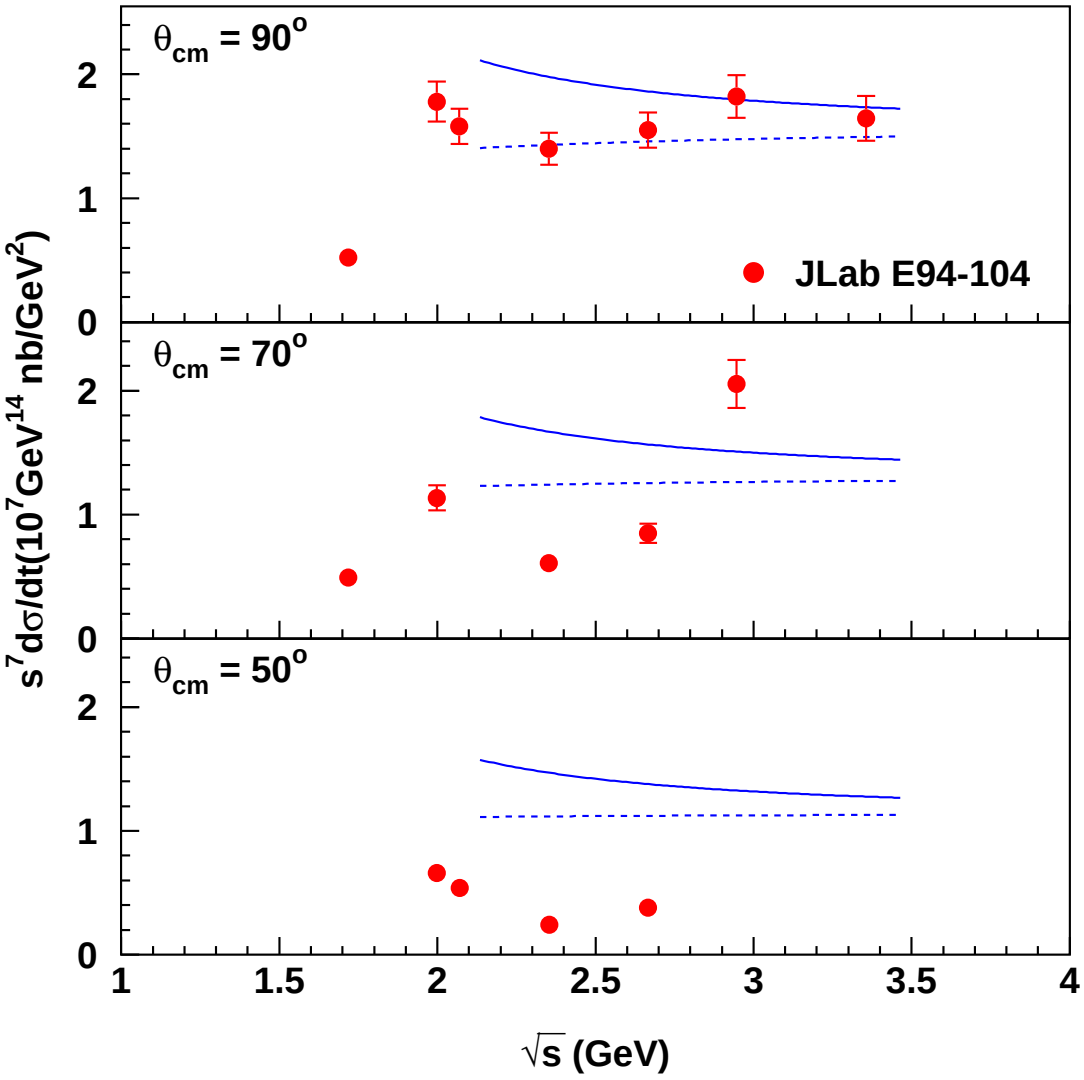

Figure 4-18: Exclusive charged pion ratio $\frac{d\sigma/dt(\gamma n \to \pi^- p)}{d\sigma/dt(\gamma p \to \pi^+ p)}$ versus center-of-mass energy $\sqrt{s}$ at different center-of-mass angles. The solid curve is calculated by using Equation 4.2, while the dashed one considers the nucleon mass by using Equation 4.3.

is not as good as the case at 90°, which might be related to the relatively lower momentum transfer. Measurements at higher energies are necessary to fully check the theoretical approach, though the current comparison between prediction and data seems to suggest that the handbag mechanism is at work for the pion photoproduction processes with dominant quark helicity non-flip amplitudes and $|C_2^p| >> |C_3^p|$.

4.3 Outlook

As mentioned in the previous sections, a new proposal E02-012 [113] has been approved in JLab Hall A to measure the $\gamma n \to \pi^- p$ process with deuterium and carbon targets, as well as the $\gamma p \to \pi^+ n$ process with a hydrogen target. With very fine steps in center-of-mass energy, approximately 0.07 GeV, as shown in Figure 4-19 [108, 123], the new experiment will be able to elucidate more details about the possible substructure of the scaling behavior. In addition, the nuclear transparency of carbon in the pion photoproduction process will be measured for the first time. This should enable us to test some theoretical predictions such as the nuclear filtering effect and color transparency. The latter was suggested by the helium transparency measurement in E94-104 [124].

The JLab 12 GeV upgrade was among the twelve projects identified as near-term priorities in the recent DOE 20-year facility plan. Since the cross section decreases relatively slowly as energy increases, the measurements for single pion photoproduction processes can be greatly extended with the JLab 12 GeV upgrade, as shown in Figure 4-19. One would be able to check the assumption [35] of the resonance at charm production threshold in an approach to explain the anomalies in pp scattering since the charm production threshold will be crossed. In addition, one would be able to further check the scaling and charged pion ratio predictions, especially at forward angles.

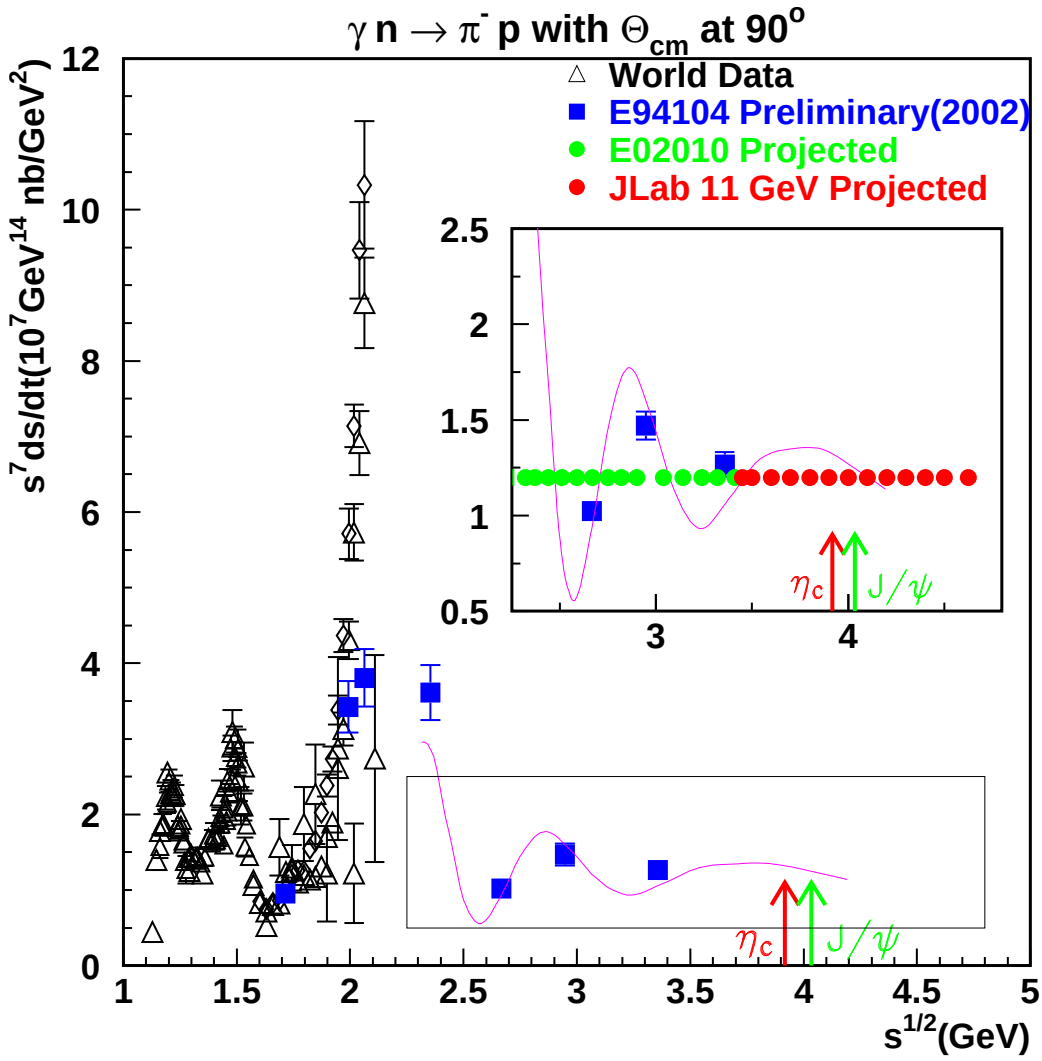

Figure 4-19: The projected data with future experiment E02-012 and with JLab energy upgrade. The curve is a fit of E94-104 data. The arrows indicate the charm production threshold.

Appendix A

Some Definitions and Formalism

A.1 Four-momentum Conservation

For any particle α, its four-momentum P_α is a four-vector under the Lorentz transformation with the form

$$P_\alpha = (E, p_x, p_y, p_z) \ , \tag{A.1}$$

where p_i $(i = x, y, z)$ are the three spatial components of the particle momentum, E is the particle energy and the speed of light c has been omitted with natural units. The relation between energy and momentum is $E = \sqrt{p_x^2 + p_y^2 + p_z^2 + m^2}$ with m the particle mass. The four-momentum conservation, or energy and momentum conservation, means the total four-momentum remains unchanged before and after any scattering process. For the two body scattering process $AB \to CD$, it can be expressed as

$$P_A + P_B = P_C + P_D \ , \tag{A.2}$$

which contains four equations for four components.

A.2 Mandelstam Variables

For the two body scattering process $AB \to CD$, it is conventional to define Mandelstam variables

$$\begin{aligned} s &= (P_A + P_B)^2 \\ t &= (P_A - P_C)^2 \\ u &= (P_A - P_D)^2 \ , \end{aligned} \tag{A.3}$$

where P_α is the four-momentum of particle α ($\alpha = A, B, C, D$).

Mandelstam variables are invariant under Lorentz transformation, which implies that they are the same in both lab frame and center-of-mass frame. s is the square of the total energy in the center-of-mass frame, where the spatial components of the momentum are zero. t is the square of momentum transfer, which is equal to $-Q^2$ often used for electron scattering. Only two of the three Mandelstam variables are independent. It can be proved that $s + t + u = m_A^2 + m_B^2 + m_C^2 + m_D^2$.

For $\gamma N \to \pi N$ process, with $P_A = (E_\gamma, 0, 0, E_\gamma)$ and $P_B = (m_N, 0, 0, 0)$, it is easy to evaluate the Mandelstam variable s in the lab frame using

$$s = m_N^2 + 2 m_N E_\gamma \ . \tag{A.4}$$

Bibliography

[1] S. J. Brodsky and G. R. Farrar, Phys. Rev. Lett. **31**, 1153 (1973).

[2] S. J. Brodsky and G. R. Farrar, Phys. Rev. D **11**, 1309 (1975).

[3] V. A. Matveev, R. M. Muradyan and A. N. Tavkhelidze, Nuovo Cimento Lett. **7**, 719 (1973).

[4] G. R. Lepage and S. J. Brodsky, Phys. Rev. D **22**, 2157 (1980).

[5] P. V. Landshoff, Phys. Rev. D **10**, 1024 (1974).

[6] P. V. Landshoff and J. C. Polkinghorne, Phys. Lett. B **44**, 293 (1973).

[7] C. White *et al.*, Phys. Rev. D **49**, 58 (1994).

[8] E. C. Schulte *et al.*, Phys. Rev. C **87**, 102302 (2001);
C. Bochna *et al.*,Phys. Rev. Lett. **81**, 4576 (1998).

[9] R. L. Anderson *et al.*, Phys. Rev. D **14**, 679 (1976).

[10] K. Wijesooriya *et al.*, Phys. Rev. Lett. **86**, 2975 (2001).

[11] K. Wijesooriya *et al.*, Phys. Rev. C **66**, 034614 (2002).

[12] T. Gousset, B. Pier and J. P. Ralston, Phys. Rev. D **53**, 1202 (1996).

[13] A. V. Belisky, X. Ji, and F. Yuan, Phys. Rev. Lett. **91**, 092003 (2003).

[14] E. A. Crosbie *et al.*, Phys. Rev. D **23**, 600 (1981);
D. G. Crabb *et al.*, Phys. Rev. Lett. **41**, 1257 (1978).

[15] A. W. Hendry, Phys. Rev. D **10**, 2300 (1974).

[16] A. S. Carroll *et al.*, Phys. Rev. Lett. **61**, 1698 (1988).

[17] JLab experiment E94-104, spokespersons: H. Gao and R.J. Holt, (1994); http://www.jlab.org/exp_prog/generated/apphalla.html.

[18] L. Y. Zhu *et al.*, Phys. Rev. Lett. **91**, 022003 (2003).

[19] D. H. Perkins, *Introduction to High Energy Physics*, Cambridge University Press, New York (2000).

[20] K. Hagiwara *et al.*, Phys. Rev. D **66**, 010001 (2002); http://pdg.lbl.gov/.

[21] http://www-theory.lbl.gov/~ianh/alpha/alpha.html.

[22] A. D. Martin, R. G. Roberts, W. J. Stirling, and R. S. Thorne, Eur. Phys. J. C **23**, 73 (2002).

[23] T. Sato and T.-S. H. Lee, Phys. Rev. C **54**, 2660 (1996).

[24] V. Yu. Grishina *et al.*, Eur. Phys. J. A **10**, 355 (2001).

[25] S. J. Brodsky and J. R. Hiller, Phys. Rev. C **28**, 475 (1983).

[26] A. E. L. Dieperink *et al.*, Phys. Lett. B **456**, 9 (1999).

[27] L. L. Frankfurt *et al.*, Phys. Rev. Lett. **84**, 3045 (2000).

[28] E. C. Schulte, Ph.D. Thesis, University of Illinois at Urbana-Champaign, (2002).

[29] E. C. Schulte *et al.*, Phys. Rev. C **66**, 042201 (2002).

[30] N. Isgur and C. H. L. Smith, Phys. Rev. Lett. **52**, 1080 (1984).

[31] J. P. Ralston and P. Jain, hep-ph/0207129, (2002); J. P. Ralston, R. V. Buniy and P. Jain, hep-ph/0206063, (2002)

[32] G. A. Miller and M. R. Frank, Phys. Rev. C **65**, 065205 (2002).

[33] M. K. Jones *et al.*, Phys. Rev. Lett. **84**, 1398 (2000); O. Gayou *et al.*, Phys. Rev. C **64**, 038202 (2001); O. Gayou *et al.*, Phys. Rev. Lett. **88**, 092301 (2002).

[34] J. P. Ralston and B. Pire, Phys. Rev. Lett. **61**, 1823 (1988).

[35] S. J. Brodsky, and G. F. de Teramond, Phys. Rev. Lett. **60**, 1924 (1988).

[36] S. J. Brodsky *et al.*, Phys. Rev. D **67**, 055008 (2003).

[37] X. Ji, J. P. Ma and F. Yuan, Phys. Rev. Lett. **90**, 241601 (2003).

[38] X. Ji, J. P. Ma and F. Yuan, Nucl. Phys. B **652**, 383 (2003).

[39] Q. Zhao and F. E. Close, Phys. Rev. Lett. **91**, 022004 (2003).

[40] E. D. Bloom and F. J. Gilman, Phys. Rev. D **4**, 2901 (1971).

[41] I. Niculescu *et al.*, Phys. Rev. Lett. **85**, 1182 (2000).

[42] H. W. Huang, private communication.

[43] H. W. Huang and P. Kroll, Eur. Phys. J. C **17**, 423 (2000); P. Kroll, hep-ph/0207118, (2002); A. Afanasev, C. E. Carlson, and C. Wahlquist, Phys. Lett. B **398**, 393 (1997).

[44] HEPDATA: REACTION DATA Database,
http://durpdg.dur.ac.uk/hepdata/reac.html;
H. Genzel, P. Joos, and W. Pfeil, *Photoproduction of Elementary Particles*, Group I Volume 8 of Numerical Data and Functional Relationships in Science and Technology, edited by K.-H. Hellwege, Springer-Verlag Press, Berlin, (1973).

[45] C. W. Leemann, D. R. Douglas, and G. A. Krafft, Ann. Rev. Nucl. Part. Sci. **51**, 413 (2001).

[46] B. D. Anderson *et al.*, *Basic Instrumentation for Hall A at Jefferson Lab*, Nucl. Instrum. Methods (to be published).

[47] X. Zheng, Ph.D. Thesis, Massachusetts Institute of Technology, (2002).

[48] D. Higinbotham, private communication.

[49] A. Saha, http://www.jlab.org/~saha/beamline/.

[50] M. K. Jones, *Report on BCM calibration* (unpublished); http://www.jlab.org/~jones/e91011/, (2000).

[51] J. H. Mitchell *et al.*, *Hall A Experimental Equipment Operations Manual* (unpublished); http://hallaweb.jlab.org/document/OPMAN/index.html.

[52] A. Saha, private communication.

[53] *Status Report on Activities in Hall A - 2000*, edited by A. J. Sarty, R. D.Ransome, and Kees de Jager, (2001).

[54] R. Gilman, http://www.jlab.org/~gilman/gammap99/hallarad2001.html.

[55] D. G. Meekins, Ph.D. Thesis, College of William and Mary, (1998); http://www.jlab.org/~meekins/gammacode.tgz.

[56] J. L. Matthews and R. O. Owens, Nucl. Instrum. Methods **111**, 157 (1973).

[57] J. L. Matthews, D. J. S. Findlay, and R. O. Owens, Nucl. Instrum. Methods **180**, 573 (1981).

[58] http://hallaweb.jlab.org/equipment/targets/cryotargets/Halla_tgt.html.

[59] NBS Report: *The thermodynamic properties of deuterium*; *The thermodynamic properties of parahydrogen*; *The thermodynamic properties of helium.*

[60] R. S. Suleiman, Ph.D. Thesis, Kent State University, (1999).

[61] http://hallaweb.jlab.org/equipment/high_resol.html.

[62] N. Liyanage, JLab Technical Note, JLAB-TN-02-012 (2002); http:www.jlab.org/*sim*nilanga/physics/optics.ps.

[63] K. G. Fissum *et al.*, Nucl. Instrum. Methods A **474**, 108 (2001); JLab Technical Note, JLAB-TN-00-016 (2000).

[64] R. Michaels and B. Reitz, *Trigger Programming for Hall A Spectrometers* (unpublished); http://hallaweb.jlab.org/equipment/daq/triggercoinc.html.

[65] http://hallaweb.jlab.org/equipment/detectors/fithteen.gif.

[66] E. J. Brash *et al.*, Nucl. Instrum. Methods A **487**, 346 (2002).

[67] D. W. Higinbotham *et al.*, Nucl. Instrum. Methods A **414**, 332 (1998).

[68] G. J. Lolos *et al.*, Nucl. Instrum. Methods A **385**, 403 (1997).

[69] B. Wojtsekhowski, *Threshold Čerenkov counters for Pions and Kaons*, poster for INPC 2001 (unpublished).

[70] L. Lagamba, R. Iommi, and B. Wojtsekowski, Jlab Technical Notes, JLab-TN-00-010 (2000); A. White, Jlab Technical Notes, JLab-TN-99-026 (1999).

[71] *Status Report on Activities in Hall A - 1999*, edited by E. J. Brash, R. D. Ransome, and Kees de Jager, (2000).

[72] J. McCann, L. Taub, and B. Wojtsekowski, Jlab Technical Notes, JLab-TN-98-033 (1998).

[73] Eric Brown, private communication.

[74] C. Zorn, *Efficiency Tests of Photonis Imaging Phototubes for Aerogel-radiator Cerenkov Detector*, Jefferson Lab Dectector Group Report, (1999).

[75] K. Armen, http://www.jlab.org/~armen/sh_web_page/welcome.html.

[76] http://www.aps.anl.gov/epics.

[77] http://coda.jlab.org; http://hallaweb.jlab.org/equipment/acquisition.html.

[78] F. Xiong, Ph.D. Thesis, Massachusetts Institute of Technology, (2002).

[79] http://hallaweb.jlab.org/espace/index.html.

[80] CERN Program Library, http://wwwasdoc.web.cern.ch/asd/index.html.

[81] CERN Program Library Long Writeup Y250, http://wwwasdoc.web.cern.ch/wwwasdoc/hbook_html3/hboomain.html.

[82] Physics Analysis Workstation, http://paw.web.cern.ch/paw.

[83] http://www.physics.odu.edu/~ulmer/mceep/mceep.html.

[84] W. Xu and L. Y. Zhu, private communication.

[85] N. Liyanage, private communication.

[86] N. Liyanage, JLab Technical Note, JLAB-TN-01-049 (2001).

[87] M. Rvachev, JLab Technical Note, JLAB-TN-01-055 (2001).

[88] http://www.jlab.org/~lerose/r-function.html.

[89] Z. Chai, Ph.D. Thesis, Massachusetts Institute of Technology, (2003).

[90] J. Arrington, X. Jiang, X. Zheng, and L. Y. Zhu, private communication.

[91] B. Rossi, *High-Energy Particles*, Prentice-Hall Press, New York,(1952).

[92] A. Deur, JLab Technical Note, Jlab-TN-98-028 (1998).

[93] H. Gao, private communication.

[94] J. P. Chen, private communication.

[95] J. Arrington, http://www.jlab.org/~johna/.

[96] J. Arrington, private communication.

[97] K. Garrow *et al.*, Phys. Rev. C **66**, 044613 (2002).

[98] H. Gao, R. J. Holt, and V. R. Pandharipande, Phys. Rev. C **54**, 2779 (1996).

[99] P. Jain, private communication.

[100] F. Xiong, private communication.

[101] R. Michaels, http://hallaweb.jlab.org/equipment/daq/dtime_faq.html.

[102] *Status Report on Activities in Hall A - 2001*, edited by Adam J. Sarty and Kees de Jager, (2002).

[103] M. K. Jones, http://www.jlab.org/~jones/e97111/report_on_deadtime.ps.gz.

[104] R. Wiringa, private communication.

[105] H. Arenhövel, private communication.

[106] R. Machleidt *et al.*, Phys. Rep. **149**, 1(1987).

[107] R. Machleidt, *Advances in Nucl. Phys.*, Vol **19**, (1989).

[108] D. Dutta, private communication.

[109] G. R. Farrar, K. Huleihel, and H. Zhang, Nucl. Phys. B **349**, 655 (1991).

[110] H.-J. Besch *et al.*, Z. Phys. C **16**, 1 (1982).

[111] R. Schumacher, private communication.

[112] S. J. Brodsky, J. R. Hiller, Chueng-Ryong Ji, and G. A. Miller, Phys. Rev. C **64**, 055204 (2001).

[113] JLab experiment E02-010, spokespersons: D. Dutta, H. Gao, and R. J. Holt, (2002).

[114] S. Capstick, Phys. Rev. D **46**, 2864 (1992); S. Capstick and W. Roberts, Phys. Rev. D **49**, 4570 (1994).

[115] I. I. Strakovsky, private communication; R. A. Arndt *et al.*, nucl-th/0205067, (2002); http://gwdac.phys.gwu.edu/.

[116] I. I. Strakovsky, private communication; S. S. Kamalov, *et al.*, Phys. Rev. C **64**, 032201 (2001)(A dynamical model); D. Drechsel, *et al.*, Nucl. Phys. A **645**, 145 (1999)(a unitary isobar model); http://www.kph.uni-mainz.de/MAID/. MAID2001 refers to the Nov. 2001 version of the MAID solution from S. S. Kamalov.

[117] H. Xiang, Proceedings for QNP2002: Quarks and Nuclear Physics (Julich, Germany), (2002).

[118] H. Xiang, private communication.

[119] Z. Bar-Yam *et al.*, Phys. Rev. Lett. **19**, 40 (1967).

[120] P. Heide *et al.*, Phys. Rev. Lett. **21**, 248 (1968).

[121] H. W. Huang, R. Jakob, P. Kroll, and K. Passek-Kumerički, hep-ph/0309071, (2003).

[122] M. Diehl, T. Feldmannn, H. W. Huang, and P. Kroll, Phys. Rev. D **67**, 037502 (2003).

[123] Hall C collaboration, *Hall C 12 GeV Upgrade Conceptual Design Report*, (2002).

[124] D. Dutta *et al.*, Phys. Rev. C **68**, 021001 (2003).